

Resonance Production in Two-Photon Collisions



R.C.W. van Gulik

Resonance Production
in Two-Photon Collisions

cover: Digitale bewerking van een foto van de zonsondergang bij Katwijk aan Zee, genomen door K.L. Refos.

©Shaker Publishing 2001

All rights reserved. No part of this publication may be reproduced, stored in a retrieval system, of transmitted, in any form or means, electronic, mechanical, photocopying, recording or otherwise, without the prior permission of the publishers.

Printed in the Netherlands.

ISBN 90-423-0175-9
Shaker Publishing BV
St. Maartenslaan 26
6221 AX Maastricht
Tel.: 043-3500424
Fax: 043-3255090
<http://www.shaker.nl>

Resonance Production in Two-Photon Collisions

PROEFSCHRIFT

Ter verkrijging van
de graad van Doctor aan de Universiteit Leiden,
op gezag van Rector Magnificus Dr. D.D. Breimer,
hoogleraar in de faculteit der Wiskunde en
Natuurwetenschappen en die der Geneeskunde,
volgens besluit van het College voor Promoties
te verdedigen op donderdag 22 november 2001
te klokke 14.15 uur

door

Robert Christiaan Wilhelmus van Gulik

geboren te Vlaardingen in 1974

Promotiecommissie:

- Promotores: Prof. Dr. F.A. Berends
Prof. Dr. F.L. Linde (Universiteit van Amsterdam)
- Referent: Prof. Dr. F.C. Erné (Universiteit Utrecht)
- Overige leden: Dr. G.J. Bobbink (NIKHEF/CERN)
Prof. Dr. A. Buijs (Universiteit Utrecht)
Prof. Dr. P.H. Kes
Prof. Dr. R.H.P. Kleiss (Katholieke Universiteit Nijmegen)
Dr. W.L.G.A.M. van Neerven

*Aan Karensa
Aan mijn ouders*

1. Introduction

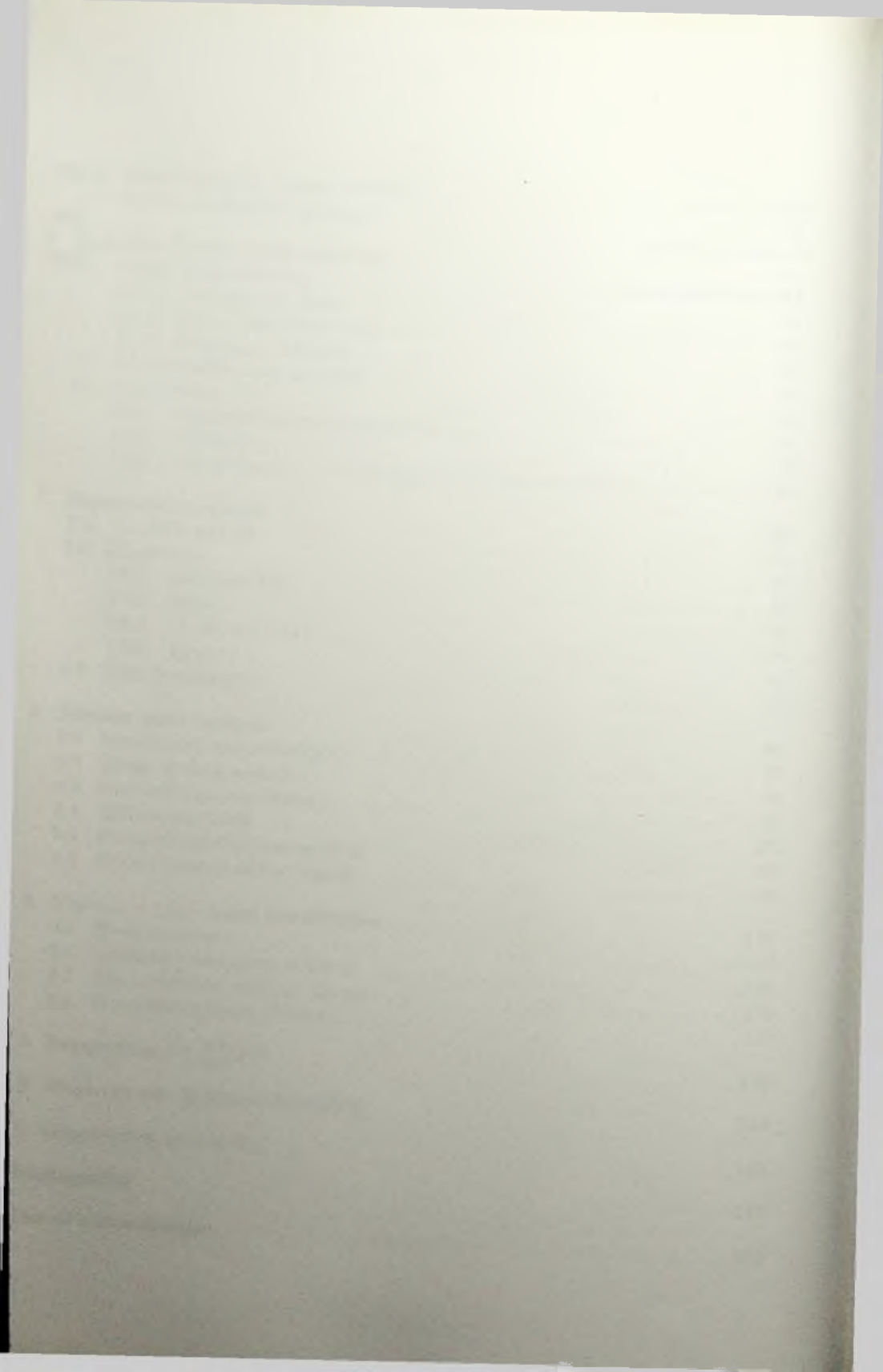
The purpose of this study is to investigate the effects of various factors on the performance of a system. The study is organized as follows: Section 2 describes the methodology used in the study. Section 3 presents the results of the study. Section 4 discusses the implications of the findings. Section 5 concludes the study.

Contents

1	General introduction and outline	1
2	Two-photon processes and resonances	3
2.1	Introduction	3
2.2	The process $e^+e^- \rightarrow e^+e^-X$	4
2.3	Two-photon reaction final states	4
2.4	Kinematics	6
2.5	The standard and the BGMS methods	10
2.6	Quarkonium	13
2.7	Two-photon width	15
2.8	Form factors	18
2.9	Resonance decays	20
2.10	Experimental status	21
2.10.1	Quarkonia and resonance masses	21
2.10.2	Resonance decays and two-photon widths	21
2.10.3	Missing mass analyses	23
2.10.4	Form factors	24
2.10.5	Helicity contributions	25
3	The resonance production mechanism	27
3.1	Theoretical framework	27
3.2	Off-shell two-photon decay amplitudes	27
3.3	The helicity decay amplitude	33
3.4	Widths for on-shell two-photon decays	35
3.5	Form factors in two-photon production	37
4	Construction of $\sum \mathcal{M} ^2$	43
4.1	$\sum \mathcal{M} ^2$ in terms of invariants	43
4.2	Weyl-van der Waerden formalism	45
4.3	Improved Weyl-van der Waerden formalism	48
4.4	Numerical stability	49
5	Density matrices	51
5.1	Production of the resonance	51
5.2	Density matrices in the BGMS formalism	53

5.3	Transforming the density matrices	57
5.4	Density matrices for the decay	58
6	GaGaRes Monte Carlo generator	67
6.1	Monte Carlo technique	67
6.1.1	Crude Monte Carlo	68
6.1.2	Hit or miss Monte Carlo	68
6.1.3	Importance sampling	69
6.2	The GaGaRes event generator	70
6.3	Some results	75
6.3.1	Cross sections and distributions	75
6.3.2	Helicities	79
6.3.3	The process $e^+e^- \rightarrow e^+e^-\chi_{c2} \rightarrow e^+e^-J/\psi\gamma \rightarrow e^+e^-l^+l^-\gamma$	80
7	Experimental set-up	83
7.1	The LEP collider	83
7.2	L3 detector	85
7.2.1	SMD and TEC	87
7.2.2	ECAL	89
7.2.3	LUMI and VSAT	89
7.2.4	Triggers	90
7.3	Data processing	91
8	Missing mass analysis	93
8.1	Introduction and motivation	93
8.2	Monte Carlo generators	94
8.3	Pure missing mass analysis	95
8.4	QED backgrounds	102
8.5	Extended missing mass analysis	107
8.6	Missing mass search at high $W_{\gamma\gamma}$	112
9	The $\chi_{c2} \rightarrow \gamma J/\psi$ decay distribution	117
9.1	Event selection	117
9.2	Production and decay of the η'	118
9.3	The two-photon width of the χ_{c2}	124
9.4	Decay distributions of the χ_{c2}	132
A	Expressions for $\sum \mathcal{M} ^2$	135
B	Weyl-van der Waerden formalism	139
C	Suppression at low $W_{\gamma\gamma}$	143
	Bibliography	147
	List of abbreviations	155

Samenvatting	157
Curriculum Vitae	161
Acknowledgements	163



Chapter 1

General introduction and outline

Particle physics studies the basic building blocks of nature. In our present understanding matter is constructed from pointlike particles with spin $\frac{1}{2}$. Having half-integer spin they belong to the class of so-called fermions. These spin- $\frac{1}{2}$ building blocks can be distinguished in leptons and quarks. There are three families of both leptons and quarks. The forces between the fermions are mediated by gauge bosons, pointlike particles with an integer spin. The so-called Standard Model, an $SU(3) \otimes SU(2) \otimes SU(1)$ gauge theory, describes the interactions of three of the four known forces in nature: the electromagnetic force, the weak nuclear force and the strong nuclear force. In spite of theoretical efforts the fourth force, gravity, has not yet been included, but is orders of magnitude weaker than the other forces on the scale of elementary particle interactions. The gauge boson of the electromagnetic force is the well-known photon. The weak force is carried by the massive W^+ , W^- and Z^0 particles, whereas the massless gluons are the carriers of the strong force. All these gauge bosons are spin-1 particles. Besides the fermions and the gauge bosons the Standard Model contains one additional particle, the spinless Higgs boson, which generates the masses of the massive particles in the Standard Model. Except for the Higgs boson all elementary particles in the Standard Model have been observed. In table 1.1 an overview of all observed particles in the Standard Model is given.

In particle physics, most of the experimental facts are obtained from scattering experiments. Beams of particles (electrons, muons, neutrinos, protons or nuclei) collide with fixed targets or other beams. In the collisions other particles may be created, elementary particles with a pointlike structure or resonances which subsequently decay. The Standard Model describes the scattering processes between these elementary particles. In fact, perturbative quantum field theory often gives accurate predictions of the measurable quantities in the scattering processes. Examples are the line-shape of the Z -boson and the production of W^+W^- pairs in electron-positron collisions. The properties of resonances are less amenable to accurate calculations and at present often qualitative considerations are needed, supplemented with some reasonable quantitative assumptions. This is a consequence of the fact that also non-perturbative effects have to be taken into account.

This thesis describes results obtained in both theoretical and experimental research. The process studied is the creation of a resonance by the collision of two photons. On one hand theoretical predictions for such a resonance production are derived, both in analytic terms and in terms of a so-called event generator. On the other hand actual experimental

Fermions					
Leptons			Quarks		
Flavour	Mass	Charge	Flavour	Mass	Charge
ν_e	$< 10^{-8}$	0	up (u)	0.003	$+\frac{2}{3}$
e	5.11×10^{-4}	-1	down (d)	0.006	$-\frac{1}{3}$
ν_μ	$< 2 \times 10^{-4}$	0	charm (c)	1.3	$+\frac{2}{3}$
μ	0.106	-1	strange (s)	0.1	$-\frac{1}{3}$
ν_τ	< 0.02	0	top (t)	175	$+\frac{2}{3}$
τ	1.77	-1	bottom (b)	4.3	$-\frac{1}{3}$

Bosons			
Force	Name	Mass	Charge
Electromagnetic	γ	0	0
Weak Force	Z^0	91.187	0
	W^+	80.4	+1
	W^-	80.4	-1
Strong Force	g	0	0

Table 1.1: Overview of the observed elementary particles in the Standard Model. The masses are given in GeV and the charges are given in units of e . All fermions have an antiparticle with identical mass and spin, but with opposite charge.

data for photon-photon collisions is extracted from the L3 data tapes and analyzed in various ways. One tool in the analyses is the above mentioned event generator, a Monte Carlo program which simulates the real physics process of creating such a resonance.

In the following chapter an introduction is given to two-photon collisions, to resonances consisting of quark-antiquark pairs and to the experimental knowledge. Chapter 3 describes the theoretical framework and some analytic results for resonance production in a two-photon reaction. Different techniques for the calculation of the square of the corresponding matrix elements are discussed in chapter 4. In chapter 5 density matrices, which are needed in the description of the decay of the resonance, are introduced. These theoretical results are implemented in the GaGaRes Monte Carlo generator which is presented in chapter 6. The relevant facts of the L3 detector and the LEP collider at CERN are summarized in chapter 7. Data collected with this detector has been used in two different but complementary analyses involving resonance production in two-photon physics. In chapter 8 a missing mass analysis to search for heavy resonances is presented, resulting in upper limits for the two-photon widths of these states. In chapter 9 the two-photon width of the χ_{c2} resonance has been determined by looking at its decay channel into a J/ψ and a photon, where the J/ψ subsequently decays into an electron-positron pair or into a muon pair.

Chapter 2

Two-photon processes and resonances

2.1 Introduction

The scattering of light by light in the Standard Model is a clear manifestation of the fact that this theory describes nature in terms of interacting quantized fields. This is in contrast to the classical Maxwell theory according to which light waves traverse one another without being scattered, because the classical Maxwell equations are linear in the electromagnetic field tensor.

The scattering of light by light in the quantized theory is in lowest order depicted by the diagrams in figure 2.1.

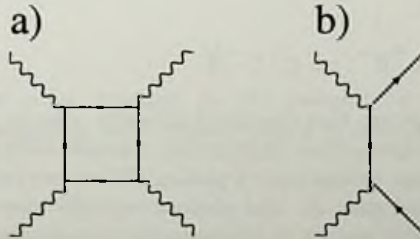


Figure 2.1: *Lowest order diagrams for elastic photon-photon scattering (a) and inelastic photon-photon scattering (b), leading to an e^+e^- pair.*

The cross section for elastic photon-photon scattering was first calculated by Euler and Kockel [1]. For visible light it is extremely small, of the order of 10^{-30} nb. However, for photons with energies near the electron mass it increases to approximately 100 nb. At these energies inelastic photon-photon scattering also takes place. The latter cross section peaks at the order of 100 mb for photon energies just above the electron mass [2,3].

Experimental devices for the study of high energetic photon-photon interactions with sufficiently high luminosity are however hard to realize. This may change with the advent

of linear electron-positron accelerators where Compton back-scattering may create intense beams of high energy photons [4, 5].

Photon-photon scattering can also be investigated when one or both of the photons are virtual. This makes an e^+e^- collider a possible means to study photon-photon scattering. Both leptons, being moving charged particles, act as sources of virtual photons. These off-shell photons subsequently scatter. This process is described by the following reaction formula,

$$e^+e^- \rightarrow e^+e^-\gamma\gamma \rightarrow e^+e^-X, \quad (2.1)$$

where the γ 's are the off-shell photons and X is the final state of the photon-photon collision.

In 1960 Low [6] proposed to measure the π^0 lifetime in this two-photon mechanism and Calogero and Zemach [7] calculated the reaction for $X = \pi^+\pi^-$. At the end of the 1960s the first experimental results from Novosibirsk and Frascati [8, 9] were presented, which concerned the final state $X = e^+e^-$. In the 1970s and 1980s two-photon physics became a very active field. At the DORIS and PETRA colliders in Hamburg as well as the SPEAR and PEP colliders in Stanford many two-photon final states were studied.

The most recent studies in the field of two-photon physics have been carried out at three e^+e^- colliders, LEP2 at CERN, CESR at Cornell and PEP II at Stanford. The LEP2 collider operated until 2000 at centre-of-mass (CM) energies in the range 91-209 GeV, whereas the CESR and PEP II colliders operate at a CM energy of the $\Upsilon(4S)$ mass.

It should, however, be noted that these colliders were designed and constructed to study primarily other processes. The LEP2 collider was constructed for the production of Z^0 and W^\pm bosons and the search for the Higgs particle. CESR and PEP II on the other hand are B factories.

2.2 The process $e^+e^- \rightarrow e^+e^-X$

Figure 2.2 depicts the four diagrams that contribute in lowest order to the process $e^+e^- \rightarrow e^+e^-X$. In figure 2.2a the multiperipheral diagram that represents the genuine two-photon reaction is given. Both incoming leptons emit a photon. These two (virtual) photons subsequently react to form the final state X . The photons typically have a small energy and are emitted at a small angle with respect to the incoming leptons. Qualitative arguments for this behaviour will be given in section 2.4. Since the photons carry a conserved multiplicative quantum number, the charge conjugation quantum number, which takes for each photon the value $C = -1$, the final state possesses the value $C = +1$.

The other three diagrams in 2.2 are all related to a bremsstrahlung process and to the basic processes of Bhabha scattering, electron-positron annihilation into photons (conversion) or into a fermion pair. In these diagrams the final state X must be C odd, so when a final state with $C = +1$ is studied, they do not contribute.

2.3 Two-photon reaction final states

In the present e^+e^- colliders the following final states in a two photon reaction $\gamma\gamma \rightarrow X$ can be studied:

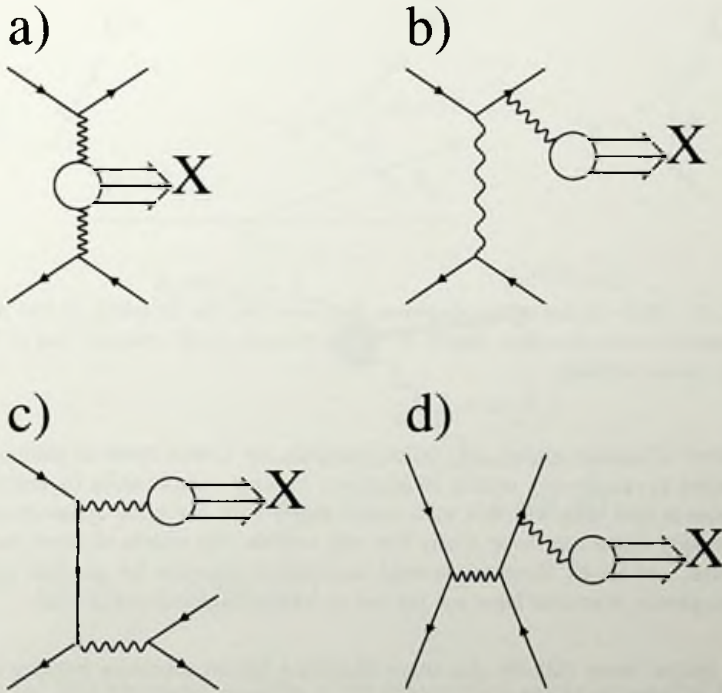


Figure 2.2: Lowest order diagrams for the process $e^+e^- \rightarrow e^+e^-X$. a) Multiperipheral b) (Bhabha scattering with) bremsstrahlung c) conversion and d) annihilation (with bremsstrahlung).

- Lepton pair production: $X = l^+l^-$ ($l = e, \mu, \tau$). In lowest order this reaction is completely described by quantum electrodynamics (QED). Note that in the process $e^+e^- \rightarrow e^+e^-l^+l^-$ all diagrams in figure 2.2 have to be included and that also electroweak diagrams contribute [10,11]. Also $\mathcal{O}(\alpha)$ radiative corrections to the two-photon part of these processes have been taken into account in the calculations [10].
- Meson resonance production: $X = R$. A neutral, C -even resonance is produced exclusively. This process will be the subject of this thesis, with the focus on resonances consisting of the ‘heavy’ c and b quarks. The resonances are unstable and will subsequently decay into photons, leptons and lighter hadrons.
- Hadron production: $X = \text{hadrons}$. This contains all the hadronic final states excluding the single resonance production mentioned above. In principle this also contains the more exotic quantum chromodynamics (QCD) states like gluonium and $q\bar{q}q\bar{q}$

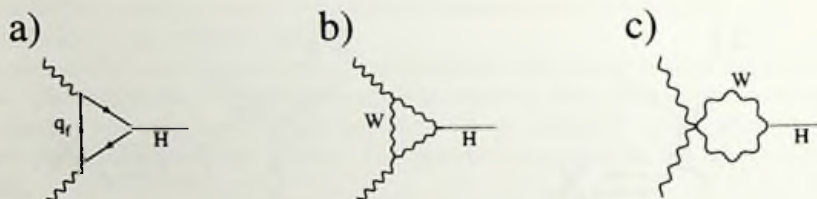


Figure 2.3: Three lowest order diagrams that describe the coupling of two photons to a Higgs particle in the Standard Model. a) quark triangle, b) W triangle and c) W loop with a quartic gauge coupling.

states. Gluonium states, also called glueballs, are bound states of gluons that are expected to couple very weakly to photons. Another complication to observe gluonium states is that they will mix with meson states with the same quantum numbers. As the $q\bar{q}q\bar{q}$ states can decay easily into two mesons, the widths of these states are very broad. Although there are several candidates, searches for glueball production in two-photon reactions have not yet led to compelling evidence [12, 13].

In a future linear collider also other Standard Model processes become accessible in two-photon reactions [4, 5, 14]:

- W -pair production: $\gamma\gamma \rightarrow W^+W^-$.
- Higgs-boson production: $\gamma\gamma \rightarrow H$. When the Higgs boson is not too heavy ($M_H < 350$ GeV) it will be possible to study its total width and different branching ratios. In the Standard Model the Higgs boson does not couple directly to photons, because the photons are massless. The lowest order loop diagrams contributing to Higgs-boson production are given in figure 2.3. Note that in chapter 8 results of such a search for the Higgs boson in the L3 data are presented.
- $t\bar{t}$ pair production: $\gamma\gamma \rightarrow t\bar{t}$. This requires very high $\gamma\gamma$ CM energies.

2.4 Kinematics

As mentioned above, we will study resonance production in a two-photon reaction. This process is in lowest order described by a multiperipheral diagram. In figure 2.4 this diagram is shown with all the relevant kinematic variables.

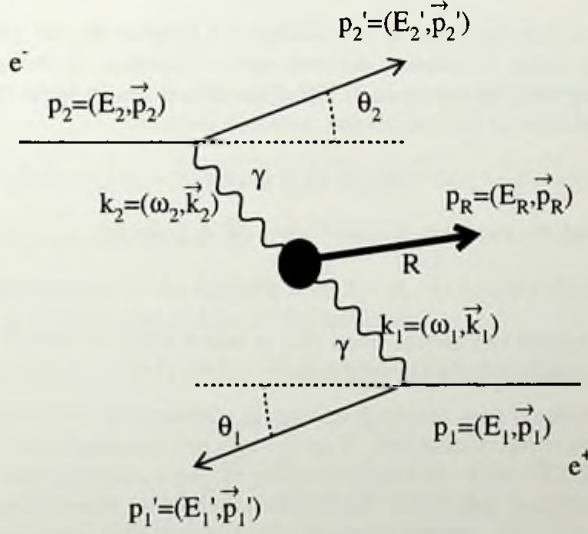


Figure 2.4: *The kinematic variables in the process $e^+e^- \rightarrow e^+e^-\gamma\gamma \rightarrow e^+e^-R$.*

This corresponds to the following reaction formula

$$\begin{aligned} e^+(p_1) + e^-(p_2) &\rightarrow e^+(p'_1) + e^-(p'_2) + \gamma(k_1) + \gamma(k_2) \\ &\rightarrow e^+(p'_1) + e^-(p'_2) + R(p_R). \end{aligned} \quad (2.2)$$

The four-momenta $p_1 = (E_1, \vec{p}_1)$ and $p_2 = (E_2, \vec{p}_2)$ correspond to the incoming positron and electron respectively¹, whereas $p'_1 = (E'_1, \vec{p}'_1)$ and $p'_2 = (E'_2, \vec{p}'_2)$ are those of the outgoing positron and electron. The four-momenta of the intermediate photons $k_1 = (\omega_1, \vec{k}_1)$ and $k_2 = (\omega_2, \vec{k}_2)$ are related to the external four-momenta by

$$k_i = p_i - p'_i. \quad (2.3)$$

These two photons subsequently react to form a resonance with four-momentum p_R

$$p_R = k_1 + k_2 = p_1 + p_2 - p'_1 - p'_2. \quad (2.4)$$

¹Throughout this thesis we will work in natural units, i.e. we have set $\hbar = c = 1$. We use the standard metric $\text{diag}(g^{\mu\nu}) = (+1, -1, -1, -1)$. The totally anti-symmetric Levi-Civita tensor is defined by $\epsilon_{0123} = +1$. The Feynman rules as given in [15] have been used.

The virtuality Q_i of an intermediate photon is defined by

$$Q_i^2 \equiv -k_i^2 = -(p_i - p'_i)^2. \quad (2.5)$$

The virtuality, or invariant mass of the photon, is a measure for the 'off-shellness' of the photon. A real photon is massless and will have a vanishing virtuality. As the virtual photons are space-like, the sign in (2.5) forces the virtualities Q_i to be real.

The invariant mass of the two-photon system is given by

$$W_{\gamma\gamma} = p_R^2 = (k_1 + k_2)^2. \quad (2.6)$$

The total available energy in the lab-frame, \sqrt{s} , is given by

$$s = (p_1 + p_2)^2. \quad (2.7)$$

Note that for a typical two photon event $W_{\gamma\gamma}$ is only a small fraction of \sqrt{s} .

Some additional invariants can be defined

$$s' = (p'_1 + p'_2)^2, \quad (2.8)$$

$$u = (p_1 - p'_2)^2, \quad (2.9)$$

$$u' = (p_2 - p'_1)^2, \quad (2.10)$$

and as equivalents of Q_i^2

$$t = (p_1 - p'_1)^2, \quad (2.11)$$

$$t' = (p_2 - p'_2)^2. \quad (2.12)$$

These invariants satisfy

$$s + s' + t_1 + t_2 + u + u' = W_{\gamma\gamma}^2 + 8m_e^2, \quad (2.13)$$

where m_e is the electron mass.

In the lab-frame one can chose the following parametrization

$$\begin{aligned} p_1 &= (E_b, 0, 0, -P_b), \\ p_2 &= (E_b, 0, 0, P_b), \\ p'_1 &= (E'_1, |\vec{p}'_1| \sin \theta_1 \cos \phi_1, |\vec{p}'_1| \sin \theta_1 \sin \phi_1, -|\vec{p}'_1| \cos \theta_1), \\ p'_2 &= (E'_2, |\vec{p}'_2| \sin \theta_2 \cos \phi_2, |\vec{p}'_2| \sin \theta_2 \sin \phi_2, |\vec{p}'_2| \cos \theta_2), \\ p_R &= (E_R, |\vec{p}_R| \sin \theta_R \cos \phi_R, |\vec{p}_R| \sin \theta_R \sin \phi_R, |\vec{p}_R| \cos \theta_R). \end{aligned} \quad (2.14)$$

This means that the z -axis is along the direction of the incoming electron. The x - and y -axes are chosen such that the xz -plane is the accelerator ring plane and the y -axis is perpendicular to that plane and is pointing upwards. In these formulae E_b is the energy of the incoming leptons and P_b their momentum, given by

$$P_b = \sqrt{E_b^2 - m_e^2}. \quad (2.15)$$

Note that the choice of parameters in (2.14) is such that we have defined the z -components of the positron with an explicit minus sign.

This parametrization allows us to find more explicit expressions for the invariants

$$s = 4E_b^2, \quad (2.16)$$

$$Q_i^2 = 2(E_b E_i' - P_b |\vec{p}_i'| \cos \theta_i - m_e^2) \approx 2E_b E_i' (1 - \cos \theta_i) = 4E_b E_i' \sin^2 \left(\frac{\theta_i}{2} \right), \quad (2.17)$$

$$\begin{aligned} W_{\gamma\gamma} &= \sqrt{2m_e^2 + 4(E_b - E_1')(E_b - E_2') - 2E_1' E_2' - 2|\vec{p}_1'| |\vec{p}_2'| \cos \theta_{12}} \\ &\approx 2\sqrt{\omega_1 \omega_2 - E_1' E_2' \cos^2 \frac{\theta_{12}}{2}}. \end{aligned} \quad (2.18)$$

The approximations are valid in the limit $E_b > E_i' \gg m_e$. In formula (2.18) the angle θ_{12} is the angle between the outgoing leptons in the lab-frame

$$\cos \theta_{12} = -\cos \theta_1 \cos \theta_2 - \sin \theta_1 \sin \theta_2 \cos(\phi_1 - \phi_2 + \pi). \quad (2.19)$$

The propagators of the intermediate photons will appear as a product of the photon virtualities in the denominator of the expressions for the matrix elements squared. This is the most dominant dependence on the photon virtualities. From (2.17) it follows that the photons are emitted most probably, as was already mentioned in section 2.2, with low energy under a small angle with respect to the incoming lepton.

When the incoming lepton scatters over a large enough angle, so that it is detected in one of the (forward) detectors, this lepton is referred to as a tagged lepton. From the detected lepton the four-momentum, and thus the virtuality, of the associated intermediate photon can be reconstructed. On basis of the tags one can distinguish three kinds of two-photon events:

- No-tag events: Both scattered leptons escape detection.
- Single-tag events: One of the scattered leptons is detected. This allows the determination of the virtuality of the photon emitted by the tagged lepton.
- Double-tag events: Both leptons are detected. In this case not only the photon virtualities but also $W_{\gamma\gamma}$ can be reconstructed from the scattered leptons.

As for a tagged lepton the scattering angle of the outgoing lepton must be scattered over some minimal angle θ_{min} , the virtuality of the emitted photon becomes non-vanishing.

If one requires the virtuality to be above a certain threshold value, $Q_{i,threshold}^2$, this puts constraints on the minimum allowed scattering angle, $\theta_{i,min}$, as well on the minimum allowed energy, $E_{i,min}$

$$\theta_{i,min} = 2 \arcsin \left(\sqrt{\frac{Q_{i,threshold}^2 + 2m_e^2}{4E_b E_{i,max}}} \right), \quad (2.20)$$

$$E_{i,min} = \frac{Q_{i,threshold}^2 + 2m_e^2}{4E_b \sin^2 \left(\frac{\theta_{i,max}}{2} \right)}. \quad (2.21)$$

In these formulae $E_{i,max}$ and $\theta_{i,max}$ are the maximal allowed energy and scattering angle of the corresponding outgoing lepton. These constraints will be useful in keeping a Monte Carlo generator efficient when cuts on $Q_{i,threshold}^2$ are applied.

Another typical feature of two-photon reactions is that the two-photon rest frame² does, in general, not coincide with the lab-frame, but is boosted along an axis, which is often close to the z -axis. This can also be understood from the bremsstrahlung-like behaviour of the intermediate photons.

2.5 The standard and the BGMS methods

As pointed out, a two-photon reaction in an e^+e^- collider can be divided into two steps. First the incoming leptons both emit a photon. These two photons subsequently react to form a final state X . This allows one to derive a general expression for the cross section in terms of a sum over the different contributions with specific photon helicities, as has been done in the classical paper by Budnev, Ginzburg, Meledin and Serbo (BGMS) [16].

On the other hand one could refrain from stressing this intermediate two-photon step and calculate by standard methods directly the cross section for reaction (2.2). Chapters 4 and 5 will contain details about this standard calculation, whereas in this subsection and in chapters 3 and 5 the BGMS method is treated.

The matrix element \mathcal{M} for reaction (2.2) can be written in the form

$$\mathcal{M} = \frac{e^2}{Q_1^2 Q_2^2} j_1^\mu j_2^\nu M_{\mu\nu}. \quad (2.22)$$

The j_i 's are the lepton currents that couple to the intermediate photons. They are given by

$$j_1^\mu = j_1^\mu(\lambda_1, \lambda'_1) = \bar{v}_{\lambda_1}(p_1) \gamma^\mu v_{\lambda'_1}(p'_1), \quad (2.23)$$

$$j_2^\mu = j_2^\mu(\lambda_2, \lambda'_2) = \bar{u}_{\lambda'_2}(p'_2) \gamma^\mu u_{\lambda_2}(p_2), \quad (2.24)$$

where the λ_i 's denote the helicities of the corresponding external leptons. The tensor $M_{\mu\nu}$ denotes the scattering amplitude for $\gamma\gamma \rightarrow X$.

The cross section follows from this matrix element by

$$d\sigma = \frac{(2\pi)^4 \delta^{(4)}(k_1 + k_2 - P)}{4\sqrt{(p_1 \cdot p_2)^2 - m_e^4}} \frac{1}{4} \sum |\mathcal{M}|^2 \frac{d^3\vec{p}'_1}{(2\pi)^3 2E'_1} \frac{d^3\vec{p}'_2}{(2\pi)^3 2E'_2} d^{3n}\Gamma. \quad (2.25)$$

In this expression the square of the matrix element is summed over the outgoing lepton helicities and averaged over the incoming lepton helicities, i.e. we are considering unpolarized lepton beams. In chapters 4 and 5 a direct calculation of $\sum |\mathcal{M}|^2$ will be given, here we shall introduce the intermediate step of virtual photons characterized by a density matrix ρ . Using the helicity summations, the lepton currents yield

$$L_i^{\alpha\beta} \equiv \sum_{\lambda_i, \lambda'_i} j_i^\beta(\lambda_i, \lambda'_i) j_i^{\alpha*}(\lambda_i, \lambda'_i) = 4 \left(p_i^\alpha p_i^\beta + p_i'^\alpha p_i'^\beta - \frac{1}{2} Q_i^2 g^{\alpha\beta} \right). \quad (2.26)$$

²This frame is defined by the condition $\vec{k}_1 + \vec{k}_2 = \vec{0}$.

The quantity $d^{3n}\Gamma$ in (2.25) represents the phase space integration over the particles of the final state X . The four-momenta $q_i = (E_{q,i}, \vec{q}_i)$ of the n particles in this final state must satisfy $P = \sum_{i=1}^n q_i$ and the phase space volume element reads

$$d^{3n}\Gamma = \prod_i \frac{d^3\vec{q}_i}{(2\pi)^3 2E_{q,i}}. \quad (2.27)$$

The summation \sum in (2.25) also includes the summation over the polarizations of the n particles in the final state X .

Introducing $\rho_i^{\mu\nu} \equiv L_i^{\mu\nu}/(2Q_i^2)$ the cross section can be expressed as

$$d\sigma = \frac{\alpha^2}{Q_1^2 Q_2^2} \rho_1^{\mu\mu'} \rho_2^{\nu\nu'} \delta^{(4)}(k_1 + k_2 - P) \frac{\sum M_{\mu\nu} M_{\mu'\nu'}^*}{\sqrt{(p_1 \cdot p_2)^2 - m_e^4}} \frac{d^3\vec{p}_1}{2E_1'} \frac{d^3\vec{p}_2}{2E_2'} d^{3n}\Gamma, \quad (2.28)$$

where we have introduced the fine structure constant $\alpha = e^2/(4\pi)$ and have carried out the lepton helicities summation in (2.26).

At this point it is convenient to introduce the hadronic tensor $W_{\mu'\nu'\mu\nu}$

$$W_{\mu'\nu'\mu\nu} = \frac{1}{2}(2\pi)^4 \int \delta^{(4)}(k_1 + k_2 - P) \sum M_{\mu'\nu'}^* M_{\mu\nu} d^{3n}\Gamma, \quad (2.29)$$

where \sum denotes the sum over polarizations in the final state X .

One may wonder how many independent cross section structures arise in (2.28) when one sums over all polarizations and also integrates over the phase space of the n particles. One way to obtain this number is first to list the independent structures of the tensor $W_{\mu'\nu'\mu\nu}$. A priori this fourth rank tensor has $256 (= 4^4)$ elements, but this number is reduced to 10 by applying electromagnetic current conservation to both indices of $M_{\mu\nu}$ and consequently to $W_{\mu'\nu'\mu\nu}$. It can be seen by constructing the most general tensor $W_{\mu'\nu'\mu\nu}$ from the available vectors k_1, k_2 and the metric tensor $g_{\mu\nu}$. These tensorial structures are now contracted with the specific tensors ρ in (2.28). It then turns out that two contractions vanish and that four contractions lead twice to the same scalar structure. In other words, only 6 independent functions arise in the cross section in (2.28).

Another way of obtaining this number of independent structures is to count first the photon helicity amplitudes and then the cross sections. The virtual photons have helicities m and n , which can take the values $\pm, 0$ and the amplitude can be transformed into $M_{mn,l}$, where l refers to all helicities in the state X . Parity conservation implies a relation between two amplitudes with opposite helicities, e.g.

$$M_{-m-n,-l} = \pm M_{mn,l}, \quad (2.30)$$

or

$$M_{-m-n,-l} = \pm M_{mn,l}^*, \quad (2.31)$$

depending on the conventions of the polarization vectors. Of course, when the amplitudes happen to be real or imaginary the latter case reduces to the former. In the actual model calculations in this thesis this happens to be the case (see equation (3.55)). For the quantity

$$M_{m'n'mn} = \frac{1}{2}(2\pi)^4 \int \delta^{(4)}(k_1 + k_2 + P) \sum_l M_{m'n',l}^* M_{mn,l} d^{3n}\Gamma \quad (2.32)$$

we anyhow have

$$M_{m'n'mn}^* = M_{mnm'n'}, \quad (2.33)$$

and depending on conventions

$$M_{-m'-n'-m-n} = M_{m'n'mn}, \quad (2.34)$$

or

$$M_{-m'-n'-m-n} = M_{mnm'n'}. \quad (2.35)$$

For pure initial states, only the five independent diagonal elements would be relevant

$$\begin{aligned} M_{++++} &= M_{----}, & M_{+--+} &= M_{-++-}, \\ M_{+0+0} &= M_{-0-0}, & M_{0+0+} &= M_{0-0-}, \\ M_{0000} & & & \end{aligned} \quad (2.36)$$

The fact that $\rho^{++} = \rho^{--}$ will give rise to the combination $M_{++++} + M_{+--+}$. This reduces the number of independent combinations to four. The photons are not in a pure state, so off-diagonal elements (ρ^{+0} and ρ^{+-}) occur, hence some off-diagonal elements of $M_{m'n'mn}$ arise, leading in the end to two more terms in the cross section. In BGMS [16] the result for the cross section is given in terms of transverse (T ; helicity ± 1) and scalar (S ; helicity 0) photons. They introduce six expressions

$$\begin{aligned} \sigma_{TT} &= \frac{1}{4\sqrt{X_{\gamma\gamma}}}(M_{++++} + M_{+--+}), \\ \sigma_{TS} &= \frac{1}{2\sqrt{X_{\gamma\gamma}}}M_{+0+0}, \\ \sigma_{ST} &= \frac{1}{2\sqrt{X_{\gamma\gamma}}}M_{0+0+}, \\ \sigma_{SS} &= \frac{1}{2\sqrt{X_{\gamma\gamma}}}M_{0000}, \\ \tau_{TT} &= \frac{1}{2\sqrt{X_{\gamma\gamma}}}M_{+--+}, \\ \tau_{TS} &= \frac{1}{4\sqrt{X_{\gamma\gamma}}}(M_{+0+0} + M_{0+0-}). \end{aligned} \quad (2.37)$$

Here $X_{\gamma\gamma}$ is the photon flux defined by

$$X_{\gamma\gamma} = (k_1 \cdot k_2)^2 - k_1^2 k_2^2. \quad (2.38)$$

As the variables in equation (2.37) are scalars, the only parameters on which they can depend are k_1^2 , k_2^2 and $W_{\gamma\gamma}^2$.

The cross section reads in terms of these elements

$$\begin{aligned} d\sigma &= \frac{\alpha^2}{16\pi^4 Q_1^2 Q_2^2} \sqrt{\frac{(k_1 \cdot k_2)^2 - k_1^2 k_2^2}{(p_1 \cdot p_2)^2 - m_e^2}} \left[4\rho_1^{++} \rho_2^{++} \sigma_{TT} \right. \\ &\quad + 2|\rho_1^{+-} \rho_2^{+-}| \cos(2\tilde{\phi}) \tau_{TT} + 2\rho_1^{++} \rho_2^{00} \sigma_{TS} + 2\rho_1^{00} \rho_2^{++} \sigma_{ST} \\ &\quad \left. + \rho_1^{00} \rho_2^{00} \sigma_{SS} - 8|\rho_1^{+0} \rho_2^{+0}| \cos(\tilde{\phi}) \tau_{TS} \right] \frac{d^3\vec{p}_1}{E_1} \frac{d^3\vec{p}_2}{E_2}. \end{aligned} \quad (2.39)$$

In this formula $\tilde{\phi}$ is the angle between the two scattering planes of the external leptons in the $\gamma\gamma$ rest frame. Explicit expressions for the photon density matrices can be found in

appendix D of [16]. In section 5.2 where the density matrix for resonance production is derived in the BGMS formalism it will be seen that its trace leads to equation (2.39). The derivations in section 5.2 will give a better understanding of the structure of (2.39). By introducing the fluxfactors \mathcal{L}_{AB} and Λ_{AB} we can rewrite this expression into

$$d\sigma = \int \sum_{A,B} (\mathcal{L}_{AB}\sigma_{AB} + \Lambda_{AB}\tau_{AB}) \frac{d^3\vec{p}'_1}{E'_1} \frac{d^3\vec{p}'_2}{E'_2}. \quad (2.40)$$

In this formalism different models for the process $\gamma\gamma \rightarrow X$ can be implemented in the explicit formulae for the σ 's and τ 's.

Note that in the limit $Q_i^2 \rightarrow 0$ all the longitudinal cross sections have to vanish as real photons do not have a longitudinal component. Only σ_{TT} and τ_{TT} contribute in this limit. However, if the detector is azimuthally symmetric and no explicit determination of $\vec{\phi}$ is performed, the contributions from τ_{TT} will average out.

In this limit the only two relevant lepton density matrices, ρ_1^{++} and ρ_2^{++} reduce to functions that only depend on the parameters of the associated photon. This allows one to factorize formula (2.39) into two independent contributions from two photon densities $N(\omega_1/E_b)$ and $N(\omega_2/E_b)$. If we define $x_i \equiv \omega_i/E_b$, change variables and perform the integrations over q_i^2 and ϕ_i , we can write this as

$$d\sigma = N(x_1)N(x_2)\sigma_{\gamma\gamma \rightarrow R}dx_1dx_2. \quad (2.41)$$

This factorization is known as the equivalent photon approximation³ (EPA) [16].

It should be noted that in the computer simulations we have not applied any of these approximations. The full expression for the total cross section in (2.39) has been used in the calculations. Nevertheless, the approximations are useful to reveal the overall dependence of the cross section on parameters like the beam energy and the mass of the produced resonance.

2.6 Quarkonium

The resonances produced in two-photon reactions are neutral, flavourless, C -even mesons. Mesons are bound states of a quark q and an anti-quark \bar{q} , which can be characterized by the flavours of the constituent quarks and by the wave function of the two-quark system. In the spectroscopic notation this state is denoted by $^{2S+1}L_J$, where $S(=0, 1)$ is the total spin of the $q\bar{q}$ system, $L(=0, 1, 2, \dots = S, P, D, \dots)$ is its orbital momentum and J the total angular momentum. The parity \mathcal{P} of a bound state of two fermions is given by $\mathcal{P} = (-1)^{L+1}$, whereas the charge conjugation is given by $C = (-1)^{L+S}$. As the mesons produced in two-photon reactions must be C -even, it means that for $S = 0, 1$ L is even, odd respectively and, therefore \mathcal{P} is -1 or $+1$ and the states $^1S_0, ^3P_J, ^1D_2, \dots$ can be produced. Besides this spectroscopic notation an alternative notation, J^{PC} , is used. Having a negative parity the 0^{-+} and 2^{-+} states are referred to as pseudoscalar or pseudotensor states.

For the resonances composed of the 'heavy' c and b quarks the binding energy is relatively small compared to the quark masses. In these resonances the relative velocity v of the

³It is also referred to as the Weizsäcker-Williams approximation [17, 18].

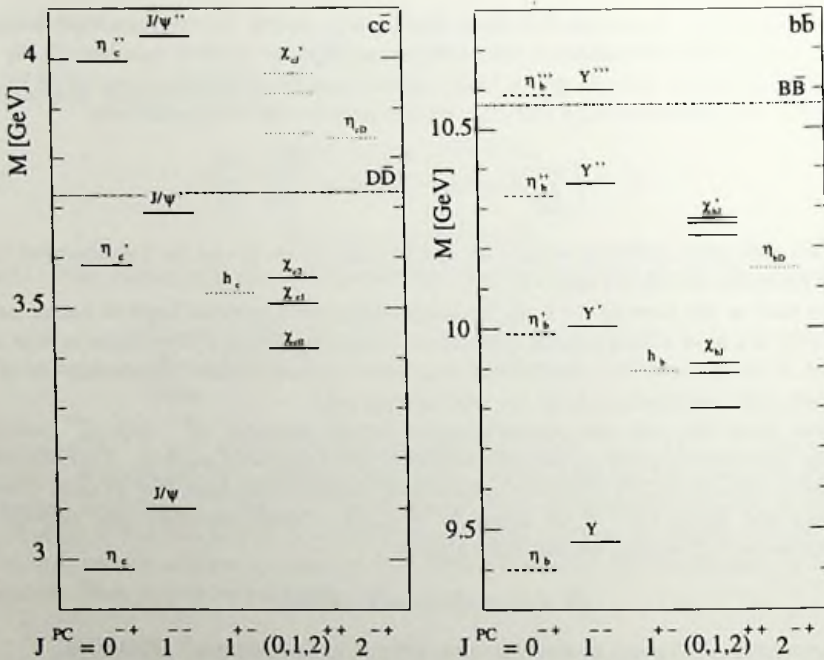


Figure 2.5: The mass spectra of a) charmonium and b) bottomonium. The states drawn with full lines have been experimentally observed. The masses of the the unobserved states (dotted lines) follow from theoretical calculations [19]. The dashed dotted line marks the transition between the bound states and quasi-bound states. Note that the states are allowed to decay radiatively to a lighter state with the selection rule $|\Delta L| = 1$.

quarks obeys $\langle v^2 \rangle \approx 0.3$ or 0.1 for the $c\bar{c}$ or the $b\bar{b}$ mesons respectively. As the relativistic corrections are suppressed by powers of v , one can describe in good approximation these bound states by a non-relativistic model.

Although of a completely different order of magnitude, the mass spectra of these bound states strongly resemble the spectrum of another bound state, that of an electron and a positron, positronium. In analogy the bound states of heavy quarks are called quarkonium states. More specifically the $c\bar{c}$ mesons are referred to as charmonium states and the $b\bar{b}$ mesons as bottomonium states. The mass spectra for charmonium and bottomonium are given in figure 2.5. In section 2.10.1 we will discuss the quarkonium spectra in more detail.

In positronium the interaction between the electron and the positron is purely electromagnetic. One can use the Coulomb interaction to describe this bound state to solve the non-relativistic Schrödinger equation exactly. For the quarkonium states some complications occur:

- The interaction between the $q\bar{q}$ is described by QCD. At present it is not known how to derive from QCD the potential for this bound state. Some educated guesses can be

made [20]. At short distance the quarks interact dominantly by one-gluon exchange and the system strongly resembles positronium, where the interaction is dominated by one-photon exchange. At short distances this should result in a Coulomb-like behaviour of the potential. At large distances we expect the potential to account for quark confinement, so the potential must increase to infinity. A potential that satisfies these requirements is

$$V(r) = -\frac{a}{r} + br. \quad (2.42)$$

However, other potentials that also satisfy the requirements cannot be ruled out by experimental data. Having chosen a potential one can try to solve the Schrödinger equation or the Bethe-Salpeter equation, its relativistic correct generalization [21]. Due to the more complex structure of the potential it is now impossible to find an exact analytical solution for the wave function, even for the non-relativistic Schrödinger equation. So numerical methods are needed.

- The relativistic corrections are not entirely negligible. Most authors [22–24] find that taking into account higher order relativistic corrections leads to a reduction of the predicted two-photon width.
- As the coupling parameter of QCD, α_s , is of the order of 0.3 for charmonium and 0.1 for bottomonium, higher order QCD corrections should be taken into account. This will result in correction factors on the two-photon width (see section 3.2).

Mesons composed of the light u , d and s quarks are relativistic systems. The potential model is not expected to give good two-photon widths for these mesons. However, in section 3.2 we will see that after having performed some minor corrections the potential model also provides reasonable predictions for the light mesons.

2.7 Two-photon width

Mesons are unstable particles. They decay with a mean life time $\tau = 1/\Gamma_{tot}$ to some final state X . In section 2.10.2 we will discuss the observed final states of some resonances. One of the possible decay channels for the C -even resonances is the decay into two photons. The two-photon width $\Gamma_{\gamma\gamma}(R)$ of the resonance R is related to the product of the branching ratio of this decay, $BR(R \rightarrow \gamma\gamma)$, and the total width $\Gamma_{tot}(R)$ of the resonance, $\Gamma_{\gamma\gamma}(R) = BR(R \rightarrow \gamma\gamma)\Gamma_{tot}(R)$.

The cross section for resonance production in a two-photon reaction can now be connected to this two-photon width $\Gamma_{\gamma\gamma}$. The decay of R into two unpolarized real photons yields⁴

$$\begin{aligned} \Gamma_{\gamma\gamma}(R) &= \frac{1}{2M} \int (2\pi)^4 \delta^{(4)}(P - k_1 - k_2) \frac{1}{2(2J+1)} \sum_{\lambda_i, \lambda_R} |\mathcal{M}|^2 \frac{d^3\vec{k}'_1}{(2\pi)^3 2\omega_1} \frac{d^3\vec{k}'_2}{(2\pi)^3 2\omega_2} \\ &= \int \frac{1}{(2\pi)^2 32M} \frac{1}{(2J+1)} \sum_{\lambda_i, \lambda_R} |\mathcal{M}|^2 d^2\Omega_1. \end{aligned} \quad (2.43)$$

⁴We are working in the rest frame of the resonance.

In these formulae \mathcal{M} is the matrix element representing this decay process. The λ_i 's are the helicities of the final state photons and λ_R is the helicity of the resonance. It should be noted that there is an extra factor $\frac{1}{2}$ due to the fact that we have two identical particles in the final state.

For a two-body decay of an unpolarized particle the matrix element does not depend on the angles. Performing the angular integrations yields

$$\Gamma_{\gamma\gamma}(R) = \frac{1}{32\pi M(2J+1)} \sum_{\lambda_i, \lambda_R} |\mathcal{M}|^2. \quad (2.44)$$

One can also consider the inverse process. The cross section for the production of a resonance from two unpolarized photons in the centre-of-mass frame of the two photons reads

$$\sigma_{\gamma\gamma \rightarrow R} = \int (2\pi)^4 \delta^{(4)}(k_1 + k_2 - p_R) \frac{1}{4\sqrt{X_{\gamma\gamma}}} \frac{1}{4} \sum_{\lambda_i, \lambda_R} |\mathcal{M}|^2 \frac{d^3\vec{p}_R}{(2\pi)^3 2M}. \quad (2.45)$$

The matrix element for this process can be obtained from the matrix element in the inverse process by crossing. In this way one can eliminate the matrix element from the expression for the cross section

$$\sigma_{\gamma\gamma \rightarrow R} = 8\pi^2 \frac{(2J+1)\Gamma_{\gamma\gamma}(R)}{M} \delta(p_R^2 - M^2). \quad (2.46)$$

Some remarks are in order. For resonances with a finite width, $\Gamma_{tot}(R)$, one should replace the δ function in (2.46) by a Breit-Wigner distribution for the invariant mass of the resonance⁵

$$BW(p_R^2; M, \Gamma_{tot}(R)) = \frac{1}{\pi} \frac{M\Gamma_{tot}(R)}{(p_R^2 - M^2)^2 + (M\Gamma_{tot}(R))^2}. \quad (2.47)$$

Inserting the expression (2.46) in the EPA (2.41) and performing the integrations yields

$$\sigma = 16\alpha^2 \ln^2\left(\frac{E_b}{m_e}\right) f\left(\frac{M}{2E_b}\right) \frac{(2J+1)\Gamma_{\gamma\gamma}(R)}{M^3}, \quad (2.48)$$

where

$$f(z) = (2+z^2) \ln\left(\frac{1}{z}\right) - (1-z^2)(3+z^2). \quad (2.49)$$

Equation (2.48) is referred to as the Low approximation [6]. The function f is called the Low function. Expression (2.48) is interesting as it gives some qualitative information on the behaviour of the total cross section. Firstly, the total cross section is proportional to the two-photon width of the produced resonance. Secondly, the total cross section increases logarithmically with the beam energy, which is in strong contrast to annihilation processes which typically fall off with $1/s$. Finally, there is a third power of the resonance mass in the denominator. Production rates for heavy resonances are strongly suppressed by this factor.

⁵The Breit-Wigner distribution satisfies

$$\lim_{\Gamma_{tot}(R) \rightarrow 0} BW(p_R^2; M, \Gamma_{tot}(R)) = \delta(p_R^2 - M^2).$$

So far we have only considered real photons. Any Q_i dependences have been disregarded. Taking into account these photon virtualities will lead to additional form factors, as will be discussed in the next section.

For spin-1 resonances the discussion is more complicated. The Landau-Yang theorem [25, 26] forbids a particle with spin 1 to decay into two identical massless spin-1 particles. As a consequence, these resonances have a vanishing two-photon width. Nevertheless, one can obtain an expression similar to (2.46) by introducing a reduced two-photon width $\bar{\Gamma}_{\gamma\gamma}(R)$ [27, 28]. This is the transverse-transverse two-photon width divided by a factor $[(k_1^2 - k_2^2)/(2k_1 \cdot k_2)]^2$.

Several models have been constructed to describe the decay of a resonance into two photons and to give numerical predictions for the two-photon widths:

- *Potential Models.* The heavy resonances can be described by a potential model, as has been mentioned in section 2.6. Such a model also predicts the two-photon widths. In the next chapter a potential model will be introduced where the photons are allowed to be virtual. The models will require as input the value of the L -th derivative of the radial part of the wave-function in the origin. As will be explained, the amplitude is factorized into a perturbative short distance part and a non-perturbative long distance part that describes the mesons in their bound state. The perturbative part gives the coupling to two free quarks to the outgoing photons. This is illustrated in figure 2.6.
- *NRQCD.* The potential models have several intrinsic problems. For P waves the factorization that is used is spoiled by logarithmic infrared divergences in the α_s^3 corrections. For S wave states logarithmic divergences also appear in some of the relativistic corrections. An alternative approach has been followed by Bodwin, Braaten and Lepage [29]. They have performed a rigorous non-relativistic QCD analysis. After having recast the analysis in an effective field theory, they also obtain a factorization into a long distance and a short distance contribution. In their approach the non-perturbative long distance term can be identified with well-defined matrix elements that can be obtained from fits to experimental data or lattice QCD calculations. Another advantage of the NRQCD approach is that the contributions from different orders of v can be clearly separated.

First attempts have been made to fit the NRQCD parameters to experimental data in hadronic and two-photon decays of the χ_c resonances [30].

- *Dispersion Relation Models.* Dispersion relations are used to construct QCD sum rules that relate the quarkonium states to other processes (see e.g. [31]).

In the potential model we can relate the two photon width $\Gamma_{\gamma\gamma}(R)$ of the resonance to the width for the decay of the resonance into two gluons, $\Gamma_{gg}(R)$. The only difference between the decay of a resonance to two photons or two gluons is the coupling constant at the vertices and an overall colour projection operator for the two-gluon decay to require the final state to be a colour singlet. This yields for the ratio

$$\mathcal{R}(R) = \frac{\Gamma_{gg}(R)}{\Gamma_{\gamma\gamma}(R)} = \left(\frac{\alpha_S}{\alpha}\right)^2 \frac{N_C^2 - 1}{4e_Q^2 N_C^2} = \left(\frac{\alpha_S}{\alpha}\right)^2 \frac{8}{36e_Q^4}, \quad (2.50)$$

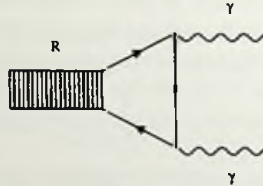


Figure 2.6: *The factorization of the decay of a resonance to two photons. The non-perturbative bound state R decays into two photons through the perturbative annihilation of the quark-antiquark pair.*

where N_C is the number of colours ($N_C = 3$), e_Q is the fractional charge of the quark that couples to the photon and α_S is the coupling constant of QCD. For charmonium ($e_Q = 2/3$) and bottomonium ($e_Q = -1/3$) this yields $\mathcal{R} = 9/8(\alpha_S/\alpha)^2$ respectively $\mathcal{R} = 18(\alpha_S/\alpha)^2$. Of course the gluons cannot be directly observed. In this decay a subsequent hadronization will take place.

2.8 Form factors

In the previous section we considered real photons. In two-photon processes however we are dealing with virtual photons. This requires some modifications of the formulae; an additional form factor has to be added to the expressions.

If one wants to determine the charge distribution of a static spinless object X , one can scatter a beam of electrons on X and compare the angular distribution of the scattered electrons $d\sigma/d\Omega$ to the analytically known differential cross section for the scattering of electrons to a static spinless point charge $(d\sigma/d\Omega)_{point}$. This is illustrated in figure 2.7 [32]. The form factor $F(k)$ is defined as

$$|F(k^2)|^2 = \frac{\left(\frac{d\sigma}{d\Omega}\right)}{\left(\frac{d\sigma}{d\Omega}\right)_{point}}, \quad (2.51)$$

where the momentum k is the momentum transfer from the scattered electron to X , $k = p - p'$. One can relate the form factor to the normalized charge distribution $\rho(\vec{x})$ of X by a Fourier transformation, as can be found in textbooks [32].

When the object X also carries a spin, one needs in general several form factors. A nice illustration is elastic electron-proton scattering ($e^- p \rightarrow e^- p$), where a photon emitted by the electron probes the proton. Two form factors are required, the electric and magnetic form

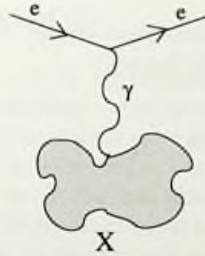


Figure 2.7: *The scattering of an electron on X by the exchange of a photon.*

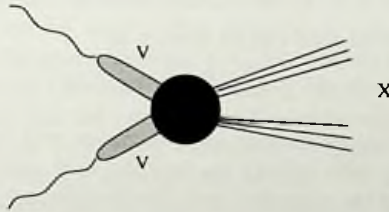


Figure 2.8: *In the VDM picture both photons fluctuate to a vector meson V. These vector mesons subsequently react to form the final state X.*

factors G_E and G_M . Experimental analysis shows that both form factors have the same k dependence: $G_E, G_M \approx (0.71)/((0.71)^2 - k^2)$, where k^2 should be taken in GeV^2 . This leads to the conclusion that both the charge and magnetic moment distribution have an exponential distribution in configuration space. For large energy transfers the photon may break up the proton. This is the region of inelastic electron-proton scattering ($e^-p \rightarrow e^-X$). The form factors for this inelastic process are related to the so-called structure functions and give information about the constituent quarks and gluons inside the proton.

To understand how the form factors come into play in two-photon physics, one could consider the process with the help of a model.

In this vector-meson dominance model (VDM) the two photons each couple to a 1^{--} vector meson with the same quantum numbers as the photon. These two mesons subsequently react to form some final state X. This is illustrated in figure 2.8. In this model each photon gives rise to a form factor

$$F(Q_i^2) = \frac{1}{1 + \frac{Q_i^2}{M_V^2}}, \quad (2.52)$$

where M_V is the mass of the vector meson to which the photon fluctuates. For the light resonances one uses the mass of the ρ meson. For charmonium states the mass of the J/ψ is substituted, whereas for bottomonium states the Υ should be used. The form factor in (2.52) is referred to as the pole-mass form factor.

In the next chapter we will elaborate more on the form factors and discuss some other models for the description of the form factors.

2.9 Resonance decays

The produced resonances are not stable and will decay to some final state X . In general, the resonances have a large number of decay channels and in most of the cases the measured decay channels do not yet add up to the total decay width of the resonance. In section 2.10.2 an overview of the decay channels and branching ratios of some resonances is given.

Let us consider the decay of a resonance into some final state X

$$e^+e^- \rightarrow e^+e^-R \rightarrow e^+e^-X. \quad (2.53)$$

The total amplitude for this process can be written as

$$\mathcal{M} = \sum_{\lambda_R} \xi(P, M) \mathcal{A}_{\lambda_R} \mathcal{D}_{\lambda_R}. \quad (2.54)$$

\mathcal{A}_{λ_R} describes the two-photon production of a resonance with helicity λ_R . \mathcal{D}_{λ_R} describes the decay of the resonance with helicity λ_R into the final state X . The factor $\xi(P, M)$ represents the propagator of the resonance and numerical factors. The total matrix element still depends on the external four-momenta. No implicit integrations over the outgoing momenta have been carried out at this stage. The square of the total matrix element is given by

$$\sum |\mathcal{M}|^2 = |\xi(P, M)|^2 \sum_{\lambda_R, \lambda'_R} \mathcal{A}_{\lambda_R \lambda'_R} \mathcal{D}_{\lambda_R \lambda'_R} = |\xi(P, M)|^2 \text{Tr}(\mathcal{A} \mathcal{D}^*). \quad (2.55)$$

The summation on the left hand side represents a summation over the helicities of the initial and final state particles. The quantities $\mathcal{A}_{\lambda_R \lambda'_R}$ and $\mathcal{D}_{\lambda_R \lambda'_R}$ are $\mathcal{A}_{\lambda_R} \mathcal{A}_{\lambda'_R}^*$ and $\mathcal{D}_{\lambda_R} \mathcal{D}_{\lambda'_R}^*$, summed over the helicities of all particles but the resonance. These are the density matrices for the production and decay of the resonance. For a spin- J resonance the density matrices are formed by $(2J+1) \times (2J+1)$ -matrices. The normalized density matrix for the production of a resonance is defined by

$$\rho_{\lambda\lambda'} = \frac{\sum_{\lambda_i} \mathcal{A}_{\lambda_i, \lambda} \mathcal{A}_{\lambda_i, \lambda'}^*}{\sum_{\lambda_i, \lambda_R} \mathcal{A}_{\lambda_i, \lambda_R} \mathcal{A}_{\lambda_i, \lambda_R}^*}, \quad (2.56)$$

where the λ_i are the helicities of all particles but the resonance. From this definition we can immediately derive three properties of this normalized density matrix:

- ρ is Hermitian.
- $\text{Tr}(\rho) = 1$, or alternatively, the diagonal elements of $\mathcal{A}_{\lambda_R \lambda'_R}$ add up to the total matrix element squared for the the production of the resonance.
- $|\rho_{ij}| \leq 1 \quad \forall \quad i, j$.

In section 5.1 we will show that the density matrix for the production of a resonance contains an additional symmetry. The diagonal elements of the density matrix are real and give the fraction of the contribution of the corresponding helicity to the total cross section. The density matrix $\rho_{\lambda\lambda'}$ can be calculated directly or in the BGMS-formalism, as will be done in chapter 5.

2.10 Experimental status

In this section we give an overview of the experimental status of two-photon physics and give a summary of the observed resonances. As we are mainly interested in resonances that can be produced in two-photon events, in most cases only the C -even resonances have been taken into account. As we are mainly interested in heavy resonances, most of our attention will be paid to them.

2.10.1 Quarkonia and resonance masses

The lightest charmonium state is the η_c meson. The charmonium state that was first observed simultaneously by two different experiments in 1974 is the J/ψ [33, 34], the 1^{--} state or in other words, the 3S_1 state. This observation was the first indication of the existence of quarks with the charm flavour. For charmonium the radial excitations with $n \geq 3$ lie above the mass of a $D\bar{D}$ pair⁶ to which they can decay. As a consequence, these states have a short lifetime and are referred to as quasi-bound states, whereas the states below this $D\bar{D}$ threshold can only decay radiatively to lighter charmonium states or via gluons to lighter hadrons, which is a suppressed process. The J/ψ is also known to decay through an intermediate virtual photon, that can subsequently decay into a lepton pair [13]. Together with the selection rule for radiative decay this gives the χ_{c2} the 'golden' decay channel $\chi_{c2} \rightarrow J/\psi\gamma \rightarrow l^+l^-\gamma$, which will be used in one of the analyses presented in this thesis.

The first bottomonium state that was discovered was also the 3S_1 state. This particle was called the $\Upsilon(1S)$ [35]. However, the lightest bottomonium state, 1S_0 , called the η_b , has not yet been seen. One of the analyses that is presented in this thesis, sets an upper limit on the two-photon width of the η_b meson by performing a missing mass analysis in a two-photon reaction. In bottomonium the radially excited states with $n \geq 4$ lie above the $B\bar{B}$ threshold and are called quasibound states. In figure 2.5 the spectra for charmonium and bottomonium are given.

By analogy, a bound state of a top(t) and an anti-top quark(\bar{t}) should be called a toponium state. However, the top quark is because of its high mass kinematically allowed to decay to a real W boson ($t \rightarrow W^+b$), which results in an extremely short lifetime. As a matter of fact, the lifetime is shorter than the revolution time of the toponium state. This makes it meaningless to speak of a bound state [36].

In table 2.1 a summary of all relevant C even resonances together with their masses is given. The masses for the observed resonances are taken from [13]. The masses of resonances that have not yet been seen have been taken from theoretical calculations [19, 37].

2.10.2 Resonance decays and two-photon widths

The total widths of the resonances that have been observed are collected in table 2.2. The values were taken from [13].

⁶A D is a bound state of a c quark with a lighter quark (u, d, s): $D^+ = c\bar{d}$, $D^0 = c\bar{u}$ and $D_s^+ = c\bar{s}$. Analogously the B mesons (B^+ , B^0 and B_s^+) are bound states of a b quark with a light quark

$^{2S+1}P_J/q\bar{q}$	$I = 1$	$I = 0$	$(I = 0)'$	$c\bar{c}$	$b\bar{b}$
1S_0	π^0 0.135	η 0.547	η' 0.958	η_c 2.98	η_b (9.40)
3P_0	a_0 0.984	f_0 0.980	f'_0 1.37	χ_{c0} 3.42	χ_{b0} 9.86
3P_1	a_1 1.23	f_1 1.28	f'_1 1.51	χ_{c1} 3.51	χ_{b1} 9.89
3P_2	a_2 1.32	f_2 1.28	f'_2 1.53	χ_{c2} 3.56	χ_{b2} 9.91
1D_2	π_2 1.67	η_D (1.68)	η'_D (1.89)	η_{cD} (3.84)	η_{bD} (10.15)

Table 2.1: Overview of resonances that can be produced in a two photon reaction. The numbers below the names are the masses in GeV. The particles with their mass between parentheses have not yet been observed. The masses of those particles are taken from theoretical calculations (see text).

Three different types of decay modes can be observed. The resonance decays into a state of two or more lighter hadrons, into two photons or into a lighter hadron under the emission of a photon. The last two decay modes are referred to as radiative decays. The second decay mode is forbidden for 1^+ resonances. In table 2.3 the most important decay modes, together with the branching ratios are given. It should be noted that for the heavy resonances the branching ratios of the observed final states only represent a small fraction of the possible decay modes of the resonances.

For a large number of these resonances also the two-photon widths have been determined. The results are collected in table 2.4.

The two-photon widths have been determined in three different kinds of experiments: in fixed target collisions, in radiative decays of C -odd resonances and in two-photon collisions in e^+e^- collisions.

In fixed target collisions a beam of (anti)protons is brought into collision with a fixed target. The two photons that come from the decay of the resonance produced in this collision are detected in the final state. One example of fixed target measurements is the measurement of the branching ratio for the decay of an η into two photons in the reaction $pd \rightarrow {}^3\text{He}\eta$ at the SPES2 facility at Saclay [38]. Other examples are $p\bar{p}$ experiments (R704 at CERN [39] and E760 and E835 [40] at Fermilab) where a cooled antiproton beam is intersected with a hydrogen target. By changing the energy of the beam, the cross section is measured as a function of the CM-energy of the colliding particles. From this spectrum the resonance mass, its total width and the product of the branching ratios $\text{Br}(R \rightarrow p\bar{p})\text{Br}(R \rightarrow \gamma\gamma)$ can be derived by applying a fit with a Breit-Wigner and a background function.

Radiative decay measurements have been performed by the Crystall Ball Collaboration at the SPEAR collider, the CLEO(2) collaboration at CESR and the BES collaboration at

$^{2S+1}P_J/q\bar{q}$	$I = 1$	$I = 0$	$(I = 0)'$	$c\bar{c}$	$b\bar{b}$
1S_0	π^0 $7.83 \cdot 10^{-6}$	η $1.18 \cdot 10^{-3}$	η' 0.300	η_c 13.2	η_b <i>n.o.</i>
3P_0	a_0 75	f_0 70	f'_0 350	χ_{c0} 13.5	χ_{b0} 162.3
3P_1	a_1 425	f_1 24	f'_1 73	χ_{c1} 0.880	χ_{b1} 130.6
3P_2	a_2 107	f_2 185	f'_2 76	χ_{c2} 2	χ_{b2} <i>n.o.</i>
1D_2	π_2 258	η_D <i>n.o.</i>	η'_D <i>n.o.</i>	η_{cD} <i>n.o.</i>	η_{bD} <i>n.o.</i>

Table 2.2: The total width of the resonances that can be produced in a two-photon reaction. The total widths are given in MeV. (*n.o.* = not observed)

the BEPC accelerator (Beijing). In these experiments a C -odd resonance \mathcal{R}_O is produced in electron-positron annihilation. For charmonium this usually is the $\psi(2S)$ state whereas for bottomonium the $\Upsilon(2S)$ state is taken. The double radiative decay of this resonance $\mathcal{R}_O \rightarrow \mathcal{R}\gamma \rightarrow \gamma\gamma$ is studied. The BES collaboration has only published results on charmonium states [41]. The Crystall Ball Collaboration and the CLEO collaboration have published results on both charmonium and bottomonium states [42–46].

At e^+e^- colliders operating at higher energies the C -even resonances can also be formed in the photon-photon fusion process. From (2.46) it follows that the production rate of these resonances is proportional to the two-photon width. The decay products of the resonance are observed in the detector, from which the invariant mass is reconstructed. These processes were studied in a large number of experiments. The advantage of this method is that at one go all the different resonances can be observed. The disadvantage is that in general the remnants of the resonance are strongly boosted along the z -axis. Examples are the detection of the η_c meson [47, 48] and the χ_{c2} meson [49–51]. All χ_{c2} analyses study the decay channel $\chi_{c2} \rightarrow J/\psi\gamma \rightarrow l^+l^-\gamma$ ($l = e, \mu$) and reconstruct $\Gamma_{\gamma\gamma}$ from the spectrum $M_{ll\gamma} - M_{ll}$, which will be explained in chapter 9.

2.10.3 Missing mass analyses

In double-tag events the invariant mass $W_{\gamma\gamma}$ of the two-photon system can also be reconstructed from the information on the tagged leptons. The $W_{\gamma\gamma}$ spectrum can be used to search for heavy states with a narrow width that couple strongly to two photons. This analysis has been performed at the TPC/Two-Gamma collaboration [52, 53], which searched in the range $4.5 \text{ GeV} < W_{\gamma\gamma} < 20 \text{ GeV}$. No evidence for narrow-width resonances has been found. The 95 % C.L. upper limits on the two-photon width are given in figure 2.9. In chapter 8 a similar missing mass analysis has been performed.

In [54] also a double-tag analysis, using the L3 luminosity monitors, has been performed and the $W_{\gamma\gamma}$ spectrum is given. However, no upper limits on resonances has been set in

	$I = 1$	$I = 0$	$(I = 0)'$	$c\bar{c}$	$b\bar{b}$
1S_0 decay	π^0 $\gamma\gamma(98)$ $e^+e^-\gamma(1.2)$	η $\gamma\gamma(39.3)$ $\pi^0\pi^0\pi^0(32.1)$ $\pi^+\pi^-\pi^0(23.2)$ $\pi^+\pi^-\gamma(4.8)$	η' $\pi^+\pi^-\eta(43.7)$ $\rho^0\gamma(30.2)$ $\pi^0\pi^0\eta(20.8)$ $\omega\gamma(3.0)$	η_c $\eta'\pi\pi(4.1)$ $\rho\rho(2.6)$ $K\bar{K}\pi(5.5)$ $\eta\pi\pi(4.9)$	η_b <i>n.o.</i>
3P_0 decay	a_0 $\eta\pi(\text{dom})$ $K\bar{K}(\text{seen})$ $\rho\pi(\text{seen})$ $\gamma\gamma(\text{seen})$	f_0 $\pi\pi(78.1)$ $K\bar{K}(21.9)$	f_0' $\pi\pi(\text{seen})$ $4\pi(\text{seen})$ $\eta\eta(\text{seen})$ $\gamma\gamma(\text{seen})$	χ_{c0} $2(\pi^+\pi^-)(2.0)$ $\pi^+\pi^-K^+K^-(1.8)$ $\rho^0\pi^+\pi^-(1.6)$ $3(\pi^+\pi^-)(1.2)$	χ_{b0} $\gamma\Upsilon(1S)(< 6)$
3P_1 decay	a_1 $\rho\pi(\text{dom})$	f_1 $4\pi(33.1)$ $\eta\pi\pi(52)$ $K\bar{K}\pi(9)$ $\gamma\rho^0(5.5)$	f_1' $K\bar{K}^* + c.c.(\text{seen})$	χ_{c1} $\gamma J/\psi(27.3)$	χ_{b1} $\gamma\Upsilon(1S)(35)$
3P_2 decay	a_2 $\rho\pi(70.1)$ $\eta\pi(14.5)$ $\omega\pi\pi(10.6)$ $K\bar{K}(4.9)$	f_2 $\pi\pi(84.7)$ $\pi^+\pi^-2\pi^0(7.2)$ $K\bar{K}(4.6)$	f_2' $K\bar{K}(88.8)$ $\eta\eta(10.3)$	χ_{c2} $2(\pi^+\pi^-)(1.2)$ $\pi^+\pi^-K^+K^-(1.9)$ $3(\pi^+\pi^-)(1.2)$ $\gamma J/\psi(13.5)$	χ_{b2} $\gamma\Upsilon(1S)(22)$
1D_2 decay	π_2 $f_2(1270)\pi(56.2)$ $\rho\pi(31)$ $f_0(1370)(8.7)$	η_D <i>n.o.</i>	η'_D <i>n.o.</i>	η_{cD} <i>n.o.</i>	η_{bD} <i>n.o.</i>

Table 2.3: The most important decay channels for the resonances produced in a two-photon reaction [13]. Between parentheses the branching ratios are given (*dom* = dominant decay mode, *seen* = the decay has been observed, but no branching ratios are given, *n.o.* = not observed)

this analysis.

2.10.4 Form factors

The Q^2 dependence of several resonances has been determined experimentally. For the light resonances π^0 , η and η' the VDM form factor where the pole mass is set to the ρ mass is found to give a good description of the Q^2 dependence for $Q^2 < 5 \text{ GeV}^2$ [55–58]. Recently, L3 has also published the first measurement of the form factor of the η_c [47, 59]. The data favours the mass of the J/ψ as the pole mass above the ρ mass. However, a flat form factor is also in agreement with data. The results are plotted in figure 2.10.

	$I = 1$	$I = 0$	$(I = 0)'$	$c\bar{c}$	$b\bar{b}$
1S_0	π^0 $(7.74 \pm 0.55) \cdot 10^{-3}$	η 0.46 ± 0.04	η' 4.29 ± 0.15	η_c 7.4 ± 1.4	η_b <i>n.o.</i>
3P_0	a_0 0.30 ± 0.10	f_0 $0.39^{+0.10}_{-0.13}$	f'_0 5.4 ± 2.3	χ_{c0} 4.0 ± 2.8	χ_{b0} <i>n.o.</i>
3P_1	a_1 <i>n.o.</i>	f_1 <i>n.o.</i>	f'_1 <i>n.o.</i>	χ_{c1} <i>n.o.</i>	χ_{b1} <i>n.o.</i>
3P_2	a_2 1.0 ± 0.06	f_2 2.6 ± 0.24	f'_2 0.100 ± 0.021	χ_{c2} 0.46 ± 0.17	χ_{b2} <i>n.o.</i>
1D_2	π_2 1.41 ± 0.36	η_D <i>n.o.</i>	η'_D <i>n.o.</i>	η_{cD} <i>n.o.</i>	η_{bD} <i>n.o.</i>

Table 2.4: The experimentally determined two-photon widths in keV.

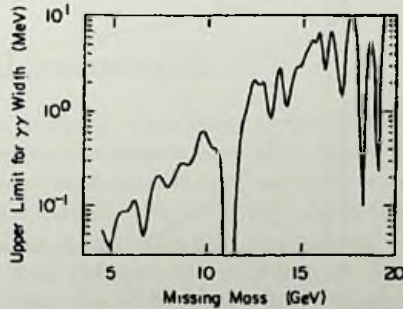


Figure 2.9: The 95% C.L. upper limit on the two-photon width as published by the TPC/Two-Gamma collaboration [52, 53].

2.10.5 Helicity contributions

Theory predicts that for spin-2 resonances the production process is at low Q_1^2 dominated by the helicity-2 contribution [23, 60]. The model presented in the next chapter also predicts this dominance. For the f'_2 meson L3 has performed an analysis that indeed shows a dominant helicity-2 contribution [12]. In the χ_{c2} analyses [49–51] it is also assumed that the helicity-2 contribution is dominant. The generated events that were uniformly distributed are reweighted according to this helicity contribution.

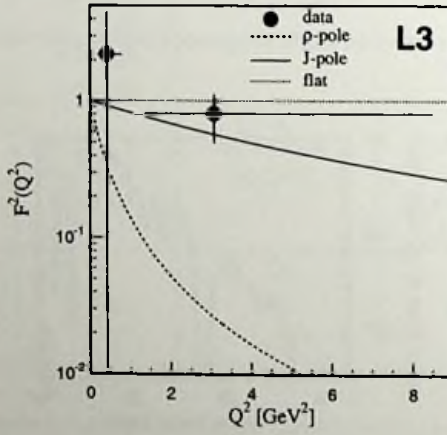


Figure 2.10: The form factor $F^2(Q^2)$ as a function of Q^2 . Picture taken from [47].

Chapter 3

The resonance production mechanism

In this chapter a model is introduced for the calculation of the meson-photon-photon transition form factor. The meson will be treated as a non-relativistic bound state of a heavy quark-antiquark pair. First the decay of a resonance into two photons is studied. Then this process is crossed for a description of resonance production in a two-photon reaction.

A large part of the work presented in this chapter has been published in [27].

3.1 Theoretical framework

Several theoretical studies on the Q^2 dependence of the (single) form factor that governs the production of the pseudoscalar mesons have been carried out [61–69]. Much less is known about the (in general several) form factors associated with the other C -even mesons [60, 70, 71]. For experimental data we refer to [72, 73]. One of the aims of this chapter is to take the Q^2 dependence of the cross section fully into account.

The calculations start from the limit of heavy quarks. In this limit the meson can be considered a non-relativistic bound state of a heavy quark and antiquark. The theoretical description of production and decay of heavy quarkonia is based on the NRQCD factorization framework [29], where relativistic corrections and higher-Fock-state contributions are suppressed by powers of v , the relative velocity of the quarks in the meson¹. With some minor modifications to incorporate $SU(3)$ -flavour breaking also the light mesons are included in the calculations. It will be argued that this procedure is justified.

3.2 Off-shell two-photon decay amplitudes

In this subsection the general amplitude is derived for the decay of a resonance into two photons

$$R(P) \rightarrow \gamma(k_1)\gamma(k_2), \quad (3.1)$$

where we allow the photons to be off shell. The amplitude for this process is denoted by \mathcal{M} . Again, we will only look at resonances that are of direct interest to us, i.e. we will study the 1S_0 , 3P_J and 1D_2 mesons. The derivation of \mathcal{M} starts with an expression containing

¹For charmonia and bottomonia $\langle v^2 \rangle \approx 0.3$ respectively ≈ 0.1 .

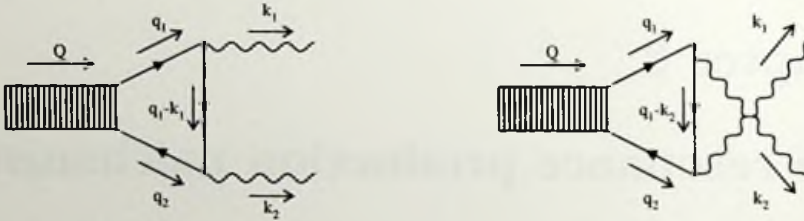


Figure 3.1: Illustration of the factorization of the quarkonium decay process. The left part of the diagrams represents the quarkonium state. The right part of the diagrams describes the perturbative annihilation of the free quarks into two photons. The right parts of the two diagrams contribute to the perturbative part \mathcal{A} of the amplitude.

the decay mechanism and the wave function of the quark-antiquark system. Both these parts are then evaluated in a non-relativistic approximation and finally combined into the amplitude \mathcal{M} .

We label the momenta of the quark-antiquark pair by q_1 and q_2 . The amplitude can be factorized into two contributions [74, 75], χ and \mathcal{A} ,

$$\mathcal{M}(Q) = \int \text{Tr} [\mathcal{A}(q)\chi(Q, q)] \frac{d^4 q}{(2\pi)^4}, \quad (3.2)$$

where

$$\begin{aligned} Q &= q_1 + q_2 = (M, \vec{0}), \\ 2q &= q_1 - q_2 = (0, 2\vec{q}). \end{aligned} \quad (3.3)$$

The parametrizations of Q and q are given in the rest frame of the resonance. This is illustrated in figure 3.1. The quantity $\chi(Q, q)$ is the Bethe-Salpeter wave function [21] for the given quarkonium state, while \mathcal{A} represents the perturbative parts of the diagrams in figure 3.1. For the decay process (3.1) we find for \mathcal{A}

$$\mathcal{A}(q) = (ie_q e \not{\epsilon}_2^*) \frac{1}{\not{q}_1 - \not{k}_1 - m} (ie_q e \not{\epsilon}_1^*) + (ie_q e \not{\epsilon}_1^*) \frac{1}{\not{q}_1 - \not{k}_2 - m} (ie_q e \not{\epsilon}_2^*), \quad (3.4)$$

where ϵ_i^* are the polarization vectors of the outgoing photons and e_q is the fractional charge of the quarks in units of e .

When one now would take $\chi = u(q_1)\bar{v}(q_2)$ equation (3.2) would lead to the usual quark-antiquark annihilation amplitude. However, the quarks are in a bound state, in particular we assume that the resonance is a non-relativistic bound state, which gives simplifications. It implies that the relative momentum q between the quark and the antiquark is small compared to the mass of the resonance. As a consequence, the bound-state wave function is sharply damped for larger relative momenta. This allows us to neglect terms with a

higher order q dependence in formula (3.2). For S -waves one can replace $\mathcal{A}(q)$ by $\mathcal{A}(0)$. From (3.2) it will then follow that this expression has to be multiplied by the S -state wave function in the origin of configuration space. For P -waves the wave function vanishes at the origin. In this case one has to retain in \mathcal{A} terms linear in q . From (3.2) it will now follow that \mathcal{M} will be proportional to the first derivative of the P -wave function in the origin in configuration space. For D -waves also this first derivative vanishes in the origin and one has to go to terms proportional to q^2 , which results in a decay amplitude that is proportional to the second derivative of the wave function in the origin of configuration space².

In the non-relativistic approach we can make one more approximation. As the binding energy is small compared to the quark masses, the resonance mass M and the quark mass m are related by

$$M \approx 2m. \quad (3.5)$$

We now turn to the Bethe-Salpeter wave function, which in the non-relativistic limit can be written as

$$\chi(Q, q; J, J_z, L, S) = \sum_{M, S_z} 2\pi\delta(q^0 - \frac{q^2}{2m}) \psi_{LM}(\vec{q}) P_{SS_z}(Q, q) \langle LM; SS_z | JJ_z \rangle. \quad (3.6)$$

This equation originates from combining $u(q_1)$ and $\bar{v}(q_2)$ into an $S = 0$ or $S = 1$ object, which then gives with an orbital non-relativistic wave function ψ_{LM} a state with total spin J . For that the Clebsch-Gordan coefficient $\langle LM; SS_z | JJ_z \rangle$ is needed. The spin projection operators P_{SS_z} can be found in [74] and read

$$\begin{aligned} P_{00}(Q, q) &= \sqrt{\frac{3}{M^3}} \left[\left(\frac{1}{2} Q + \not{q} \right) + m \right] \gamma_5 \left[-\left(\frac{1}{2} Q - \not{q} \right) + m \right], \\ P_{1S_z}(Q, q) &= \sqrt{\frac{3}{M^3}} \left[\left(\frac{1}{2} Q + \not{q} \right) + m \right] \not{\epsilon}(Q, S_z) \left[-\left(\frac{1}{2} Q - \not{q} \right) + m \right]. \end{aligned} \quad (3.7)$$

Here $\epsilon(Q, S_z)$ is the spacelike polarization vector of a spin-1 system. The standard polarization vectors have been used. These polarization vectors satisfy as usual the relations

$$Q^\mu \epsilon_\mu(Q, J_z) = 0, \quad (3.8)$$

$$\sum_{J_z} \epsilon^\mu(Q, J_z) \epsilon^{\nu*}(Q, J_z) = -g^{\mu\nu} + \frac{Q^\mu Q^\nu}{M^2} \equiv \mathcal{P}^{\mu\nu}. \quad (3.9)$$

In the rest frame of the resonance the polarization vectors are given by

$$\begin{aligned} \epsilon_\pm &= \frac{1}{\sqrt{2}}(0, \mp 1, -i, 0), \\ \epsilon_0 &= (0, 0, 0, 1). \end{aligned} \quad (3.10)$$

The spin projection operators in (3.7) can be directly interpreted. The factors in the square brackets are boost factors, the spin content is then projected out by γ_5 and $\not{\epsilon}(Q, S_z)$.

²This behaviour of the wave function can be understood by noting that in the non-relativistic limit the Bethe-Salpeter wave function is proportional to the Schrödinger wave function. For the short distances the interaction potential is dominated by the Coulomb-like part. The Schrödinger wave function that is a solution to the Coulomb-potential contains a term $\left(\frac{2r}{nr_B}\right)^L$ (e.g. see (5.28) in [20]) where r_B is the Bohr radius of the hydrogen atom.

The amplitude for the S -waves is easily obtained. In the absence of orbital angular momentum the total angular momentum is given by the spin of the resonance ($J = S$, $J_z = S_z$).

$$\mathcal{M}(Q) = \frac{1}{(2\pi)^3} \text{Tr} [A^0 P_{JJ_z}^0] \int \psi_{00}(\vec{q}) d^3 \vec{q}. \quad (3.11)$$

Here we have introduced the short-hand notation for the small \vec{q} approximation

$$A^0 \equiv A(0), \quad P_{SS_z}^0(Q) \equiv P_{SS_z}(Q, 0). \quad (3.12)$$

The integration is nothing but a Fourier transformation

$$\frac{1}{(2\pi)^3} \int \psi_{00}(\vec{q}) d^3 \vec{q} = \frac{1}{\sqrt{4\pi}} \mathcal{R}_S(0), \quad (3.13)$$

where \mathcal{R} is the radial part of the wave function in configuration space.

For the P waves one has to retain terms linear in q

$$\begin{aligned} \mathcal{M}(Q) = & \frac{1}{(2\pi)^3} \sum_{M, S_z} \langle 1M; SS_z | JJ_z \rangle \text{Tr} [A^\alpha P_{SS_z}^0(Q) + \\ & A^0 P_{SS_z}^\alpha(Q)] \int q_\alpha \psi_{1M}(\vec{q}) d^3 \vec{q}, \end{aligned} \quad (3.14)$$

where

$$A^\alpha \equiv \left. \frac{\partial}{\partial q_\alpha} A(q) \right|_{q=0}, \quad P_{SS_z}^\alpha(Q) \equiv \left. \frac{\partial}{\partial q_\alpha} P_{SS_z}(Q, q) \right|_{q=0}. \quad (3.15)$$

Again, the integration represents a Fourier transformation

$$\frac{1}{(2\pi)^3} \int q^\alpha \psi_{1M}(\vec{q}) d^3 \vec{q} = -i\epsilon^\alpha(M) \sqrt{\frac{3}{4\pi}} \mathcal{R}'_P(0). \quad (3.16)$$

For the 1D_2 state we have to go to terms of second order in q

$$\begin{aligned} \mathcal{M}(Q) = & \sum_{M, S_z} \langle 2M; SS_z | JJ_z \rangle \frac{1}{2} \text{Tr} [A^{\alpha\beta} P_{SS_z}^0(Q) + 2A^\alpha P_{SS_z}^\beta(Q) + \\ & A^0 P_{SS_z}^{\alpha\beta}(Q)] \int q_\alpha q_\beta \psi_{2M}(\vec{q}) d^3 \vec{q}. \end{aligned} \quad (3.17)$$

In this equation we have introduced

$$A^{\alpha\beta} \equiv \left. \frac{\partial^2}{\partial q_\alpha \partial q_\beta} A(q) \right|_{q=0}, \quad P_{SS_z}^{\alpha\beta}(Q) \equiv \left. \frac{\partial^2}{\partial q_\alpha \partial q_\beta} P_{SS_z}(Q, q) \right|_{q=0}. \quad (3.18)$$

This time the integration yields

$$\frac{1}{(2\pi)^3} \int q^\alpha q^\beta \psi_{2M}(\vec{q}) d^3 \vec{q} = \sqrt{\frac{15}{8\pi}} \epsilon^{\alpha\beta}(Q, M) \mathcal{R}''_D(0). \quad (3.19)$$

From (3.7) we can calculate the relevant projection operators.

$$P_{00}^0(Q) = \sqrt{\frac{3}{4M}} \gamma_5 (-\mathcal{Q} + M), \quad (3.20)$$

$$P_{00}^\alpha(Q) = \sqrt{\frac{3}{M}} \left(\gamma_5 \gamma^\alpha \frac{\mathcal{Q}}{M} - \gamma_5 \frac{Q^\alpha}{M} \right), \quad (3.21)$$

$$P_{00}^{\alpha\beta}(Q) = -2\sqrt{\frac{3}{M^3}} g^{\alpha\beta} \gamma_5, \quad (3.22)$$

$$P_{1S_z}^0(Q) = \sqrt{\frac{3}{4M}} \not{S}(Q, S_z) (-\mathcal{Q} + M), \quad (3.23)$$

$$P_{1S_z}^\alpha(Q) = \sqrt{\frac{3}{4M}} \left[\gamma^\alpha \frac{\mathcal{Q}}{M} \not{S}(Q, S_z) + \varepsilon^\alpha(Q, S_z) \frac{(M + \mathcal{Q})}{M} \right]. \quad (3.24)$$

In order to obtain the amplitude \mathcal{M} , one also needs the relations [74]

$$\sum_{M, S_z} \langle 1M; 1S_z | 00 \rangle \varepsilon^\alpha(M) \varepsilon^\beta(S_z) = -\sqrt{\frac{1}{3}} \left(-g^{\alpha\beta} + \frac{Q^\alpha Q^\beta}{M^2} \right) = -\sqrt{\frac{1}{3}} \mathcal{P}^{\alpha\beta}, \quad (3.25)$$

$$\sum_{M, S_z} \langle 1M; 1S_z | 1J_z \rangle \varepsilon^\alpha(M) \varepsilon^\beta(S_z) = i\sqrt{\frac{1}{2}} \varepsilon^{\alpha\beta\gamma\delta} \frac{Q_\gamma}{M} \varepsilon_\delta(Q, J_z), \quad (3.26)$$

$$\sum_{M, S_z} \langle 1M; 1S_z | 2J_z \rangle \varepsilon^\alpha(M) \varepsilon^\beta(S_z) = \varepsilon^{\alpha\beta}(Q, J_z). \quad (3.27)$$

In (3.19) and (3.27) we have introduced the polarization tensor $\varepsilon^{\alpha\beta}(Q, J_z)$ for the spin-2 resonances. The polarization tensors satisfy the following relations

$$\varepsilon^{\mu\nu}(Q, J_z) = \varepsilon^{\nu\mu}(Q, J_z), \quad g_{\mu\nu} \varepsilon^{\mu\nu}(Q, J_z) = 0, \quad Q_\mu \varepsilon^{\mu\nu}(Q, J_z) = 0. \quad (3.28)$$

$$\sum_{J_z} \varepsilon_{\mu\nu}(Q, J_z) \varepsilon_{\alpha\beta}^*(Q, J_z) = \frac{1}{2} (\mathcal{P}_{\mu\alpha} \mathcal{P}_{\nu\beta} + \mathcal{P}_{\mu\beta} \mathcal{P}_{\nu\alpha}) - \frac{1}{3} \mathcal{P}_{\mu\nu} \mathcal{P}_{\alpha\beta}. \quad (3.29)$$

In the rest frame of the resonance the standard spin-2 polarization vectors $\varepsilon(Q, \lambda_R)^{\mu\nu}$ are given by

$$\varepsilon(0, 0) = \frac{1}{\sqrt{6}} \begin{pmatrix} 0 & 0 & 0 & 0 \\ 0 & -1 & 0 & 0 \\ 0 & 0 & -1 & 0 \\ 0 & 0 & 0 & 2 \end{pmatrix}, \quad \varepsilon(0, \pm 1) = \frac{1}{2} \begin{pmatrix} 0 & 0 & 0 & 0 \\ 0 & 0 & 0 & \mp 1 \\ 0 & 0 & 0 & -i \\ 0 & \mp 1 & -i & 0 \end{pmatrix}, \quad (3.30)$$

$$\varepsilon(0, \pm 2) = \frac{1}{2} \begin{pmatrix} 0 & 0 & 0 & 0 \\ 0 & 1 & \pm i & 0 \\ 0 & \pm i & -1 & 0 \\ 0 & 0 & 0 & 0 \end{pmatrix}.$$

From now on the Q -dependence of the polarization vectors and tensors will no longer be explicitly denoted.

Now we have arrived at the point where we can construct the amplitudes \mathcal{M} , which can now be written as (omitting overall phase factors)

$$\mathcal{M}(^1S_0) = \frac{1}{4} \sqrt{\frac{3}{\pi M}} \mathcal{R}_S(0) \text{Tr} \left[\mathcal{A}^0 \gamma_5 (-\mathcal{Q} + M) \right], \quad (3.31)$$

$$\mathcal{M}(^3P_0) = \frac{1}{4} \mathcal{R}'_P(0) \sqrt{\frac{3}{\pi M}} \text{Tr} \left[6\mathcal{A}^0 + \left(\mathcal{A} + \frac{\mathcal{A}^\mu Q_\mu}{M^2} \right) (-\mathcal{Q} + M) \right], \quad (3.32)$$

$$\mathcal{M}(^3P_1) = \frac{3}{4M} \sqrt{\frac{1}{2\pi M}} \mathcal{R}'_P(0) \text{Tr} \left[2\mathcal{A}^0 \gamma_\alpha \frac{\mathcal{Q}}{M} \gamma_\beta + \mathcal{A}_\alpha \gamma_\beta (-\mathcal{Q} + M) \right] \varepsilon^{\alpha\beta\gamma\delta} Q_\gamma \varepsilon_\delta(J_z), \quad (3.33)$$

$$\mathcal{M}(^3P_2) = \frac{3}{4} \sqrt{\frac{1}{\pi M}} \mathcal{R}'_P(0) \text{Tr} \left[\mathcal{A}^\mu \gamma^\nu \frac{M - \mathcal{Q}}{2} \right] \varepsilon_{\mu\nu}(J_z), \quad (3.34)$$

$$\begin{aligned} \mathcal{M}(^1D_2) = & \frac{3}{8} \sqrt{\frac{10}{\pi M}} \mathcal{R}'_D(0) \varepsilon_{\alpha\beta}(Q, J_z) \text{Tr} \left[\frac{1}{2} \mathcal{A}^{\alpha\beta} \gamma_5 (-\mathcal{Q} + M) + 2\mathcal{A}^\alpha \gamma_5 \gamma^\beta \frac{\mathcal{Q}}{M} \right. \\ & \left. - g^{\alpha\beta} \mathcal{A}^0 \sqrt{\frac{3}{M^2}} \gamma_5 \right]. \end{aligned} \quad (3.35)$$

As the polarization tensors have a vanishing trace (3.28), the last term in the trace of (3.35) will not contribute to the decay amplitude. From the last property in (3.28) it also follows that the second term in (3.21) will not contribute and thus has been discarded in (3.35).

The last step is to insert the explicit expressions for the (derivatives of the) amplitude (3.4) into these expressions. From [75] we have the expressions for \mathcal{A}^0 and \mathcal{A}^μ

$$\mathcal{A}^0 = \frac{-e^2 e_q^2}{D} [\not{\epsilon}_2^* \not{\epsilon}_1^* \not{k}_1 - \not{k}_1 \not{\epsilon}_1^* \not{\epsilon}_2^*], \quad (3.36)$$

$$\mathcal{A}^\mu = \frac{4e^4 e_q^2}{D^2} [(k_1 \cdot k_2) \varepsilon_{1,\mu}^* \not{\epsilon}_2^* - k_{1,\mu} (\varepsilon_1^* \cdot \varepsilon_2^*) \not{k}_1 + \not{\epsilon}_2^* (\varepsilon_1^* \cdot k_2) - \not{\epsilon}_1^* (k_1 \cdot \varepsilon_2^*)]. \quad (3.37)$$

In these expressions we have used the abbreviation D for the term that occurs in the denominator, which becomes in the limit $\vec{q} \rightarrow 0$

$$D = \left[\frac{1}{2} (k_1 - k_2) \right]^2 - m^2 = -k_1 \cdot k_2. \quad (3.38)$$

When D is needed in the reaction (2.2) it can be expressed through (2.7)-(2.10) as follows

$$D = \frac{1}{2} (s + s' + u + u' - 8m_e^2). \quad (3.39)$$

For $\mathcal{A}^{\mu\nu}$ we found the following expression

$$\mathcal{A}^{\mu\nu} = -\frac{2e^2 e_q^2}{D^3} \left(\frac{1}{4} (k_1 - k_2)^2 - m^2 \right) g^{\mu\nu} - (k_1 - k_2)^\mu (k_1 - k_2)^\nu (\not{k}_1 \not{\epsilon}_1^* \not{\epsilon}_2^* - \not{\epsilon}_2^* \not{\epsilon}_1^* \not{k}_1). \quad (3.40)$$

Finally, the amplitudes for the decay of a resonance into two photons read³

$$\mathcal{M}(Q, {}^1S_0) = 2e_q^2 e^2 \frac{\mathcal{R}_S(0)}{D} \sqrt{\frac{3}{\pi M}} \varepsilon(k_1, k_2, \varepsilon_1^*, \varepsilon_2^*), \quad (3.42)$$

$$\begin{aligned} \mathcal{M}(Q, {}^3P_0) &= 4e_q^2 e^2 \frac{\mathcal{R}'_P(0)}{D^2 M} \sqrt{\frac{3}{\pi M}} \{[(\varepsilon_1^* \cdot \varepsilon_2^*)(k_1 \cdot k_2) - (\varepsilon_1^* \cdot k_2)(\varepsilon_2^* \cdot k_1)] \\ &\quad \times [M^2 + (k_1 \cdot k_2)] - (\varepsilon_1^* \cdot \varepsilon_2^*) k_1^2 k_2^2\}, \end{aligned} \quad (3.43)$$

$$\mathcal{M}(Q, {}^3P_1) = 6e_q^2 e^2 \frac{\mathcal{R}'_P(0)}{D^2} \sqrt{\frac{2}{\pi M}} \{k_1^2 \varepsilon(\varepsilon, \varepsilon_1^*, \varepsilon_2^*, k_2) + k_2^2 \varepsilon(\varepsilon, \varepsilon_2^*, \varepsilon_1^*, k_1)\}, \quad (3.44)$$

$$\begin{aligned} \mathcal{M}(Q, {}^3P_2) &= 12e_q^2 e^2 \frac{\mathcal{R}'_P(0)}{D^2} \sqrt{\frac{M}{\pi}} \varepsilon^{\mu\nu} \{(k_1 \cdot k_2) \varepsilon_{1,\mu}^* \varepsilon_{2,\nu}^* \\ &\quad + (\varepsilon_1^* \cdot \varepsilon_2^*) k_{1,\mu} k_{2,\nu} - (\varepsilon_1^* \cdot k_2) k_{1,\mu} \varepsilon_{2,\nu}^* - (\varepsilon_2^* \cdot k_1) k_{2,\mu} \varepsilon_{1,\nu}^*\}, \end{aligned} \quad (3.45)$$

$$\mathcal{M}(Q, {}^1D_2) = 12e_q^2 e^2 \frac{\mathcal{R}''_D(0)}{D^3} \sqrt{\frac{10}{\pi M}} \varepsilon^{\mu\nu} k_{1,\mu} k_{2,\nu} \varepsilon(k_1, k_2, \varepsilon_1^*, \varepsilon_2^*). \quad (3.46)$$

We can compare our results to the results obtained by other authors. Up to an overall phase factor, some colour factors and adding the fractional quark charge our results agree with Gastmans *et al.* [76, 77], Guberina *et al.* [74] and Kühn *et al.* [75]. In some of the papers the amplitudes for the production of a quarkonium state are described. This results in the replacement $Q \rightarrow -Q$.

3.3 The helicity decay amplitude

In order to cast the results into a form that is suitable for implementation in the BGMS-formalism, we express the amplitudes \mathcal{M} in terms of helicity decay amplitudes $\mathcal{D}(\lambda_1, \lambda_2)$, where the λ_i 's are the helicities of the outgoing photons. In the rest frame we choose the direction of photon 1 as the polarization axis. With this choice the helicity $\lambda_R (= J_z)$ of the resonance is related to these photon helicities by

$$\lambda_R = \lambda_1 - \lambda_2. \quad (3.47)$$

Let us define the following invariants

$$W = \sqrt{Q^2}, \quad (3.48)$$

$$K_i = \sqrt{k_i^2}, \quad (3.49)$$

$$\nu = k_1 \cdot k_2, \quad (3.50)$$

$$X = \nu^2 - K_1^2 K_2^2, \quad (3.51)$$

$$Q_i^2 = -k_i^2. \quad (3.52)$$

³In some of the expressions we have introduced the following notation for the contraction of four four-vectors with the totally anti-symmetric Levi-Civita tensor $\varepsilon^{\alpha\beta\gamma\delta}$.

$$\varepsilon(v_1, v_2, v_3, v_4) \equiv \varepsilon^{\alpha\beta\gamma\delta} v_{1,\alpha} v_{2,\beta} v_{3,\gamma} v_{4,\delta}. \quad (3.41)$$

J^P	$\mathcal{D}(+-)$	$\mathcal{D}(++)$	$\mathcal{D}(+0)$	$\mathcal{D}(00)$
0^-	0	\sqrt{X}	0	0
0^+	0	$\frac{2(X+\nu W^2)}{\sqrt{3}W}$	0	$-\frac{2}{\sqrt{3}}K_1K_2W$
1^+	0	$-\frac{\sqrt{2}\nu}{W}(K_1^2 - K_2^2)$	$\sqrt{2}K_2(\nu - K_1^2)$	0
2^+	$2W\nu$	$\sqrt{\frac{2}{3}}\frac{\nu(K_1^2+K_2^2)+2K_1^2K_2^2}{W}$	$\sqrt{2}K_2(\nu + K_1^2)$	$2\sqrt{\frac{2}{3}}WK_1K_2$
2^-	0	$4\frac{X^{\frac{3}{2}}}{M^2}$	0	0

Table 3.1: The decay amplitudes $\mathcal{D}(\lambda_1, \lambda_2)$ in units of c_L .

At this point W equals the rest mass of the resonance, M . However, the two variables may differ for the crossed reaction when one wants to take into account the Breit-Wigner formula in the production.

The amplitudes are normalized such that the on-shell two-photon decay widths are given by (2.44)

$$\Gamma_{\gamma\gamma}(^{2S+1}L_J) = \frac{1}{32\pi M(2J+1)} \sum_{\lambda_1, \lambda_2=\pm 1} |\mathcal{D}(\lambda_1, \lambda_2)|^2. \quad (3.53)$$

We have listed the results for the helicity decay amplitudes in table 3.1. In this table the decay amplitudes are expressed in terms of c_L , given by

$$c_L = \sqrt{\frac{3}{M}} e_q^2 16\pi\alpha \frac{\mathcal{R}_{nL}^{(L)}(0) Y_{L0}(0,0)}{D^{L+1}}, \quad (3.54)$$

where $Y_{LM}(\theta, \phi)$ are the spherical harmonics. The variable D has been introduced in formula (3.38). $\mathcal{R}_{nL}^{(L)}$ is a different notation for the L -th derivative of the radial part of the wave function. For the L -values S , P and D will be used and n denotes the radial quantum number. The other decay amplitudes can be derived from the given decay amplitudes by exploiting

$$\begin{aligned} \mathcal{D}(\lambda_1, \lambda_2) &= \eta_R \mathcal{D}(-\lambda_1, -\lambda_2), \\ \mathcal{D}(\lambda_1, \lambda_2) &= (-1)^J \mathcal{D}(\lambda_2, \lambda_1) \Big|_{K_1 \leftrightarrow K_2}, \end{aligned} \quad (3.55)$$

where $\eta_R = 1(-1)$ for the "normal" ("abnormal") J^P series, $J^P = 0^+, 1^-, 2^+, \dots$ ($J^P = 0^-, 1^+, 2^-, \dots$). The first relation remains valid after crossing to a photon-photon reaction.

J^P	0^-	0^+	1^+	2^+	2^-
$\Gamma_{\gamma\gamma}(J^P)$	4	144	32	$\frac{192}{5}$	64

Table 3.2: The two-photon decay widths in units of d_L (for 1^+ the reduced width $\tilde{\Gamma}_{\gamma\gamma}$ has been given).

3.4 Widths for on-shell two-photon decays

We can use the above expressions and formula (3.53) to obtain expressions for the two-photon widths. The results are collected in table 3.2. The entries of the table are given in units of d_L

$$d_L = 3e_q^4 \alpha^2 \frac{|\mathcal{R}_{nL}^{(L)}(0)|^2}{M^{2(L+1)}}. \quad (3.56)$$

In the case of the 1^+ meson the reduced width $\tilde{\Gamma}_{\gamma\gamma}$ has been given, which has been introduced in section 2.7. This is the transverse-transverse two-photon width divided by the factor $[K_1^2 - K_2^2]/(2\nu)$.

For the numerical results for the two-photon widths we have to discuss the input parameters in equation (3.56). They will lead to a set of widths, which are in reasonable agreement with experiment. For the heavy charmonium and bottomonium states the fractional charges are given by the charges of the constituent quarks, $e_q = +2/3$ and $e_q = -1/3$ respectively. The wave functions follow from a calculation where the Schrödinger equation is solved for a phenomenological inter-quark potential [78]. The input values are given in table 3.3. Furthermore, we multiply for some resonances the two-photon width by a QCD correction factor C_{QCD} [79]⁴

$$\begin{aligned} {}^1S_0 &: C_{QCD} = 1 + \frac{\alpha_S(m_q)}{3\pi}(\pi^2 - 20), \\ {}^3P_0 &: C_{QCD} = 1 + \frac{\alpha_S(m_q)}{9\pi}(3\pi^2 - 28), \\ {}^3P_2 &: C_{QCD} = 1 - \frac{16\alpha_S(m_q)}{3\pi}. \end{aligned} \quad (3.57)$$

We have taken the values $\alpha_S(m_c) = 0.298$ and $\alpha_S(m_b) = 0.190$.

For the light mesons the validity of the potential model is not self-evident and one has to assume this model to be still a good approximation. For the light mesons we assume a linear potential $\propto \lambda r$. This results in $|\mathcal{R}_{1S}(0)|^2 = 2\mu\lambda$, $|\mathcal{R}'_{1P}(0)|^2 = 0.268(2\mu\lambda)^{5/3}$ and $|\mathcal{R}''_{1D}(0)|^2 = 0.151(2\mu\lambda)^{7/3}$, where μ is the reduced mass. We use the canonical values for the string tension λ and the constituent quark masses, $2\mu\lambda = 0.74 \text{ GeV}^3$. $SU(3)$ -flavour symmetry breaking has been accounted for by multiplying the square of these wave functions

⁴Although it has not been mentioned explicitly in [27], these correction factors have also been used in the calculations of the two-photon widths.

$\mathcal{R}_{nL}^{(L)}$	$c\bar{c}$	$b\bar{b}$
$ \mathcal{R}_{1S}(0) ^2/\text{GeV}^3$	0.81	6.5
$ \mathcal{R}'_{1P}(0) ^2/\text{GeV}^5$	0.075	1.4
$ \mathcal{R}''_{1D}(0) ^2/\text{GeV}^7$	0.015	0.64

Table 3.3: The input values for the (derivatives of the) radial part of of the wave function in the origin for charmonium and bottomonium states.

by a factor r_M^{2L+1} , where

$$r_M = \frac{M}{\mu_0}. \quad (3.58)$$

The quantity μ_0 is a hadronic scale of about 1 GeV and M is the resonance mass. For the light mesons e_q^2 is replaced by the effective squared charge $\langle e_q^2 \rangle$. It depends on the mixing angle θ that parametrizes the breaking of $SU(3)$ -flavour symmetry [13,80].

$$\langle e_q^2 \rangle = \begin{cases} \frac{1}{3\sqrt{2}} & \pi, a_0, a_1, a_2, \pi_2 \\ \frac{1}{3\sqrt{6}}(\cos\theta - 2\sqrt{2}\sin\theta) & \eta, f_0, f'_1, f'_2, \eta_D \\ \frac{2}{3\sqrt{3}}(\cos\theta + \frac{1}{2}\sin\theta) & \eta', f'_0, f_1, f_2, \eta'_D. \end{cases} \quad (3.59)$$

For the 1S_0 and 1D_2 also the effect of the centrifugal barrier has to be taken into account. For the J^+ states parity allows the total photonic orbital momentum to be zero⁵. However, for the negative parity states 0^- and 2^- the photonic orbital angular momentum is required to be at least 1. In the expressions for the decay amplitude (3.42) and (3.46) this suppression shows up as the factor $\varepsilon(k_1, k_2, \varepsilon_1, \varepsilon_2)$. For the decay widths this implies that one has to multiply the square of (the derivatives of the) radial part of the wave function by an additional factor r_M^4 . The final results for the wave functions for the light mesons are listed in table 3.4. From the results in table 3.4 and the factor d_L it now follows that the two-photon widths scale with M^3 for the 0^- and 2^- mesons whereas the two-photon widths for the J^+ states scale as $1/M$. This can be compared with results obtained by other authors [22,82]. In the "conventional approach" all mesons scale as M^3 , a scaling behaviour that was also found in the Low approximation (2.48).

In table 3.5 we have collected the numerical results that follow from this approach. The masses of the mesons are taken from the PDG [13], where known, and the others are taken

⁵The parity \mathcal{P}_{12} of a two particle system is given by [81]

$$\mathcal{P}_{12} = \mathcal{P}_1 \mathcal{P}_2 (-1)^L, \quad (3.60)$$

where \mathcal{P}_i are the intrinsic parities of the two particles and L is the total orbital momentum.

$\mathcal{R}_{nL}^{(L)}$	Light Mesons
$ \mathcal{R}_{1S}(0) ^2/\text{GeV}^3$	$0.074r_M^5$
$ \mathcal{R}'_{1P}(0) ^2/\text{GeV}^5$	$3.5 \times 10^{-3}r_M^3$
$ \mathcal{R}''_{1D}(0) ^2/\text{GeV}^7$	$0.35 \times 10^{-3}r_M^9$

Table 3.4: *The input values for the (derivatives of the) radial part of of the wave function in the origin for the light resonances.*

from a potential-model calculation [82]⁶. Despite their questionable status the a_0 , $f_0(980)$ and $f'_0(1370)$ have been taken as the lowest-lying scalars.

The only free parameters that are left are the QCD scale μ_0 and the mixing angles θ . The scale μ_0 has been adjusted by the π^0 decay width to $\mu_0 = 0.96$ GeV. We determine the mixing angles from the quadratic mass formula ((13.5) in [13]), $\theta[0^-] = -11.5^\circ$, $\theta[2^+] = 32^\circ$. For the other P -states we have taken the latter value as well. For the D -waves the mixing angle has been set to zero.

In table 3.5 also the experimentally observed two-photon widths are given. A comparison reveals that we find good agreement with the measured decay widths for almost all mesons. This gives us confidence that the model will provide sensible results for the two-photon production of these light states.

3.5 Form factors in two-photon production

In this section we will derive the cross sections and interference terms in the BGMS formalism. By crossing the results for the two-photon decay process we can obtain the cross section of resonance production in a two-photon reaction

$$\gamma(q_1)\gamma(q_2) \rightarrow R(J^P). \quad (3.61)$$

The crossed amplitudes are obtained by replacing K_i by iQ_i in the helicity amplitudes, where Q_i is defined by $Q_i = \sqrt{-q_i^2}$. Crossing changes the second relation in (3.55) to

$$\mathcal{D}(\lambda_1, \lambda_2) = (-1)^{J-\lambda_1+\lambda_2} \mathcal{D}(\lambda_2, \lambda_1) \Big|_{Q_1 \leftrightarrow Q_2}. \quad (3.62)$$

The amplitudes (2.32) are related to the decay amplitudes by

$$M_{\lambda_1 \lambda_2 \lambda_1 \lambda_2} = \pi \delta(P^2 - M^2) |\mathcal{D}(\lambda_1, \lambda_2)|^2 \quad (3.63)$$

⁶These include the $\eta_b(9400)$ and the D wave states $\eta_D(1680)$, $\eta'_D(1890)$, $\eta_{cD}(3840)$ and $\eta_{bD}(10150)$, where the masses in MeV are given between the parentheses.

	$I = 1$	$I = 0$	$(I = 0)'$	$c\bar{c}$	$b\bar{b}$
1S_0	π^0 $7.74 \cdot 10^{-3}(7.74 \cdot 10^{-3})$	η $0.41(0.46)$	η' $6.1(4.9)$	η_c $7.8(7.4)$	η_b $0.46(-)$
3P_0	a_0 $5.1(0.3)$	f_0 $0.72(0.39)$	f'_0 $10.4(5.4)$	χ_{c0} $2.5(4.0)$	χ_{b0} $0.043(-)$
3P_1	a_1 $0.90(-)$	f_1 $2.5(2.4)$	f'_1 $0.10(-)$	χ_{c1} $0.50(-)$	χ_{b1} $0.92 \cdot 10^{-2}(-)$
3P_2	a_2 $1.0(1.0)$	f_2 $3.0(2.6)$	f'_2 $0.12(0.10)$	χ_{c2} $0.28(0.46)$	χ_{b2} $0.74 \cdot 10^{-2}(-)$
1D_2	π_2 $1.3(1.41)$	η_D $0.43(-)$	η'_D $5.0(-)$	η_{cD} $0.95 \cdot 10^{-2}(-)$	η_{bD} $0.74 \cdot 10^{-4}(-)$

Table 3.5: The numerical values for $\Gamma_{\gamma\gamma}$ in keV. In parentheses the central values of experimental measurements [13] are given. For the 3P_1 resonances the reduced widths are given and the experimental measurement is taken from [28].

for the cross sections and by

$$M_{\lambda_1\lambda_2\lambda'_1\lambda'_2} = \pi\delta(P^2 - M^2)D(\lambda_1, \lambda_2)D^*(\lambda'_1, \lambda'_2) \quad (3.64)$$

for the interference terms.

Inserting the above expressions in (2.37) we obtain ($A, B = T, S$)

$$\sigma_{AB} = \delta(P^2 - M^2)8\pi^2 \frac{(2J+1)\Gamma_{\gamma\gamma}(J^P)}{M} f_{AB}(J^P), \quad (3.65)$$

$$\tau_{AB} = \delta(P^2 - M^2)8\pi^2 \frac{(2J+1)\Gamma_{\gamma\gamma}(J^P)}{M} g_{AB}(J^P). \quad (3.66)$$

As discussed in section 2.8, form factors f_{AB} and g_{AB} will appear. They are listed in table 3.6. For the 1^+ resonances again the reduced width has to be inserted into the formulae. In the form factors we have introduced the variable κ

$$\kappa = \frac{M^2}{2\sqrt{X}}, \quad (3.67)$$

where X is defined in equation (3.51).

Before we start to compare our results for the form factors to those obtained by other theoretical models or from experimental data, it is important to realize that the Q_i^2 dependence of the form factor is convention dependent. What is unique is the Q_i^2 dependence of the $e^-e^+ \rightarrow e^+e^-R$ cross section. Conventions different from (3.65) and (3.66) are in use. For the pseudoscalar mesons it has become standard to define the meson-photon transition form factor by writing the amplitude for the process $\gamma\gamma \rightarrow R(0^-)$ as

J^P	f_{TT}	f_{TS}	f_{SS}
0^-	$\kappa \frac{X}{\nu^2}$	0	0
0^+	$\kappa \left(\frac{X+\nu M^2}{3\nu^2} \right)$	0	$2\kappa \left(\frac{M^2 \sqrt{Q_1^2 Q_2^2}}{3\nu^2} \right)^2$
1^+	$\kappa \left(\frac{Q_1^2 - Q_2^2}{2\nu} \right)^2$	$2\kappa \frac{M^2 Q_2^2}{2\nu} \left(\frac{\nu + Q_1^2}{\nu} \right)^2$	0
2^+	$\kappa \left(\frac{M^2}{2\nu} \right)^2 \left\{ 1 + \frac{[2Q_1^2 Q_2^2 - \nu(Q_1^2 + Q_2^2)]^2}{6M^4 \nu^2} \right\}$	$\kappa \frac{M^2 Q_2^2 (\nu - Q_1^2)^2}{4\nu^4}$	$\kappa \frac{M^4 Q_1^2 Q_2^2}{3\nu^4}$
2^-	$\kappa \left[\frac{X}{\nu^2} \right]^3$	0	0

J^P	g_{TT}	g_{TS}
0^-	$-2\kappa \frac{X}{\nu^2}$	0
0^+	$2\kappa \left(\frac{X+\nu M^2}{3\nu^2} \right)$	$\kappa \left(\frac{M}{3\nu^2} \right)^2 Q_1 Q_2 (X + \nu M^2)$
1^+	$-2\kappa \left(\frac{Q_1^2 - Q_2^2}{2\nu} \right)^2$	$\kappa \left(\frac{M}{2\nu^2} \right)^2 Q_1 Q_2 (\nu + Q_1^2)(\nu + Q_2^2)$
2^+	$\frac{\kappa}{12} \left(\frac{2Q_1^2 Q_2^2 - \nu(Q_1^2 + Q_2^2)}{\nu^2} \right)^2$	$\kappa \left(\frac{M}{\nu^2} \right)^2 \frac{Q_1 Q_2}{8} \left(\frac{2}{3} (2Q_1^2 Q_2^2 - \nu(Q_1^2 + Q_2^2)) + (\nu - Q_1^2)(\nu - Q_2^2) \right)$
2^-	$-2\kappa \left[\frac{X}{\nu^2} \right]^3$	0

Table 3.6: The form factors f_{AB} and g_{AB} .

$\mathcal{M} = F_{P\gamma\gamma}(Q_1, Q_2) e^2 i \varepsilon_{\mu\nu\rho\sigma} q_1^\mu q_2^\nu \varepsilon_1^\rho \varepsilon_2^\sigma$. In this convention we find for the only non-vanishing cross section term

$$\sigma_{TT}[0^-] = \delta(W^2 - M^2) 8\pi^2 \frac{\Gamma_{\gamma\gamma}[0^-]}{M} \frac{1}{\kappa} \left[\frac{F_{P\gamma\gamma}(Q_1, Q_2)}{F_{P\gamma\gamma}(0, 0)} \right]^2. \quad (3.68)$$

Hence, this form factor $F_{P\gamma\gamma}$ is related to our form factor by

$$\begin{aligned} \frac{F_{P\gamma\gamma}(Q_1, Q_2)}{F_{P\gamma\gamma}(0, 0)} &= \sqrt{\kappa f_{TT}(0^-)} = \frac{M^2}{M^2 + Q_1^2 + Q_2^2}, \\ F_{P\gamma\gamma}(0, 0) &= \frac{4}{M} \sqrt{\frac{3e_s^2 |\mathcal{R}(0)|^2}{\pi M^3}} = \frac{2}{M} \sqrt{\frac{\Gamma_{\gamma\gamma}}{\pi \alpha^2 M}} = \frac{4e_s^2 f_P}{M^2}, \end{aligned} \quad (3.69)$$

where f_P is the pseudoscalar decay constant, $f_P = |\mathcal{R}_S(0)| \sqrt{\frac{3}{\pi M}}$. Equation (3.69) agrees with a calculation where also the effects from the transverse-momentum (q_T) of the quarks within the bound state were taken into account [67]. This effectively amounts to adding a factor $2q_T^2$ to the denominator in (3.69).

The CLEO collaboration has measured the single Q^2 dependence ($Q = Q_1, Q_2 \approx 0$) of the π^0 , η and η' form factors very precisely [58]. The data is consistent with a monopole behaviour with a pole mass close to the ρ mass for the π^0 and η mesons and a slightly larger mass for the η' meson. This agrees with so-called power counting rules [83]. In (3.69)

we also found a monopole form factor. But for these light mesons we have to replace the meson mass by the mass of the ρ meson⁷ (\approx twice the mass of the light quarks) whereas for the other mesons we identify the pole mass with the meson mass.

It is important to realize that the expression for $F_{P\gamma\gamma}$ does not factorize into the product of two form factors $F_R(Q_1^2)F_R(Q_2^2)$, as is suggested in the VMD-model [31]. In the VMD model

$$F_R(Q^2) = \frac{M_P^2}{M_P^2 + Q^2}, \quad (3.70)$$

where one takes for the light resonances $M_P = M_\rho$, for the charmonium states $M_P = M_{J/\psi}$ and for the bottomonium states $M_P = M_\Upsilon$. In particular, at large Q_i^2 's the form factor in (3.69) only falls off as $M^2/(Q_1^2 + Q_2^2)$ rather than $M^4/(Q_1^2 Q_2^2)$, as is in agreement with [83].

It might seem to be a coincidence that we obtain the correct asymptotic behaviour. The non-relativistic model is expected to give a meaningful description for Q_i values not much larger than $M/2$ and is expected to become insufficient at asymptotic Q_i values where large logarithmic corrections $\propto \ln(Q_i/M)$ become important. In this regime it is more appropriate to set up a scheme in which calculations are done with massless quarks, but incorporating the Q^2 evolution of the quark distribution amplitudes in the meson. Such an approach is provided by the hard-scattering approach (HSA) [61].

In the HSA the meson-photon-photon transition amplitude factorizes into a hard (perturbative) scattering amplitude and a soft (non-perturbative) distribution amplitude $\phi(x)$, so that asymptotically

$$F_{P\gamma\gamma}(Q_1, Q_2) \rightarrow 2 \langle e^2 \rangle f_P \int_0^1 \frac{\phi(x)}{xQ_1^2 + (1-x)Q_2^2} dx. \quad (3.71)$$

All meson distribution amplitudes approach the asymptotic form $\phi_{AS}(x) = 6x(1-x)$. The asymptotic limit then yields

$$F_{P\gamma\gamma} \rightarrow 6 \langle e^2 \rangle f_P \frac{Q_1^4 - Q_2^4 - 2Q_1^2 Q_2^2 \ln\left(\frac{Q_1^2}{Q_2^2}\right)}{(Q_1^2 - Q_2^2)^3}. \quad (3.72)$$

For two special limits this gives

$$F_{P\gamma\gamma} \rightarrow \begin{cases} \frac{6 \langle e^2 \rangle f_P}{Q^2} & Q_1 = Q, Q_2 = 0 \\ \frac{2 \langle e^2 \rangle f_P}{Q^2} & Q_1 = Q_2 = Q. \end{cases} \quad (3.73)$$

Although the full Q_i dependence looks more complicated than in (3.69), the two limiting cases in (3.73) show that the asymptotic power behaviours for large Q_1 and/or large Q_2 are identical. The reason is that in both calculations the hard vertex is $Q\bar{Q}(^1S_0) \rightarrow \gamma\gamma$ and asymptotically the HSA distribution amplitude becomes Q -independent, as is also the case in our non-relativistic model. From the normalization condition $\int_0^1 \phi(x) dx = 1$, it follows that in the symmetric asymptotic limit ($Q_1 = Q_2$) (3.69) and (3.71) yield identical results. In the single asymptotic limit ($Q_1 \rightarrow \infty, Q_2 = 0$) the results differ by a factor 2/3. For other meson-photon transition form factors the asymptotic Q_i power behaviour will

⁷This replacement is justified as these mesons are Goldstone bosons and thus exceptionally light.

J^P	$Q_1 \neq Q_2$			$Q_1 = Q_2 = Q$		
	F_{TT}	F_{TS}	F_{SS}	F_{TT}	F_{TS}	F_{SS}
0^-	1	0	0	1	0	0
0^+	$\frac{\Delta}{3}$	0	$\frac{4\sqrt{2} M^2 Q_1 Q_2}{3 \Delta (Q_1^2 + Q_2^2)^2}$	$\frac{2M}{3Q}$	0	$\frac{\sqrt{2} M}{3Q}$
1^+	1	$\frac{\sqrt{2} M Q_2 (3Q_1^2 + Q_2^2)}{\Delta (Q_1^2 + Q_2^2)^2}$	0	0	$\sqrt{2}$	0
2^+	$\frac{\Delta}{\sqrt{6}}$	$\frac{M Q_2}{Q_1^2 + Q_2^2}$	$\frac{4 M^2 Q_1 Q_2}{\sqrt{3} \Delta (Q_1^2 + Q_2^2)^2}$	$\frac{\sqrt{42} M}{12 Q}$	$\frac{M^2}{4 Q^2}$	$\frac{M}{\sqrt{3} Q}$
2^-	Δ^2	0	0	$\frac{M^2}{Q^2}$	0	0

Table 3.7: The structure function F_{AB} in the symmetric and asymmetric asymptotic limit.

also be identical. There may be a difference in numerical factors, caused by the different distribution amplitudes for the two calculations.

Let us now consider the other mesons. In analogy to $F_{P\gamma\gamma}$ for the pseudoscalar case, we define

$$F_{AB} = \lim_{Q_i \rightarrow \infty} \left[\frac{Q_1^2 + Q_2^2}{M^2} \sqrt{\kappa f_{AB}} \right]. \quad (3.74)$$

In table 3.7 the results are collected for the symmetric, as well as the asymmetric limit. In the expressions we have introduced Δ

$$\Delta = \frac{|Q_1^2 - Q_2^2|}{Q_1^2 + Q_2^2}. \quad (3.75)$$

In the asymmetric limit the F_{TT} 's are the dominant form factor. The other form factors are suppressed by a factor $1/\max_i Q_i$. In the asymmetric limit the F_{SS} form factors have the same Q_i dependence as the F_{TT} form factors for the 0^+ and 2^+ resonances.

Ideally the aim is to measure the dependence on both Q_1 and Q_2 and to separate the form factors f_{SS} , f_{TS} , f_{TT} (as well the helicity-2 as the helicity-0 components), g_{TT} and g_{TS} . This would require high statistics and excellent tagging efficiencies. Single-tag measurements are experimentally more feasible. On the non-tagged lepton often an anti-tag is imposed in order to ensure $Q_2 \approx 0$. Such measurements are only sensitive to an effective form factor. We therefore introduce the following generalization of the pseudoscalar form factor.

$$(F_{eff}(Q^2))^2 = \lim_{Q_2 \rightarrow 0} \kappa [f_{TT} + \xi f_{TS}]|_{Q_1^2=Q^2}. \quad (3.76)$$

In this equation ξ is the ratio of the flux factors \mathcal{L}_{TS} to \mathcal{L}_{TT} that were introduced in (2.40).

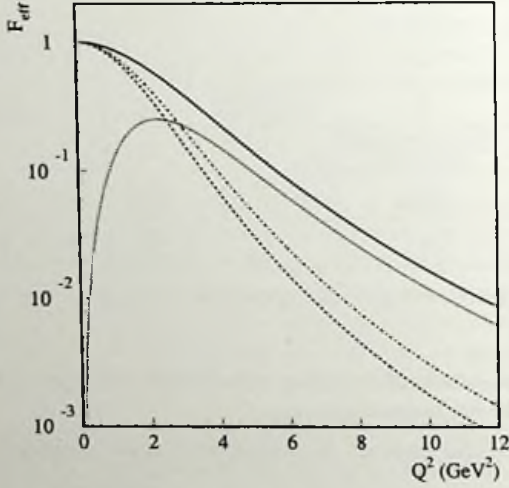


Figure 3.2: The single-tag effective form factor $F_{eff}(Q^2, J^P)$ for the charmonium states for $\xi = 1$. The η_{cD} form factor has not been plotted as it would lie almost on top of the η_c form factor.

For the effective form factors we find

$$\begin{aligned}
 F_{eff}(0^-) &= \frac{M^2}{M^2+Q^2}, \\
 F_{eff}(0^+) &= \frac{1}{3} \frac{M^2}{M^2+Q^2} \left(1 + \frac{2M^2}{M^2+Q^2} \right) \rightarrow \frac{M^2}{M^2+Q^2} \left[1 - \frac{2}{3} \frac{Q^2}{M^2} \right], \\
 F_{eff}(1^+) &= \sqrt{2} \left(\frac{M^2}{M^2+Q^2} \right)^2 \left[\frac{Q^2}{M^2} \left\{ \xi + \frac{Q^2}{2M^2} \right\} \right]^{\frac{1}{2}} \rightarrow \frac{M^2}{M^2+Q^2} \sqrt{2\xi} \frac{Q}{M}, \\
 F_{eff}(2^+) &= \frac{M^2}{M^2+Q^2} \left[\frac{Q^4+6M^4+6\xi M^2 Q^2}{6(M^2+Q^2)^2} \right]^{\frac{1}{2}} \rightarrow \frac{M^2}{M^2+Q^2} \left[1 - \frac{2-\xi}{2} \frac{Q^2}{M^2} \right], \\
 F_{eff}(2^-) &= \frac{M^2}{M^2+Q^2}.
 \end{aligned} \tag{3.77}$$

The limits for the J^+ states denote the limit $Q \rightarrow 0$. For Q small compared to M , all but the 1^+ form factors are similar to the VMD form factor that was also found for the pseudoscalar. All form factors asymptotically behave as $1/Q^2$, but the hierarchy changes. $Q^2 F_{eff}/M^2 \rightarrow 1, 1/3, 1, 1/\sqrt{6}, 1$. Hence, at large Q^2 we predict

$$\frac{M\sigma(e^+e^- \rightarrow e^+e^-R)}{\Gamma_{\gamma\gamma}(R)} = 1 : \frac{1}{9} : 3 : \frac{5}{6} : 5 \quad \text{for } J^P = 0^- : 0^+ : 1^+ : 2^+ : 2^-. \tag{3.78}$$

In figure 3.2 an illustration of the the Q^2 dependence of the effective form factors is given for the different wave functions.

Chapter 4

Construction of $\Sigma |\mathcal{M}|^2$

For quantitative results, we will have to calculate $\Sigma |\mathcal{M}|^2$ numerically, possibly on the basis of an analytical expression. In the previous section the expressions for the cross sections have been obtained by using the BGMS formalism. They have been implemented in a Monte Carlo generator Galuga [84]. Here we shall discuss the direct evaluation of the square of the matrix element, which is implemented in the generator GaGaRes, to be discussed in chapter 6. Thus one has two event generators which should give the same but independent results. The direct calculation offers a simple way to calculate the resonance production density matrices, which will be done in chapter 5.

Even the direct calculation of $\Sigma |\mathcal{M}|^2$ will be done in three different ways, one gives expressions in terms of Lorentz inner products, the others in spinorial expressions.

4.1 $\Sigma |\mathcal{M}|^2$ in terms of invariants

We will first obtain an expression for the total matrix element squared using the most conventional approach¹.

We start with the expressions for the decay of the resonance into two off-shell photons (3.42)-(3.46). These expressions are crossed and the polarization vectors of the photons are replaced by the QED currents $e j_1/Q_1^2$ and $e j_2/Q_2^2$. For the amplitudes this yields

$$\mathcal{M}(^1S_0; \lambda_1, \lambda_2, \lambda'_1, \lambda'_2) = \frac{c_1 e^2}{tt'} \varepsilon [k_1, k_2, j_1(\lambda_1, \lambda'_1), j_2(\lambda_2, \lambda'_2)], \quad (4.1)$$

$$\begin{aligned} \mathcal{M}(^3P_0; \lambda_1, \lambda_2, \lambda'_1, \lambda'_2) &= \frac{c_2 e^2}{tt'} ([j_1(\lambda_1, \lambda'_1) \cdot j_2(\lambda_2, \lambda'_2) k_1 \cdot k_2 \\ &\quad - j_1(\lambda_1, \lambda'_1) \cdot k_2 j_2(\lambda_2, \lambda'_2) \cdot k_1] (W^2 + k_1 \cdot k_2) \\ &\quad - j_1(\lambda_1, \lambda'_1) \cdot j_2(\lambda_2, \lambda'_2) tt'), \end{aligned} \quad (4.2)$$

$$\begin{aligned} \mathcal{M}(^3P_1; \lambda_1, \lambda_2, \lambda'_1, \lambda'_2, \lambda_R) &= \frac{c_3 e^2}{tt'} (t \varepsilon [\varepsilon^*(\lambda_R), j_1(\lambda_1, \lambda'_1), j_2(\lambda_2, \lambda'_2), k_2] \\ &\quad + t' \varepsilon [\varepsilon^*(\lambda_R), j_2(\lambda_2, \lambda'_2), j_1(\lambda_1, \lambda'_1), k_1]), \end{aligned} \quad (4.3)$$

¹Unless the opposite is stated explicitly, a summation over the external helicities is always implied.

$$\begin{aligned} \mathcal{M}(^3P_2; \lambda_1, \lambda_2, \lambda'_1, \lambda'_2, \lambda_R) &= \frac{e_s e^2}{iW} (k_1 \cdot k_2 j_{1\mu}(\lambda_1, \lambda'_1) j_{2\nu}(\lambda_2, \lambda'_2) \\ &\quad + k_{1\mu} k_{2\nu} j_1(\lambda_1, \lambda'_1) \cdot j_2(\lambda_2, \lambda'_2) \\ &\quad - k_{1\mu} j_{2\nu}(\lambda_2, \lambda'_2) j_1(\lambda_1, \lambda'_1) \cdot k_2 \\ &\quad - k_{2\mu} j_{1\nu}(\lambda_1, \lambda'_1) j_2(\lambda_2, \lambda'_2) \cdot k_1) \varepsilon^{*\mu\nu}(\lambda_R), \end{aligned} \quad (4.4)$$

$$\begin{aligned} \mathcal{M}(^1D_2; \lambda_1, \lambda_2, \lambda'_1, \lambda'_2, \lambda_R) &= \frac{e_s e^2}{iW} \varepsilon^{*\mu\nu}(\lambda_R) k_{1\mu} k_{2\nu} \\ &\quad \varepsilon [k_1, k_2, j_1(\lambda_1, \lambda'_1), j_2(\lambda_2, \lambda'_2)]. \end{aligned} \quad (4.5)$$

The $\lambda_i^{(\prime)}$ represent the helicity of the associated external particles. The lepton currents j_1 and j_2 have been defined in (2.23) and (2.24).

$$j_1^\mu = j_1^\mu(\lambda_1, \lambda'_1) = \bar{v}_{\lambda_1}(p_1) \gamma^\mu v_{\lambda'_1}(p'_1), \quad (2.23)$$

$$j_2^\mu = j_2^\mu(\lambda_2, \lambda'_2) = \bar{u}_{\lambda'_2}(p'_2) \gamma^\mu u_{\lambda_2}(p_2). \quad (2.24)$$

Being conserved currents, these currents obey

$$j_i(\lambda_m, \lambda_n) \cdot k_i = 0 \quad (i = 1, 2). \quad (4.6)$$

The pre-factors c_1, \dots, c_5 are given by

$$c_1 = g_0, \quad c_2 = 4g_1/W, \quad c_3 = 2\sqrt{6}g_1, \quad c_4 = 4\sqrt{3}Wg_1, \quad c_5 = 8\sqrt{30}g_2, \quad (4.7)$$

where we have introduced

$$g_i = \frac{16e_q^2 |\mathcal{R}^{(i)}(0)| \alpha}{(s + s' + u + u' - 8m_e^2)^{i+1}} \sqrt{\frac{3\pi}{W}}. \quad (4.8)$$

The Mandelstam invariants s, s', t, t', u and u' have been introduced in section 2.4 and W in section 3.3.

The algebraic manipulation program FORM [85] has been used to obtain expressions for the absolute square of the matrix elements. In these calculations we need expressions for the tensors formed by the product of a lepton-current and its complex conjugate, summed over all helicities

$$L_1^{\mu\nu} = \sum_{\lambda_1, \lambda'_1} j_1^\mu(\lambda_1, \lambda'_1) j_1^{*\nu}(\lambda_1, \lambda'_1) = 4(p_1^\mu p_1^\nu + p_1'^\mu p_1'^\nu + \frac{1}{2} t g^{\mu\nu}), \quad (4.9)$$

$$L_2^{\mu\nu} = \sum_{\lambda_2, \lambda'_2} j_2^\mu(\lambda_2, \lambda'_2) j_2^{*\nu}(\lambda_2, \lambda'_2) = 4(p_2^\mu p_2^\nu + p_2'^\mu p_2'^\nu + \frac{1}{2} t' g^{\mu\nu}). \quad (4.10)$$

Note that the factors $\frac{1}{2}$ for the spin averaging are not included in these tensors.

When the produced resonance carries a spin we also sum over the helicities of the resonance. For the spin-1 and spin-2 resonances we use the completeness relations (3.9) respectively (3.29). The resulting matrix elements squared are collected in appendix A,

where every term has been expressed in the Mandelstam variables and W . Note that we have kept all the particles massive to obtain numerically stable expressions.

In order to write these expression in a compact form, symmetries have been exploited. The first symmetry follows from Bose symmetry of the two intermediate photons ($k_1 \leftrightarrow k_2$). It implies that the matrix element squared is invariant under the following simultaneous change of variables

$$t \leftrightarrow t', \quad u \leftrightarrow u'. \quad (4.11)$$

More symmetries follow from two crossing symmetries of the matrix element squared, following from $p_i \leftrightarrow -p'_i$ for $i = 1, 2$ respectively. As a result, the matrix element squared is invariant under the simultaneous exchange of

$$s \leftrightarrow u', \quad s' \leftrightarrow u, \quad (4.12)$$

and similarly under the simultaneous interchange of

$$s \leftrightarrow u, \quad s' \leftrightarrow u'. \quad (4.13)$$

4.2 Weyl-van der Waerden formalism

Another way to obtain $\sum |\mathcal{M}|^2$ is to use the Weyl-van der Waerden (WvdW) formalism [86–89]. There is an important argument to use this formalism and it is related to the density matrices we need in the next chapter. The density matrices for the production of the resonances require the evaluation of the matrix elements before calculating the square. As a consequence, the completeness relations for the polarization vectors/tensors that have been used in the previous section and which led to dramatic simplifications of the expressions cannot be exploited anymore. For these calculations one needs a different approach.

The WvdW formalism is well suited for the evaluation of amplitudes and, therefore for density matrices. In appendix B a short overview of the WvdW-formalism is given. We will use the conventions and polarization vectors used by Dittmaier [89].

The lepton currents read in the WvdW-formalism

$$\begin{aligned} J_i^{\dot{R}S}(++) &= 2 \left[(p'_i)_1^{\dot{R}}(p_i)_1^S + (p_i)_2^{\dot{R}}(p'_i)_2^S \right], \\ J_i^{\dot{R}S}(+-) &= 2 \left[(p'_i)_2^{\dot{R}}(p_i)_1^S - (p_i)_2^{\dot{R}}(p'_i)_1^S \right], \\ J_i^{\dot{R}S}(-+) &= 2 \left[(p'_i)_1^{\dot{R}}(p_i)_2^S - (p_i)_1^{\dot{R}}(p'_i)_2^S \right], \\ J_i^{\dot{R}S}(--) &= 2 \left[(p_i)_1^{\dot{R}}(p'_i)_1^S + (p'_i)_2^{\dot{R}}(p_i)_2^S \right]. \end{aligned} \quad (4.14)$$

These currents satisfy current conservation (4.6), which reads in the WvdW-formalism

$$J_i^{AB}(\lambda_m, \lambda_n) K_{i,AB} = 0 \quad (i = 1, 2). \quad (4.15)$$

The expressions for the amplitudes (4.1)-(4.5) in the WvdW formalism now become

$$\begin{aligned}
\mathcal{M}(^1S_0)(\lambda_1, \lambda_2, \lambda'_1, \lambda'_2) &= \frac{c_1 e^2}{4W'} \left\{ J_{1,\dot{C}Y}(\lambda_1, \lambda'_1) K_1^{\dot{B}Y} K_{2,\dot{B}Z} J_2^{\dot{C}Z}(\lambda_2, \lambda'_2) \right. \\
&\quad \left. - J_{1,\dot{C}Y}(\lambda_1, \lambda'_1) K_1^{\dot{C}X} K_{2,\dot{D}X} J_2^{\dot{D}Y}(\lambda_2, \lambda'_2) \right\}, \\
\mathcal{M}(^3P_0)(\lambda_1, \lambda_2, \lambda'_1, \lambda'_2) &= \frac{c_2 e^2}{4W'} \left\{ 2H J_{1,\dot{A}B}(\lambda_1, \lambda'_1) J_2^{\dot{A}B}(\lambda_2, \lambda'_2) \right. \\
&\quad \left. - G J_{1,\dot{A}B}(\lambda_1, \lambda'_1) J_{2,\dot{C}D}(\lambda_2, \lambda'_2) K_2^{\dot{A}B} K_1^{\dot{C}D} \right\}, \\
\mathcal{M}(^3P_1)(\lambda_1, \lambda_2, \lambda'_1, \lambda'_2, \lambda_R) &= \frac{c_3 e^2}{4W'} \left\{ t [J_{2,\dot{C}Y}(\lambda_2, \lambda'_2) \varepsilon^{\dot{B}Y}(\lambda_R) J_{1,\dot{B}Z}(\lambda_1, \lambda'_1) K_2^{\dot{C}Z} \right. \\
&\quad - J_{2,\dot{C}Y}(\lambda_2, \lambda'_2) \varepsilon^{\dot{C}X}(\lambda_R) J_{1,\dot{D}X}(\lambda_1, \lambda'_1) K_2^{\dot{D}Y}] \\
&\quad + t' [J_{1,\dot{C}Y}(\lambda_1, \lambda'_1) \varepsilon^{\dot{B}Y}(\lambda_R) J_{2,\dot{B}Z}(\lambda_2, \lambda'_2) K_1^{\dot{C}Z} \\
&\quad \left. - J_{1,\dot{C}Y}(\lambda_1, \lambda'_1) \varepsilon^{\dot{C}X}(\lambda_R) J_{2,\dot{D}X}(\lambda_2, \lambda'_2) K_1^{\dot{D}Y}] \right\}, \quad (4.16) \\
\mathcal{M}(^3P_2)(\lambda_1, \lambda_2, \lambda'_1, \lambda'_2, \lambda_R) &= \frac{c_4 e^2}{8W'} \left\{ 2F J_{1,\dot{A}B}(\lambda_1, \lambda'_1) J_{2,\dot{C}D}(\lambda_2, \lambda'_2) \right. \\
&\quad + K_{1,\dot{A}B} K_{2,\dot{C}D} J_{1,\dot{E}F}(\lambda_1, \lambda'_1) J_2^{\dot{E}F}(\lambda_2, \lambda'_2) \\
&\quad - K_{1,\dot{A}B} J_{2,\dot{C}D}(\lambda_2, \lambda'_2) J_{1,\dot{E}F}(\lambda_1, \lambda'_1) K_2^{\dot{E}F} \\
&\quad - K_{2,\dot{A}B} J_{1,\dot{C}D}(\lambda_1, \lambda'_1) J_{2,\dot{E}F}(\lambda_2, \lambda'_2) K_1^{\dot{E}F} \\
&\quad \left. \varepsilon^{\dot{A}B\dot{C}D}(\lambda_R) \right\}, \\
\mathcal{M}(^1D_2)(\lambda_1, \lambda_2, \lambda'_1, \lambda'_2, \lambda_R) &= \frac{c_5}{4c_1} \left\{ K_{1,\dot{A}B} K_{2,\dot{C}D} \varepsilon^{\dot{A}B\dot{C}D}(\lambda_R) \right\} \\
&\quad \mathcal{M}(^1S_0)(\lambda_1, \lambda_2, \lambda'_1, \lambda'_2),
\end{aligned}$$

where we have introduced

$$\begin{aligned}
F &= k_1 \cdot k_2, \\
G &= W^2 + F, \\
H &= FG - tt'.
\end{aligned} \quad (4.17)$$

FORM has been used to rewrite these expressions in terms of the standard spinor inner products (B.3). Since the results are lengthy, they are not explicitly given in this thesis, but they are present in the code of GaGaRes.

The amplitudes do not have to be evaluated for every helicity configuration. From the definition of the polarization vectors and tensors in (B.14) and (B.19) respectively, and the lepton currents (4.14) the following equations follow from parity conservation

$$\begin{aligned}
\text{Spin-0 } \mathcal{M}(\{-\lambda_i\}) &= \text{sgn}(\prod_i \lambda_i) \mathcal{M}^*(\{\lambda_i\}), \\
\text{Spin-1 } \mathcal{M}(\{-\lambda_i, -\lambda_R\}) &= \text{sgn}(\prod_i \lambda_i) \mathcal{M}^*(\{\lambda_i, \lambda_R\}), \\
\text{Spin-2 } \mathcal{M}(\{-\lambda_i, -\lambda_R\}) &= \text{sgn}(\prod_i \lambda_i) (-1)^{\lambda_R} \mathcal{M}^*(\{\lambda_i, \lambda_R\}).
\end{aligned} \quad (4.18)$$

The absolute square of these amplitudes, summed over all external helicities should yield the same expressions as in Appendix A. Numerically this has been checked, but also analytically for the limit $m_e \rightarrow 0$. We illustrate this with an explicit verification for the 1S_0 resonances. In the limit $m_e \rightarrow 0$ all WvdW spinors with spinor index 2 associated to an external lepton vanish, which leads to a simplification of the lepton currents in (4.14). In this limit no spin flips of the external leptons are allowed. Furthermore, the WvdW tensors related to the external leptons can be written in a convenient dyad form

$$K_i^{\dot{A}B} = P_i^{\dot{A}B} - P_i^{\dot{A}B} = p_i^{\dot{A}} p_i^{\dot{B}} - p_i^{\dot{B}} p_i^{\dot{A}}, \quad (4.19)$$

where a four-vector p_i^μ leads to the bispinor P_i^{AB} and to a dyad built from the spinors p_i^A and p_i^B . In the following the four-vector and the spinor will be denoted by p_i . From the context the interpretation as a four-vector or a spinor follows.

One now evaluates the amplitudes for different helicity configurations. With the shorthand notation for the spinor inner product

$$\langle p_i p_j \rangle \equiv \langle ij \rangle, \quad (4.20)$$

the amplitude $\mathcal{M}(+, +, +, +)$ reads

$$\mathcal{M}(+, +, +, +) = \frac{ie_1 e^2}{t' u'} (\langle 11' \rangle^* \langle 21 \rangle \langle 12 \rangle \langle 2'2 \rangle^* - \langle 2'1' \rangle^* \langle 1'1 \rangle \langle 1'2' \rangle^* \langle 22' \rangle). \quad (4.21)$$

The square results in

$$\begin{aligned} |\mathcal{M}(+, +, +, +)|^2 &= \frac{e_1^2 e^4}{t^2 t'^2} (|\langle 2'1' \rangle|^2 |\langle 1'1 \rangle|^2 |\langle 1'2' \rangle|^2 |\langle 22' \rangle|^2 \\ &\quad + |\langle 11' \rangle|^2 |\langle 21 \rangle|^2 |\langle 12 \rangle|^2 |\langle 2'2 \rangle|^2 \\ &\quad - (\langle 2'1' \rangle^*)^2 (\langle 1'1 \rangle)^2 (\langle 22' \rangle)^2 (\langle 12 \rangle^*)^2 \\ &\quad - (\langle 2'1' \rangle)^2 (\langle 1'1 \rangle^*)^2 (\langle 22' \rangle^*)^2 (\langle 12 \rangle)^2). \end{aligned} \quad (4.22)$$

Using the standard identity $a^2 + (a^*)^2 = (a + a^*)^2 - 2|a|^2$, we find

$$\begin{aligned} |\mathcal{M}(+, +, +, +)|^2 &= \frac{16e_1^2 e^4}{t^2 t'^2} [(1'2')^2 (11')(22') + (12)^2 (11')(22') \\ &\quad - ((12)(1'2') - (12')(21') + (11')(22'))^2 \\ &\quad + 2(12)(22')(1'2')(11')], \end{aligned} \quad (4.23)$$

where we introduced the shorthand notation for the standard four-momentum inner product

$$(ij) \equiv p_i \cdot p_j. \quad (4.24)$$

In terms of the standard invariants this reads

$$|\mathcal{M}(+, +, +, +)|^2 = \frac{c_1^2 e^4}{t^2 t'^2} [t't' s_+^2 - (t't' + \sigma_{2-})^2]. \quad (4.25)$$

For $|\mathcal{M}(-, -, -, -)|^2$ we obtain the same result. For the other non-vanishing contributions we find

$$|\mathcal{M}(+, -, +, -)|^2 = |\mathcal{M}(-, +, -, +)|^2 = \frac{c_1^2 e^4}{t^2 t'^2} [t't' u_+^2 - (t't' - \sigma_{2-})^2]. \quad (4.26)$$

The total matrix element squared follows from

$$\sum_{\lambda_i} |\mathcal{M}| = |\mathcal{M}(+, +, +, +)|^2 + |\mathcal{M}(+, -, +, -)|^2 + |\mathcal{M}(-, +, -, +)|^2 + |\mathcal{M}(-, -, -, -)|^2, \quad (4.27)$$

which results in an expression that is the same as (A.2) for $m_e = 0$. For the other resonances this exercise also resulted in identical results in the limit of a vanishing electron mass.

The expressions for the matrix elements can now be evaluated numerically and the density matrix is then easily obtained. Its trace gives $\sum |\mathcal{M}|^2$, thus avoiding the lengthy and cumbersome expressions in terms of invariants as given in appendix A. When only $\sum |\mathcal{M}|^2$ is needed the numerical evaluation of those lengthy expressions still is the fastest. However, the WvdW calculation can be speeded up, as will be shown in the next section.

$2S+1 P_J$	$\frac{\tau_{WvdW}}{\tau_{iWvdW}}$
1S_0	11.0
3P_0	9.2
3P_1	7.6
3P_2	31.0
1D_2	20.6

Table 4.1: A comparison of the typical CPU time τ_{WvdW} requested for the generation of 1,000,000 events using the 'standard' WvdW formalism presented in section 4.2 and the typical CPU time τ_{iWvdW} requested for the same number of events using the improved WvdW formalism.

4.3 Improved Weyl-van der Waerden formalism

Improvements on the time of calculations can be made by rewriting the amplitudes into traces of complex 2×2 matrices. We refer to this technique as the improved WvdW formalism. So one refrains from the intermediate step of spinor inner product expressions. The reason is that FORTRAN contains the possibility to perform fast calculations with 2×2 -matrices. The method works as follows.

Let us start by introducing a down-matrix K_{\downarrow}

$$K_{\downarrow} \equiv K_{\dot{A}B}, \quad (4.28)$$

and an up-matrix K^{\uparrow}

$$K^{\uparrow} \equiv (K_{\downarrow})^T, \quad K_{\uparrow} \equiv K^{\dot{A}B}. \quad (4.29)$$

Using these matrices the product of an even number of WvdW bispinors can be rewritten as the trace of a product of these up- and down-matrices.

$$\begin{aligned} P^{\dot{A}B} K_{\dot{A}B} &= \text{Tr} [P^{\uparrow} K_{\downarrow}] = 2p \cdot k, \\ P_{\dot{A}B} Q^{\dot{C}B} R_{\dot{C}D} S^{\dot{A}D} &= \text{Tr} [P_{\downarrow} Q^{\uparrow} R_{\downarrow} S^{\uparrow}]. \end{aligned} \quad (4.30)$$

For the spin-2 polarization vectors one needs the additional expressions (see (B.19))

$$\begin{aligned} \text{Tr} [P^{\uparrow} \epsilon_{\dot{\mu}\dot{\nu}}^*(\pm 2) K^{\uparrow}] &= \text{Tr} [P^{\uparrow} \epsilon_{\dot{1}\dot{1}}^*(\pm 1)] \text{Tr} [K^{\uparrow} \epsilon_{\dot{1}\dot{1}}^*(\pm 1)], \\ \text{Tr} [P^{\uparrow} \epsilon_{\dot{\mu}\dot{\nu}}^*(\pm 1) K^{\uparrow}] &= \frac{\pm 1}{\sqrt{2}} (\text{Tr} [P^{\uparrow} \epsilon_{\dot{1}\dot{1}}^*(\pm 1)] \text{Tr} [K^{\uparrow} \epsilon_{\dot{1}\dot{1}}^*(0)] \\ &\quad + \text{Tr} [P^{\uparrow} \epsilon_{\dot{1}\dot{1}}^*(0)] \text{Tr} [K^{\uparrow} \epsilon_{\dot{1}\dot{1}}^*(\pm 1)]), \\ \text{Tr} [P^{\uparrow} \epsilon_{\dot{\mu}\dot{\nu}}^*(0) K^{\uparrow}] &= \frac{1}{\sqrt{6}} (-\text{Tr} [P^{\uparrow} \epsilon_{\dot{1}\dot{1}}^*(+1)] \text{Tr} [K^{\uparrow} \epsilon_{\dot{1}\dot{1}}^*(-1)] \\ &\quad + 2 \text{Tr} [P^{\uparrow} \epsilon_{\dot{1}\dot{1}}^*(0)] \text{Tr} [K^{\uparrow} \epsilon_{\dot{1}\dot{1}}^*(0)] \\ &\quad - \text{Tr} [P^{\uparrow} \epsilon_{\dot{1}\dot{1}}^*(-1)] \text{Tr} [K^{\uparrow} \epsilon_{\dot{1}\dot{1}}^*(+1)]). \end{aligned} \quad (4.31)$$

Having introduced these expressions, the amplitudes can now be written as

$$\begin{aligned}
\mathcal{M}(^1S_0) &= \frac{e_1 e^2}{4t'} \text{Tr} \left[J_{1\downarrow}(\lambda_1, \lambda'_1) \left\{ K_1^\dagger K_{2\downarrow} J_2^\dagger(\lambda_2, \lambda'_2) \right. \right. \\
&\quad \left. \left. - J_2^\dagger(\lambda_2, \lambda'_2) K_{2\downarrow} K_1^\dagger \right\} \right], \\
\mathcal{M}(^3P_0) &= \frac{e^2 e_2}{4t''} \left(2H \text{Tr} \left[J_{1\downarrow}(\lambda_1, \lambda'_1) J_2^\dagger(\lambda_2, \lambda'_2) \right] \right. \\
&\quad \left. - G \text{Tr} \left[J_{1\downarrow}(\lambda_1, \lambda'_1) K_2^\dagger \right] \text{Tr} \left[J_{2\downarrow}(\lambda_2, \lambda'_2) K_1^\dagger \right] \right), \\
\mathcal{M}(^3P_1) &= \frac{e_3 e^2}{4t''} \left(t \text{Tr} \left[J_2^\dagger(\lambda_2, \lambda'_2) \left\{ \varepsilon_{\downarrow}^*(\lambda_R) J_1^\dagger(\lambda_1, \lambda'_1) K_{2\downarrow} \right. \right. \right. \\
&\quad \left. \left. - K_{2\downarrow} J_1^\dagger(\lambda_1, \lambda'_1) \varepsilon_{\downarrow}^*(\lambda_R) \right\} \right] \\
&\quad + t' \text{Tr} \left[J_1^\dagger(\lambda_1, \lambda'_1) \left\{ \varepsilon_{\downarrow}^*(\lambda_R) J_2^\dagger(\lambda_2, \lambda'_2) K_{1\downarrow} \right. \right. \\
&\quad \left. \left. - K_{1\downarrow} J_2^\dagger(\lambda_2, \lambda'_2) \varepsilon_{\downarrow}^*(\lambda_R) \right\} \right] \right), \\
\mathcal{M}(^3P_2) &= \frac{e_4 e^2}{8t''} \left(2F \text{Tr} \left[J_1^\dagger(\lambda_1, \lambda'_1) \varepsilon_{\downarrow\downarrow}^*(\lambda_R) J_2^\dagger(\lambda_2, \lambda'_2) \right] \right. \\
&\quad + \text{Tr} \left[K_1^\dagger \varepsilon_{\downarrow\downarrow}^*(\lambda_R) K_2^\dagger \right] \text{Tr} \left[J_{1\downarrow}(\lambda_1, \lambda'_1) J_2^\dagger(\lambda_2, \lambda'_2) \right] \\
&\quad - \text{Tr} \left[K_1^\dagger \varepsilon_{\downarrow\downarrow}^*(\lambda_R) J_2^\dagger(\lambda_2, \lambda'_2) \right] \text{Tr} \left[J_{1\downarrow}(\lambda_1, \lambda'_1) K_2^\dagger \right] \\
&\quad \left. - \text{Tr} \left[K_2^\dagger \varepsilon_{\downarrow\downarrow}^*(\lambda_R) J_1^\dagger(\lambda_1, \lambda'_1) \right] \text{Tr} \left[J_{2\downarrow}(\lambda_2, \lambda'_2) K_1^\dagger \right] \right), \\
\mathcal{M}(^1D_2) &= \frac{e_5}{4c_1} \text{Tr} \left[K_1^\dagger \varepsilon_{\downarrow\downarrow}^*(\lambda_R) K_2^\dagger \right] \mathcal{M}(^1S_0).
\end{aligned} \tag{4.32}$$

These expressions can be directly evaluated in FORTRAN and have been implemented into GaGaRes. It leads to a considerable gain in calculation speed. In table 4.1 a comparison between the two WvdW methods is given. In doing calculations this method is used whereas the ones of the previous section merely serve as a cross check.

4.4 Numerical stability

In GaGaRes all matrix elements and amplitudes are evaluated in quadruple precision (i.e. REAL*16 and COMPLEX*32) in order to obtain numerically stable calculations. Especially for events where the outgoing leptons are scattered over a very small angle large cancellations in the matrix elements occur requiring these high precision variables. The use of these high precision variables leads to a drop in calculational speed, but is, especially for no-tag events, unavoidable.

Chapter 5

Density matrices

The WvdW method of the previous chapter makes the calculation of amplitudes and, therefore of density matrices straightforward, as will be indicated in section 5.1. In order to have an independent calculation, an extension of the BGMS method would be welcome. With this extension implemented in Galuga, the extended Galuga generator and GaGaRes provide completely independent programs to evaluate both cross sections and density matrices for resonance production. The main part of this chapter is devoted to this extension, which means an extension of the BGMS formalism and the necessary transformation of the density matrices between different reference systems. Furthermore, resonance decay density matrices are required for detailed decay studies. They can only be constructed on the basis of a model decay amplitude. In section 5.4 we give an example for this, which is relevant for the analysis of chapter 9.

5.1 Production of the resonance

The normalized density matrix for the production of the resonance has been defined in chapter 2

$$\rho_{\lambda\lambda'} = \frac{\sum_{\lambda_i} \mathcal{A}_{\lambda_i, \lambda} \mathcal{A}_{\lambda_i, \lambda'}^*}{\sum_{\lambda_i, \lambda_R} \mathcal{A}_{\lambda_i, \lambda_R} \mathcal{A}_{\lambda_i, \lambda'_R}^*}. \quad (2.56)$$

In practice one calculates the density matrix

$$\rho_{\lambda\lambda'} = \sum_{\lambda_i} \mathcal{A}_{\lambda_i, \lambda} \mathcal{A}_{\lambda_i, \lambda'}^* \quad (5.1)$$

and normalizes later on. From the context it will be clear whether one deals with this density matrix or the normalized one. This density matrix is Hermitian and the trace of the real, positive definite diagonal elements adds up to 1. However, from the choice of polarization vectors (B.14) and parity conservation (4.18) one additional symmetry of the density matrix can be derived. For the spin-2 density matrices it reads

$$\begin{aligned} \rho_{\lambda\lambda'} &= \sum_{\lambda_i} \mathcal{A}(\lambda_i, \lambda) \mathcal{A}^*(\lambda_i, \lambda') = \sum_{\lambda_i} \text{sgn}^2(\Pi_i \lambda_i) (-1)^{\lambda+\lambda'} \mathcal{A}^*(-\lambda_i, -\lambda) \mathcal{A}(-\lambda_i, -\lambda') \\ &= (-1)^{\lambda+\lambda'} \sum_{\lambda_i} \mathcal{A}(\lambda_i, -\lambda') \mathcal{A}^*(\lambda_i, -\lambda) = (-1)^{\lambda+\lambda'} \rho_{-\lambda, -\lambda'}. \end{aligned} \quad (5.2)$$

Analogously for spin-1 resonances one finds

$$\rho_{\lambda\lambda'} = \rho_{-\lambda'-\lambda}. \quad (5.3)$$

In general, the density matrix corresponding to a spin- m resonance, where m has an integer value, contains $2m(m + \frac{3}{2})$ independent real parameters. The above symmetry has not been used in GaGaRes, although it could increase the calculation speed. However, checks have been made that these symmetry relations are satisfied.

The elements of the density matrix depend on a particular combination of the helicities of the resonance. As a consequence, the density matrix elements depend on the choice of polarization vectors and the choice of reference frame. Only the trace of the density matrix, i.e. the cross section for the resonance production process is independent from these choices.

The density matrix is constructed in the rest frame of the resonance (RRF). As quantization axis, the z -axis, we have chosen the direction of the boost which leads from the lab-system to the resonance rest frame, i.e. the direction of the resonance in the lab-system. From an experimental point of view this is the most natural choice as the boost direction can be reconstructed from the detected remnants of the resonance.

The Lorentz transformation \mathcal{L}_{LR} from the lab-frame to the RRF is chosen to consist of three transformations, two rotations (\mathcal{L}_θ and \mathcal{L}_ϕ) and a boost (\mathcal{L}_B)

$$\mathcal{L}_{LR} = \mathcal{L}_B \mathcal{L}_\theta \mathcal{L}_\phi. \quad (5.4)$$

The rotations are given by

$$\mathcal{L}_\theta = \begin{pmatrix} 1 & 0 & 0 & 0 \\ 0 & \cos \theta & 0 & -\sin \theta \\ 0 & 0 & 1 & 0 \\ 0 & \sin \theta & 0 & \cos \theta \end{pmatrix}, \quad \mathcal{L}_\phi = \begin{pmatrix} 1 & 0 & 0 & 0 \\ 0 & \cos \phi & \sin \phi & 0 \\ 0 & -\sin \phi & \cos \phi & 0 \\ 0 & 0 & 0 & 1 \end{pmatrix}. \quad (5.5)$$

The boost is given by

$$\mathcal{L}_B = \begin{pmatrix} \gamma & 0 & 0 & -\gamma\beta \\ 0 & 1 & 0 & 0 \\ 0 & 0 & 1 & 0 \\ -\gamma\beta & 0 & 0 & \gamma \end{pmatrix}. \quad (5.6)$$

In the above expressions θ and ϕ are the polar and azimuthal angle of the resonance in the lab-frame. So \mathcal{L}_ϕ rotates the momentum \vec{p}_R into the xz -plane and then \mathcal{L}_θ brings \vec{p}_R along the z -axis [cf (2.14)]. The factors β and γ are given by

$$\beta = \frac{|\vec{p}_R|}{E_R}, \quad \gamma = \frac{1}{\sqrt{1-\beta^2}} = \frac{E_R}{M}. \quad (5.7)$$

Combining these expressions yields

$$\mathcal{L}_{LR} = \begin{pmatrix} \gamma & -\gamma\beta \cos \phi \sin \theta & -\gamma\beta \sin \phi \sin \theta & -\gamma\beta \cos \theta \\ 0 & \cos \phi \cos \theta & \sin \phi \cos \theta & -\sin \theta \\ 0 & -\sin \phi & \cos \phi & 0 \\ -\gamma\beta & \gamma \cos \phi \sin \theta & \gamma \sin \phi \sin \theta & \gamma \cos \theta \end{pmatrix}. \quad (5.8)$$

The x - and y -axis in the RRF are defined by these transformations. They are the axes of the lab-system. Every event has a resonance which moves along the z -axis in the RRF system.

The calculation of the density matrix in this reference frame using the WvdW formalism now proceeds in GaGaRes as follows. When an event in the lab system is known, i.e. GaGaRes specifies all four-momenta, the transformation \mathcal{L}_{LR} is applied to this event and the amplitudes and the normalized density matrices are then calculated for the four-momenta in the RRF. By repeating this for all generated events GaGaRes evaluates the density matrix which governs the decay distribution of the resonance in the RRF. This average density matrix is calculated by taking the weighted average of the density matrix.

The next problem is to obtain the same density matrix using the BGMS formalism.

5.2 Density matrices in the BGMS formalism

In section 2.5 we have introduced the BGMS formalism. In this section we will extend this formalism to the construction of the density matrices. We first discuss some details of the formalism.

The BGMS formalism is formulated in the rest frame of the resonance but instead of the boost direction one chooses the direction of one of the intermediate photons, say photon 1, as z -axis and quantization axis. It is convenient to refer to this reference system as the Budnev frame. Furthermore, the standard set of spin-1 polarization vectors is used for a resonance with 3-momentum \vec{k} in the θ, ϕ direction

$$\begin{aligned}\varepsilon_{\pm}^{\mu} &= \frac{1}{\sqrt{2}}(0, \mp \cos \phi \cos \theta + i \sin \phi, \mp \sin \phi \cos \theta - i \cos \phi, \pm \sin \theta), \\ \varepsilon_0^{\mu} &= \frac{k_0}{m} \left(\frac{|\vec{k}|}{k_0}, \cos \phi \sin \theta, \sin \phi \sin \theta, \cos \theta \right).\end{aligned}\quad (5.9)$$

In this convention the spin-2 polarization tensors are given by

$$\begin{aligned}\varepsilon^{\mu\nu}(\pm 2) &= \varepsilon^{\mu}(\pm 1)\varepsilon^{\nu}(\pm 1), \\ \varepsilon^{\mu\nu}(\pm 1) &= \frac{1}{\sqrt{2}}(\varepsilon^{\mu}(\pm 1)\varepsilon^{\nu}(0) + \varepsilon^{\mu}(0)\varepsilon^{\nu}(\pm 1)), \\ \varepsilon^{\mu\nu}(0) &= \frac{1}{\sqrt{6}}(\varepsilon^{\mu}(+1)\varepsilon^{\nu}(-1) + 2\varepsilon^{\mu}(0)\varepsilon^{\nu}(0) + \varepsilon^{\mu}(-1)\varepsilon^{\nu}(1)),\end{aligned}\quad (5.10)$$

where the standard Clebsch Gordan coefficients have been used (page 58 of [90]).

In appendix B another convention is used for polarization vectors in order to apply conveniently the WvdW formalism. When we label the sets of polarization vectors and tensors of equations (5.9) and (5.10) with the index A and the polarization vectors and corresponding tensors as introduced by Dittmaier in (B.14) with an index B , the two sets are related by

$$\begin{aligned}\varepsilon_B^{\mu\nu}(0) = \varepsilon_A^{\mu\nu}(0), \quad \varepsilon_{B,\pm}^{\mu} &= \pm e^{\mp i\phi} \varepsilon_{A,\pm}^{\mu}, \quad \varepsilon_{B,0}^{\mu} = \varepsilon_{A,0}^{\mu}, \\ \varepsilon_B^{\mu\nu}(\pm 1) &= e^{\mp i\phi} \varepsilon_A^{\mu\nu}(\pm 1), \quad \varepsilon_B^{\mu\nu}(\pm 2) = e^{\mp 2i\phi} \varepsilon_A^{\mu\nu}(\pm 2).\end{aligned}\quad (5.11)$$

As the two different sets of polarization vectors differ in overall phase factors, the off-diagonal elements may have different phase factors for the two different choices of polarization vectors. For the diagonal elements of the density matrix this will not be the case as the phase factors are multiplied by the complex conjugate phase factors.

With the choice (5.9) of polarization vectors the density matrices for the virtual photons can be written as [16]

$$(\rho_i) = \begin{pmatrix} \rho_i^{++} & -i|\rho_i^{+0}|e^{i\tilde{\phi}_i} & -|\rho_i^{+-}|e^{2i\tilde{\phi}_i} \\ i|\rho_i^{+0}|e^{-i\tilde{\phi}_i} & \rho_i^{00} & -i|\rho_i^{+0}|e^{i\tilde{\phi}_i} \\ -|\rho_i^{+-}|e^{-2i\tilde{\phi}_i} & i|\rho_i^{+0}|e^{-i\tilde{\phi}_i} & \rho_i^{++} \end{pmatrix}. \quad (5.12)$$

In this matrix $\tilde{\phi}_i$ is the azimuthal angle of the associated incoming lepton in the Budnev frame.

In the Budnev frame the photons are back-to-back along the z -axis. As a consequence, the resonance helicity and the photon helicities are related in a trivial way

$$\lambda_R = \lambda_1 - \lambda_2, \quad (5.13)$$

where the λ_i are the photon helicities.

An element of the resonance density matrix for the process $e^+e^- \rightarrow e^+e^-R$, which we denote in this formalism by $\Sigma_{\lambda\lambda'}$, is given by

$$\Sigma_{\lambda\lambda'} = \sum_{\lambda_1, \lambda_2, \lambda'_1, \lambda'_2} \rho_1^{\lambda_1 \lambda'_1} \rho_2^{\lambda_2 \lambda'_2} M_{\lambda_1' \lambda_2' \lambda_1 \lambda_2}, \quad (5.14)$$

$$\lambda = \lambda_1 - \lambda_2$$

$$\lambda' = \lambda'_1 - \lambda'_2$$

where $M_{\lambda_1' \lambda_2' \lambda_1 \lambda_2}$ has been defined in equation (2.32) and equation (2.34) holds.

For the diagonal elements we find

$$\Sigma_{2+2+} = \Sigma_{2-2-} = \rho_1^{++} \rho_2^{++} M_{+-+-} = 4\sqrt{X_{\gamma\gamma}} \rho_1^{++} \rho_2^{++} \sigma_{TT}^B, \quad (5.15)$$

$$\begin{aligned} \Sigma_{++} = \Sigma_{--} &= \rho_1^{++} \rho_2^{00} M_{+0+0} + \rho_1^{00} \rho_2^{++} M_{0+0+} - 2|\rho_1^{+0}| |\rho_2^{+0}| M_{0-+0} \cos(\tilde{\phi}) \\ &= 2\sqrt{X_{\gamma\gamma}} (\rho_1^{++} \rho_2^{00} \sigma_{TS} + \rho_1^{00} \rho_2^{++} \sigma_{ST} - 4|\rho_1^{+0}| |\rho_2^{+0}| \cos(\tilde{\phi}) \tau_{TS}^B), \end{aligned} \quad (5.16)$$

$$\begin{aligned} \Sigma_{00} &= 2\rho_1^{++} \rho_2^{++} M_{++++} + \rho_1^{00} \rho_2^{00} M_{0000} + 2|\rho_1^{+-}| |\rho_2^{+-}| \cos(2\tilde{\phi}) M_{--++} \\ &\quad - 4|\rho_1^{+0}| |\rho_2^{+0}| \cos(\tilde{\phi}) M_{00++} \\ &= 2\sqrt{X_{\gamma\gamma}} (4\rho_1^{++} \rho_2^{++} \sigma_{TT}^A + \rho_1^{00} \rho_2^{00} \sigma_{SS} + 2|\rho_1^{+-}| |\rho_2^{+-}| \cos(2\tilde{\phi}) \tau_{TT} \\ &\quad - 8|\rho_1^{+0}| |\rho_2^{+0}| \cos(\tilde{\phi}) \tau_{TS}^A), \end{aligned} \quad (5.17)$$

where the notation from section 2.5 has been used. Furthermore, we have split up the σ_{TT} and τ_{TS} expressions:

$$\sigma_{TT} \equiv \sigma_{TT}^A + \sigma_{TT}^B = \frac{1}{4\sqrt{X_{\gamma\gamma}}} (M_{++++} + M_{+-+-}), \quad (5.18)$$

$$\tau_{TS} \equiv \tau_{TS}^A + \tau_{TS}^B = \frac{1}{4\sqrt{X_{\gamma\gamma}}} (M_{+00+} + M_{-00+}). \quad (5.19)$$

In the formulae $\tilde{\phi}$ is the angle between the two scattering planes in the Budnev frame.

For the off-diagonal elements we do the same. The results are summarized below

$$\Sigma_{+-} = e^{2i\tilde{\phi}_1} \left(2|\rho_1^{+0}\|\rho_2^{+0}|e^{-i\tilde{\phi}}M_{0++0} - |\rho_1^{+-}\|\rho_2^{00}|M_{-0+0} - \rho_1^{00}\|\rho_2^{+-}|e^{-2i\tilde{\phi}}M_{0+0-} \right), \quad (5.20)$$

$$\begin{aligned} \Sigma_{+0} = & i e^{i\tilde{\phi}_1} \left(\rho_1^{++}\|\rho_2^{+0}|e^{-i\tilde{\phi}}M_{++++} - |\rho_1^{+0}\|\rho_2^{00}|M_{00+0} \right. \\ & + |\rho_1^{+-}\|\rho_2^{+0}|M_{--+0}e^{i\tilde{\phi}} - |\rho_1^{+0}\|\rho_2^{+-}|e^{-2i\tilde{\phi}}M_{--0+} \\ & \left. + \rho_1^{00}\|\rho_2^{+0}|e^{-i\tilde{\phi}}M_{000+} - |\rho_1^{+0}\|\rho_2^{++}|M_{++0+} \right). \end{aligned} \quad (5.21)$$

For the spin-2 resonances one has additionally

$$\Sigma_{2++} = i e^{i\tilde{\phi}_1} \left(\rho_1^{++}\|\rho_2^{+0}|e^{-i\tilde{\phi}}M_{+0+-} - |\rho_1^{+0}\|\rho_2^{++}|M_{0-+-} \right), \quad (5.22)$$

$$\begin{aligned} \Sigma_{2+0} = & -e^{2i\tilde{\phi}_1} \left(\rho_1^{++}\|\rho_2^{+-}|e^{-2i\tilde{\phi}}M_{++++} - |\rho_1^{+0}\|\rho_2^{+0}|e^{-i\tilde{\phi}}M_{00+-} \right. \\ & \left. + |\rho_1^{+-}\|\rho_2^{++}|M_{--+-} \right), \end{aligned} \quad (5.23)$$

$$\Sigma_{2+-} = i e^{3i\tilde{\phi}_1} \left(-|\rho_1^{+-}\|\rho_2^{+0}|e^{-i\tilde{\phi}}M_{-0+-} + |\rho_1^{+0}\|\rho_2^{+-}|e^{-2i\tilde{\phi}}M_{0+--} \right), \quad (5.24)$$

$$\Sigma_{2+2-} = e^{4i\tilde{\phi}_1} |\rho_1^{+-}\|\rho_2^{+-}|e^{-2i\tilde{\phi}}M_{-++-}. \quad (5.25)$$

Note that besides the $\tilde{\phi}$ dependence, for the off-diagonal elements there is also an overall $\tilde{\phi}_1$ dependence.

In analogy with the σ and the τ terms we can introduce

$$\chi_{+0} = \frac{i}{2\sqrt{X_{\gamma\gamma}}} M_{++++}, \quad \chi_{0+} = \frac{i}{2\sqrt{X_{\gamma\gamma}}} M_{++++}, \quad (5.26)$$

$$\xi_{+0} = \frac{i}{2\sqrt{X_{\gamma\gamma}}} M_{00+0}, \quad \xi_{0+} = \frac{i}{2\sqrt{X_{\gamma\gamma}}} M_{000+}, \quad (5.27)$$

$$\zeta_{++} = \frac{1}{2\sqrt{X_{\gamma\gamma}}} M_{++++}, \quad \zeta_{00} = \frac{1}{2\sqrt{X_{\gamma\gamma}}} M_{00+-}, \quad (5.28)$$

$$\zeta_{+0} = \frac{i}{2\sqrt{X_{\gamma\gamma}}} M_{+0+-}, \quad \zeta_{0+} = \frac{i}{2\sqrt{X_{\gamma\gamma}}} M_{0+--}. \quad (5.29)$$

The ζ functions are only non-vanishing for spin-2 resonances.

Now the off-diagonal elements can be written as

$$\begin{aligned} \Sigma_{+0} = & e^{i\tilde{\phi}_1} \sqrt{X_{\gamma\gamma}} \left(\rho_1^{++}\|\rho_2^{+0}|e^{-i\tilde{\phi}}\chi_{+0} - |\rho_1^{+0}\|\rho_2^{00}\xi_{+0} + |\rho_1^{+-}\|\rho_2^{+0}\|\eta_R e^{i\tilde{\phi}}\chi_{+0} \right. \\ & \left. - |\rho_1^{+0}\|\rho_2^{+-}|e^{-2i\tilde{\phi}}\eta_R\chi_{0+} + \rho_1^{00}\|\rho_2^{+0}|e^{-i\tilde{\phi}}\xi_{0+} - |\rho_1^{+0}\|\rho_2^{++}\chi_{0+} \right), \end{aligned} \quad (5.30)$$

$$\Sigma_{+-} = e^{2i\tilde{\phi}_1} \sqrt{X_{\gamma\gamma}} \left(4|\rho_1^{+0}\|\rho_2^{+0}|e^{-i\tilde{\phi}}\eta_{RTS}^B - |\rho_1^{+-}\|\rho_2^{00}\eta_{RST} - \rho_1^{00}\|\rho_2^{+-}|e^{-2i\tilde{\phi}}\eta_{RST} \right), \quad (5.31)$$

$$\Sigma_{2+1+} = e^{i\tilde{\phi}_1} \sqrt{X_{\gamma\gamma}} \left(\rho_1^{++}\|\rho_2^{+0}|e^{-i\tilde{\phi}}\zeta_{+0} - |\rho_1^{+0}\|\rho_2^{++}\eta_R\zeta_{0+} \right), \quad (5.32)$$

$$\Sigma_{2+0} = -e^{2i\tilde{\phi}_1} \left(\rho_1^{++}\|\rho_2^{+-}|e^{-2i\tilde{\phi}}\zeta_{++} - |\rho_1^{+0}\|\rho_2^{+0}|e^{-i\tilde{\phi}}\zeta_{00} + |\rho_1^{+-}\|\rho_2^{++}\eta_R\zeta_{++} \right), \quad (5.33)$$

$$\Sigma_{2+1-} = e^{3i\tilde{\phi}_1} \sqrt{X_{\gamma\gamma}} \left(-|\rho_1^{+-}| |\rho_2^{+0}| e^{-i\tilde{\phi}} \eta_R \zeta_{+0} + |\rho_1^{+0}| |\rho_2^{+-}| e^{-2i\tilde{\phi}} \zeta_{0+} \right), \quad (5.34)$$

$$\Sigma_{2+2-} = e^{4i\tilde{\phi}_1} e^{-2i\tilde{\phi}} \sqrt{X_{\gamma\gamma}} |\rho_1^{+-}| |\rho_2^{+-}| \eta_R \sigma_{TT}^B. \quad (5.35)$$

In these formulae η_R is a phase factor which is 1 for the "normal" J^P series ($J^P = 0^+, 1^-, 2^+, \dots$) and -1 for the "abnormal" J^P series ($J^P = 0^-, 1^+, 2^-, \dots$). The ξ functions and ζ_{00} vanish for the 3P_1 resonance ($M_{00\lambda\lambda'}$ and $M_{\lambda\lambda'00}$ vanish).

The density matrix after integration over the phase space of the outgoing leptons, denoted by Σ^{int} , is then given by

$$\Sigma_{\lambda\lambda'}^{int} = \frac{\alpha^2}{32\pi^4 Q_1^2 Q_2^2} \frac{1}{\sqrt{(p_1 \cdot p_2)^2 - m_e^4}} \Sigma_{\lambda\lambda'} \frac{d^3 \vec{p}'_1}{E'_1} \frac{d^3 \vec{p}'_2}{E'_2}. \quad (5.36)$$

The trace should equal the total cross section. When we use the expressions for the diagonal elements we indeed obtain

$$\begin{aligned} \text{Tr}(\Sigma^{int}) = & \frac{\alpha^2}{16\pi^4 Q_1^2 Q_2^2} \sqrt{\frac{(k_1 \cdot k_2)^2 - k_1^2 k_2^2}{(p_1 \cdot p_2)^2 - m_e^4}} \left[4\rho_1^{++} \rho_2^{++} \sigma_{TT} + 2|\rho_1^{+-} \rho_2^{+-}| \tau_{TT} \cos(2\tilde{\phi}) \right. \\ & \left. + 2\rho_1^{++} \rho_2^{00} \sigma_{ST} + 2\rho_1^{00} \rho_2^{++} \sigma_{TS} + \rho_1^{00} \rho_2^{00} \sigma_{SS} - 8|\rho_1^{+0} \rho_2^{+0}| \cos(\tilde{\phi}) \tau_{TS} \right] \frac{d^3 \vec{p}'_1}{E'_1} \frac{d^3 \vec{p}'_2}{E'_2}, \end{aligned} \quad (5.37)$$

which is identical to (2.39) in section 2.5.

In analogy with the form factors f_{AB} and g_{AB} for the σ and τ terms defined in (3.65) and (3.66) we can introduce form factors related to the functions χ , ξ and ζ for the model that has been introduced in chapter 3 ($A, B = +, 0, -$)

$$\chi_{AB} = \delta(P^2 - M^2) 8\pi^2 \frac{(2J+1)\Gamma_{\gamma\gamma}(J^P)}{M} k_{AB}(J^P), \quad (5.38)$$

$$\xi_{AB} = \delta(P^2 - M^2) 8\pi^2 \frac{(2J+1)\Gamma_{\gamma\gamma}(J^P)}{M} m_{AB}(J^P), \quad (5.39)$$

$$\zeta_{AB} = \delta(P^2 - M^2) 8\pi^2 \frac{(2J+1)\Gamma_{\gamma\gamma}(J^P)}{M} n_{AB}(J^P). \quad (5.40)$$

Using the crossed expressions for the amplitudes from table 3.1, we have obtained the results that are summarized in table 5.1.

From table 5.1 it can be seen that for the 2^- resonance all form factors k , m and n vanish. The form factors f_{TT} and g_{TT} are the only non-vanishing form factors for this resonance. For f_{TT} the non-vanishing contribution comes from the σ_{TT}^A part. As a consequence, the only non-vanishing density matrix element for the 2^- resonance in the Budnev frame is the 00 component. This behaviour can be understood by comparing the expression for the amplitudes for the production of a 0^- and a 2^- resonance (e.g. eqns (4.1) and (4.5)). The matrix element for the spin-2 resonance is essentially the amplitude for the production of the spin-0 resonance multiplied by a prefactor to take into account the spin.

J^P	k_{+0}	m_{+0}
1^+	$-\kappa \frac{M}{2} \frac{Q_2^2}{\nu^3} (\nu + Q_1^2)(Q_1^2 - Q_2^2)$	0
2^+	$-\kappa \frac{M Q_2}{4\sqrt{3}} \frac{(\nu - Q_1^2)}{\nu^4} [2Q_1^2 Q_2^2 - \nu(Q_1^2 + Q_2^2)]$	$\kappa \frac{M^3 Q_1 Q_2^2}{2\sqrt{3}\nu^4} (\nu - Q_1^2)$
2^-	0	0

J^P	n_{++}	n_{+0}	n_{00}
2^+	$\kappa \frac{1}{2\sqrt{6}} \frac{M^2}{\nu^3} [2Q_1^2 Q_2^2 - \nu(Q_1^2 + Q_2^2)]$	$\kappa \frac{\sqrt{2}}{4} \frac{M^3 Q_2}{\nu^3} (\nu - Q_1^2)$	$-\kappa \frac{M^4 Q_1 Q_2}{\sqrt{6}\nu^3}$
2^-	0	0	0

Table 5.1: The form factors k_{AB} , m_{AB} and n_{AB} ($A, B = +, 0, -$).

5.3 Transforming the density matrices

In the previous section we have constructed the complete density matrix in the Budnev frame. However, from an experimental point of view the RRF is a more convenient reference frame. As the elements of the density matrix depend on the chosen polarization vectors/tensors, the density matrix is frame dependent. When one wants to rotate the quantization axis over the angles θ_p and ϕ_p the density matrix ρ changes into the density matrix $\tilde{\rho}$ according to

$$\tilde{\rho}_{\lambda\lambda'} = A_{\lambda\mu} A_{\lambda'\mu'}^* \rho_{\mu\mu'}. \quad (5.41)$$

Thus a density matrix ρ calculated in the Budnev frame can be transformed to the RRF. In the Budnev frame the boost direction which was needed to get to the χ_{c2} rest system is characterized by θ_p and ϕ_p .

For spin-1 resonances this transformation matrix A can be shown to be

$$A_{\lambda\mu} = \begin{pmatrix} \frac{1+c}{2} e^{-i\phi} & \frac{s}{\sqrt{2}} & \frac{1-c}{2} e^{i\phi} \\ -\frac{s}{\sqrt{2}} e^{-i\phi} & c & \frac{s}{\sqrt{2}} e^{i\phi} \\ \frac{1-c}{2} e^{-i\phi} & -\frac{s}{\sqrt{2}} & \frac{1+c}{2} e^{i\phi} \end{pmatrix} \quad (5.42)$$

The order of the indices λ, μ is taken to be $(+, 0, -)$. For spin-2 resonances this transform-

ation matrix reads (with order +2, +1, 0, -1, -2)

$$A_{\lambda\mu} = \begin{pmatrix} \left(\frac{1+c}{2}\right)^2 e^{-2i\phi} & \frac{(1+c)s}{2} e^{-i\phi} & \frac{s^2}{2} \sqrt{\frac{3}{2}} & \frac{(1-c)s}{2} e^{i\phi} & \left(\frac{1-c}{2}\right)^2 e^{2i\phi} \\ -\frac{(1+c)s}{2} e^{-2i\phi} & \frac{(1+c)(2c-1)}{2} e^{-i\phi} & cs\sqrt{\frac{3}{2}} & \frac{(1-c)(2c+1)}{2} e^{i\phi} & \frac{(1-c)s}{2} e^{2i\phi} \\ \frac{1}{2} \sqrt{\frac{3}{2}} s^2 e^{-2i\phi} & -\sqrt{\frac{3}{2}} s c e^{-i\phi} & \frac{3c^2-1}{2} & \sqrt{\frac{3}{2}} s c e^{i\phi} & \frac{1}{2} \sqrt{\frac{3}{2}} s^2 e^{2i\phi} \\ -\frac{(1-c)s}{2} e^{-2i\phi} & \frac{(1-c)(2c+1)}{2} e^{-i\phi} & -cs\sqrt{\frac{3}{2}} & \frac{(1+c)(2c-1)}{2} e^{i\phi} & \frac{(1+c)s}{2} e^{2i\phi} \\ \left(\frac{1-c}{2}\right)^2 e^{-2i\phi} & -\frac{(1-c)s}{2} e^{-i\phi} & \frac{s^2}{2} \sqrt{\frac{3}{2}} & -\frac{(1+c)s}{2} e^{i\phi} & \left(\frac{1+c}{2}\right)^2 e^{2i\phi} \end{pmatrix} \quad (5.43)$$

In the expressions for the transformation matrices we have introduced the shorthand notation

$$c = \cos(\theta_p), s = \sin(\theta_p), \phi = \phi_p. \quad (5.44)$$

For the transformation matrices it can be checked that for $\theta_p = \phi_p = 0$ they reduce to the unit matrix. Furthermore, the transformed density matrix is Hermitian and satisfies the additional symmetry.

One can also make a transition from the density matrix corresponding to one set of polarization vectors to the density matrix corresponding to the other set of polarization vectors. The off-diagonal elements will have some phase shifts. For an element of the density matrix one finds, using (5.11),

$$\rho_{\lambda\lambda', B} = e^{i\Delta\phi_{\lambda\lambda'}} \rho_{\lambda\lambda', A}, \quad (5.45)$$

with for the spin-1 density matrix

$$\Delta\phi_{\lambda\lambda'} = \begin{pmatrix} 0 & \phi & 2\phi + \pi \\ -\phi & 0 & \phi + \pi \\ -(2\phi + \pi) & -(\phi + \pi) & 0 \end{pmatrix}. \quad (5.46)$$

For the spin-2 density matrices we find analogously

$$\Delta\phi_{\lambda\lambda'} = \begin{pmatrix} 0 & \phi & 2\phi & 3\phi & 4\phi \\ -\phi & 0 & \phi & 2\phi & 3\phi \\ -2\phi & -\phi & 0 & \phi & 2\phi \\ -3\phi & -2\phi & -\phi & 0 & \phi \\ -4\phi & -3\phi & -2\phi & -\phi & 0 \end{pmatrix}. \quad (5.47)$$

5.4 Density matrices for the decay

As was pointed out in equation (2.55) in section 2.9, we also need a density matrix to describe the decay of the resonance. The expression for this decay density matrix will

depend on the decay mode and the model used to describe this decay. In this section we will focus on one decay: the decay of a spin-2 resonance into two spin-1 particles, where one of the particles is massive and the other is massless. We have chosen this decay mode as it will be used in the analysis presented in chapter 9 where the spin-2 resonance decays into a J/ψ and a photon. Later on in this section we will extend the density matrix so that also the decay of the J/ψ resonance into a lepton pair is included. In the following discussion we will refer to the massless spin-1 particle as the photon and to the massive spin-1 particle as the J/ψ . The spin-2 resonance will be called χ_{c2} . This decay can be denoted by

$$\chi_{c2}(p_R) \rightarrow \gamma(k_1)J/\psi(k_2). \quad (5.48)$$

For the amplitude \mathcal{M} of the decay of the spin-2 resonance we use the amplitude that is given in equation (3.45)

$$\begin{aligned} \mathcal{M}(\lambda, \lambda_1, \lambda_2) &= c[(k_1 \cdot k_2)\varepsilon_1^{*\mu}(\lambda_1)\varepsilon_2^{*\nu}(\lambda_2) + (\varepsilon_1^*(\lambda_1) \cdot \varepsilon_2^*(\lambda_2))k_1^\mu k_2^\nu \\ &\quad - (k_1 \cdot \varepsilon_2^*(\lambda_2))\varepsilon_1^{*\mu}(\lambda_1)k_2^\nu - (k_2 \cdot \varepsilon_1^*(\lambda_1))\varepsilon_2^{*\mu}(\lambda_2)k_1^\nu] \varepsilon_{\mu\nu}(\lambda) \\ &= cF_1^{*\rho\mu}(\lambda_1)F_{2\rho\nu}^*(\lambda_2)\varepsilon_\mu^\nu(\lambda), \end{aligned} \quad (5.49)$$

where $F_i^{\alpha\beta}$ is the field strength

$$F_i^{\alpha\beta}(\lambda_i) = k_i^\alpha \varepsilon_i^\beta(\lambda_i) - k_i^\beta \varepsilon_i^\alpha(\lambda_i). \quad (5.50)$$

In these equations the index 1 refers to the photon and 2 refers to the massive J/ψ . The λ 's refer to the helicity of the associated particles. From equation (5.49) one sees that the $\chi_{c2} \rightarrow \gamma\gamma$ amplitude is also used for process (5.48). The parameter c is not specified here, but its complex square will contain the width for the decay of the spin-2 particle into these two spin-1 particles.

The density matrix \mathcal{D} for the decay of the resonance is then constructed by

$$\mathcal{D}_{\lambda\lambda'} = \sum_{\lambda_1, \lambda_2} \mathcal{M}(\lambda, \lambda_1, \lambda_2)\mathcal{M}^*(\lambda', \lambda_1, \lambda_2). \quad (5.51)$$

In the evaluation of this density matrix we make use of the invariant spin summations for spin-1 particles. For the massless photon this relation reads

$$\sum_{\lambda_1} \varepsilon_{1,\alpha}(\lambda_1)\varepsilon_{1,\beta}^*(\lambda_1) = -g_{\alpha\beta}, \quad (5.52)$$

whereas for the massive J/ψ it reads

$$\sum_{\lambda_2} \varepsilon_{2,\alpha}(\lambda_2)\varepsilon_{2,\beta}^*(\lambda_2) = -g_{\alpha\beta} + \frac{k_{2,\alpha}k_{2,\beta}}{M^2}, \quad (5.53)$$

where M is its mass. In fact, due to the gauge invariance of the field strength in equation (5.49) only the $g_{\alpha\beta}$ term in equation (5.53) contributes. This leads to the following expression for the density matrix for the decay of the resonance

$$\begin{aligned} \mathcal{D}_{\lambda\lambda'} &= |c|^2 \left[(k_1 \cdot k_2)\varepsilon^{\alpha\beta}(\lambda)\varepsilon_{\alpha\beta}^*(\lambda') + 2(k_1 \cdot \varepsilon(\lambda) \cdot k_1)(k_1 \cdot \varepsilon^*(\lambda') \cdot k_1) \right. \\ &\quad \left. (k_2^2 + 4(k_1 \cdot k_2))(k_1 \cdot \varepsilon(\lambda) \cdot \varepsilon^*(\lambda') \cdot k_1) \right]. \end{aligned} \quad (5.54)$$

In this equation a polarization tensor in between two dots indicates that one Lorentz index has to be contracted with the four-vector on the left side of the tensor whereas the other Lorentz index has to be contracted with the four-vector on the right side of the tensor, i.e.

$$p \cdot A \cdot q \equiv A^{\mu\nu} p_\mu q_\nu. \quad (5.55)$$

In the derivation we have used that the final state photon is massless and we have used equation (3.28) to replace k_2 in contractions with the polarization tensor by $-k_1$.

The density matrix for the decay of the χ_{c2} is constructed in the rest frame of the resonance with the z -axis as polarization axis and some x - and y -axes. The density matrix will depend on the polar and azimuthal angles of the photon in this reference system. The specific choice of the axes in the χ_{c2} rest system is at this point arbitrary. In the applications they should be the same as for the χ_{c2} production density matrix. The polarization tensor looks very simple and one can use equations (B.15) and (B.19) to verify that the following useful relations hold

$$\varepsilon^\mu(\lambda)\varepsilon_\mu^*(\lambda') = -\delta_{\lambda\lambda'}, \quad \varepsilon^{\mu\nu}(\lambda)\varepsilon_{\mu\nu}^*(\lambda') \equiv \delta_{\lambda\lambda'}. \quad (5.56)$$

In this frame the four-momentum of particle 1 can be parametrized by¹

$$k_1^\mu = |\vec{k}|(1, \sin\theta \cos\phi, \sin\theta \sin\phi, \cos\theta) = |\vec{k}|(1, s \cos\phi, s \sin\phi, c). \quad (5.57)$$

It can be shown that with these definitions the density matrix for the decay of the spin-2 particle can be written in a compact form as the sum of three matrices

$$\begin{aligned} \mathcal{D}_{\lambda\lambda'} &= |c|^2 \left[(k_1 \cdot k_2)^2 \delta_{\lambda\lambda'} + 2|\vec{k}|^4 v_\lambda v_{\lambda'}^* + (k_2^2 + 4(k_1 \cdot k_2))|\vec{k}|^2 R_{\lambda\lambda'} \right] \\ &= |c|^2 \left(\frac{M_R^2 - M^2}{2} \right)^2 \left[\delta_{\lambda\lambda'} + \frac{1}{2}\alpha^2 v_\lambda v_{\lambda'}^* + (1 + \alpha)R_{\lambda\lambda'} \right]. \end{aligned} \quad (5.58)$$

In this expression δ is the Kronecker symbol. The vector v is given by

$$v = (v_2, v_1, v_0, v_{-1}, v_{-2}) = \left(\frac{s^2}{2} e^{2i\phi}, -s c e^{i\phi}, \frac{1}{\sqrt{6}}(3c^2 - 1), s c e^{-i\phi}, \frac{s^2}{2} e^{-2i\phi} \right). \quad (5.59)$$

The tensor R is given by (the indices run from 2 to -2)

$$R_{\lambda\lambda'} = \begin{pmatrix} -\frac{s^2}{2} & \frac{cs}{2} e^{i\phi} & \frac{s^2}{2\sqrt{6}} e^{2i\phi} & 0 & 0 \\ \frac{cs}{2} e^{-i\phi} & -\frac{1+c^2}{4} & \frac{sc}{2\sqrt{6}} e^{i\phi} & \frac{s^2}{4} e^{2i\phi} & 0 \\ \frac{s^2}{2\sqrt{6}} e^{-2i\phi} & \frac{sc}{2\sqrt{6}} e^{-i\phi} & -\frac{3c^2+1}{6} & -\frac{sc}{2\sqrt{6}} e^{i\phi} & \frac{s^2}{2\sqrt{6}} e^{2i\phi} \\ 0 & \frac{s^2}{4} e^{-2i\phi} & -\frac{sc}{2\sqrt{6}} e^{-i\phi} & -\frac{1+c^2}{4} & -\frac{cs}{2} e^{i\phi} \\ 0 & 0 & \frac{s^2}{2\sqrt{6}} e^{-2i\phi} & -\frac{cs}{2} e^{-i\phi} & -\frac{s^2}{2} \end{pmatrix}. \quad (5.60)$$

¹In this expression we have introduced the same shorthand notation as in equation (5.44). From the context it should be clear which definition is used.

In the second line of equation (5.58) the expansion parameter α has been introduced.

$$\alpha = 1 - \frac{M^2}{M_R^2}. \quad (5.61)$$

Others [91] use a simplified expression for the matrix element, based on an electric dipole transition

$$\mathcal{M} = c [(k_1 \cdot k_2) \varepsilon_1^{*\mu}(\lambda_1) \varepsilon_2^{*\nu}(\lambda_2) - (k_2 \cdot \varepsilon_1^*(\lambda_1)) k_1^\mu \varepsilon_2^{*\nu}(\lambda_2)] \varepsilon_{\mu\nu}(\lambda). \quad (5.62)$$

This leads to the following density matrix

$$\begin{aligned} \mathcal{D}_{\lambda\lambda'} &= |c|^2 \left[(k_1 \cdot k_2)^2 \delta_{\lambda\lambda'} - \frac{1}{M^2} (k_2^2 + 2(k_1 \cdot k_2)) |\vec{k}|^4 v_\lambda v_{\lambda'}^* + (k_2^2 + 2(k_1 \cdot k_2)) \right. \\ &\quad \left. - \frac{(k_1 \cdot k_2)^2}{M^2} \right] |\vec{k}|^2 R_{\lambda\lambda'} \\ &= |c|^2 \left(\frac{M_R^2 - M^2}{2} \right)^2 \left[\delta_{\lambda\lambda'} - \frac{\alpha^2}{4(1-\alpha)} v_\lambda v_{\lambda'}^* + \left(1 - \frac{\alpha^2}{4(1-\alpha)} \right) R_{\lambda\lambda'} \right]. \end{aligned} \quad (5.63)$$

In the limit of vanishing α the density matrices of equations (5.58) and (5.63) become equal. For the actual α , based on $M = 3.09687$ GeV and $M_R = 3.55618$ GeV [13] we find $\alpha \approx 0.242$, there are some differences, e.g.

$$\begin{aligned} \mathcal{D}_{22} + \mathcal{D}_{-2-2} &\sim 1 + 1.570 \cdot c^2 + 0.0190 \cdot c^4 \quad \text{for equation (5.58),} \\ &\sim 1 + 1.028 \cdot c^2 - 0.00956 \cdot c^4 \quad \text{for equation (5.63),} \end{aligned}$$

whereas for $\alpha = 0$ one would have

$$\mathcal{D}_{22} + \mathcal{D}_{-2-2} \sim 1 + c^2. \quad (5.64)$$

These distributions can be compared to the experimentally observed distribution [92],

$$\mathcal{D}_{22} + \mathcal{D}_{-2-2} \sim 1 + 1.96 \cdot c^2 + 0.0142 \cdot c^4,$$

where the central values of the coefficients are taken and the errors are omitted. Three distributions are shown in figure 5.1

One could also take into account the possible decay of the massive J/ψ into two leptons

$$\chi_{c2}(k) \rightarrow \gamma(k_1) J/\psi(k_2) \rightarrow \gamma(k_1) l^+(p_1) l^-(p_2). \quad (5.65)$$

The matrix element for this reaction can be obtained from equation (5.49) by replacing the polarization vector of the J/ψ by the lepton current

$$J_{rs}^\mu = \bar{u}_r(p_2) \gamma^\mu v_s(p_1), \quad (5.66)$$

where r and s denote the spins of the final state leptons. In the following the lepton mass m_l will be neglected, which is a reasonable approximation for this decay.

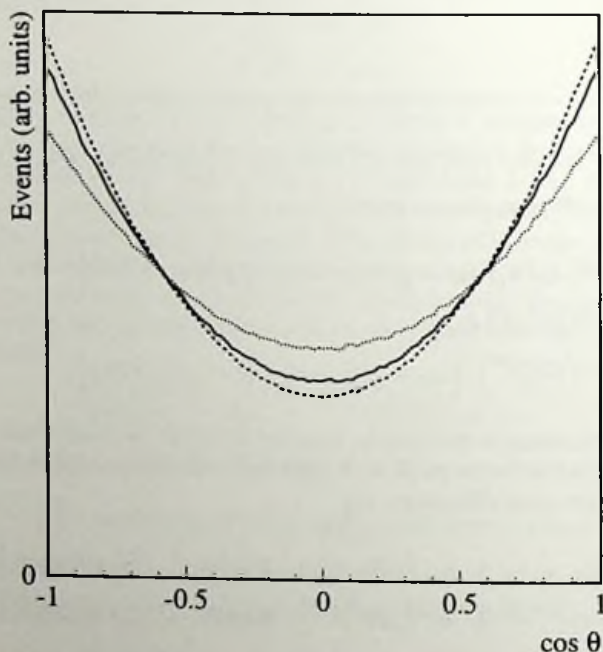


Figure 5.1: The three distributions of the angle of the outgoing photon in the resonance rest frame (RRF) with respect to the χ_{c2} boost direction for the pure helicity-2 decay of the χ_{c2} . The continuous line shows the distribution according to the complete matrix element (equation (5.58)), the dashed line shows the distribution according to the simplified matrix element based on a simple electric dipole transition (equation (5.63)) and the dotted line shows the experimentally observed distribution [92]. The vertical scale is linear.

In the construction of the density matrix for this decay one has to use that for the lepton current one finds

$$\sum_{r,s} J_{r\alpha}^{\mu} J_{s\beta}^{*\nu} = 4[p_1^{\alpha} p_2^{\nu} + p_1^{\nu} p_2^{\alpha} - \frac{1}{2} k_2^2 g^{\mu\nu}] = 2[k_2^{\alpha} k_2^{\nu} - l^{\mu} l^{\nu} - k_2^2 g^{\mu\nu}]. \quad (5.67)$$

In this equation the vector $l = p_1 - p_2$ has been introduced. This has been done as the term proportional to $k_2^{\alpha} k_2^{\nu}$ will not contribute to the density matrix. For l we use the following parametrization

$$l^{\mu} = (l_0, l_x, l_y, l_z) \quad (5.68)$$

in the above chosen reference frame, where (5.57) holds. The density matrix now reads

$$\begin{aligned}
\mathcal{D}_{\lambda\lambda'} &= |\tilde{c}|^2 \left(\varepsilon^{\alpha\beta}(\lambda) \varepsilon_{\alpha\beta}^*(\lambda') (k_1 \cdot k_2)^2 k_2^2 \right. \\
&\quad + (2k_2^2 + l^2) (k_1 \cdot \varepsilon(\lambda) \cdot k_1) (k_1 \cdot \varepsilon^*(\lambda') \cdot k_1) \\
&\quad - (k_1 \cdot k_2) [(k_1 \cdot \varepsilon(\lambda) \cdot k_1) (l \cdot \varepsilon^*(\lambda') \cdot l) + (l \cdot \varepsilon(\lambda) \cdot l) (k_1 \cdot \varepsilon^*(\lambda') \cdot k_1)] \\
&\quad + (2(k_1 \cdot k_2) + k_2^2) (k_1 \cdot \varepsilon(\lambda) \cdot l) (k_1 \cdot \varepsilon^*(\lambda') \cdot l) \\
&\quad + [(k_2^2)^2 + 4(k_1 \cdot k_2) k_2^2 + (k_1 \cdot l)^2] (k_1 \cdot \varepsilon(\lambda) \cdot \varepsilon^*(\lambda') \cdot k_1) \\
&\quad + (k_1 \cdot k_2) (k_1 \cdot l) [(k_1 \cdot \varepsilon(\lambda) \cdot \varepsilon^*(\lambda') \cdot l) + (l \cdot \varepsilon(\lambda) \cdot \varepsilon^*(\lambda') \cdot k_1)] \\
&\quad \left. + (k_1 \cdot k_2)^2 (l \cdot \varepsilon(\lambda) \cdot \varepsilon^*(\lambda') \cdot l) \right). \tag{5.69}
\end{aligned}$$

In the derivation we have used that $(k_2 \cdot l) = 0$. This density matrix can also be written in a more compact form

$$\begin{aligned}
\mathcal{D}_{\lambda\lambda'} &= |\tilde{c}|^2 \left((k_1 \cdot k_2)^2 k_2^2 \delta_{\lambda\lambda'} \right. \\
&\quad + [2k_2^2 + l^2] |\vec{k}|^4 v_\lambda v_{\lambda'}^* - (k_1 \cdot k_2) |\vec{k}|^2 [v_\lambda x_\lambda^* + x_\lambda v_\lambda^*] \\
&\quad + (2(k_1 \cdot k_2) + k_2^2) |\vec{k}|^2 w_\lambda w_{\lambda'}^* \\
&\quad + [(k_2^2)^2 + 4(k_1 \cdot k_2) k_2^2 + (k_1 \cdot l)^2] |\vec{k}|^2 R_{\lambda\lambda'} \\
&\quad \left. + (k_1 \cdot k_2) (k_1 \cdot l) |\vec{k}| [S_{\lambda\lambda'} + S_{\lambda'\lambda}^*] + (k_1 \cdot k_2)^2 T_{\lambda\lambda'} \right). \tag{5.70}
\end{aligned}$$

In this density matrix the coefficients can again be written as functions of α

$$\begin{aligned}
\mathcal{D}_{\lambda\lambda'} &= |\tilde{c}|^2 \left(\frac{M_R^2 - M^2}{2} \right)^2 M^2 \left(\delta_{\lambda\lambda'} + \frac{\alpha^2}{4} v_\lambda v_{\lambda'}^* - \frac{\alpha}{2M^2} (v_\lambda x_\lambda^* + x_\lambda v_\lambda^*) \right. \\
&\quad + \frac{1}{M^2} w_\lambda w_{\lambda'}^* + (1 + \alpha + \frac{\alpha^2}{4(1-\alpha)}) \cos^2 \theta^* R_{\lambda\lambda'} \\
&\quad \left. + \frac{\alpha}{2M\sqrt{1-\alpha}} \cos \theta^* (S_{\lambda\lambda'} + S_{\lambda'\lambda}^*) + \frac{1}{M^2} T_{\lambda\lambda'} \right), \tag{5.71}
\end{aligned}$$

where a convenient expression

$$k_1 \cdot l = \frac{M_R^2 - M^2}{2} \cos \theta^* \tag{5.72}$$

has been used. The angle θ^* is the polar angle of the outgoing l^+ in the rest system of the J/ψ where the z -axis is given by the direction of the boost from the RRF to the rest frame of the J/ψ , i.e. opposite to the photon direction. In the expressions some additional vectors and tensors have been introduced.

$$w = \left(\frac{sl_+}{2} e^{i\phi}, -\frac{1}{2} [l_z s e^{i\phi} + l_+ c], -\frac{1}{\sqrt{6}} [s(l_z \cos \phi + l_y \sin \phi) - 2cl_z], \frac{1}{2} [l_z s e^{-i\phi} + l_- c], \frac{sl_-}{2} e^{-i\phi} \right), \tag{5.73}$$

$$x = \left(\frac{1}{2}l_+^2, -l_+l_z, -\frac{1}{\sqrt{6}}[l_x^2 + l_y^2 - 2l_z^2], l_-l_z, \frac{1}{2}l_-^2 \right), \quad (5.74)$$

$$S_{\lambda\lambda'} = \begin{pmatrix} -\frac{sl_-}{2}e^{i\phi} & \frac{sl_+}{2}e^{i\phi} & \frac{sl_+}{2\sqrt{6}}e^{i\phi} \\ \frac{cl_-}{2} & -\frac{1}{2}\left[\frac{sl_-}{2}e^{i\phi} + cl_z\right] & \frac{1}{2\sqrt{6}}[2sl_+e^{i\phi} - cl_+] \\ \frac{sl_-}{2\sqrt{6}}e^{-i\phi} & \frac{1}{2\sqrt{6}}[2cl_- - sl_+e^{-i\phi}] & -\frac{1}{6}[s(l_x \cos \phi + l_y \sin \phi) + 4cl_z] \\ 0 & \frac{sl_-}{4}e^{-i\phi} & -\frac{1}{2\sqrt{6}}[2sl_+e^{-i\phi} - cl_-] \\ 0 & 0 & \frac{sl_-}{2\sqrt{6}}e^{-i\phi} \end{pmatrix} \quad (5.75)$$

$$T_{\lambda\lambda'} = \begin{pmatrix} 0 & 0 \\ \frac{sl_+}{4}e^{i\phi} & 0 \\ -\frac{1}{2\sqrt{6}}[2cl_+ - sl_+e^{i\phi}] & \frac{sl_+}{2\sqrt{6}}e^{i\phi} \\ -\frac{1}{2}\left[\frac{sl_+}{2}e^{-i\phi} + cl_z\right] & -\frac{cl_+}{2} \\ -\frac{sl_+}{2}e^{-i\phi} & -\frac{sl_+}{2}e^{-i\phi} \end{pmatrix},$$

$$T_{\lambda\lambda'} = \begin{pmatrix} -\frac{1}{2}(l_x^2 + l_y^2) & \frac{l_+l_z}{2} & \frac{l_z^2}{2\sqrt{6}} & 0 & 0 \\ \frac{l_-l_z}{2} & -\frac{1}{4}[(|l|^2 + l_z^2)] & \frac{l_+l_z}{2\sqrt{6}} & \frac{l_z^2}{4} & 0 \\ \frac{l_z^2}{2\sqrt{6}} & \frac{l_-l_z}{2\sqrt{6}} & -\frac{1}{6}[(|l|^2 + 3l_z^2)] & -\frac{l_+l_z}{2\sqrt{6}} & \frac{l_z^2}{2\sqrt{6}} \\ 0 & \frac{l_z^2}{4} & -\frac{l_-l_z}{2\sqrt{6}} & -\frac{1}{4}[(|l|^2 + l_z^2)] & -\frac{l_+l_z}{2} \\ 0 & 0 & \frac{l_z^2}{2\sqrt{6}} & -\frac{l_-l_z}{2} & -\frac{1}{2}(l_x^2 + l_y^2) \end{pmatrix}. \quad (5.76)$$

In the expressions the variables l_+ and l_- have been introduced.

$$\begin{aligned} l_+ &= l_x + il_y, \\ l_- &= l_x - il_y. \end{aligned} \quad (5.77)$$

The decay density matrix is now completely specified once the lepton momenta in the χ_{c2} rest system are inserted in l_μ . It is sometimes convenient to parametrize l_μ in terms of decay angles θ^* and ϕ^* ,

$$s^* = \sin \theta^*, \quad c^* = \cos \theta^*, \quad c_\phi^* = \cos \phi^*, \quad s_\phi^* = \sin \phi^*, \quad (5.78)$$

of the l^+ in the rest system of the J/ψ .

The components of the four-momentum l in the RRF then become ($c_\phi = \cos \phi$, $s_\phi = \sin \phi$, the angles of equation (5.57))

$$\begin{aligned} l_0 &= \frac{M_R^2 - M^2}{2M_R} c^*, \\ l_x &= M(s^*(c^* c c_\phi + s^* s_\phi) - c^* s c_\phi), \\ l_y &= M(s^*(c^* c s_\phi + s^* c_\phi) - c^* s s_\phi), \\ l_z &= -M(s^* c_\phi^* s + c^* c). \end{aligned} \quad (5.79)$$

Since the χ_{c2} will be predominantly produced in helicity ± 2 states, we have a closer look at those density matrix elements. In the limit of vanishing α the sum of density matrix elements $\mathcal{D}_{-2-2} + \mathcal{D}_{22}$ reads

$$\begin{aligned} \mathcal{D}_{-2-2} + \mathcal{D}_{22} &= |\tilde{c}|^2 \left(\frac{M_R^2 - M^2}{2} \right)^2 M^2 \left(2 + \frac{1}{M^2} (w_{-2} w_{-2}^* + w_2 w_2^*) \right) \\ &\quad + \frac{1}{M^2} (T_{-2-2} + T_{22}) + R_{-2-2} + R_{22}. \end{aligned} \quad (5.80)$$

Inserting the expressions for the vectors and the tensors gives

$$\mathcal{D}_{-2-2} + \mathcal{D}_{22} = |\tilde{c}|^2 \left(\frac{M_R^2 - M^2}{2} \right)^2 M^2 (1 + c^2) \left[1 - \frac{l_+ l_-}{2M^2} \right]. \quad (5.81)$$

Integrating over the angles associated to the outgoing leptons yields for the sum $\mathcal{D}_{-2-2} + \mathcal{D}_{22}$ a result that is proportional to $1 + c^2$, which is in agreement with the previously found results for the decay of a χ_{c2} into J/ψ and γ , equation (5.64) in the limit $\alpha = 0$. Using the expressions for l_+ and l_- results in

$$\mathcal{D}_{-2-2} + \mathcal{D}_{22} = |\tilde{c}|^2 \left(\frac{M_R^2 - M^2}{2} \right)^2 M^2 (1 + c^2) \left(1 - \frac{1}{2} [(s^* c_\phi^* c - c^* s)^2 + (s^* s_\phi^*)^2] \right). \quad (5.82)$$

For helicity-2 predictions these results can be compared to the weight function for the angular distribution, $f_{|\lambda|=2}$, presented in [59] and [92]

$$\begin{aligned} f_{|\lambda|=2}(\theta, \theta^*, \phi^*) &= \frac{1}{8} A_2^2 (1 + c^{*2}) (1 + 6c^2 + c^4) + A_1^2 (1 - c^{*2}) (1 - c^4) \\ &\quad + \frac{3}{4} A_0^2 (1 + c^{*2}) (1 - 2c^2 + c^4) + \frac{\sqrt{2}}{4} A_2 A_1 c_\phi^* 2s^* c^* s (c^3 + 3c) \\ &\quad + \frac{\sqrt{6}}{4} A_2 A_0 (c_\phi^{*2} - s_\phi^{*2}) s^2 (1 - c^4) - \frac{\sqrt{3}}{2} A_1 A_0 c_\phi^* 2s^* c^* s^3 c. \end{aligned} \quad (5.83)$$

A pure electric dipole transition would result in amplitudes $A_0 = 0.316$, $A_1 = 0.548$ and $A_2 = 0.775$. Experimentally [92] the values $A_0 = 0.21$, $A_1 = 0.49$ and $A_2 = 0.85$ have been found. It turns out that the compact expression (5.82) amounts to expression (5.83) with the pure electric dipole values for A_i .

Chapter 6

GaGaRes Monte Carlo generator

The model of chapters 3 and 4 has been implemented in the GaGaRes Monte Carlo generator. Before introducing this generator, first a brief introduction into Monte Carlo techniques is given. The chapter ends with a summary of results obtained with the GaGaRes generator.

The contents of this chapter have also been partially published elsewhere [93].

6.1 Monte Carlo technique

There exist many publications on Monte Carlo techniques. For our purposes it is sufficient to refer to [10, 94, 95]. However, it remains useful to give a short introduction into the Monte Carlo techniques that are used in the generator.

James [95] defines a Monte Carlo technique as “any technique which makes use of random numbers to solve a problem.” To understand why we need Monte Carlo techniques, we make a few observations. Comparison between theoretical predictions and experimental results is generally performed at cross section level. As a consequence, the exact differential cross section, which includes the square of the matrix element of the relevant process, has to be integrated over the phase-space. The latter is defined by energy-momentum conservation and the set-up of the experiment.

An analytical calculation of the total cross section, i.e. integrating the differential cross-section over the allowed phase-space, is very difficult to perform and has several drawbacks:

- The integrand can be very complex and its primitive may be difficult to find. In particular, if one wants to consider differential cross sections with respect to a specific variable, the integrand can become even more complicated because of the Jacobian that has to be inserted as a consequence of the change of variables.
- A different experimental set-up or cuts on kinematical variables can result in different boundaries of the phase-space and, as a consequence, may lead to a new calculation of the total cross section.
- Besides a total cross section one would also like to have a sample of simulated events that can be compared to the experimentally observed events.

Monte Carlo techniques are a possible solution to these problems.

6.1.1 Crude Monte Carlo

The principle of Monte Carlo integration can best be illustrated in one dimension.

Suppose that one would like to consider the integral I of a function $f(x)$ on an interval $[a, b]$

$$I = \int_a^b f(x) dx. \quad (6.1)$$

This integral can be numerically approximated by dividing the interval into N subintervals and evaluating the function f in the centre of each subinterval

$$I' = \frac{b-a}{N} \sum_{i=1}^N f(x_i), \quad x_i = a + \frac{(b-a)(i - \frac{1}{2})}{N} \quad (6.2)$$

A Monte Carlo approach would be to use instead of the equidistant set of points in (6.2) the following set of points

$$x_i = a + (b-a)\mathcal{R}_i. \quad (6.3)$$

where the \mathcal{R}_i form a collection of random points that is uniformly distributed on the interval $[0, 1]$.

The central limit theorem then states that for large N the estimate $I' \rightarrow I$ and that the error on the estimate I' is given by $(b-a)\sigma_f/\sqrt{N}$, where σ_f^2 is the variance of the function f on the integration interval $[a, b]$.

A generalization to n dimensions is straightforward. The x_i 's are in this case n -dimensional vectors and one has to replace in (6.2) the interval $(b-a)$ by the n -dimensional volume of integration.

6.1.2 Hit or miss Monte Carlo

Besides the numerical approximation of the integral, the previous procedure also results in a collection of randomly distributed points x_i where each point has its own weight, $f(x_i)$. In the following only positive functions $f(x)$ will be considered. As differential cross sections are probabilities, they are automatically positive.

For the simulation of events that we can compare to experimentally observed events, we would like to have a sample of events with unit weight, i.e. a sample in which the events are distributed according to the integrand. To obtain a set of unweighted events, a rejection algorithm has to be applied. This rejection algorithm is called the hit or miss method.

One introduces an f_{max} such that for all allowed values of x , $f(x) < f_{max}$. For each generated x_i we compare the ratio $r_i = f(x_i)/f_{max}$ to a point y_i that is uniformly distributed on the interval $[0, 1]$. If $r_i > y_i$ the event is accepted (hit), otherwise the event is rejected (miss). The collection of accepted events now is an unweighted sample.

The difficulty in this algorithm is the choice of the value of f_{max} , that has to be determined in advance. A too large value of f_{max} results in correct results, but makes the method inefficient. A too low value of f_{max} results in an under-estimation of the integral¹.

¹In GaGaRes this problem is overcome by first generating a large number of events to determine f_{max} and subsequently performing the integration.

This method also results in a numerical estimate of the integral. If the number of accepted events is given by N_{acc} and the total number of generated events is given by N , the integral I' can be estimated by

$$I' = (b - a) f_{max} \frac{N_{acc}}{N}. \quad (6.4)$$

The error is given by

$$\Delta I' = \frac{N_{acc}}{N} \sqrt{\left(1 - \frac{N_{acc}}{N}\right) (b - a) f_{max}}. \quad (6.5)$$

The ratio of the mean weight and the maximum weight f_{max} is a measure for the efficiency of the hit or miss algorithm.

Again, the formalism can trivially be extended to higher dimensional integrations.

6.1.3 Importance sampling

As mentioned in 6.1.1, the error on the estimate I' is proportional to σ_f/\sqrt{N} . To reduce this error, one could increase the number N , but this gives a slow convergence. It would be more efficient to reduce the variance of the integrand. In GaGaRes the technique of importance sampling has been used to this end.

In importance sampling one performs a change of variables to obtain a new integral with smaller variance:

$$\int_a^b f(x) dx = \int_a^b \frac{f(x)}{g(x)} g(x) dx = \int_{G(a)}^{G(b)} \frac{f(G^{-1}(y))}{g(G^{-1}(y))} dy, \quad y = G(x) = \int^x g(x') dx'. \quad (6.6)$$

The function g must satisfy several criteria:

- g is a positive function on the interval $[a, b]$.
- The function G is known analytically.
- The inverse of the function G is known analytically.

The essence is that one has to choose a g such that the variance of f/g is smaller than the original variance σ_f^2 .

The variable y is uniformly distributed in the interval $[G(a), G(b)]$ when

$$y = (G(b) - G(a))\mathcal{R} + G(a), \quad (6.7)$$

where \mathcal{R} is a random variable that is uniformly distributed on the interval $[0, 1]$. This results in a distribution of the original variable x according to

$$x = G^{-1}((G(b) - G(a))\mathcal{R} + G(a)). \quad (6.8)$$

In section IV.2 in [31] a nice illustration of the importance sampling method, applied to a Breit-Wigner distribution, can be found.

6.2 The GaGaRes event generator

The general expression for the cross section of a $2 \rightarrow 3$ process reads

$$\sigma = \int (2\pi)^4 \delta^{(4)}(p_1 + p_2 - p'_1 - p'_2 - P) \frac{1}{4\sqrt{(p_1 \cdot p_2)^2 - m_e^2}} \frac{1}{4} \sum |\mathcal{M}|^2 \frac{d^3 \vec{p}'_1}{(2\pi)^3 2E'_1} \frac{d^3 \vec{p}'_2}{(2\pi)^3 2E'_2} \frac{d^3 \vec{P}}{(2\pi)^3 2E_P} \quad (6.9)$$

We are working in the lab-frame and will use the parametrization given in (2.14). Performing the integration over \vec{P} and rewriting the remaining delta-function gives

$$\sigma = \int \frac{1}{(2\pi)^5} \frac{1}{8sE'_1 E'_2} \frac{1}{4} \sum |\mathcal{M}|^2 \delta(4E_b^2 - 4E_b(E'_1 + E'_2) + 2m_e^2 + 2E'_1 E'_2 - 2|\vec{p}'_1||\vec{p}'_2| \cos \theta_{12} - M^2) d^3 \vec{p}'_1 d^3 \vec{p}'_2. \quad (6.10)$$

$\cos \theta_{12} \equiv c_{12}$ has been defined in (2.19). Solving the delta-function for E'_1 yields

$$E'_1 = \frac{\xi(2E_b - E'_2) \pm D}{2\{(E'_2 - 2E_b)^2 - |\vec{p}'_2|^2 c_{12}^2\}}, \quad (6.11)$$

where

$$\begin{aligned} \xi &= 4E_b^2 - 4E_b E'_2 + 2m_e^2 - M^2, \\ D &= |\vec{p}'_2| c_{12} |\tilde{\Delta}|, \\ \tilde{\Delta}^2 &= \xi^2 - 4(E'_2 - 2E_b)^2 m_e^2 + 4|\vec{p}'_2|^2 c_{12}^2 m_e^2. \end{aligned} \quad (6.12)$$

The two signs in (6.11) lead to a division of the phase-space into two parts. The cross sections of the two solutions are denoted by σ_{\pm} , where the subscript corresponds to the sign in (6.11).

For the two solutions we find

- - solution

$$\begin{aligned} E'_{2,\min} &= m_e, \\ E'_{2,\max} &= E_b - \frac{m_e M}{2E_b} - \frac{M^2}{4E_b}, \end{aligned} \quad (6.13)$$

$$m_e \leq E'_2 \leq \tilde{E}_2 \text{ then } -1 \leq c_{12} \leq +1,$$

$$\tilde{E}_2 \leq E'_2 \leq E'_{2,\max} \text{ then } -1 \leq c_{12} \leq -c_0$$

- + solution

$$\begin{aligned} E'_{2,\min} &= \tilde{E}_2, \\ E'_{2,\max} &= E_b - \frac{m_e M}{2E_b} - \frac{M^2}{4E_b}, \end{aligned} \quad (6.14)$$

$$-1 \leq c_{12} \leq -c_0,$$

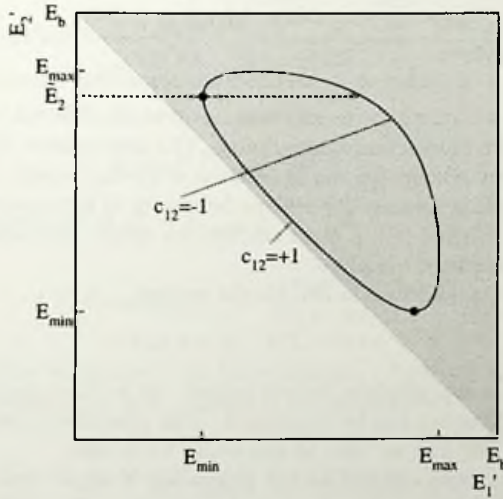


Figure 6.1: The Dalitz plot for E'_1 and E'_2 . The shaded area represents the allowed values for E'_1 and E'_2 in the case of three massless particles in the final state. In the plot the electron mass has been set to $0.3E_b$ whereas the resonance mass has been set to $0.5E_b$.

where

$$\bar{E}_2 = \frac{4E_b^2 - 4m_e E_b + 2m_e^2 - M^2}{4E_b - 2m_e}, \tag{6.15}$$

and

$$c_a = \sqrt{\frac{4(2E_b - E'_2)^2 m_e^2 - (4E_b^2 - 4E'_2 E_b + 2m_e^2 - M^2)^2}{4|\vec{p}'_2|^2 m_e^2}}. \tag{6.16}$$

The occurrence of two solutions for E'_1 for $E'_2 > \bar{E}_2$ and $c_{12} < -c_a$ is illustrated in figure 6.1 where the Dalitz plot for E'_1 and E'_2 is plotted. The line represents the boundary of allowed values of E'_1 and E'_2 . On this line the final state particles have a collinear configuration. Note that in this plot the electron mass and the resonance mass are set to 30 % respectively 50 % of E_b to make the effect clearly visible. In practice E_{\max} and \bar{E}_2 are close to E_b . For an χ_{e2} resonance produced at $\sqrt{s} = 190$ GeV one finds $E_{\max} = 94.9666$ GeV and $\bar{E}_2 = 94.9663$ GeV. Thus the region for the + solution is very small.

Changing of variables and performing the integration over E'_1 leads to

$$\sigma_{\pm} = \int \frac{1}{4} \sum |\mathcal{M}|^2 \frac{1}{\sqrt{1 - \frac{4m_e^2}{s}}} \frac{|\vec{p}'_1| |\vec{p}'_2|}{|4E_b - 2E'_2 + 2\frac{|\vec{p}'_2| E'_1}{|\vec{p}'_1}| c_{12}|} dE'_2 d^2\Omega_1 d^2\Omega_2. \tag{6.17}$$

$d^2\Omega_i$ represent the angular integrations of the outgoing leptons, $d^2\Omega_i \equiv \cos\theta_i d\theta_i d\phi_i$.

The next step is to normalize all variables to the beam energy E_b .

$$\sigma_{\pm} = \int \frac{1}{4} \sum |\mathcal{M}|^2 \frac{1}{256\pi^5 s} \frac{|\vec{p}'_1||\vec{p}'_2|}{\sqrt{1 - \frac{4m_e^2}{s}} |4 - 2E'_2 + 2\frac{|\vec{p}'_2|E'_1}{|\vec{p}'_1}|} c_{12}|} dE'_2 d^2\Omega_1 d^2\Omega_2. \quad (6.18)$$

In GaGaRes there is a choice between two schemes in which different sets of variables are generated to perform the Monte Carlo integration. The first scheme (I) is based on [96]. This is the most efficient scheme for the generation of no-tag events, as for events with small scattering angles of the leptons the peaking behaviour of the matrix element is better described. The second scheme (II) is more efficient for single- and double-tag events, as both polar angles are generated variables.

Generation scheme I is described in [96] for the process

$$e^+e^- \rightarrow e^+e^-l^+l^- \quad (l = e, \mu, \tau),$$

where the initial electron and positron are not tagged. As we have one particle less in the final state, some simplifications can be introduced. This generation scheme is very similar to the one described in [96] and we refer to this paper for details.

Scheme II is not only more efficient for the generation of single- and double-tag events, but also the generation of events with a cut on the minimum allowed Q_i^2 .

We start from expression (6.18). The first approximation is a replacement for the expression for the square of the matrix element

$$\frac{1}{4} \sum |\mathcal{M}|^2 \rightarrow \frac{64}{tt'}, \quad (6.19)$$

where the factor 64 is just chosen for convenience. The scale will be accounted for by the weight. The corresponding weight factor is given by

$$W_1 = \frac{tt' \frac{1}{4} \sum |\mathcal{M}|^2}{64}. \quad (6.20)$$

The matrix element squared is approximated by a factor $1/tt'$ rather than a factor $1/(tt')^2$ as one would naively expect from the formulae in appendix A. A closer look tells us that in the limit where t and t' are of order m_e^2 the numerators are also of order m_e^2 , for it can be shown that in this limit the invariant σ_{2-} , which had been introduced in equation (A.1) in appendix A, is also proportional to m_e^2 . This reduces effectively the dependence of the matrix element squared to $1/tt'$ in the limit of small momentum transfers. This feature is also responsible for the logarithmic dependence of the total cross section on the beam energy.

The cross section now reads

$$\sigma_{\pm} = \frac{1}{4\pi^5 s} \frac{1}{\sqrt{1 - \frac{4m_e^2}{s}}} \int \frac{1}{tt'} \frac{|\vec{p}'_1||\vec{p}'_2|}{|4 - 2E'_2 + 2\frac{|\vec{p}'_2|E'_1}{|\vec{p}'_1}|} c_{12}|} dE'_2 d^2\Omega_1 d^2\Omega_2. \quad (6.21)$$

The next approximations concern the photon virtualities. In particular, the square of the invariant mass of the photon, emitted by the incoming positron, can be written as

$$t = -2E'_1(1 - c_1 + \delta_1), \quad (6.22)$$

with

$$\delta_1 = \left(1 - \frac{|\vec{p}'_1| P_b}{E'_1}\right) c_1 - \frac{m_e^2}{E'_1}. \quad (6.23)$$

We have also introduced the shorthand notation $c_i \equiv \cos \theta_i$, $s_i \equiv \sin \theta_i$ ($i = 1, 2$). Now $\delta_{1,min}$ is defined as

$$\delta_{1,min} \equiv \delta_1|_{c_1=1} = \frac{m_e^2(1 - E'_1)^2}{2E_1'^2}, \quad (6.24)$$

which reaches its minimum at $E'_1 = E'_{1,max} = 1 - \frac{1}{2}m_e M - \frac{1}{4}M^2$ and is denoted by

$$\varepsilon \equiv \delta_{1,min}|_{E'_1=E'_{1,max}} = \frac{m_e^2(m_e M + \frac{1}{2}M^2)^2}{8(1 - \frac{1}{2}m_e M - \frac{1}{4}M^2)^2}. \quad (6.25)$$

For t' we find a similar expression with the subscripts 1 replaced by 2.

The second approximation now consists of the substitution

$$\frac{1}{tt'} \rightarrow \frac{1}{4E'_1 E'_2 (1 - c_1 + \varepsilon)(1 - c_2 + \varepsilon)}, \quad (6.26)$$

with a corresponding weight factor

$$W_2 = \frac{4E'_1 E'_2 (1 - c_1 + \varepsilon)(1 - c_2 + \varepsilon)}{tt'}. \quad (6.27)$$

The third approximation consists of the approximation in the denominator

$$\frac{E'_1 E'_2}{|\vec{p}'_1| |\vec{p}'_2|} |2 - E'_2 + \frac{|\vec{p}'_2| E'_1}{|\vec{p}'_1|} c_{12}| \rightarrow 1 - E'_2. \quad (6.28)$$

This approximation works rather well, as for most generated events the outgoing leptons are energetic and go (almost) back to back ($c_{12} \approx -1$). The required weight factor now is

$$W_3 = \frac{|\vec{p}'_1| |\vec{p}'_2|}{E'_1 E'_2} \frac{1 - E'_2}{|2 - E'_2 + \frac{|\vec{p}'_2| E'_1}{|\vec{p}'_1|} c_{12}|}. \quad (6.29)$$

After these approximations the cross section becomes

$$\sigma_{\pm} = \frac{1}{32\pi^5 s} \frac{1}{\sqrt{1 - \frac{4m_e^2}{s}}} \int \frac{dE'_2 d^2\Omega_1 d^2\Omega_2}{(1 - c_1 + \varepsilon)(1 - c_2 + \varepsilon)(1 - E'_2)}. \quad (6.30)$$

The trivial integrations of ϕ_1 and ϕ_2 over $[\phi_{min}, \phi_{max}]$ can be performed. The integrations over the polar angles and over E'_2 use the standard integral

$$\int_{x_{min}}^{x_{max}} \frac{dx}{a - x} = \ln \left| \frac{a - x_{min}}{a - x_{max}} \right|. \quad (6.31)$$

The results of these integrations are put in the last two weights

$$W_4 = \ln \left| \frac{1+\varepsilon-c_{1,\min}}{1+\varepsilon-c_{1,\max}} \right| \ln \left| \frac{1+\varepsilon-c_{2,\min}}{1+\varepsilon-c_{2,\max}} \right| (\phi_{1,\max} - \phi_{1,\min})(\phi_{2,\max} - \phi_{2,\min}), \quad (6.32)$$

$$W_{5,\pm} = \ln \left| \frac{1-E'_{5,\min}}{1-E'_{5,\max}} \right|,$$

leaving as integrated cross section

$$\sigma_{tot} = \frac{1}{32\pi^5 s} \frac{1}{\sqrt{1 - \frac{4m^2}{s}}}. \quad (6.33)$$

Using (6.2) the real total cross section is given by²

$$\sigma = \sigma_{tot} \langle W_1 W_2 W_3 W_4 (W_{5+} + W_{5-}) \rangle, \quad (6.34)$$

where $\langle W_1 W_2 W_3 W_4 (W_{5+} + W_{5-}) \rangle$ is defined as the average weight. During the generation of events there is a probability $W_{5-}/(W_{5+} + W_{5-})$ that an event is generated in the phase space of the $-$ solution. Especially for the heavier resonances almost all events will be generated in this part of the phase space.

The variables are now generated by importance sampling in the following order: $\phi_1, \phi_2, \cos \theta_1, \cos \theta_2$. The generation of the azimuthal angles is trivial

$$\phi_i = (\phi_{i,\max} - \phi_{i,\min})\mathcal{R} + \phi_{i,\min} \quad (i = 1, 2). \quad (6.35)$$

The variables that are distributed like the integrand of (6.31) should be generated according to

$$x = a - (a - x_{\max}) \left(\frac{a - x_{\min}}{a - x_{\max}} \right)^{\mathcal{R}}, \quad (6.36)$$

where it should be noted that in the program $1 - x$ rather than x is generated in order to guarantee the best numerical stability. This is used for $x = \cos \theta_1$ and $x = \cos \theta_2$.

At this point $\cos \theta_{12}$ can be evaluated. Then E'_2 is obtained from (6.31) and (6.36). When $E'_2 < \bar{E}_2$ one has only a contribution from the $-$ solution of the delta function. When $E'_2 > \bar{E}_2$ one has to check whether c_{12} is in the allowed interval. If so, one has contributions from both solutions of the delta function.

Cuts on the generated variables are incorporated in the generation mechanism. They do not lead to a drop in efficiency (exactly the reason why scheme II is favoured for single- and double-tag reactions). For scheme II the program also offers the possibility to impose cuts on E'_1 , on the photon virtualities Q_i^2 and on c_{12} . The cuts are applied by the following replacement

$$|\mathcal{M}|^2 \rightarrow |\mathcal{M}|^2 \prod \theta, \quad (6.37)$$

where $\prod \theta$ is a product of step functions representing the cuts.

These cuts lead to a drop in generation efficiency. However, for the cuts on the photon virtualities Q_i^2 the values of the corresponding polar angles are adapted in order to avoid this

²As mentioned before, the weight of an event is determined by the value of the integrand for this event.

drop in efficiency. When we require for the photon virtuality Q_i the restriction $Q_i > Q_{i,min}$ the minimum values of the angles and E'_1 can be set to

$$\theta_{i,min} = 2\arcsin\sqrt{\frac{Q_{i,min}^2 + 2m_e^2}{4E_b E_{i,max}'}} \quad (6.38)$$

$$E'_{1,min} = \frac{Q_{1,min}^2 + 2m_e^2}{4E_b \sin^2\left(\frac{\theta_{1,max}}{2}\right)} \quad (6.39)$$

where $\theta_{i,min}$ is the minimum polar angle of the outgoing lepton corresponding to the photon virtuality Q_i .

6.3 Some results

In this section some of the results and tests done with GaGaRes are summarized. Furthermore, the generator has also been used in the two analyses that are presented in this thesis.

6.3.1 Cross sections and distributions

The BGMS expressions for density matrices derived in the previous chapter were implemented by us in the Monte Carlo generator Galuga [84]. For all resonances the cross sections and density matrices found by both generators were identical within the errors. Some of the results for the cross sections are summarized in table 6.1.

In figure 6.2 the cross section for the process $e^+e^- \rightarrow e^+e^-\eta_c$ as a function of \sqrt{s} is given. From this plot one can clearly see the logarithmic rise of the cross section with increasing \sqrt{s} . We have also given the results of the Low approximation, see equation (2.48) on page 16.

In figures 6.3a-6.3d some distributions for the production of η_b mesons at $\sqrt{s} = 190$ GeV are given. In the production of these events no cuts on the outgoing particles have been applied. In figure 6.3a the energy spectra for an outgoing lepton and the outgoing resonance are given. The energy of the scattered lepton peaks at high energies. As a consequence, the energy of the intermediate photons peaks at low energies. The energy spectrum for the outgoing resonance starts at 9.4 GeV, the rest energy of the η_b . Furthermore, events are displayed with respect to their photon energies in figure 6.3b. The variables along the x - and y -axes are the logarithms of the normalized photon energies $x_i = \omega_i/E_b$. The dense band in the figure can be understood when one realizes that the resonances are produced at the fixed mass $M = 9.4$ GeV and that the dominant term in (2.18) is the product of the photon energies. The angular distributions of the resonance in figures 6.3c and 6.3d show that the resonances are produced isotropically in the azimuthal angle ϕ_R and that they are strongly boosted along the beam direction.

In figure 6.4 the Q distributions for the virtual photons emitted by the incoming positron for the generation of $b\bar{b}$ states at $\sqrt{s} = 190$ GeV are given. The η_b , χ_{b0} and χ_{b2} states have essentially the same distribution of Q . Only for the χ_{b1} resonance a wider Q spectrum is observed. For the Q distributions of the photons emitted by the incoming electron identical

π^0	η	η'	η_c	η_b
3.550	2.180	5.333	0.1731	0.2162×10^{-3}
a_0	f_0	f'_0	χ_{c0}	χ_{b0}
3.837	0.5499	2.716	0.03398	0.1601×10^{-4}
a_1	f_1	f'_1	χ_{c1}	χ_{b1}
0.07120	0.1707	0.4170×10^{-2}	0.1239×10^{-2}	0.6574×10^{-6}
a_2	f_2	f'_2	χ_{c2}	χ_{b2}
1.511	4.972	0.1152	0.01660	1.390×10^{-5}
π_2	η_D	η'_D	η_{cD}	η_{bD}
0.9336	0.3108	2.416	0.4518×10^{-3}	0.1325×10^{-6}

Table 6.1: *The cross sections (in nb) for $\sqrt{s} = 180$ GeV in the absence of cuts on the external particles.*

spectra have been found, as it should be. In figure 6.5 we compare the differential cross sections $d^2\sigma/(d\log_{10}(Q_1^2/W_r^2)d\log_{10}(Q_2^2/W_r^2))$, $W_r = 1$ GeV, for χ_{c1} and χ_{c2} production. The production of tensor mesons is dominated by the phase-space region where both photon virtualities Q_i are small. This region is suppressed for the production of the axial-vector meson. However, this difference is pronounced only at very low Q_i . From figure 6.5 it follows that for example $Q_1^2 = 10^{-1}$ GeV² is large enough to reach very small Q_2 values without suppressing the cross section too much. As could be seen in figure 6.4, for the χ_{b1} resonance, the single- Q^2 distribution is still peaked at low Q . In fact, in [27] it has been shown that an anti-tag cut, say at $Q_2^2 < 0.1$ GeV², is not a good way to enrich 1^+ states with respect to other states in two-photon samples. Applying this upper cut leads to a suppression of 1^+ states.

Next, results for the $\Delta\phi = \phi_1 - \phi_2$ distributions for the 1S_0 and 3P_J bottomonium states are given for $\sqrt{s} = 190$ GeV. From figures 6.6a-6.6d it is seen that there are marked differences between distributions for different resonances. The characteristics can be qualitatively understood when the dominant features of the cross sections are considered. In the first place it is clear from figure 6.4 that the largest contributions to the cross sections come from the region $Q_i^2 \ll M^2$. In those regions $\Delta\phi \approx \tilde{\phi}$ (cf [16]) such that a qualitative understanding of the $\tilde{\phi}$ distribution in the BGMS cross section formula (2.39) is sufficient to explain the features of figures 6.6a-6.6d. The behaviour of the BGMS formula for the various resonances now follows from the form factors f_{AB} and g_{AB} in table 3.6 on page 39 and the small Q_i^2 approximation. One then obtains $\tilde{\phi}$ distributions, where different

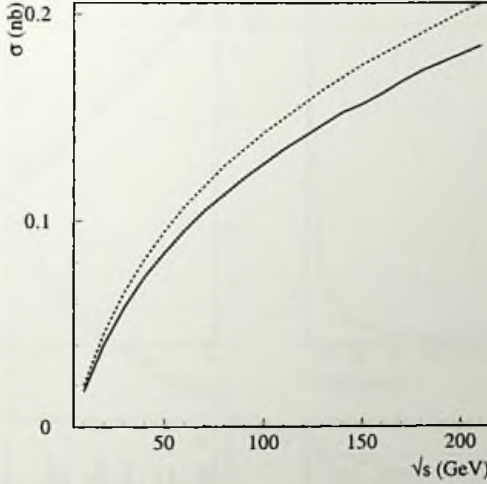


Figure 6.2: The cross section for the process $e^+e^- \rightarrow e^+e^-\eta_c$ as a function of \sqrt{s} as calculated by GaGaRes (solid line) and from the Low approximation (dashed line).

photon density matrices play a role. Using the approximate numerical relations valid at $\sqrt{s} = 190$ GeV and in the small Q_i^2 region

$$\rho^{++} \approx \rho^{+-}, \quad \rho^{+0} \approx 1.5\rho^{++}, \quad \rho^{00} \approx 2.3\rho^{++}, \quad (6.40)$$

one arrives at the following shapes for the $\vec{\phi}$ distributions:

η_b :

$$\begin{aligned} \frac{d\sigma}{d\phi} &\sim \kappa \frac{8X}{3\nu^2} (\rho_1^{++}\rho_2^{++} - \rho_1^{+-}\rho_2^{+-} \cos(2\vec{\phi})) \\ &\sim \kappa \frac{16X}{\nu^2} \rho_1^{++}\rho_2^{++} \sin^2 \vec{\phi}, \end{aligned} \quad (6.41)$$

χ_{b0} :

$$\begin{aligned} \frac{d\sigma}{d\phi} &\sim 4\kappa \left(\frac{X+\nu M^2}{3\nu^2} \right) (\rho_1^{++}\rho_2^{++} + \rho_1^{+-}\rho_2^{+-} \cos(2\vec{\phi})) \\ &\sim 8\kappa \left(\frac{X+\nu M^2}{3\nu^2} \right) \rho_1^{++}\rho_2^{++} \cos^2 \vec{\phi}, \end{aligned} \quad (6.42)$$

χ_{b1} :

$$\begin{aligned} \frac{d\sigma}{d\phi} &\sim 4\kappa \left(\frac{Q_1^2 - Q_2^2}{2\nu} \right)^2 (\rho_1^{++}\rho_2^{++} - \rho_1^{+-}\rho_2^{+-} \cos(2\vec{\phi})) \\ &\quad + 4\kappa \left(\frac{M}{2\nu} \right)^2 (\rho_1^{++}\rho_2^{00}Q_2^2 + \rho_1^{00}\rho_2^{++}Q_1^2 - 2\rho_1^{+0}\rho_2^{+0}Q_1Q_2 \cos \vec{\phi}) \\ &\sim \frac{2\kappa}{\nu^2} \rho_1^{++}\rho_2^{++} (M^2(Q_1^2 + Q_2^2) - 2M^2Q_1Q_2 \cos \vec{\phi} + (Q_1^2 - Q_2^2)^2 \sin^2 \vec{\phi}), \end{aligned} \quad (6.43)$$

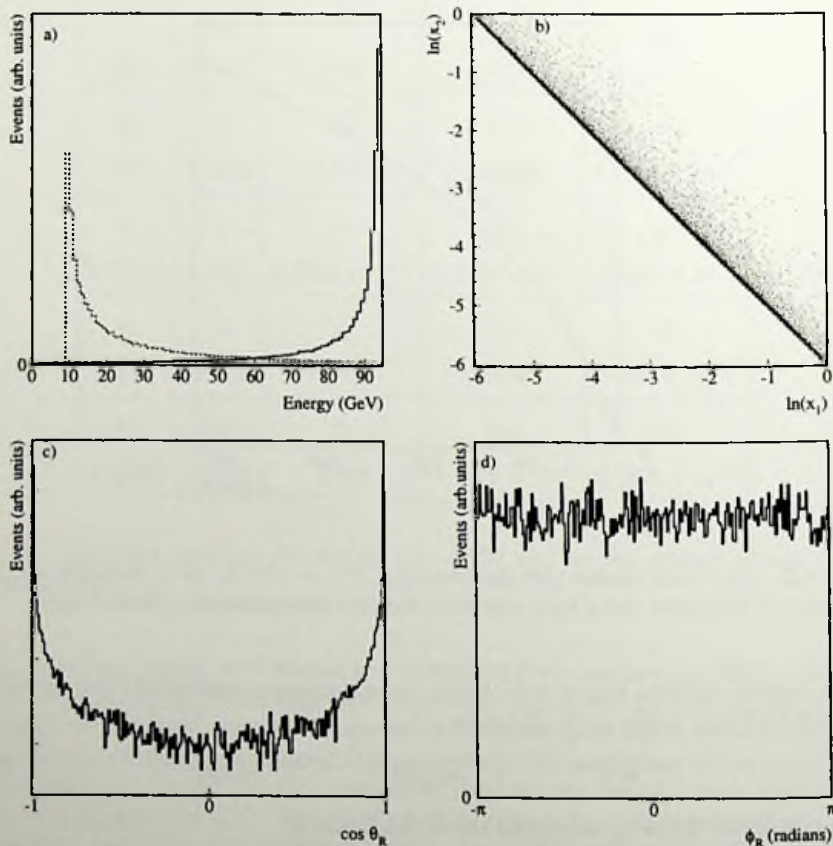


Figure 6.3: Distributions from the event generation of the η_b meson at a beam energy of 95 GeV in the absence of additional cuts on the external particles. In figure a) the energy distributions of the scattered positron (continuous line) and the outgoing resonance (dashed line) are given. In figure b) the distribution of the logarithms of the normalized energies x_1 and x_2 is given. Figures c) and d) show the angular distributions of the outgoing resonance. All vertical scales are linear, except for figure c), where the vertical scale is logarithmic.

χ_{b2} :

$$\frac{d\sigma}{d\phi} \sim \kappa \left(\frac{M^2}{2\nu} \right)^2. \quad (6.44)$$

It is clear that the $\sin^2 \tilde{\phi}$ and $\cos^2 \tilde{\phi}$ and constant distributions show up in figures 6.6 a, b and d. A more complex structure arises in figure 6.6 c, but also here the $\cos \tilde{\phi}$ and $\sin^2 \tilde{\phi}$ distributions can be recognized on a constant background.

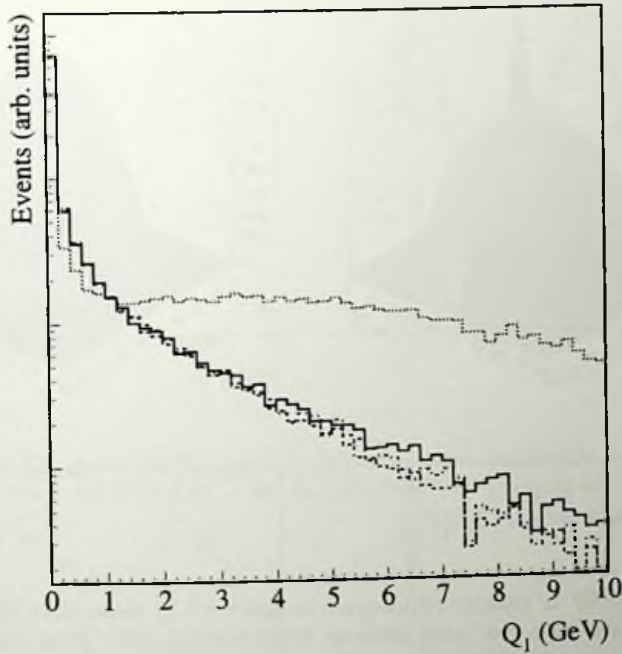


Figure 6.4: The Q spectrum of the photon emitted by the incoming positron for the generated $b\bar{b}$ states, the η_b (continuous line), the χ_{b0} (dashed line), the χ_{b1} (dotted line) and the χ_{b2} (dash-dotted line). The events were generated at $\sqrt{s} = 190$ GeV without cuts on the external particles. The vertical scale is logarithmic.

The 1D_2 $b\bar{b}$ state has not been included in the plot as it would lie exactly on top of the plot for the 1S_0 $b\bar{b}$ state.

For completeness we note that for the $c\bar{c}$ states a similar $\Delta\phi$ behaviour has been found.

Similar qualitative arguments but without numerical results have been given in [97] in connection with Pomeron production of resonances.

6.3.2 Helicities

GaGaRes can also calculate the density matrices for the production of a resonance. As has already been stated, the diagonal elements of this density matrix add up to the total cross section for the production of this resonance. For the $c\bar{c}$ resonances χ_{c2} and χ_{c1} we have studied how the different helicities of the resonance contribute to the cross section as a function of the Q_i^2 cuts. The results for the diagonal elements in the rest system of

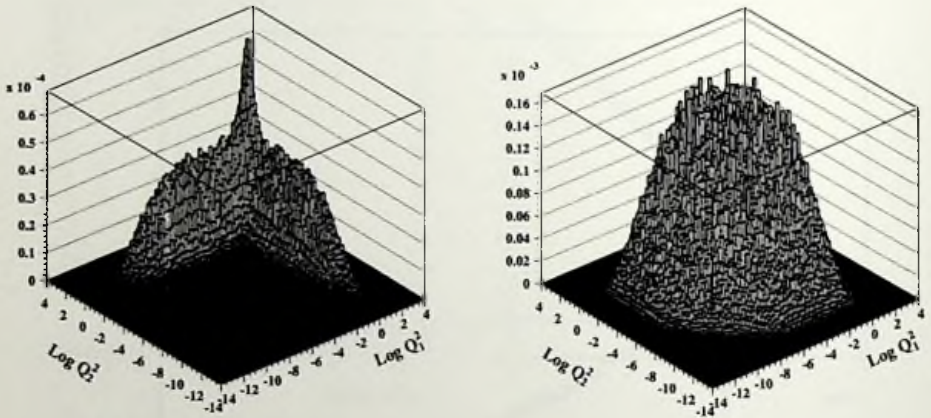


Figure 6.5: The differential cross section $d^2\sigma/(d\log_{10}(Q_1^2/W_\tau^2)d\log_{10}(Q_2^2/W_\tau^2))$, $W_\tau = 1$ GeV, in nb for the process $e^+e^- \rightarrow e^+e^-\chi_{cJ}$ at $\sqrt{s} = 92.5$ GeV for $J = 1$ (left plot) and $J = 2$ (right plot).

the resonance (RRF in chapter 5) are given in figure 6.7 In these plots both Q_1^2 and Q_2^2 have to be greater than the value given on the horizontal axis. From the right plot in figure 6.7 one can see that in the absence of cuts the dominant contribution comes from the helicity-2 components. This is in agreement with [12] where a similar dominance was found for the helicity-2 component for the $f'_2(1525)$ resonance. For high Q_i^2 cuts the helicity-0 component starts to dominate. In the BGMS-formalism [16] this contribution comes from the σ_{SS} component that is proportional to $Q_1^2 Q_2^2$. This result also agrees with theoretical predictions found by Close [98], in which he states that the helicity-0 contribution is of the order $\mathcal{O}(t\bar{t}M^2)$. From the left plot in figure 6.7 one can see that in the case of the χ_{c1} resonance in the absence of cuts the helicity-1 component is dominant. It would be interesting to verify this statement with experimental data. For higher Q_i^2 cuts again the helicity-0 component starts to dominate.

6.3.3 The process $e^+e^- \rightarrow e^+e^-\chi_{c2} \rightarrow e^+e^-J/\psi\gamma \rightarrow e^+e^-l^+l^-\gamma$

In section 5.4 we have constructed the density matrix for the complete decay of a χ_{c2} resonance into a J/ψ and a photon, where the J/ψ subsequently decays into two electrons or muons. We can now use equation (2.55) in section 2.9 to combine the density matrix for the two-photon production of a χ_{c2} resonance with the density matrix for the complete decay of the resonance to get the full matrix element squared. This full matrix element has been used to generate the distribution of the angle between the outgoing photon and the boost direction in the RRF. The results are given in figure 6.8. In this figure also previously shown results (figure 5.1) are included. The angular distribution agrees well

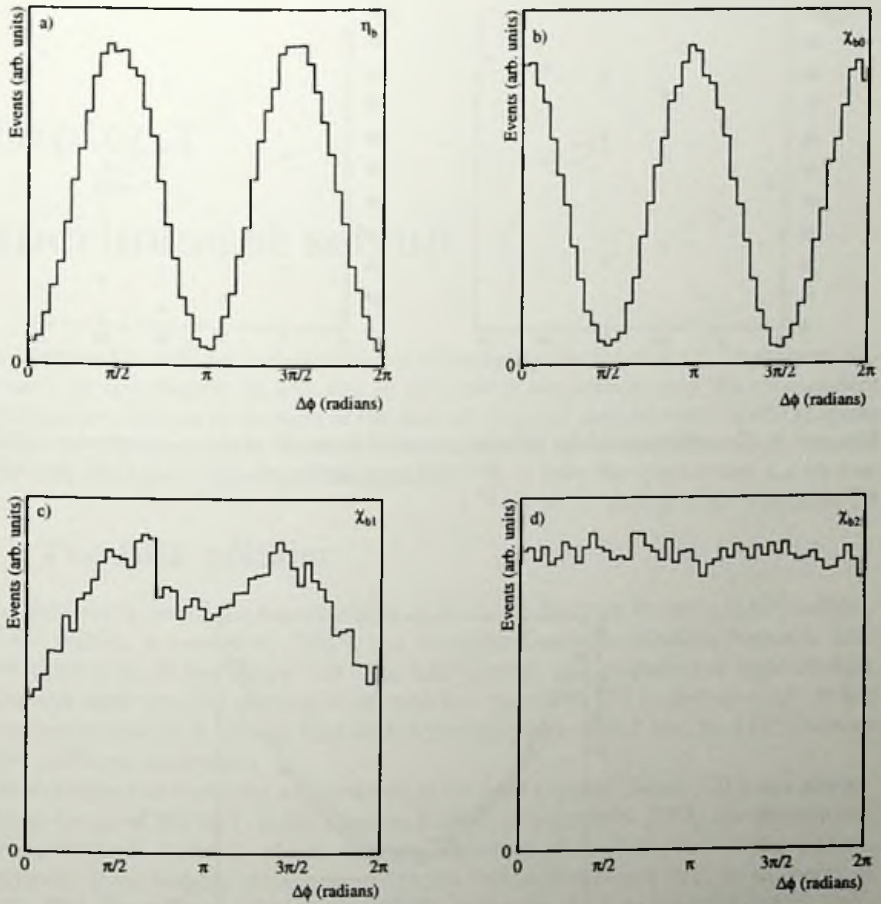


Figure 6.6: The $\Delta\phi$ spectra for the $b\bar{b}$ states η_b (a), χ_{b0} (b), χ_{b1} (c) and χ_{b2} (d). The events have been generated at $\sqrt{s} = 190$ GeV in the absence of additional cuts on the external particles. All vertical scales are linear.

with the previously found result for the density matrix for the decay of the χ_{c2} into a J/ψ and a photon, equation (5.58). This implies that the production of the resonance is indeed dominated by the helicity-2 contribution, as has been pointed out before. Secondly, the decay of the J/ψ does not influence the distribution of the photon, a result that also was to be expected.

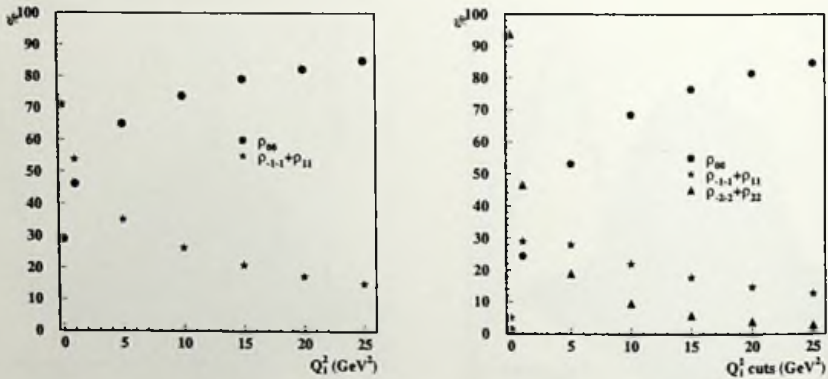


Figure 6.7: Contributions of the different diagonal elements of the χ_{c1} resonance (left plot) and the χ_{c2} resonance (right plot) to the total cross section at $\sqrt{s} = 91.5 \text{ GeV}$, for different Q_1^2 cuts. (I.e. $Q_1^2 > 0, 1, 5, \dots, 25 \text{ GeV}^2$.)

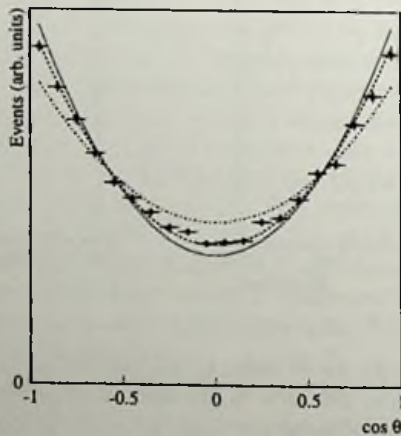


Figure 6.8: The distribution of the polar angle of the outgoing photon in the RRF. The datapoints show the result from the calculation using the complete matrix element for the production and decay. The dashed line shows the distribution for the complete density matrix for the decay of the resonance where the production is purely helicity-2. The dotted lines represents the distribution according to the pure dipole transition and the dashed-dotted line shows the distribution that has been experimentally observed [92]. The vertical scale is linear.

Chapter 7

Experimental set-up

In the analyses that will be presented in this thesis data collected with the L3 detector has been used. In this chapter we will give an overview of the detector and the subdetectors with strong emphasis on those parts of the detector that are most relevant for the analyses in this thesis. The description represents the situation up to october 2000. Since then the collider and the detector have been dismantled.

7.1 The LEP collider

The L3 detector is one of the four detectors at the Large Electron Positron (LEP) collider. The LEP collider is located at CERN, the European Centre for Nuclear Research, near Geneva (Switzerland) (see figure 7.1). The LEP storage ring consisting of eight straight sections and eight bending sections is situated in a tunnel 50-170 m underground. It has in good approximation a circular form with a circumference of 26.7 km. At LEP electron-positron collisions are studied.

The electrons and positrons are produced in the LEP Injector Linacs (LIL) and accelerated to an energy of 600 MeV. In the Electron Positron Accumulator (EPA) the electron and positron pulses are accumulated into bunches, discrete packets of electrons and positrons. Subsequently these bunches are accelerated in the Proton Synchrotron (PS) to an energy of 3.5 GeV. The Super Proton Synchrotron (SPS) accelerates them to an energy of 20 GeV. At this energy the bunches enter the LEP ring, where the particles are accelerated to the desired energy. This acceleration is performed by (superconducting) radio frequency (RF) cavities. The latter also have to compensate the energy loss due to synchrotron radiation, which gives the most stringent constraint to the highest obtainable beam energies. A total of 3304 bending magnets guide the particles through the bending sections. The beams are focused by a system of quadrupole and sextupole magnets. A more detailed description can be found in [99–101].

In four of the straight segments the electron and positron beams are brought into collisions at the so-called interaction points. Around these, four large experiments have been built: ALEPH, DELPHI, L3 and OPAL.

The LEP collider has been commissioned to study the properties of the carriers of the weak force, the Z and W^\pm vector bosons. In LEP's existence two periods can be distinguished. During the first period from 1989 to 1995, referred to as LEP1, data was

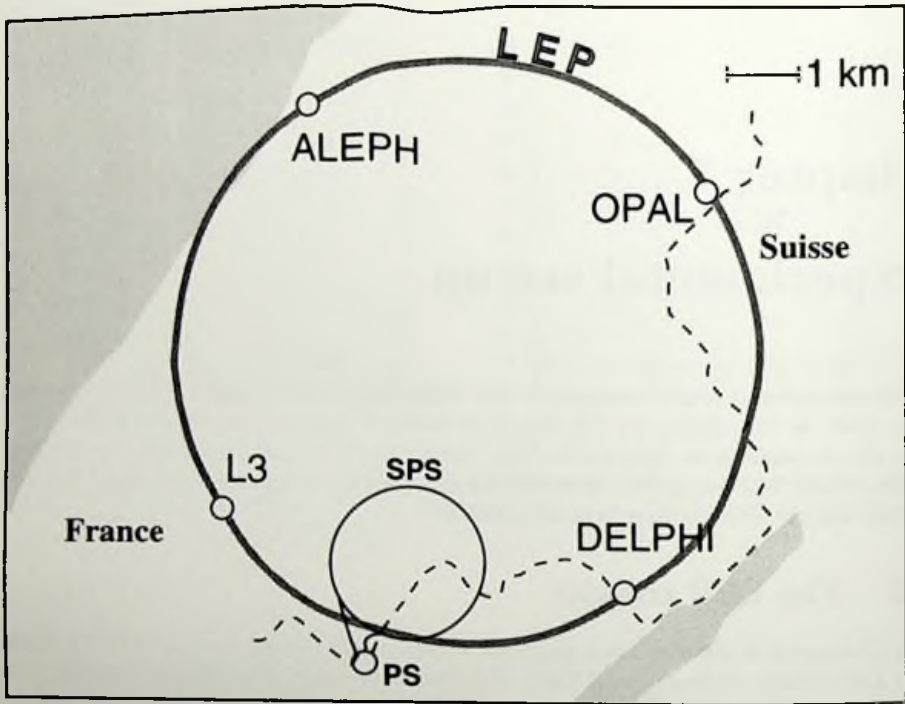


Figure 7.1: The LEP ring and the four experiments.

collected at a centre-of-mass energy around 90 GeV, the mass of the Z boson. In 1995 the machine was upgraded. Superconducting RF cavities were installed to increase the centre of mass energy beyond the threshold energy for W -pair production. In the period from 1996 to 2000 (LEP2) energies from 161 to 209 GeV have been reached.

The event rate for a certain physical process is given by the product of the cross section corresponding to this process and the luminosity (L) which is defined by

$$L = \int \rho_1(\vec{x}) \rho_2(\vec{x}) |\vec{v}_1 - \vec{v}_2| d^3\vec{x}. \quad (7.1)$$

Here $\rho_1(\vec{x})$ and $\rho_2(\vec{x})$ are the densities of the particles in the two colliding beams. The quantity $|\vec{v}_1 - \vec{v}_2|$ is the relative velocity of the two beams. The luminosity is a flux. The luminosity depends on a number of accelerator parameters, e.g. the beam energy, the beam-currents (I_b), the beam strength (ξ_y) which takes into account the force between the beams and the so-called betatron amplitude (β_y^*) which specifies the focusing strength at the interaction points [102]. At LEP2 the luminosity is of the order of $10^{32} \text{ cm}^{-2}\text{s}^{-1}$ for the high energy runs.

The collected luminosity at an experiment is determined by measuring the event rate for a process that is theoretically well understood and whose cross section has been calculated

Year	Luminosity \mathcal{L} (pb^{-1})	Energy Range(GeV)
1997	51	183
1998	176	189
1999	221	192-201
2000	215	201-209

Table 7.1: *The collected integrated luminosity and centre of mass energies of the LEP2 running periods.*

to a high precision. For electron-positron collisions, small-angle Bhabha scattering is used. In table 7.1 the centre of mass energies and the integrated luminosity \mathcal{L} for the LEP2 period have been collected, where

$$\mathcal{L} = \int L(t)dt. \quad (7.2)$$

In natural units the integrated luminosity is expressed in units of pb^{-1} . One barn (b) is equal to 10^{-28} m^2 , one pb to 10^{-36} cm^2 . At LEP2 energies the collected luminosity was typically of the order of $1.0 \text{ pb}^{-1}/\text{day}$.

7.2 L3 detector

A perspective view on the L3 detector is given in figure 7.2. The detector has been optimized for the measurement of electron and photon energies and the momentum of muons. It consists of a number of subdetectors that are all positioned symmetrically around the interaction point. From the interaction point outwards the following detectors have been installed:

- The Silicon Microvertex Detector (SMD).
- Time Expansion Chamber (TEC).
- Electromagnetic Calorimeter (ECAL, BGO).
- Hadronic Calorimeter (HCAL).
- Muon Chambers (MUCH).

Except for the SMD and TEC, that only consist of a central part (barrel), these detectors consist of a barrel part and parts in the forward and backward direction (endcaps). In addition to these detectors three subdetectors, only consisting of forward and backward parts, have been included:

- Luminosity Monitor (LUMI).

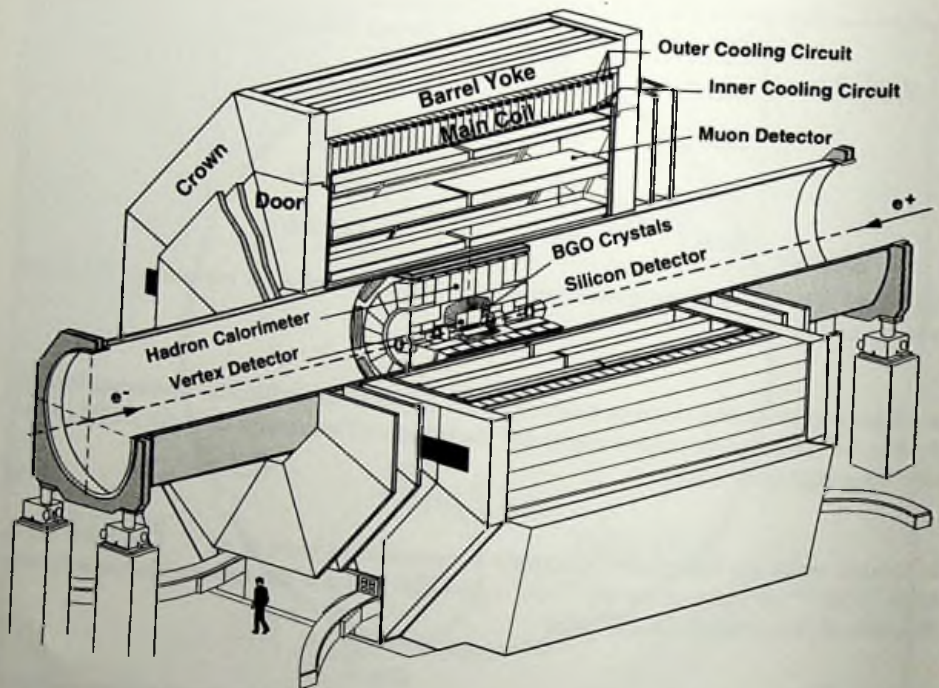


Figure 7.2: A perspective view on the L3 detector, from the outside of the LEP ring.

- Active Led Rings (ALR).
- Very Small Angle Tagger (VSAT).

All detectors are surrounded by a large octagonally shaped solenoidal magnet which provides a field of 0.5 Tesla along the beam direction. This makes it possible to measure the transverse momentum (from the curvature) and the charge-sign (from the bending direction) for charged particles.

A complete description of the L3 detector can be found in [103], whereas the upgrades are described in [59, 104, 105].

In two-photon physics the outgoing electrons and positrons are scattered over a small angle and carry away most of the available energy, whereas the remnants of the two-photon reaction typically have a low energy. As a consequence, the detectors most relevant for two-photon reaction studies are the LUMI and the VSAT to detect electrons or positrons that have been scattered over a large enough angle and the inner detectors (SMD, TEC, ECAL) to study the remnants of the two-photon system. These detectors will be further discussed. A more detailed view on some of the relevant detectors is given in figure 7.3. The VSAT detector has not been indicated in figure 7.2 and falls outside figure 7.3.

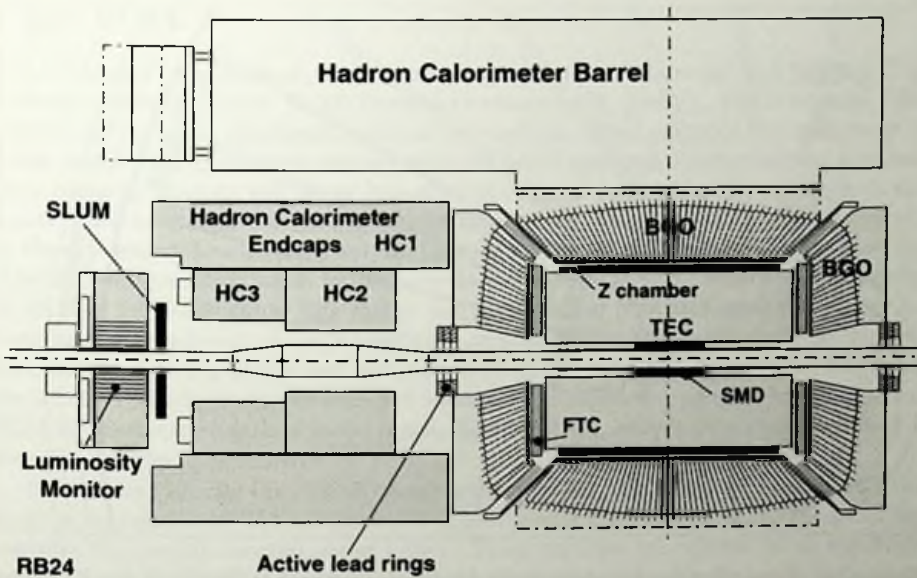


Figure 7.3: View on the inner part of the L3 detector. The Interaction point is given by the intersection point of the dash-dotted lines inside the SMD.

The following convention for the coordinates has been chosen. The direction of the incoming electrons is taken as the positive z -axis. The positive x direction points from the interaction point towards the centre of the LEP ring. As a consequence, the positive y direction is perpendicular to the LEP plane and points upwards. Polar and azimuthal angles are denoted by θ and ϕ , as usual.

7.2.1 SMD and TEC

The SMD and TEC detectors have been incorporated to study the trajectories (tracks) of charged particles. In addition, there are the z chambers and the FTC detectors.

The SMD consists of two concentric layers of silicon detectors, see figure 7.4. When a charged particle traverses the depleted region of the silicon it can create electron-hole pairs which give rise to a measurable signal. The two layers are placed at 6 and 8 cm respectively from the interaction point. The polar angle coverage of the SMD extends from 22° to 158° . The position resolution in the SMD is $8 \mu\text{m}$ (in $r\phi$) and $12 \mu\text{m}$ (in z).

The TEC is a gas drift detector. It consists of two parts, the inner TEC and the outer TEC. The inner TEC is divided into 12 sectors each containing 8 anode wires, the outer TEC is divided into 24 sectors each containing 54 anode wires. The anode wires and cathode

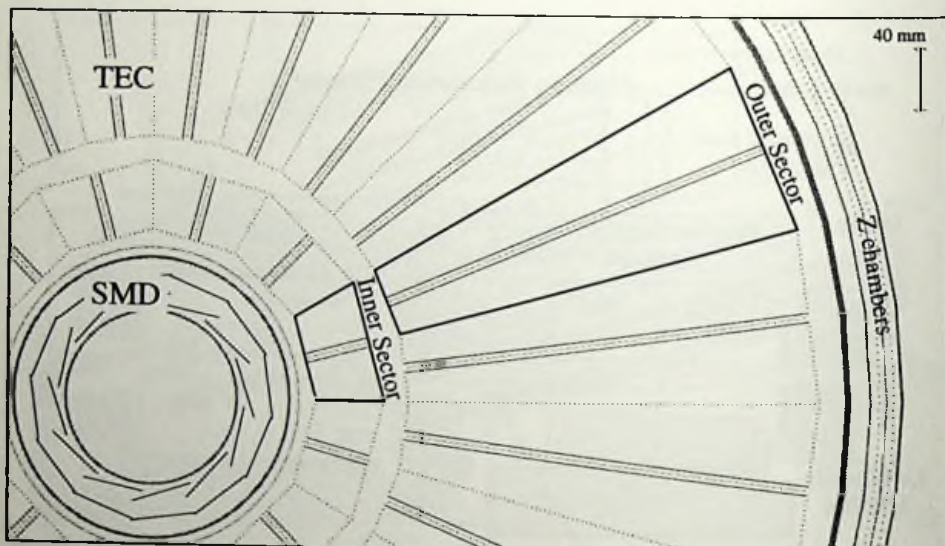


Figure 7.4: The central tracking part of the L3 detector, formed by the SMD, the TEC and the z-chambers. Figure taken from [106].

wires are parallel to the z -axis. (figure 7.4). Close to the planes of anode wires there is on both sides a plane of grid wires at ground potential. These ensure that the electric field in the region between the grid wires and the cathodes, the drift region, is homogeneous. The TEC is filled with 80 % CO_2 and 20 % iso-butane (iC_4H_{10}). When a charged particle traverses the gas it causes ionization of the gas atoms. The electrons drift to the anode wires while the positively charged ions drift to the cathode wires. After having passed the grid wires the electrons are accelerated and create an avalanche of ionizations in this so-called amplification region. The time of flight of the electrons to the anode wires can be converted into the position where the original ionization took place. Each inner (outer) TEC sector has 2 (9) charge division wires. These wires are read out on both ends and give information on the z coordinate of the hit. The radial distance of the wires to the interaction point stretches from 11 cm to 42.5 cm. Only charged particles that leave the interaction point under a polar angle in the range $44^\circ < \theta < 136^\circ$ can reach all 62 wires. Particles that leave the interaction point with an angle $\theta < 10^\circ$ or $\theta > 170^\circ$ miss the TEC detector completely. The position resolution of the TEC is $50 \mu\text{m}$ in $r\phi$.

The TEC has been optimized for measurements in the xy -plane. Additional wire chambers have been installed on the outside of the TEC, the z chambers. The resolution of the z chambers is $200 \mu\text{m}$ in z .

7.2.2 ECAL

The ECAL has been designed for the energy measurement of electrons¹ and photons. The detector consists of almost 11,000 Bismuth Germanate ($\text{Bi}_4(\text{GeO}_4)_3$, BGO) crystals. The crystals act both as a showering and detection medium. When energetic electrons move in dense matter, like BGO, they interact with the nuclei and emit bremsstrahlung photons. High energetic photons will decay into electron positron pairs when interacting with the nuclei. Thus an energetic electron or photon entering a BGO crystal will produce a cascade of these processes (a shower), until the photons and electrons have an energy below the threshold for these interaction processes to happen. This threshold energy is of the order of 10 MeV for BGO. Below this energy the electrons and photons lose their energy by ionization and excitation of the atoms in the crystal. The excited atoms will emit a green light that is detected at the end of the crystals by photodiodes. The typical length an electron or a photon travels between two interactions is called the radiation length, X_0 . For BGO this radiation length is rather small, $X_0 \approx 1.12$ cm, allowing the construction of a compact detector.

For heavier particles this critical energy is much higher and they only interact with the medium by ionization. The energy loss is approximately independent of the energy of the particles for particle energies above 1 GeV. These particles are referred to as minimum ionizing particles (MIP's). Hadronic particles can also interact with the atoms by nuclear interactions, resulting in a shower that is spread wider than electromagnetic showers.

The BGO crystals have a length of 24 cm. The front surface is typically 2×2 cm² and the back surface is typically 3×3 cm². The barrel part consists of 48 rings of 160 crystals. The endcaps consist each of 1536 crystals. The crystals are tilted 6° in ϕ to avoid particles escaping the gap between two BGO crystals. The barrel part has a polar-angle coverage from 42° to 138° , whereas the end caps have coverages from 12° to 35° and 145° to 168° .

The energy resolution is energy dependent. For low energetic photons (100 MeV) the resolution is about 9 %, whereas for photons and electrons above 1 GeV it is about 2%. The resolution in ϕ in the barrel ranges from 9 mrad (100 MeV photons) to 4 mrad (1 GeV photons). In the endcaps the resolution is a factor 2 to 3 worse. The resolution in θ is at least as good as the resolution in ϕ .

7.2.3 LUMI and VSAT

The LUMI detector has been installed to determine the luminosity from small-angle Bhabha scattering. The LUMI also consists of BGO crystals. On each side at 2.65m from the interaction point there is a cylindrical detector, each containing 304 BGO crystals. Each cylinder is divided into two halves by the yz -plane. The two parts can be moved away from the beam pipe to protect the crystals from radiation damage during periods of unstable beams, e.g. during the filling and acceleration phases of LEP or during periods of very bad background conditions. To improve the measurement of the impact position, a silicon strip detector (SLUM) has been installed in front of the LUMI. The SLUM is read out in case of a back-to-back event in the LUMI.

¹When we speak in this section of electrons, we mean electrons as well as positrons.

The angular coverage of the detectors is $1.4^\circ < \theta < 3.9^\circ$ and $176.1^\circ < \theta < 178.6^\circ$. The energy resolution for the electrons in the LUMI is around 1.5 % for LEP2 energies. The θ resolution is of the order of 0.5 mrad and the ϕ resolution is 0.5° . In LEP2 the luminosity is measured by a combined measurement of the LUMI and the SLUM with an error of 0.2%.

All electrons and positrons that are scattered over a small angle can give a hit in the LUMI, so also the ones which cause a two-photon process. This makes the detector an interesting device for two-photon physics. Especially for the missing mass analyses that is presented in the next chapter the LUMI detector plays a crucial role.

The VSAT detector consists of four boxes, two on each side at 8.17m from the interaction point. Each box contains 24 BGO crystals. The boxes are placed in the horizontal plane and can also be moved away from the beam pipe during periods of bad radiation conditions. The boxes are installed behind the quadrupole magnets (located at a distance between 3.47-6.34 m from the IP). These magnets defocus in the horizontal plane and focus in the vertical plane. The energy resolution is 3%, the resolution in θ is 0.10 mrad and in ϕ is 27 mrad. These values hold for the fiducial volume of the VSAT. Outside this volume the resolutions are worse.

It should be stressed that the LUMI and VSAT detectors do not distinguish between photons and electrons. So in double-tag events hits may also mean the detection of an electron or positron and an opposite photon or the detection of two opposite photons.

7.2.4 Triggers

The rate of bunch crossings at the L3 interaction point is 45 kHz, but only a small fraction of these bunch crossings results in an interesting e^+e^- interaction. Reading out the detector causes a dead-time during which the detector is blocked for new data. Besides the e^+e^- also so-called background events can give a signal in the L3 detector. Some sources of these background events are beam-gas interactions, beam-wall interactions, cosmic rays and noise in the electronic channels. The trigger system has been installed to separate the e^+e^- interactions from the background events and to decide whether an event should be recorded or not.

The L3 trigger consists of three levels of increasing complexity. Only when an event is accepted by a trigger level it is passed on to the next level.

The level-1 trigger consists of a logical OR of the following subtriggers: the energy trigger, the luminosity trigger, the ALR trigger, the TEC trigger, the scintillator trigger and the muon trigger. For the analyses we make use of events that are triggered by the luminosity trigger, the energy trigger or the TEC trigger. These triggers will be discussed in some more detail.

The luminosity triggers consists of the following subtriggers:

- Back-to-back trigger: Requires an energy deposition of at least 15 GeV in two opposite sectors, a typical topology for non-radiative Bhabha events.
- Asymmetric double-tag trigger: Requires an energy deposition of at least 25 GeV on one side and 5 GeV on the other side of the interaction point.
- Single-tag trigger: Requires an energy deposition of at least 30 GeV on one of the sides.

The luminosity triggers are crucial in the missing mass analysis.

Most of the the subtriggers of the energy trigger require some minimum energy deposition in either the ECAL or the HCAL. The subtriggers most relevant for the analyses presented in this thesis are:

- Cluster trigger: Requires a cluster in the ECAL or HCAL of at least 2.5 GeV, close in ϕ to a TEC track. A cluster is a localised deposit of energy.
- Single photon trigger: Is set if a BGO cluster with an energy above 1 GeV which accounts for a least 80 % of all ECAL energy is found. This trigger has been installed to trigger on the process $e^+e^- \rightarrow Z\gamma \rightarrow \nu\bar{\nu}\gamma$.
- Energy trigger: Requires at least 10 GeV in the ECAL or 15 GeV in the BGO and the barrel HCAL or 20 GeV in all calorimeters.

Finally, we also mention the TEC triggers:

- Charged track trigger: Requires in the outer TEC at least two charged tracks with transverse momentum $p_T > 100$ MeV for $28^\circ < \theta < 37^\circ$, $143^\circ < \theta < 152^\circ$ and $p_T > 150$ MeV for $37^\circ < \theta < 143^\circ$. The tracks are required to have a separation greater than 120° in the transverse plane.
- Inner TEC trigger: Uses a neural net to select non-background events. It requires at least two good tracks and one track in the outer TEC.
- Electron trigger: Requires one TEC track together with an energy deposition of at least 70 % of the beam energy on one side of the LUMI.

As only the events that pass the level-1 trigger go to the level-2 trigger, this trigger has more time to evaluate an event without introducing more dead-time in the readout system, which allows this trigger level to use more complicated algorithms. The level-2 trigger receives in addition some information that is not available to the level-1 trigger. In particular, it receives the information from the charge division wires in the TEC. Events with two or more level-1 triggers pass the level-2 trigger automatically.

The level-3 trigger has access to the complete digitized data and a complete reconstruction of the events is made. Events with both a level-1 TEC and energy trigger are always accepted. After the level-3 trigger the trigger rate has dropped to 2-3 Hz.

7.3 Data processing

After having passed the final trigger level, the information of the selected events are written to the raw data tapes. From these tapes the data is processed by the L3 offline reconstruction program which uses the databases which contain all the calibration constants. In the reconstruction the data is converted from the digitized data into physical information like energy deposits and charged tracks. After the reconstruction the information from the subdetector is combined and one tries to match tracks to energy depositions in the calorimeters.

The processed data is stored in several formats. The candidate events triggered by the LUMI or the VSAT are sent to a separate events stream, the FSB format. All other events are written to different formats, the DVN and DSU formats.

Chapter 8

Missing mass analysis

Results of a missing mass analysis to search for heavy states that couple to two photons are presented. Although the main goal of this analysis is to look for the η_b meson, the experimental upper limit on the two-photon decay of the Higgs boson will also be studied. To reject the dominant background, (radiative) Bhabha events, information from the central part of the L3 detector has been included in the analysis, leading in fact to two missing mass analyses: a pure and an extended one. The result is a 95% C.L. upper limit on the two-photon decay width of $C = +1$ states as a function of the invariant mass of the two-photon system. Also a study of the Bhabha background at the Monte Carlo level has been performed.

8.1 Introduction and motivation

As has already been mentioned in section 2.10.1, the lightest $b\bar{b}$ quarkonium state, the η_b meson, has not yet been observed. Theoretical models [22, 27, 107] predict for the η_b meson a two-photon width of 0.2-0.5 keV. In the analysis of this chapter a search for this meson is performed. In addition, one can also look for other narrow-width C -even particles that couple strongly to two photons.

We have used the missing mass technique. By measuring the four-momenta of the two scattered leptons one reconstructs the invariant mass of the two-photon system, $W_{\gamma\gamma}$, from the information of the two tagged leptons

$$W_{\gamma\gamma} = \sqrt{(p_1 + p_2 - p'_1 - p'_2)^2} = 2\sqrt{\omega_1\omega_2 - E'_1E'_2 \cos^2\left(\frac{\theta_{12}}{2}\right)} \quad (8.1)$$

where θ_{12} is the angle between the outgoing leptons in the lab-frame. The angle can be calculated from the angular information of the outgoing leptons, see equation (2.19). As the scattered leptons go almost back-to-back, the dominant contribution to $W_{\gamma\gamma}$ comes from the product of the photon energies.

The advantage of this approach, in contrast to the observation of the decay products of an exclusive decay mode of the resonance, is that one does not have to take into account the branching ratio of the resonance into a particular, exclusive final state. For heavy resonances these branching ratios are low, typically of the order of (tenths of) percents, or

even unknown, as is the case for the η_b meson. The disadvantage of this method is that one can only use the double-tag events. As a consequence of the bremsstrahlung-like nature of the intermediate photons, the rate of double-tag events is considerably lower than that of single-tag or no-tag events.

A similar search for high-mass, C -even particles has been performed by the TPC/Two-Gamma collaboration [52, 53] at the PEP collider. This search was performed in the region $4.5 < W_{\gamma\gamma} < 19$ GeV. In addition to the two tags, also some activity in the central part of the detector was required. (More than 0.8 GeV energy deposition in both electromagnetic shower detectors.) No evidence for narrow resonances in this region has been found. The 95% C.L. upper limits set by TPC/Two-Gamma were given in figure 2.9 in section 2.10.3. In particular, for the η_b resonance a 95% C.L. upper limit of 400 keV has been found, a result which will be improved in the LEP analyses of this chapter. In the present analysis the ranges $3 < W_{\gamma\gamma} < 150$ GeV are covered. This is a considerable extension of the $W_{\gamma\gamma}$ range exploited by the TPC/Two-Gamma collaboration. The region of a potential Higgs boson with a mass of 115 GeV is also covered in this analysis.

Recently, the ALEPH collaboration [108] has presented the first results of a direct search for the η_b meson. In this analysis the decays of the η_b meson into four or six charged tracks were studied. In the decay into four charged tracks no candidates were found, in the decay into six charged tracks one candidate event with an invariant mass of 9.30 ± 0.05 GeV was found. The 95% C.L. upper limits were set to $\Gamma_{\gamma\gamma}(\eta_b) \times \text{Br}(\eta_b \rightarrow 4 \text{ charged tracks}) < 57$ eV and $\Gamma_{\gamma\gamma}(\eta_b) \times \text{Br}(\eta_b \rightarrow 6 \text{ charged tracks}) < 128$ eV.

8.2 Monte Carlo generators

For the calculation of the acceptance and the efficiency of the detector we have used the GaGaRes generator that has been introduced in chapter 6. It generates the final state of the outgoing leptons and the resonance. Throughout this chapter we assume that the resonances couple as a 1S_0 state to the two photons. For the η_b this is obviously correct, for states other than 1S_0 it is a good starting point. When a hint of a resonance is found other assumptions than the 1S_0 state can be pursued. The cross section as a function of the invariant mass of the generated two-photon system for $\sqrt{s} = 190$ GeV is plotted in figure 8.1. In these calculations the two-photon width $\Gamma_{\gamma\gamma}$ has been fixed to the value 1 keV whereas the minimum allowed scattering angle of the outgoing leptons has been set to 29 mrad. The strong decrease of the cross section for increasing $W_{\gamma\gamma}$ can be clearly read off from this plot. In the range $10 \text{ GeV} < W_{\gamma\gamma} < 30 \text{ GeV}$ the cross section is proportional to $1/W_{\gamma\gamma}^{3.4}$, in quite good agreement with the Low formula (2.48). At very high $W_{\gamma\gamma}$ the cross section decreases rapidly, which is a consequence of the fact that one approaches the border of the allowed phase space. The low cross sections for high $W_{\gamma\gamma}$ will result in less strict upper limits on the two-photon widths. The cross section has been fit by the function

$$\sigma(W_{\gamma\gamma}) = A \cdot \exp\left(\sum_{i=1}^6 P_i \ln^i\left(\frac{W_{\gamma\gamma}}{W_s}\right)\right), \quad (8.2)$$

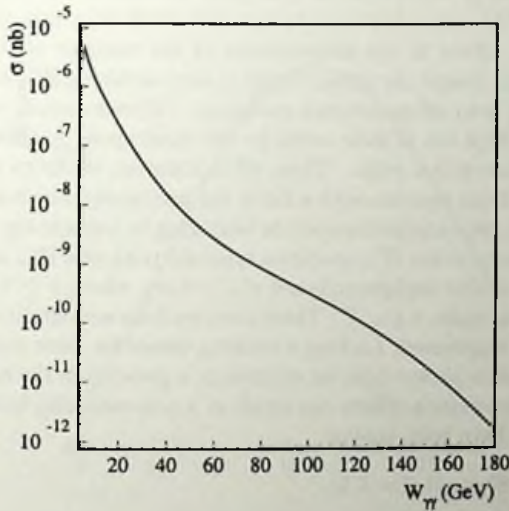


Figure 8.1: The cross section at $\sqrt{s} = 190$ GeV for the process $e^+e^- \rightarrow e^+e^-R$ as a function of $W_{\gamma\gamma}$, or in other words M of the resonance, for scattered leptons in the range $29 \text{ mrad} < \theta_i < 80 \text{ mrad}$. For all values of $W_{\gamma\gamma}$ the two-photon width $\Gamma_{\gamma\gamma}$ has been set to 1 keV.

where the best fit parameters are given by

$$\begin{aligned}
 A &= 4.90 \times 10^{-27} \text{ nb}, & P_1 &= 116.61, & P_2 &= -110.73, \\
 P_3 &= 53.658, & P_4 &= -14.175, & P_5 &= 1.9274, \\
 P_6 &= -0.10559, & W_s &= 1 \text{ GeV}.
 \end{aligned}$$

The detector simulation has been performed with the GEANT package [109].

8.3 Pure missing mass analysis

In the pure missing mass analysis (PMMA) only the information from the luminosity monitors has been taken into account. For this reason the analysis has been performed on the standard data-level for luminosity events, the fbsb-level of section 7.3. On this data level only information of the luminosity monitors is stored, independent of any triggers in the the other sub-detectors.

Besides the two-photon processes there are some other processes that can give an identical signature in the detector¹. The main background comes from (radiative) Bhabha

¹Even though for non two-photon events there clearly is no $\gamma\gamma$ -system, we can still calculate the four-

events. Although the $W_{\gamma\gamma}$ reconstructed from pure Bhabha events and single radiative Bhabha events should be zero, these events can still result in a non vanishing value for $W_{\gamma\gamma}$ due to resolution effects in the measurement of the energies of the tagged leptons. Higher radiative Bhabha events can always result in non-vanishing $W_{\gamma\gamma}$'s. Another important background comes from off-momentum radiation. Off-momentum radiation is caused by electrons that are swept out of their orbits by the quadrupole magnets that are located on both sides of the interaction point. These off-momentum electrons can end up in the luminosity monitor and can coincide with a hit in the luminosity monitor on the other side of the interaction point, for example an electron belonging to a single-tag two-photon event. The off-momentum events in the $W_{\gamma\gamma}$ spectrum typically peak at a $W_{\gamma\gamma}$ around 60 % of the beam energy. Other possible backgrounds are $e^+e^- \rightarrow n\gamma$, where $n \geq 2$, or $e^+e^- \rightarrow X\gamma\gamma$, where X can be any final state, e.g. a Z^0 . These cross sections are significantly smaller. This background cannot be suppressed. Lacking a tracking device for these scattering angles it is impossible to distinguish a photon from an electron or a positron in the luminosity monitor. Again, for $n = 2$ only resolution effects can result in a non-vanishing invariant mass.

The following cuts have been applied:

1. $29 \text{ mrad} < \theta_i < 80 \text{ mrad}$ ($i = 1, 2$),
2. $\max(E'_1, E'_2) < 0.97 E_b$,
3. $\min(E'_1, E'_2) > 0.78 E_b$,
4. $|\Delta\phi - 180| > 45^\circ$,
5. $|\phi_i - 90| > 5^\circ, |\phi_i - 270| > 5^\circ, i = 1, 2$,
6. $|y| > 0.10$,
7. $N_{\text{tag}} = 2$.

$\Delta\phi$ is the difference of the two azimuthal angles ϕ_1 and ϕ_2 . The variable y is the rapidity of the (pseudo) $\gamma\gamma$ - system, given by

$$y = \frac{1}{2} \ln \left(\frac{E_{\gamma\gamma} + P_{\gamma\gamma,z}}{E_{\gamma\gamma} - P_{\gamma\gamma,z}} \right), \quad (8.3)$$

where we have introduced the four-vector

$$P_{\gamma\gamma} = (E_{\gamma\gamma}, \vec{P}_{\gamma\gamma}) = p_1 + p_2 - p'_1 - p'_2. \quad (8.4)$$

Finally, N_{tag} is the number of tags in the luminosity monitor.

Cut 1 requires the event to have at least one tag in the luminosity monitor on each side of the interaction point. Cuts 2, 4 and 6 are introduced to suppress the background coming from the Bhabha events, as these events have outgoing leptons whose energies are close to

momentum of the "missed" system

$$P = p_1 + p_2 - p'_1 - p'_2$$

from the tagged particles and denote its invariant mass by $W_{\gamma\gamma} \equiv \sqrt{P^2}$.

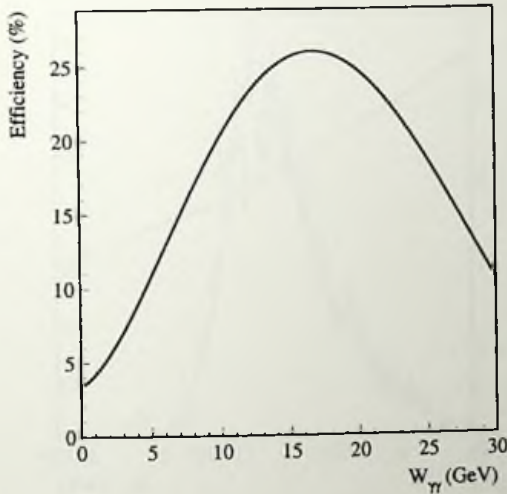


Figure 8.2: The efficiency as a function of $W_{\gamma\gamma}$ at $\sqrt{s} = 190$ GeV in the PMMA.

the beam energy, are back to back ($\Delta\phi = 180^\circ$) and result in a vanishing rapidity (8.3). The dominant error on the determination of $W_{\gamma\gamma}$ comes from the errors on the determination of the tagged energies. The dominant term in (8.1) is the product of the intermediate photon energies. Cut 2 avoids subtraction of two almost equal energies that would result in very large errors on the photon energies. Cut 3 removes most of the off-momentum leptons. The energy spectrum of the off-momentum leptons peaks around 70 % of the beam energy. Both L3 luminosity monitors consist of two halves that can be opened and closed during filling and acceleration of LEP, to protect the BGO crystals against radiation damage. The opening slits are at $\phi = 90^\circ$ and $\phi = 270^\circ$ in the xy -plane. To avoid showers passing through the slits, cut 5 has been imposed. Cut 7 is meant to avoid events with extra (radiative) photons in the luminosity monitor.

These cuts result in an efficiency as a function of the invariant mass of the two-photon system, $\varepsilon(W_{\gamma\gamma})$, as is shown in figure 8.2. The shape of $\varepsilon(W_{\gamma\gamma})$ can be qualitatively understood. The suppression at low $W_{\gamma\gamma}$ comes from cut 2. The suppression at high $W_{\gamma\gamma}$ is caused by cut 3.

Also the mass resolution as a function of $W_{\gamma\gamma}$ has been determined. At a number of values for $W_{\gamma\gamma}$ 5000 events were generated and simulated in the detector. Anticipating for the search at high $W_{\gamma\gamma}$, the mass resolution was taken to be the width of the peak in the invariant mass spectrum for the events that passed the cuts 1, 4, 5 and $\max(E'_1, E'_2) < 1.05E_b$. This exercise has been repeated for different values in the $W_{\gamma\gamma}$ spectrum. The results of this study are summarized in figure 8.3. The mass resolution is mainly determined by the energy resolution of the tagged leptons which is approximately 1.4% of the energy of

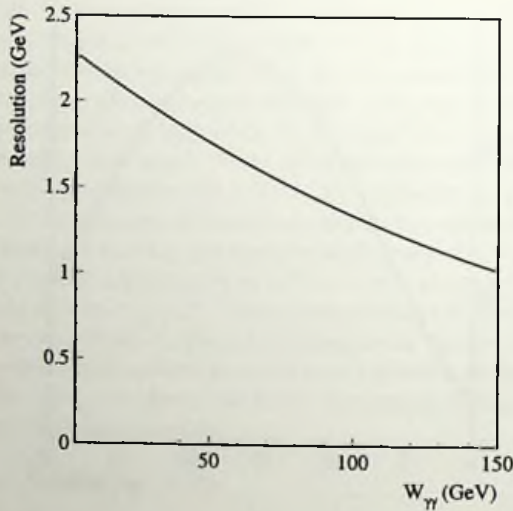


Figure 8.3: The mass resolution as a function $W_{\gamma\gamma}$ at $\sqrt{s} = 190$ GeV.

the lepton. This also explains qualitatively the shape of the plot. A low invariant mass of the two-photon system typically requires at least one of the intermediate photon energies to be low. The energy of this low-energetic photon has a relatively large error, resulting in a large error on the invariant mass of the two-photon system. This resolution is worse than the one found by TPC/Two-Gamma, which can be understood by noting that in the latter experiment the energy resolution was better (1.2 % of the measured energy) and that the beam energy was significantly lower, 14.5 GeV. To anticipate on the analysis presented in the last section of this chapter, the resolution in the range from 3 to 150 GeV has been given. The resolution has been fit by an exponential function

$$E(W_{\gamma\gamma}) = Ae^{BW_{\gamma\gamma}}, \quad (8.5)$$

where the best fit parameters are given by

$$A = 2.32 \text{ GeV}, \quad B = -5.4392 \times 10^{-3} \text{ GeV}^{-1}.$$

The cuts were applied to the data sample that has been collected in the period 1997 to 2000. The invariant mass spectrum of the events that satisfy the cuts is given in figure 8.4. Again, the typical shape can be understood from the applied cuts. At high invariant masses of the two-photon system the spectrum is suppressed by the cut on the minimum tagged energy (cut 3). At low invariant masses the spectrum is suppressed by the cut on the maximum tagged energy, although it should be noted that also without this cut there is a suppression of events around $W_{\gamma\gamma} = 0$. In appendix C it will be shown that very mild

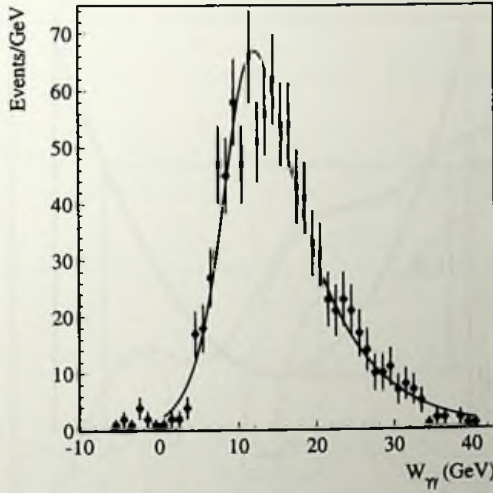


Figure 8.4: Spectrum of the invariant mass $W_{\gamma\gamma}$ of the two-photon system for all LEP 2 data in the PMMA. The spectrum is fit with the threshold function (see text).

assumptions about the energy distributions of the intermediate photons will already result in this suppression. In figure 8.4 also bins with negative $W_{\gamma\gamma}$ were filled. The second term in the most right expression in (8.1) can result in a negative value for P^2 . For these events $W_{\gamma\gamma}$ is defined by $W_{\gamma\gamma} = -\sqrt{-P^2}$, i.e. we use $W_{\gamma\gamma} = \frac{P^2}{|P^2|} \sqrt{|P^2|}$.

The missing mass spectrum in figure 8.4 has been fit with a threshold function T ,

$$T(W_{\gamma\gamma}) = t_1 \frac{e^{-\frac{W_{\gamma\gamma}}{t_2}}}{1 + e^{-\frac{W_{\gamma\gamma}}{t_4}}}. \quad (8.6)$$

The best fit gives:

$$\begin{aligned} t_1 &= 455 \text{ GeV}^{-1} & t_2 &= 7.46 \text{ GeV} \\ t_3 &= 10.04 \text{ GeV} & t_4 &= 1.85 \text{ GeV} \end{aligned}$$

Now we are at a point to set upper limits on the two-photon width as a function of $W_{\gamma\gamma}$. This is done by scanning over the $W_{\gamma\gamma}$ spectrum and fitting for each point $W_{\gamma\gamma,i}$ the spectrum with the sum of the threshold function T and a Gaussian G ,

$$G(x; \mu, \sigma, A) = \frac{A}{\sqrt{2\pi}\sigma} e^{-\frac{(x-\mu)^2}{2\sigma^2}}, \quad (8.7)$$

around $W_{\gamma\gamma,i} = \mu$ whose width is fixed to the mass resolution σ_i at $W_{\gamma\gamma,i}$. The amplitude $A_i = A(W_{\gamma\gamma,i})$ of the Gaussian is the only free parameter of the fit. For a plot typically 250

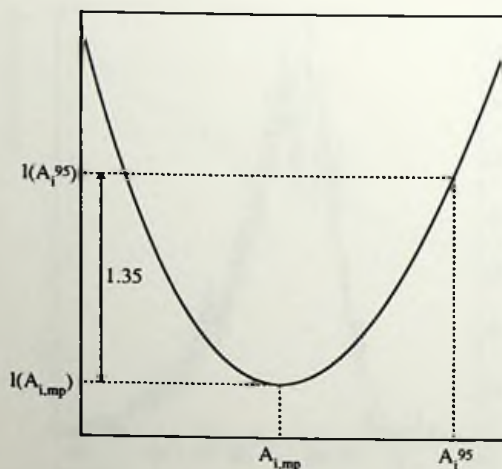


Figure 8.5: Illustration of construction of the 95 % C.L. on A_i , A_i^{95} from its likelihood function.

points $W_{\gamma\gamma,i}$ are used. For each point the most probable value $A_{i,mp}$ for A_i is determined by minimizing the logarithm of the likelihood function \mathcal{L}

$$l(A_i) = -\ln[\mathcal{L}(A_i)] = -\sum_j \ln \left[\frac{1}{N_i} (T(W_{\gamma\gamma,j}) + G(W_{\gamma\gamma,j}; W_{\gamma\gamma,i}, \sigma_i, A_i)) \right], \quad (8.8)$$

where the summation j runs over all detected events in the spectrum. The normalization factor N_i is given by

$$N_i = \int [T(W) + G(W; W_{\gamma\gamma,i}, \sigma_i, A_i)] dW. \quad (8.9)$$

In this way 250 likelihood functions $l(A_i)$ are obtained.

The 95% C.L. upper limit, A_i^{95} , on A_i can be extracted from this likelihood function by assuming that the error on A_i is normally distributed. The value A_i^{95} follows from²

$$A_i^{95} = \max \left[l^{-1} (l(A_{i,mp}) + 1.35) \right]. \quad (8.10)$$

This is illustrated in figure 8.5.

Besides this 95 % C.L. upper limit another definition for the upper limit is in use. This upper limit, $A_i^{95,cor}$, is defined as the point where 95 % of the physical region, i.e. the

²The value 1.35 comes from $1.35 = \frac{1.64^2}{2}$, where 1.64 comes from the fact that for a Gaussian distribution 95 % of the area is covered by the values below $\mu + 1.64\sigma$.

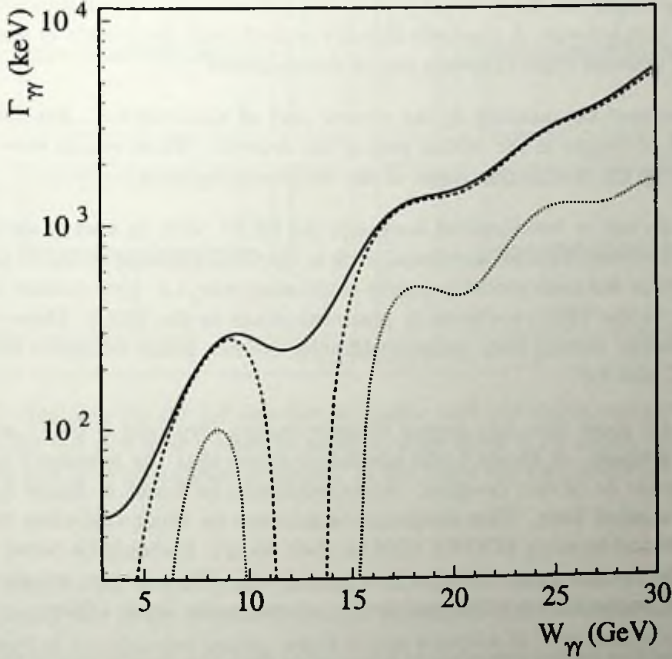


Figure 8.6: The two-photon width $\Gamma_{\gamma\gamma}(W_{\gamma\gamma})$ (dotted line), $\Gamma_{\gamma\gamma}^{95}(W_{\gamma\gamma})$ (dashed line) and $\Gamma_{\gamma\gamma}^{95,cor}(W_{\gamma\gamma})$ (continuous line) in the PMMA for all LEP 2 data.

positive values for A , lies below this value. Trivially $A_i^{95} \leq A_i^{95,cor}$ holds. Whereas A_i^{95} is allowed to become negative, $A_i^{95,cor}$ is by definition positive.

The two-photon width $\Gamma_{\gamma\gamma,i} = \Gamma_{\gamma\gamma}(W_{\gamma\gamma,i})$ can now be calculated from $A_{i,mp}$

$$\Gamma_{\gamma\gamma}(W_{\gamma\gamma,i}) = \frac{A_{i,mp}}{\sigma(W_{\gamma\gamma,i})\varepsilon(W_{\gamma\gamma,i})L_{tot}}\Gamma_{\gamma\gamma}^0, \quad (8.11)$$

where $\sigma(W_{\gamma\gamma,i})$ is the cross section given in figure 8.1, $\varepsilon(W_{\gamma\gamma,i})$ is the efficiency at the invariant mass $W_{\gamma\gamma,i}$ and L_{tot} is the total collected luminosity. $\Gamma_{\gamma\gamma}^0$ has been set to 1 keV. For the 95 % C.L. upper limit $\Gamma_{\gamma\gamma,i}^{95} = \Gamma_{\gamma\gamma}^{95}(W_{\gamma\gamma,i})$ and the corrected 95 % C.L. upper limit $\Gamma_{\gamma\gamma,i}^{95,cor} = \Gamma_{\gamma\gamma}^{95,cor}(W_{\gamma\gamma,i})$ one has to replace $A_{i,mp}$ by A_i^{95} respectively $A_i^{95,cor}$ in (8.11).

The results for the two-photon width and the two upper limits on this two-photon width as a function of the invariant mass of the two-photon spectrum are summarized in figure 8.6. In particular, in the region of the η_b -meson we find a $\Gamma_{\gamma\gamma}^{95}(M_{\eta_b}) \approx 270$ keV.

8.4 QED backgrounds

In the PMMA presented in the previous section only information of the luminosity monitor has been taken into account. A complete detector scan through the events in spectrum 8.4 tells that three different types of events can be distinguished³:

1. Events without any activity in the central part of the detector. For these events there was no trigger in the central part of the detector. These events were stored on fbsb-level by the double-tag trigger of the luminosity monitor.
2. Events with one or two localized bumps in the ECAL with an energy above 5 GeV. Some of the events have an additional track in the TEC pointing to one of the bumps. These bumps are most probably purely electromagnetic, i.e. they consist of photons (no track in the TEC), electrons or positrons (track in the TEC). These events are most probably coming from radiative Bhabha events. Some examples are given in figures 8.7 and 8.8
3. Events with more than two bumps of lower energy (typically 2 GeV) and a large number of tracks. A Monte Carlo simulation shows that the resonance production events should be of this category. An example can be found in figure 8.13, which will be discussed later. This simulation is achieved by using GaGaRes to generate resonances and by using JETSET [110] for their decays. It should be noted that some resonances like the η_b are included in a special way. Their decays are simulated by the string fragmentation model and not by actual known decay tables.

This suggests that taking into account information from the central part of the detector would be a useful tool in suppressing the background.

First it has to be shown that this background with one or two energetic, well-localized bumps in the detector is indeed coming from QED processes and is well understood. This is done by comparing the experimental distributions for these events with the distributions for the events that are generated by Monte Carlo generators. For the radiative Bhabha events we have used the Monte Carlo generator BHLumiV4.04 [111]. For the process $e^+e^- \rightarrow n\gamma$ we have used the Monte Carlo generator from Berends and Kleiss [112]. We have generated 100,000,000 Bhabha events with BHLumi and 10,000,000 events for the process $e^+e^- \rightarrow n\gamma$. These generated events have not been passed through a complete detector simulation. Instead we have assumed a Gaussian energy distribution of the measured energies in the LUMI and the ECAL where the width was given by the energy resolution of these detectors. For the angles of the outgoing particles we have not applied such a smearing procedure. In the histograms where we compare results from these Monte Carlo generators to the data, the Monte Carlo histograms are normalized to the luminosity, so it is an absolute prediction.

We first consider double-tag events where there is one charged track in the detector. For these events only the radiative Bhabha events contribute. In figure 8.9 real data and Monte Carlo events are compared. In the $W_{\gamma\gamma}$ spectrum the agreement is not very good. The

³As was mentioned before, the analysis in the previous section was performed on fbsb-level. The information about the other parts of the detector is obtained by using the run and event numbers to find these events back on the dsu-level.

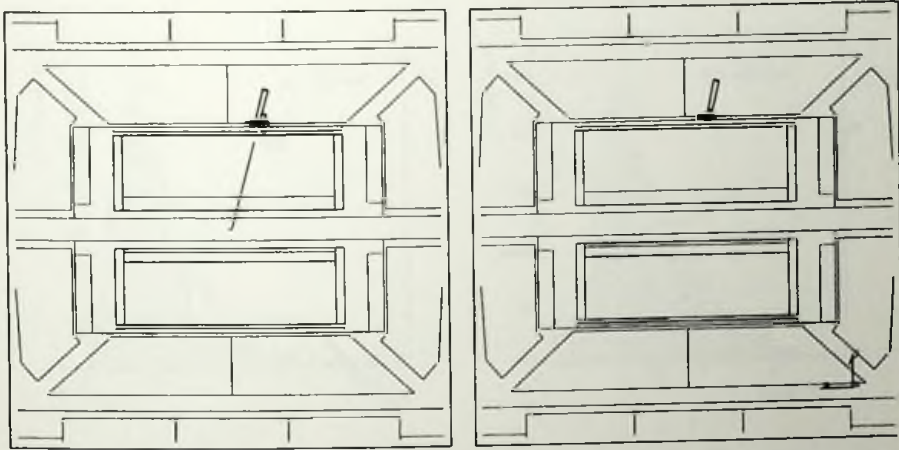


Figure 8.7: Sideview on the L3 detector for events with one additional particle in the detector. In the left plot it is a charged particle, since there is an additional charged track. In the right plot it is an additional photon. In the figure the TEC and ECAL detectors are shown.

tail of the distribution is somewhat different from the tail of the Monte Carlo distribution. This is probably due to the simplified detector simulation. On the other hand the spectrum of the energy of the charged tracks, which is less sensitive to this simulation effect, shows a very good agreement. The surplus of data events in the first bin comes from minimal ionizing particles (MIPs), e.g. charged pions and muons that deposit a small fraction of their energy in the ECAL. The results show that the double-tag events with one charged track in the $W_{\gamma\gamma}$ spectrum all come from radiative Bhabha events.

One can also look at the double-tag events where there is one additional photon in the detector and compare these to the Monte Carlo predictions. For these events both the radiative Bhabha events and the process $e^+e^- \rightarrow 3\gamma$ contribute, where it should be noted that the dominant contribution comes from the radiative Bhabha process. The plots for the $W_{\gamma\gamma}$ spectrum and the energy spectrum of the detected photon are given in figure 8.10. In these spectra Monte Carlo clearly lies somewhat below the data, indicating that there are other possible events that also contribute.

The spectra for the events with two particles in the central part of the detector, i.e. two charged tracks, one photon and one charged track or two photons are given in figure 8.11. In the plot for $W_{\gamma\gamma}$ the data events in the lowest bin of the energy spectrum of the particles have not been taken into account. These low energy particles are MIPs and it is senseless to take them into account in the $W_{\gamma\gamma}$ spectrum. Again, Monte Carlo results of radiative Bhabha events have been included in figure 8.11.

We can also consider the class of events where there is no activity in the central part of the detector. The invariant mass spectrum $W_{\gamma\gamma}$ for this class of events has been compared to the Monte Carlo simulation of (radiative) Bhabha scattering and $e^+e^- \rightarrow \gamma\gamma(\gamma)$ in figure

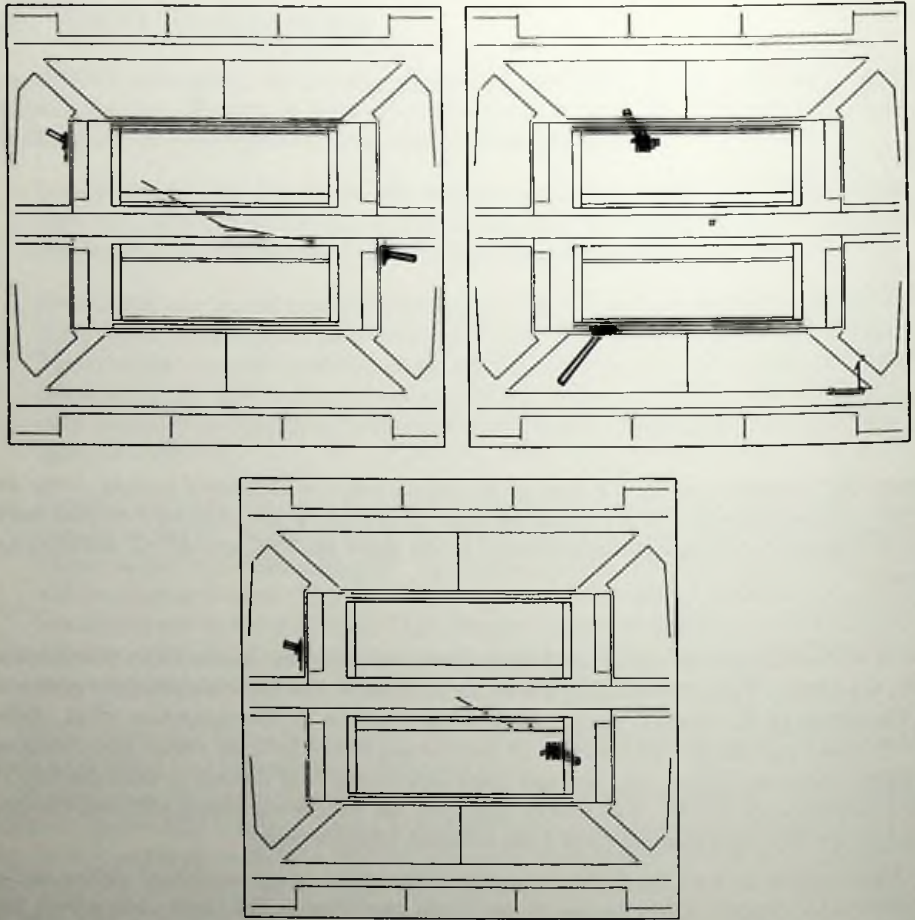


Figure 8.8: *Sideview on the L3 detector of events with two additional particles in the detector. In the first two plots there are respectively two additional charged tracks and two photons. In the last plot an event with one additional charged track and one photon is given.*

8.12. Again, good agreement between the spectra has been found.

In this section we have seen that the spectra for the classes of events where there is no activity or there are only one or two particles in the the central detector coincide with the spectra from the QED processes of higher radiative Bhabha scattering and photon production in electron-positron annihilation.

This is an illustration of the fact that the BHLumi generator and the generator of Berends and Kleiss give sensible results in this region.

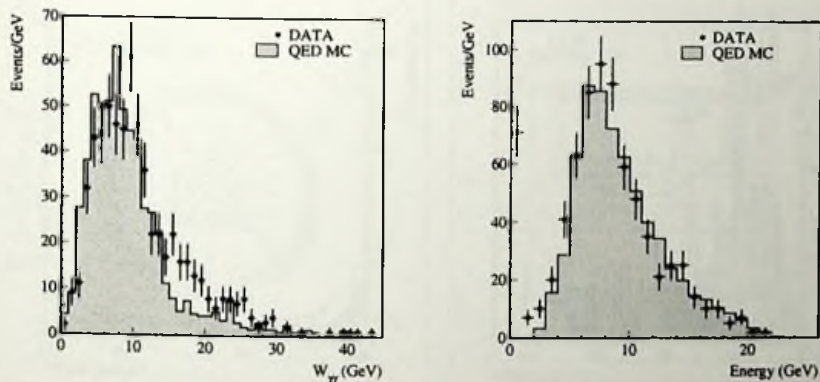


Figure 8.9: Comparison between data (dots) and Monte Carlo (histogram) for events with one charged track in the detector. In the left plot the $W_{\gamma\gamma}$ spectrum is given. In the right picture the energy spectrum of the charged particle is given. In both figures the Monte Carlo histogram is normalized to the LEP2 luminosity.

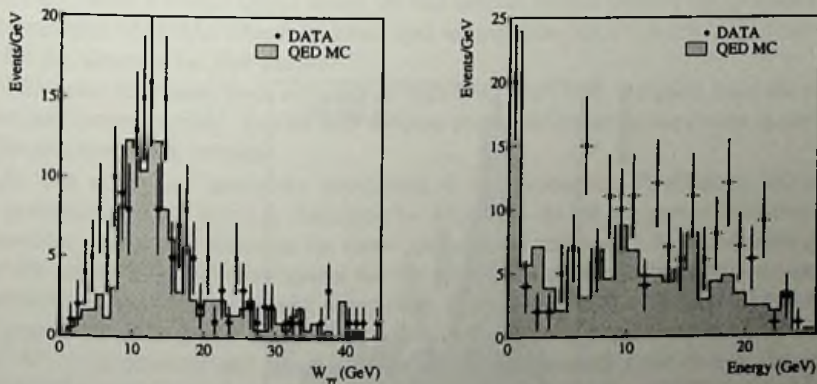


Figure 8.10: Comparison between data (dots) and Monte Carlo (histogram) for double-tag events with one additional photon in the detector. In the left plot the $W_{\gamma\gamma}$ spectrum is given. In the right picture the energy spectrum of the detected photon is given. In both figures the Monte Carlo histogram is normalized to the LEP2 luminosity.

Moreover, this observation allows us to look for cuts to remove these QED background processes. In the next section we will use information from the central part of the detector

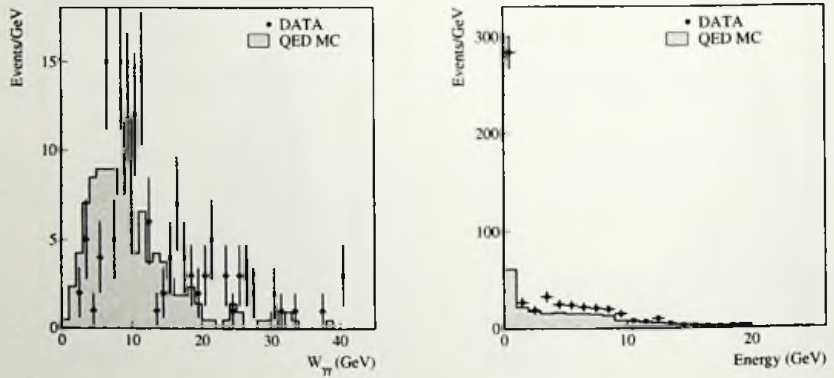


Figure 8.11: Comparison between data (dots) and Monte Carlo (histogram) for double tag events with two particles in the detector (see text). In the left plot the $W_{\gamma\gamma}$ spectrum is given. In the right picture the energy spectrum of the detected photon is given. In both figures the Monte Carlo histogram is normalized to the LEP2 luminosity.

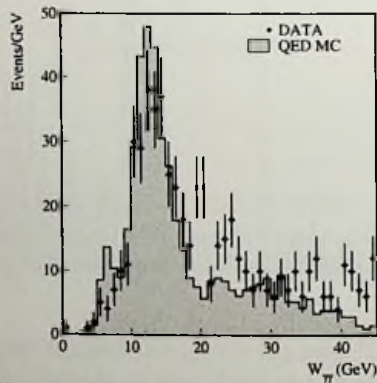


Figure 8.12: Comparison of the $W_{\gamma\gamma}$ spectrum between data (dots) and Monte Carlo (histogram) for double-tag events without any activity in the central part of the detector. Again, the Monte Carlo histogram has been normalized to the luminosity.

to do so.

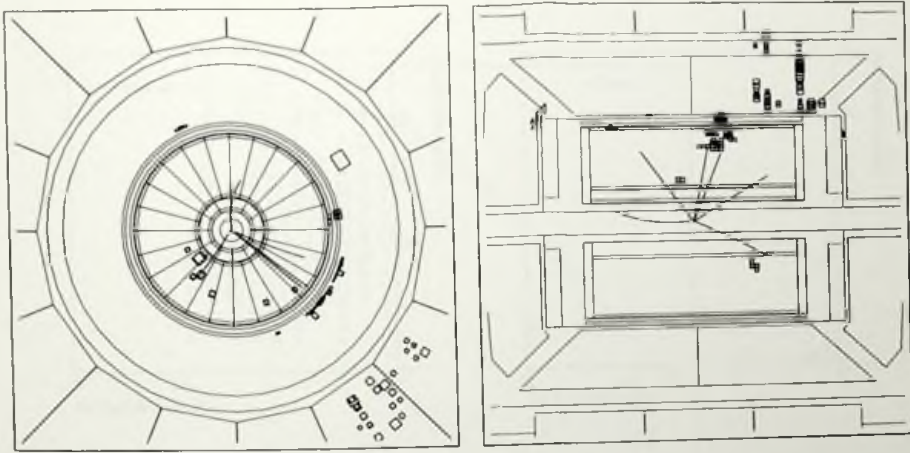


Figure 8.13: A typical example of the simulation of a generated η_b meson in the L3 detector. In the left plot the xy -view is given. In the right plot the xz -view is given.

8.5 Extended missing mass analysis

Additional information from the central detector would be useful to cut away background events and make stronger upper limits. In this section we will present the extended missing mass analysis (EMMA) where we have used information from the tracking detectors and the ECAL detector for this purpose.

All events that have been selected on fbsb-level have been stripped from the raw data tapes and reconstructed⁴. In this way we have obtained the set of the events in the PMMA in the standard data format.

At this point one needs the simulation of the production (GaGaRes) and decay of the resonances. This decay is described by JETSET. As we are partly searching for new resonances, the decay channels for these particles are unknown. In those cases JETSET uses the string fragmentation model for the simulation of the decay of the resonance. An illustration of the production and decay of an η_b resonance in the L3 detector can be found in figure 8.13. The heavy resonances typically decay to a large number of light hadrons (π 's, K 's, ...), photons and some leptons. If one puts enough trust in this decay model, this would suggest that the charged multiplicity and the photon multiplicity would be very efficient cuts to remove background events. This is illustrated in Figure 8.14. In this figure one can see that the data indeed strongly peaks for low multiplicities, the region of the QED backgrounds that have been discussed in the previous section.

Motivated by these plots we have requested the additional requirement that there are at least two photons and two charged tracks in the central detector. From figure 8.14 it follows that these additional cuts do not cost much efficiency. These cuts will also remove

⁴In selecting the fbsb-events that have been stripped we have used less strict cuts than those that were given in the PMMA in order to allow one to loosen the cuts in further analyses

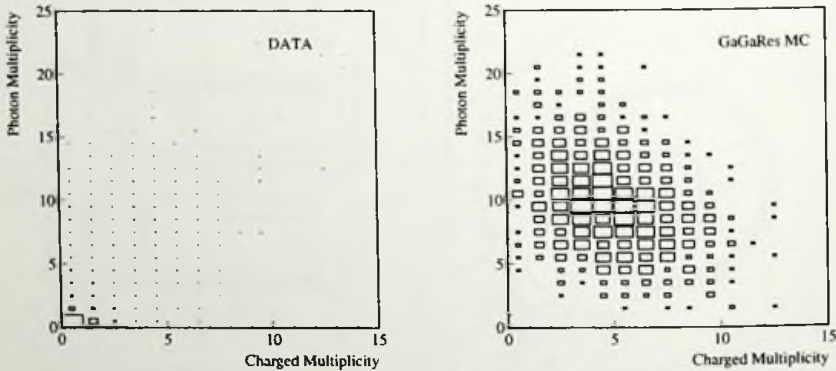


Figure 8.14: Comparison of the charged and photon multiplicities for data (left plot) and an η_b Monte Carlo simulation (right plot).

automatically those events without any activity in the central part of the detector, mostly Bhabha and off-momentum events. This allows one to release some of the cuts that were used in the PMMA. In the EMMA the following set of cuts have been used:

1. $29 \text{ mrad} < \theta_i < 80 \text{ mrad}$ ($i = 1, 2$),
2. $\max(E'_1, E'_2) < 1.01 E_b$,
3. $\min(E'_1, E'_2) > 0.75 E_b$,
4. $|\Delta\phi - 180| > 45^\circ$,
5. $N_{\text{photon}} \geq 2$,
6. $N_{\text{charged}} \geq 2$,
7. $|\phi_i - 90| > 5^\circ$, $|\phi_i - 270| > 5^\circ$, $i = 1, 2$,
8. $|y| > 0.1$,
9. $N_{\text{tag}} = 2$.

In this list N_{photon} is the number of photons in the central detector, whereas N_{charged} is the number of charged tracks in the central detector.

The plot for the efficiency as a function of $W_{\gamma\gamma}$ is given in figure 8.15. In comparison to the efficiency in the PMMA (figure 8.2) the efficiency does not show a big decrease at low invariant masses. This originates from the fact that cut 3 is less strict than the one in the PMMA.

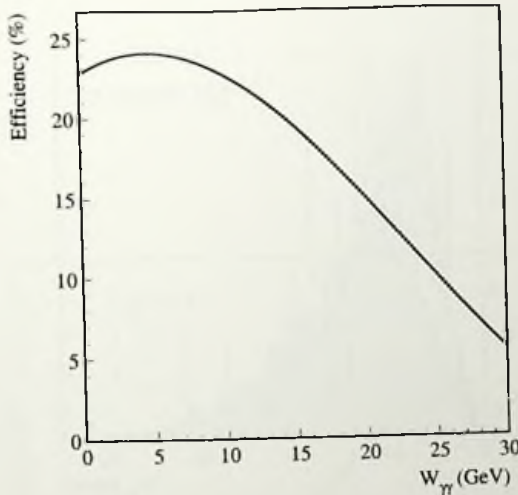


Figure 8.15: The efficiency as a function of $W_{\gamma\gamma}$ at $\sqrt{s} = 190$ GeV in the EMMA.

The invariant mass spectrum is given in figure 8.16. Again, the spectrum has been fit with a threshold function. The parameters for the threshold function read for the EMMA

$$t_1 = 39.184 \text{ GeV}^{-1}, \quad t_2 = 7.4146 \text{ GeV},$$

$$t_3 = 5.6829 \text{ GeV}, \quad t_4 = 1.3830 \text{ GeV}.$$

The results for the two-photon width and its upper limits are obtained in the same way as in section 8.3 and are given in figure 8.17. Especially for low values of $W_{\gamma\gamma}$ better upper limits are found in comparison to the PMMA. In particular, for the region of the η_b meson we find in the EMMA $\Gamma_{\gamma\gamma}^{95}(m_{\eta_b}) \approx 76$ keV, a considerable improvement on the TPC/Two-Gamma result of 400 keV [52, 53].

In the EMMA one requires significant activity in the central part of the detector. These extra requirements remove most background, which can be read off from the enormous drop of events in the missing mass spectrum. The events that survive the cuts are very likely two-photon events. To check this, we compare the $W_{\gamma\gamma}$ spectrum in the EMMA (figure 8.16) to the invariant mass spectrum generated by the PHOJET Monte Carlo generator [113], which uses the dual parton model (DPM) to describe the continuum hadron production in $\gamma\gamma$ collisions, but neglects single resonance production. The result is also included in figure 8.16, where the PHOJET results are normalized to the luminosity. For $W_{\gamma\gamma} > 10$ GeV PHOJET gives a good description of the $W_{\gamma\gamma}$ spectrum, indicating that most of the events in the spectrum are indeed coming from hadronic events, i.e. non-single-resonance events. At low $W_{\gamma\gamma}$ PHOJET seems to underestimate the number observed events. This could be

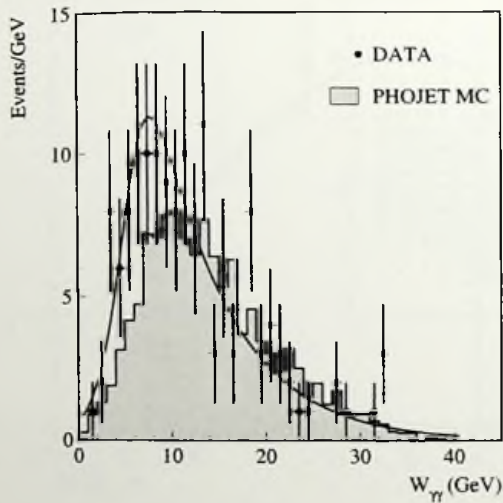


Figure 8.16: *Spectrum of the invariant mass $W_{\gamma\gamma}$ of the two-photon system for all LEP 2 data in the EMMA. The spectrum is fit with the threshold function. The filled histogram is the PHOJET Monte Carlo, normalized to the luminosity.*

caused by the fact that in the PHOJET generation only states with $W_{\gamma\gamma} > 3$ GeV have been generated. Due to resolution effects events in the data with an actual $W_{\gamma\gamma}$ below 3 GeV could be shifted to a higher reconstructed $W_{\gamma\gamma}$. The surplus could also be caused by processes that are not included in the PHOJET program.

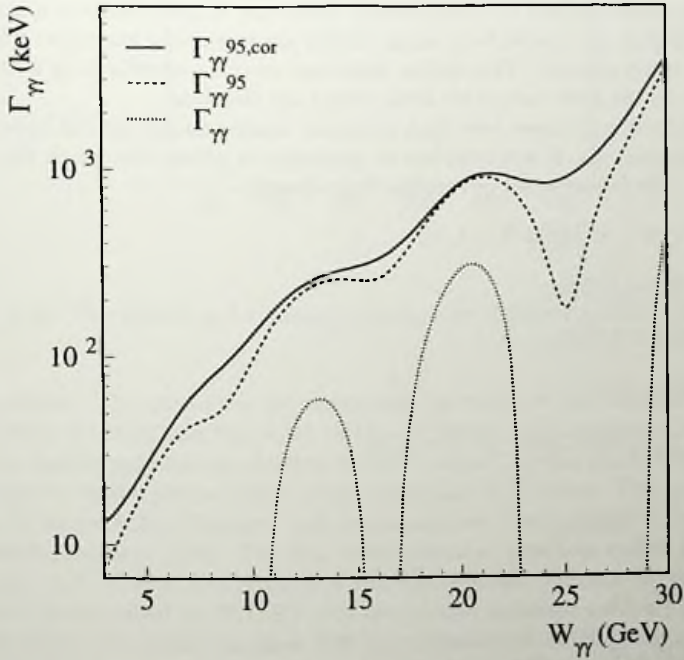


Figure 8.17: The two-photon width $\Gamma_{\gamma\gamma}(W_{\gamma\gamma})$ (dotted line), $\Gamma_{\gamma\gamma}^{95}(W_{\gamma\gamma})$ (dashed line) and $\Gamma_{\gamma\gamma}^{95,cor}(W_{\gamma\gamma})$ (continuous line) in the EMMA for all LEP 2 data.

8.6 Missing mass search at high $W_{\gamma\gamma}$

So far we have focussed on the production of resonances in the region $3 < W_{\gamma\gamma} < 30$ GeV. In principle it is however possible to create states up to an invariant mass $W_{\gamma\gamma} \approx 2E_b$. This search for particles at very high $W_{\gamma\gamma}$ is motivated by the possible first hints of the observation of the Higgs boson with a mass near 115 GeV at LEP [114, 115]. We will set an upper limit on the two-photon width of a Higgs boson at 115 GeV. In section 2.3 it has been discussed that the Standard Model Higgs boson does not couple directly to two photons and that the two-photon width is not expected to be large, of the order of keV.

As mentioned in section 8.2, the missing mass analysis uses Monte Carlo studies with a pseudoscalar meson coupled to two photons. Since the Higgs particle is a scalar boson we have verified that the results for a scalar meson are essentially the same. This is done using the 3P_0 matrix element. This similar behaviour can be understood by noting that in the limit $M \gg Q_i$ the form factors for both scalars are identical.

For the production of these very high invariant masses almost all the energy goes to the intermediate photons. It will therefore be necessary to release the cut on the minimum tagged energy. The following set of cuts has been chosen.

1. $29 \text{ mrad} < \theta_i < 80 \text{ mrad}$ ($i = 1, 2$),
2. $\max(E'_1, E'_2) < 1.05E_b$,
3. $\min(E'_1, E'_2) > 0.15E_b$,
4. $|\Delta\phi - 180| > 45^\circ$,
5. $|\phi_i - 90| > 5^\circ$, $|\phi_i - 270| > 5^\circ$ ($i = 1, 2$),
6. $N_{\text{photon}} \geq 2$,
7. $N_{\text{charged}} \geq 2$,
8. $E_{\text{ECAL}} \geq W_{\gamma\gamma}/3$,
9. $E_{\text{HCAL}} \geq W_{\gamma\gamma}/3$.

In this list of cuts E_{ECAL} and E_{HCAL} are the total energies observed in the ECAL, respectively the HCAL detector. There still is a cut on the energy of the the least energetic tag. This cut has been applied to suppress double radiative events with two low energetic photons.

The efficiency for Higgs production for this set of cuts as a function of $W_{\gamma\gamma}$ is given in figure 8.18. The shape of this plot can be qualitatively understood. At lower values for $W_{\gamma\gamma}$ the spectrum is suppressed by the required energy in the ECAL and HCAL (cuts 8 and 9). At high $W_{\gamma\gamma}$ the spectrum is suppressed by the cut on the least energetic tag (cut 3).

The data spectrum after this set of cuts is given in figure 8.19. The spectrum shows a peak around 91 GeV. Fitting the spectrum in the range $30 < W_{\gamma\gamma} < 150$ GeV with the sum of an exponential, a Gaussian function and constant, yields for the Gaussian a peak at 90.9 ± 1.4 GeV and a width of 2.1 ± 1.2 GeV. The peak corresponds to a number of

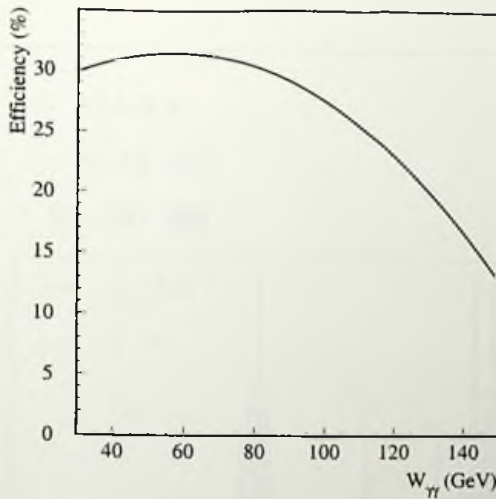


Figure 8.18: The efficiency for Higgs production for different values of $W_{\gamma\gamma} = M_H$.

5.2 ± 1.2 events. The values for the mean and the width of the Gaussian agree within the errors with the mass and the width of the Z^0 boson. This suggests that these events come from a double radiative production of the Z boson⁵. In this production process both incoming leptons emit a photon before annihilating into a Z^0 boson. This process has been illustrated in figure 8.20. To check this hypothesis, we have compared our results with the KK event generator [116]. The KK event generator produces events for the process $e^+e^- \rightarrow f\bar{f} + n\gamma$, $f = \mu, \tau, d, u, s, c, b$ in the Electroweak Standard Model. The quark hadronization is described by JETSET. For two-photon radiation an exact matrix element has been included. The result obtained with the generation of 500,000 events, normalized to the luminosity, has also been given in figure 8.19. In figure 8.19 also the results of PHOJET have been included. Again, the PHOJET output is normalized to the luminosity.

We will end this chapter with scanning over the $W_{\gamma\gamma}$ spectrum in the range 100-150 GeV to set upper limits on the two-photon widths of states in this region. Inserting the results for the cross section, the resolution and the data spectrum results in a spectrum for the upper limits as given in figure 8.21. In particular, for $W_{\gamma\gamma} = 115$ GeV we find a 95% C.L. upper limit of $\Gamma_{\gamma\gamma}^{95,cor} = 137$ MeV.

⁵In the terminology of the LEP physicists, "a double radiative return to the Z ".

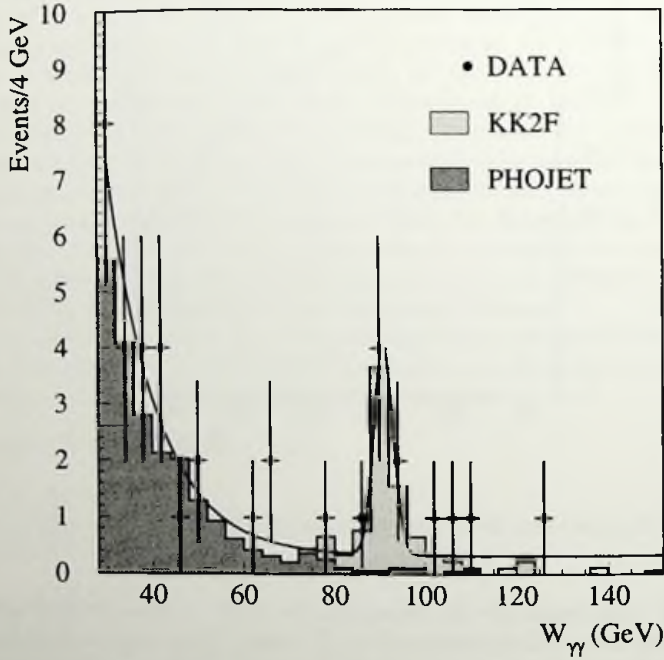


Figure 8.19: The $W_{\gamma\gamma}$ spectrum for LEP2 (dots) and the results of the fit (continuous line). The filled histograms represent the results of the KK and PHOJET generators which have been normalized to the luminosity and give therefore an absolute prediction.

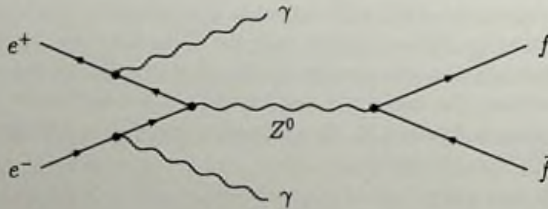


Figure 8.20: The double radiative production of a Z^0 boson in e^+e^- annihilation, where the Z^0 boson decays into two fermions.

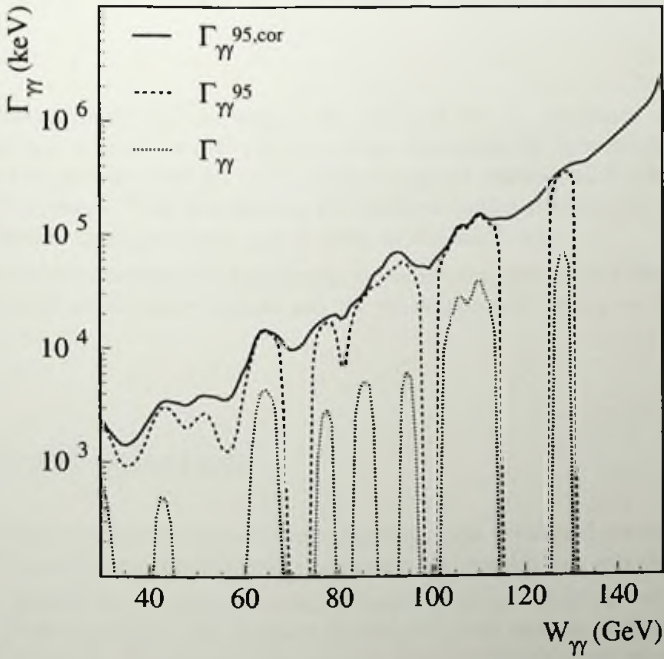


Figure 8.21: The two-photon width $\Gamma_{\gamma\gamma}(W_{\gamma\gamma})$ (dotted line), $\Gamma_{\gamma\gamma}^{95}(W_{\gamma\gamma})$ (dashed line) and $\Gamma_{\gamma\gamma}^{95,cor}(W_{\gamma\gamma})$ for all LEP 2 data.

Chapter 9

The $\chi_{c2} \rightarrow \gamma J/\psi$ decay distribution

The two-photon production as well as the decay of the χ_{c2} resonance are studied. The decay mode $\chi_{c2} \rightarrow J/\psi \gamma \rightarrow l^+ l^- \gamma$ ($l = e, \mu$) has been used for these studies. The analysis results in a two-photon width for the χ_{c2} and an angular distribution for the decay products of the χ_{c2} resonance. This distribution is compared to the distributions predicted by the GaGaRes Monte Carlo generator and a decay model amplitude.

To check the corrections to the energy measurement, also a brief section on the two-photon production of the η' meson and its decay mode $\eta' \rightarrow \rho \gamma \rightarrow \pi^+ \pi^- \gamma$ has been included.

9.1 Event selection

As we are looking for the decays of a resonance into a pair of charged particles and a photon, events with exactly two charged tracks and one additional photon are selected.

In this analysis we require the charged tracks to give a hit in at least 18 TEC wires. The span of the track, i.e. the distance between the first and the last hit, is required to be at least 15 wires. As a result, the angular region in which these requirements can be satisfied is limited to $22^\circ < \theta < 158^\circ$. The distance of closest approach (DCA) of the track to the beam line is required to be less than 3 mm. The transverse momentum, p_T , of the track is required to be in the range $0.05 < p_T < 15$ GeV. The two tracks are required to be oppositely charged.

Photon candidates are bumps in the ECAL detector which are required to give a measured energy deposition of at least 100 MeV. They should not be matched with a track in the TEC. A neural network must separate the photons from signals caused by other processes as electronic noise and energy deposition by hadronic particles. This neural net mainly looks at the energy distribution of the bump over the crystals, which is in the case of photons more localized than for hadronic particles.

In the analyses presented in this chapter the selected events were, besides possible tags in the LUMI and the VSAT, not allowed to have additional activity in the detector.

9.2 Production and decay of the η'

One of the possible decay channels for the η' resonance is $\eta' \rightarrow \rho^0 \gamma \rightarrow \pi^+ \pi^- \gamma$. The branching ratio, $\text{Br}(\eta' \rightarrow \pi^+ \pi^- \gamma)$ for this decay channel is $29.5 \pm 1.0\%$ [13].

It is useful to study this channel as it can serve as a cross check for the calibrations and the energy corrections that have been applied. In particular, the corrections for the non-linearity of the low energetic photons are important because the determination of the two-photon width of the χ_{c2} resonance strongly depends on the resolution of the photon energy as will be discussed in the next section.

For the analysis of the η' meson we do require some additional cuts:

- The photons are required to end up in the barrel region of the ECAL, $|\cos \theta_\gamma| < 0.76$, where θ_γ is the polar angle of the outgoing photon in the lab-frame. The minimum allowed energy of the photon has been set to 140 MeV.
- To eliminate those radiative events where the photon is emitted from the pions, the angle between the photons and the charged tracks must be sufficiently large, $|\cos(\angle(\pi^\pm, \gamma))| < 0.95$, where the angles are calculated in the rest frame of the ρ^0 particle.
- The events were required to be transversely balanced: $|\vec{p}_T(\pi^+ \pi^- \gamma)|^2 < 0.01 \text{ GeV}^2$ for the untagged events and $|\vec{p}_T(e^\pm \pi^+ \pi^- \gamma)|^2 < 0.01 \text{ GeV}^2$ for the single-tag events. In addition, for the pions a minimum transverse momentum was required: $|\vec{p}_T(\pi^+ \pi^-)|^2 > 0.001 \text{ GeV}^2$.

In figure 9.1 the invariant mass spectrum of the sum of the four-momenta of the two tracks and the photon is given. A clear signal in the region of the η' meson is observed. There is also an enhancement around 1230 MeV, which is coming from the a_2 resonance. One of the decay channels of this resonance is $a_2 \rightarrow \rho^0 \pi \rightarrow \pi^+ \pi^- \pi^0 \rightarrow \pi^+ \pi^- \gamma \gamma$. When one of the photons escapes detection one has the same topology as that of the η' decay under study. This also explains why the peak of this spectrum is below the mass of the a_2 resonance. The spectrum in figure 9.1 has been fitted by the sum of a second order polynomial and two Gaussians, one for the η' signal and one for the a_2 resonance, with a rest mass of 1.32 GeV. The best fit gives for the Gaussian describing the η' resonance

$$\begin{aligned}
 M &= 955.7 \pm 0.8 \text{ MeV}, \\
 \sigma &= 24.1 \pm 0.3 \text{ MeV}, \\
 N_{\eta'} &= 8262 \pm 37.3,
 \end{aligned} \tag{9.1}$$

where M is the mass of the η' meson, σ is the width of the Gaussian and $N_{\eta'}$ is the number of events under the Gaussian. The observed mass is in reasonable agreement with the previously measured values, $m_{\eta'} = 957.78 \pm 0.14 \text{ MeV}$ [13], which gives us confidence in the determination of the measured energies. In figure 9.1 also a signal region and two sideband regions are indicated. These will be used later in this section in the determination of the angular distribution of the outgoing photon.

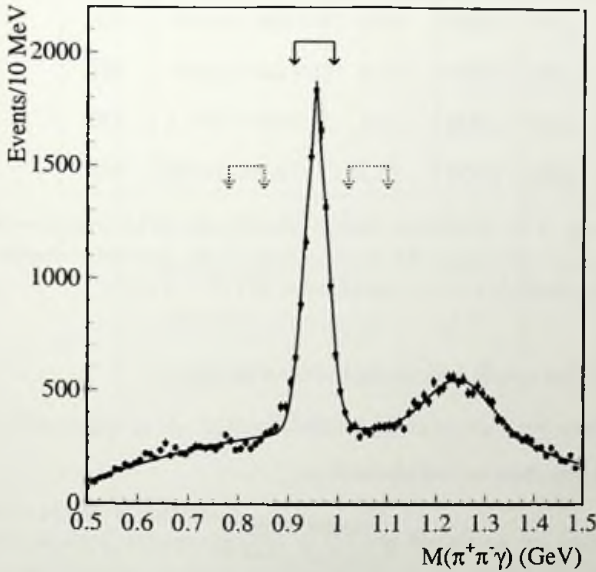


Figure 9.1: The $\pi^+\pi^-\gamma$ mass spectrum. The spectrum has been fitted with the sum of a second order polynomial and two Gaussians. The solid arrows indicate the signal region, the dotted arrows the sideband regions.

From the number of events in the η' signal we can easily perform a rough calculation of the two-photon width of the η' resonance. For each LEP2 year 9,000 events have been generated with the GaGaRes Monte Carlo generator. In the generation of events, also the decay of the η' into a ρ^0 and a photon and the subsequent decay of the ρ^0 meson into two charged pions have been simulated. In both decays the outgoing particles were in first instance uniformly distributed. The η' meson, being a pseudoscalar, is indeed supposed to have a uniform distribution. However, in the decay of the ρ^0 meson into the two charged pions, there is an angular dependence in the distribution of the outgoing particles. In fact, the coupling of two spin-1 particles to a pseudoscalar particle is represented by a matrix element

$$\mathcal{M} \sim \epsilon^{\mu\nu\alpha\beta} \epsilon_\mu^\gamma k_\nu^\gamma \epsilon_\alpha^{\rho^0} p_\beta^{\rho^0} \sim \epsilon^{\mu\nu\alpha\beta} \epsilon_\mu^\gamma k_\nu^\gamma p_\alpha^{\pi^+} p_\beta^{\pi^-}, \quad (9.2)$$

where the polarization vector of the ρ^0 and its momentum have been replaced by the pion current $p_\alpha^{\pi^+} - p_\beta^{\pi^-}$ and the sum of the pion-momenta $p_\alpha^{\pi^+} + p_\beta^{\pi^-}$. This leads to

$$|\mathcal{M}|^2 \sim \sin^2 \theta^*, \quad (9.3)$$

where θ^* is the angle between the outgoing photon and the π^+ in the rest frame of the ρ^0

year	N_{gen}	ε_{trig} (%)	ε_{sel} (%)	E_b	σ (nb)
1997	9,000	32.0	4.8	95	867
1998	9,000	37.4	4.2	95	867
1999	9,000	16.3	4.1	97.5	876
2000	9,000	23.7	4.1	102	898

Table 9.1: *The results of the event simulation. The number of generated events, the trigger efficiency, the selection efficiency, the beam energy of the generated events and the cross section calculated by GaGaRes for an input value of $\Gamma_{\gamma\gamma} = 1$ keV.*

meson. Accordingly the events are reweighted by a factor

$$f_{\eta'} = \sin^2 \theta^*. \quad (9.4)$$

The efficiency ε can then be calculated from

$$\varepsilon = \frac{\sum_{\text{selected events}} f_{\eta'}}{\sum_{\text{generated events}} f_{\eta'}}. \quad (9.5)$$

The efficiencies for the different LEP2 years together with the other results of the Monte Carlo generation are given in table 9.1. In the simulation also a trigger simulation has been performed to obtain the level-1 trigger efficiency. The level-1 trigger efficiency is calculated by dividing the number of selected Monte Carlo events after the level-1 trigger simulation by the number of selected Monte Carlo events in the absence of a trigger simulation. The level-1 trigger is dominated by the TEC triggers. The level-2 and level-3 trigger efficiencies are taken from [117], where the trigger efficiencies have been determined from a sample of events with two charged tracks and two photons. The efficiency due to the selection cuts is denoted by ε_{sel} . The total trigger efficiency is denoted by ε_{trig} .

The experimental cross section, σ_{exp} , for the two-photon production of the η' that subsequently decays into a charged pion pair and a photon is now given by

$$\sigma_{exp} = \frac{N_{\eta'}}{\text{Br}(\eta' \rightarrow \pi^+\pi^-\gamma)\varepsilon_{\eta'}\mathcal{L}} \quad (9.6)$$

The variable $\varepsilon_{\eta'}$ is the product of the trigger efficiency and the selection efficiency. As has been demonstrated in section 2.7, the cross section for resonance production in two-photon reactions is proportional to the two-photon width of the resonance. This allows us to calculate the two-photon width of the η' , $\Gamma_{\gamma\gamma}(\eta')$, in the following way

$$\Gamma_{\gamma\gamma}(\eta') = \Gamma_{\gamma\gamma}^{MC}(\eta') \left(\frac{\sigma_{exp}}{\sigma_{MC}} \right). \quad (9.7)$$

This results in a two-photon width for the η' meson of

$$\Gamma_{\gamma\gamma}(\eta') = 4.46 \pm 0.02 \text{ keV}, \quad (9.8)$$

Error Source	$\Delta\Gamma_{\gamma\gamma}/\Gamma_{\gamma\gamma}$
Trigger efficiency	15 %
Branching ratio	3.4 %
Cut on E_γ	5.0 %
Cut on $ \vec{p}_T(\pi^+\pi^-\gamma) ^2$	2.0 %
Cut on $ \cos(\angle(\gamma, \pi^\pm)) $	3.0 %
Cut on $ \vec{p}_T(\pi^+\pi^-) ^2$	1.0 %
Background subtraction	4.5 %
Total systematic error	17.2 %

Table 9.2: Summary of the different contributions to the total systematic error.

where the error is purely statistical.

In figure 9.2 graphical representations of the cut variations are given. In table 9.2 an overview of all contributions to the systematic error on the two-photon width is given. The dominant error comes from the trigger efficiency. The error on the trigger efficiency is large due to the low p_T^2 of the two charged tracks. The error has safely been set to 15%. The error from the background is determined by varying the background function within the errors from the fit and see how the number of observed η' events varies. The largest deviation from the measured two-photon width is 4.3 %. The error is set to 4.5 %. All the errors are added in quadrature, resulting in a total systematical error of 17.2 %. This yields for the two-photon width

$$\Gamma_{\gamma\gamma}(\eta') = 4.46 \pm 0.02(\text{stat.}) \pm 0.77(\text{sys.}) \text{ keV}, \quad (9.9)$$

which is in good agreement with the results found in literature, $\Gamma_{\gamma\gamma}(\eta') = 4.29 \pm 0.15$ keV [13].

It should be noted that this is not the optimal determination of the two-photon width of the η' . In [57] it is argued that in the matrix element corrections have to be applied for non-resonant contributions in the process $\eta' \rightarrow \pi^+\pi^-\gamma$. Moreover, in the simulation for the decays we have also taken all particles, including the ρ^0 meson, on their mass shell.

One could also look at the distribution of the polar angle of the photon, θ_γ , in the rest frame of the η' meson, where the z -axis is given by the direction of the boost from the lab-frame to the rest frame of the η' . We will study the $\cos\theta_\gamma$ in the signal region $0.91 < M_{\pi^+\pi^-\gamma} < 0.99$ GeV. The background below the η' signal has been subtracted by considering the spectrum of the sidebands, I : $0.84 < M_{\pi^+\pi^-\gamma} < 0.89$ GeV and II : $1.02 < M_{\pi^+\pi^-\gamma} < 1.1$ GeV. The two sideband spectra are added and normalized to the number of background events in the signal region. This is illustrated in figure 9.3. The signal region and the sideband regions are indicated in figure 9.1. In figure 9.4 the $\cos\theta_\gamma$ distribution in the signal region after background subtraction is given. In this figure the distribution is

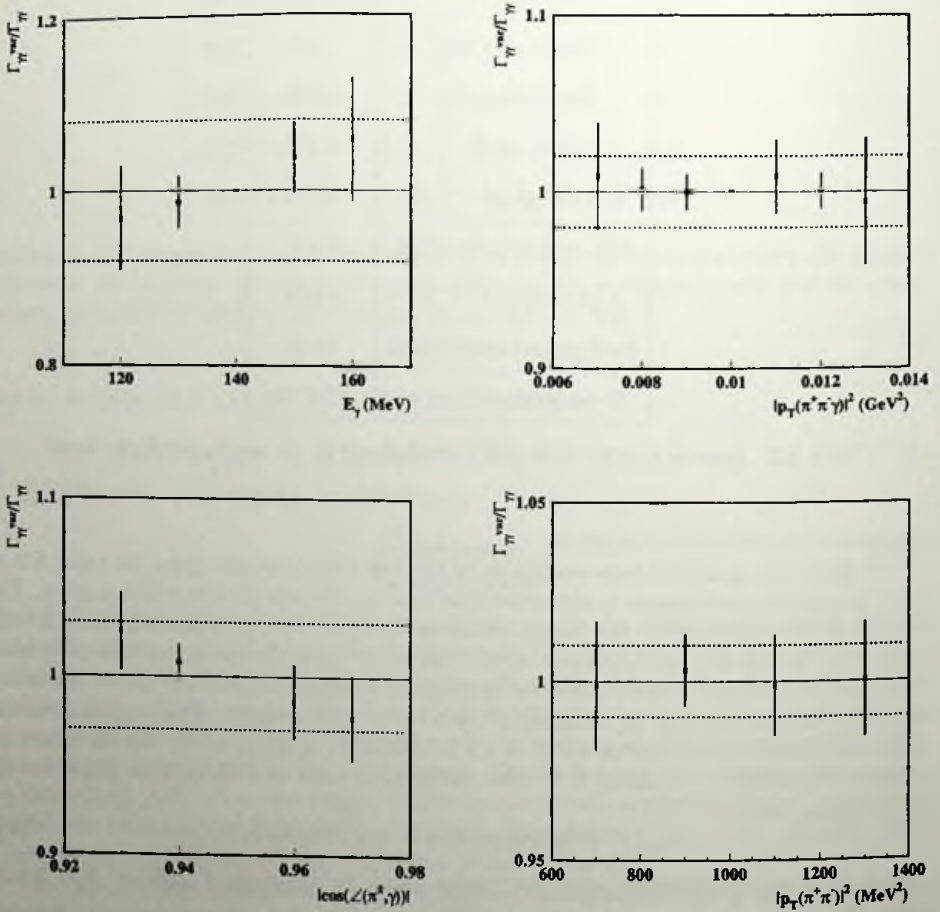


Figure 9.2: The variation of $\Gamma_{\gamma\gamma}$ due to variations of the cut on E_γ , $|\vec{p}_T(\pi^+\pi^-\gamma)|^2$, $|\cos(\angle(\pi^\pm, \gamma))|$ and $|\vec{p}_T(\pi^+\pi^-)|^2$. The dashed lines show the errors that are assigned to the cuts. The dotted line indicates the central value of our measurement.

compared to the distribution of 40,000 events that have been generated with the GaGaRes Monte Carlo generator. For the two distributions we calculate the χ^2

$$\chi^2 = \sum_{\text{bins}} \frac{(N_{\text{exp},i} - N_{\text{MC},i})^2}{\sigma_{\text{exp},i}^2 + \sigma_{\text{MC},i}^2}. \quad (9.10)$$

This gives for the distributions a χ^2/dof of 18.96/19. This corresponds to a confidence level of 46.0 %. The confidence level is better than one would expect from a first view on

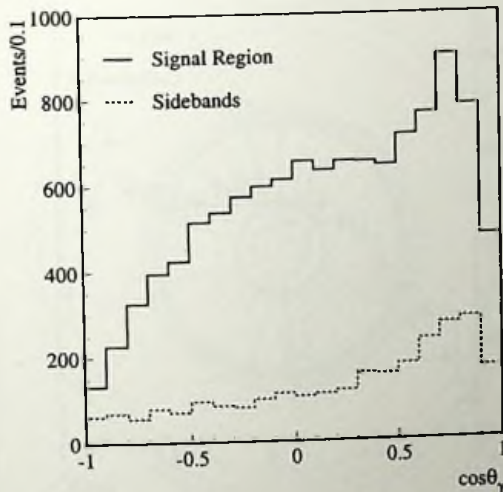


Figure 9.3: The distribution of $\cos \theta_\gamma$ for data the signal region (continuous) line and the sidebands (dashed) line. The histogram for the sidebands has been normalized to the number of background events in the signal region.

figure 9.4. This is due to the small sample of Monte Carlo events. As a consequence, the statistical error on these Monte Carlo events is of the same order as the error on the data points.

As mentioned before, one expects the distribution in figure 9.4 to be uniform. However, from the figure it follows that due to detector acceptance most of the outgoing photons have a polar angle in the rest frame of the η' in the range $0 < \theta_\gamma < \frac{\pi}{2}$, which we will call the forward region. The produced η' meson is in the lab-frame in most cases strongly defined along the beam direction. If the ρ^0 meson would be produced in the previously defined forward region it will be strongly boosted along the direction of the η' and so will its decay products, the charged pions. As a consequence, the opening angle between the outgoing pions will be small, which can cause difficulties to assign two separate tracks in the TEC. So there will be fewer forward $\pi^+\pi^-$ events, i.e. fewer backward γ events. Also in the very forward direction of the outgoing photon (the most right bin in figure 9.4) fewer events are observed. This is due to a similar effect. In this case the photon is emitted almost parallel to the η' and thus in most cases almost parallel to the beam pipe. As a consequence, the photon escapes detection in the ECAL.

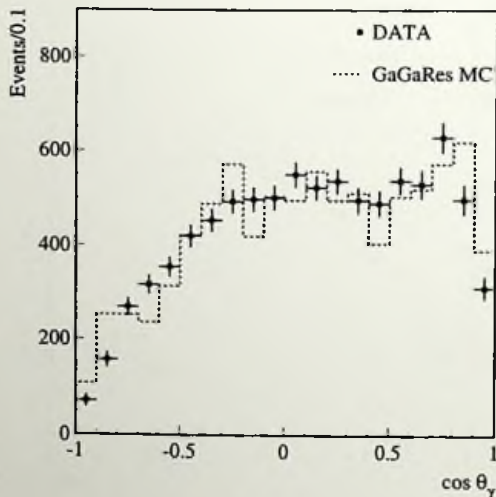


Figure 9.4: The distributions of $\cos \theta_\gamma$ for the signal region after background subtraction and for the Monte Carlo events. The latter results are scaled to the number of events in the η' signal.

9.3 The two-photon width of the χ_{c2}

The above analysis of the η' showed in particular that the observed peak was at the correct mass, giving us confidence in the measured energies. We will now focus on a similar decay: $\chi_{c2} \rightarrow J/\psi \gamma \rightarrow l^+ l^- \gamma$ ($l = e, \mu$). The branching ratio for this channel is $1.59 \pm 0.13\%$ [13]. The contributions from the $e^+ e^- \gamma$ and $\mu^+ \mu^- \gamma$ final states are almost equal. In figure 9.5 an example of a typical χ_{c2} decay into two electrons and a photon is given.

In the analysis we want to identify the charged tracks as either two electron tracks or two muon tracks. The energy of the leptons coming from the decay of the J/ψ is not very high, Monte Carlo simulations show that it is typically of the order of 1.0-2.5 GeV. An electron with an energy of this order of magnitude deposits all its energy in the ECAL detector. Therefore, we require that the measured energy E in the ECAL for the bump that has been matched to the track is for electrons close to the measured momentum p of the track. One of the electrons must satisfy $0.9 < E/p < 1.1$, whereas the second electron must satisfy the less strict condition $0.7 < E/p < 1.3$.

Muons in this energy range do not reach the muon chambers. In the ECAL these muons give a MIP signal. For the muons the maximum allowed energy of the ECAL bump matched to the track has been set to 0.45 GeV. At least one of the tracks is required to have an associated bump in the ECAL detector. It should be noted that this cut does not remove charged pions from the sample. They usually also leave a MIP signal in the ECAL.

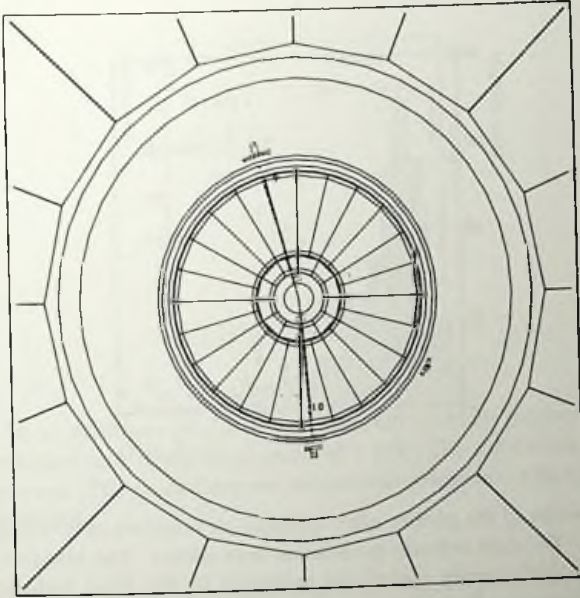


Figure 9.5: A typical example of a χ_{c2} resonance decaying into an electron-positron pair and a photon. In the figure the hits in the SMD and the tracks in the inner and outer TEC are visible, together with the three bumps in the ECAL detector. All particles were detected in the barrel region.

From energy-momentum conservation¹ it follows that in the rest frame of the χ_{c2} the photon in the decay $\chi_{c2} \rightarrow \gamma J/\psi$ has an energy of 0.429 GeV. Monte Carlo studies show that in the lab-frame the photon energy typically peaks at an energy of 0.46 GeV. The energy spectrum of the photons in the data sample, which contains both the χ_{c2} signal and a substantial background, is steeply falling. This has been illustrated in figure 9.6. The photons are required to have a minimum energy of 0.3 GeV, this selection criterium has also been indicated in the figure.

The photon is required not to be too close to either of the two tracks. This condition is fulfilled by the requirement that the angle between the photon and each of the two tracks is greater than 16° in the rest frame of the χ_{c2} . This avoids overlapping bumps in the ECAL. In addition, this cut rejects events from the process $e^+e^- \rightarrow e^+e^-l^+l^-\gamma$ ($l = e, \mu$), where the lepton pair is not produced in the decay of a J/ψ .

We require events in which all particles of the final state of the χ_{c2} resonance are detected. To exclude events not satisfying this condition, the square of the sum of the

¹For the decay $A \rightarrow BC$, where C is a massless particle, the energy of this massless particle is given in the rest frame of particle A by

$$E_C = \frac{M_A^2 - M_B^2}{2M_A} \quad (9.11)$$

where M_A and M_B are the masses of the particles A and B .

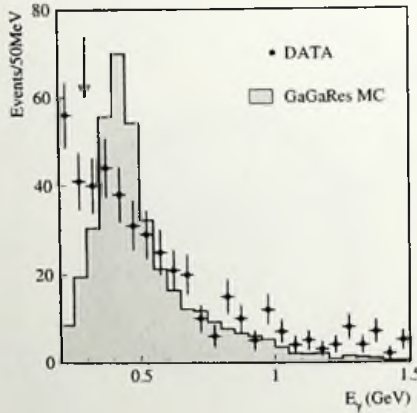


Figure 9.6: The energy of the photon after applying all selection cuts, except for the cut on the photon energy. The dots indicate the selected data events. The Monte Carlo predictions for χ_{c2} production (arbitrarily scaled) are indicated by the filled histogram. The arrow indicates the minimum required photon energy in this analysis.

transverse momenta of the final state particles, $(\sum \vec{p}_T)^2$, is required to be small, $(\sum \vec{p}_T)^2 < 0.08 \text{ GeV}^2$. For tagged events the transverse momentum of the tagged lepton is included in the sum. For tags in the LUMI we have the same requirement on $(\sum \vec{p}_T)^2$. For hits in the VSAT the cut is loosened to $(\sum \vec{p}_T)^2 < 0.10 \text{ GeV}^2$. If the square of the sum is larger when the transverse momentum of the tagged lepton is included than without the inclusion of the tag, the event is considered to be an untagged event.

The last cut is on the invariant mass M_{l+l-} of the lepton pair. This invariant mass is required not to differ too much from the mass of the J/ψ , $|M_{l+l-} - M_{J/\psi}| < 0.1 \text{ GeV}$, which is the signal region. In figure 9.7 the M_{l+l-} spectrum has been plotted. In the figure also the sidebands are indicated, which will be used in the study of the background.

Instead of plotting the mass spectrum of the invariant mass, $M_{l+l-\gamma}$, of all final state particles the mass spectrum of $\Delta M = M_{l+l-\gamma} - M_{l+l-}$ is plotted. The ΔM distribution is narrower than the $M_{l+l-\gamma}$ spectrum. The ΔM spectrum mainly depends on the resolution of the photon energy, which is better determined than the resolution of the the combination of the tracks and the photon². The resulting ΔM spectrum for LEP2 events satisfying the selection criteria is shown in figure 9.8.

For the simulation of the production and decay we have used the GaGaRes Monte Carlo generator. For both the $e^+e^-\gamma$ and $\mu^+\mu^-\gamma$ final states we have generated for every year 8,000 events. The results of the Monte Carlo generation are summarized in table 9.3. In

²Also the variable $\Delta\tilde{M} = \sqrt{M_{l+l-\gamma}^2 - M_{l+l-}^2}$ has been considered, but the ΔM spectrum is more convenient than the $\Delta\tilde{M}$ spectrum, as the peak for the χ_{c2} resonance is narrower in the ΔM spectrum.

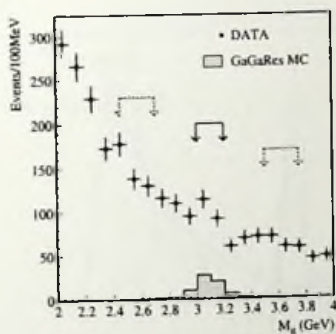


Figure 9.7: The M_{l+l-} spectrum for LEP2 data after all selection requirements. The Monte Carlo results are scaled to a two-photon width of 1 keV. The solid arrows indicate the cut on the M_{l+l-} spectrum. The dashed arrows indicate the sidebands, which will be used in the study of the background.

year	N_{gen}	ϵ_{trig} (%)	ϵ_{sel} (%)	E_b	σ (pb)
1997	16,000	8.5	84	95	60.7
1998	16,000	8.0	88	95	60.7
1999	16,000	8.6	84	97.5	61.4
2000	16,000	7.9	89	102	62.9

Table 9.3: The results of the event simulation. The number of generated events, the trigger efficiency, the selection efficiency, the beam energy of the generated events and the cross section calculated by GaGaRes for an input value of $\Gamma_{\gamma\gamma}(\chi_{c2}) = 1$ keV.

the efficiency due to the selection criteria we have combined the results of both final states. Due to the different selection criteria, the selection efficiency for the $\mu^+\mu^-\gamma$ is 35 % higher than the one for the $e^+e^-\gamma$ final state. The table also includes the efficiencies due to the selection cuts. The level-1 trigger is again determined by dividing the number of selected events when the trigger simulation is included, by the number of selected events when no trigger simulation is done. The level-2 and -3 trigger efficiencies were taken from [117] and [59]. The trigger efficiencies are considerably higher compared to the η' analysis, due to the higher momenta of the outgoing particles. In figure 9.8 the results of the Monte Carlo simulation, normalized to the luminosity, have been included.

The ΔM spectrum in figure 9.8 has been used to determine the two-photon width of the χ_{c2} resonance. This requires a description of the background spectrum. A threshold

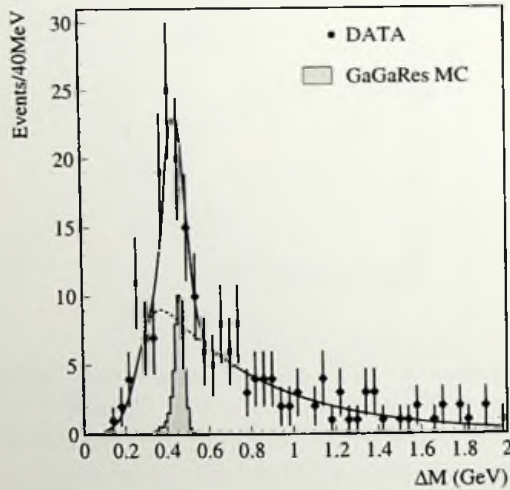


Figure 9.8: The $\Delta M = M_{l+l-\gamma} - M_{l+l-}$ spectrum for LEP2 data in the signal region after all selection requirements. The Monte Carlo results are scaled to a two-photon width of 1 keV and normalized to the luminosity. The bin size of the Monte Carlo predictions is three times smaller.

function is used to describe the background. The shape of the threshold function is fixed by the ΔM spectrum of the the sidebands in the M_{l+l-} spectrum. The sidebands are defined by $0.4 < |M_{l+l-} - M_{J/\psi}| < 0.65$ GeV. The ΔM spectrum of the sidebands and the best fit with the threshold function are given in figure 9.9. The ΔM spectrum of the signal region in figure 9.8 is fitted with the sum of this threshold function, where the scale has to be determined, and an additional Gaussian for the χ_{c2} signal. The dotted line gives the threshold function below the resonance, the solid line the sum of the threshold function and the Gaussian. The best fit in figure 9.8 corresponds to a total number of 45.4 ± 14.3 observed χ_{c2} events. Using equations similar to (9.6) and (9.7) this number can be transformed into a value for the two-photon width of the χ_{c2} resonance

$$\Gamma_{\gamma\gamma}(\chi_{c2}) = 0.97 \pm 0.31 \text{ keV}, \quad (9.12)$$

where the error is purely statistical. The systematic errors are discussed below.

The error on the branching ratio of the χ_{c2} resonance into $l^+l^-\gamma$ is 8.3 % [13].

The errors on the trigger efficiency, which are dominated by the outer TEC trigger efficiency, are safely set to 10%.

The errors from the required number of hits in the TEC and the photon selection are taken from [59] and set to 6 % and 2% respectively.

The errors due to the selection criteria are again estimated by slightly varying the cuts

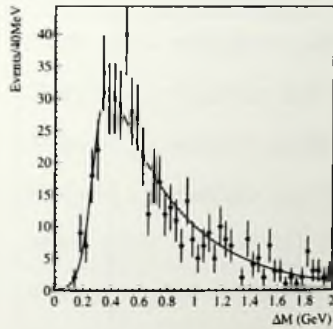


Figure 9.9: The $\Delta M = M_{l+l-\gamma} - M_{l+l-}$ spectrum for LEP2 data of the selected sideband events. The continuous line represents the best fit of the threshold function.

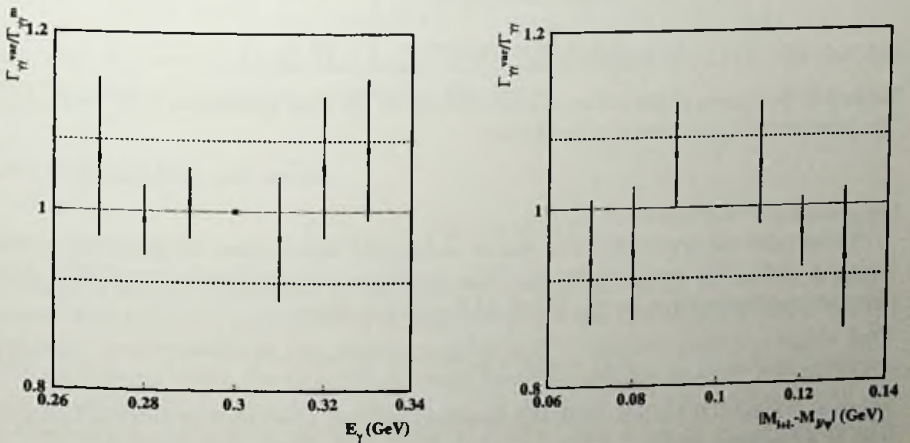


Figure 9.10: The variation of $\Gamma_{\gamma\gamma}$ due to variations on the cut of E_γ and $|M_{l+l-\gamma} - M_{J/\psi}|$. The dashed lines show the errors that are assigned to the cuts. The dotted line shows the measured value.

and by observing how that influences the measured value of the two-photon width. For the cut on the photon energy and the mass window of the M_{l+l-} spectrum, this is illustrated in figure 9.10. These two variations result in a systematic error of 8 % for both selection requirements. For the variation of the minimum required angle between the photon and the two leptons in the χ_{c2} rest frame we find in a similar way a systematic error of 4 %.

The error due to the criteria to select the two charged tracks as either two electrons or

Error Source	$\Delta\Gamma_{\gamma\gamma}/\Gamma_{\gamma\gamma}$
Branching ratio	8.3 %
Cut on N_{hits}	6 %
Photon Selection	2 %
Trigger efficiency	10 %
Cut on E_γ	8 %
Cut on $ M_{l^+l^-} - M_{J/\psi} $	8 %
Cut on $ \cos(\angle(\gamma, l^\pm)) $	4 %
e^+e^- and $\mu^+\mu^-$ selection	10 %
Background subtraction	7 %
Monte Carlo statistics	1 %
Total systematic error	22 %

Table 9.4: Summary of the different contributions to the total systematic error on $\Gamma_{\gamma\gamma}(\chi_{c2})$. The contributions are added in quadrature.

two muons has been set to 10 %.

To estimate the systematic error due to background subtraction, the threshold function is varied within the errors of the fit. This results in a largest deviation of 7%. Also a different parametrization for the threshold function is chosen.

$$\tilde{T}(x) = a_1(x - a_2)^{a_3} e^{(a_4(x - a_2) + a_5(x - a_2)^2)}, \quad (9.13)$$

where a_2 is fixed at 0.15 GeV. With this threshold function a two-photon width of $\Gamma_{\gamma\gamma}(\chi_{c2}) = 0.98$ keV has been found.

The finite Monte Carlo statistics result in a systematic error of 1 %.

As we have included in the GaGaRes Monte Carlo generator the complete density matrices for the production and decay of the resonance, which in addition contained the complete Q_i dependence, no errors due to neglected helicity contributions, ad hoc form factors and neglected terms in the cross section have to be introduced.

All contributions to the systematic error on $\Gamma_{\gamma\gamma}(\chi_{c2})$ have been summarized in table 9.4. The errors are added in quadrature, which results in a total systematic error of 22%. This yields for the two-photon width

$$\Gamma_{\gamma\gamma}(\chi_{c2}) = 0.97 \pm 0.31(\text{stat.}) \pm 0.21(\text{sys.}) \text{ keV}. \quad (9.14)$$

This value should be compared to the world average [13], combined with the more recent

Experiment	Production Mechanism	$\Gamma_{\gamma\gamma}(\chi_{c2})$ keV
L3 [49]	$\gamma\gamma \rightarrow \chi_{c2} \rightarrow J/\psi\gamma$	$1.02 \pm 0.40 \pm 0.17$
OPAL [50]	$\gamma\gamma \rightarrow \chi_{c2} \rightarrow J/\psi\gamma$	$1.76 \pm 0.47 \pm 0.40$
CLEO [120]	$\gamma\gamma \rightarrow \chi_{c2} \rightarrow J/\psi\gamma$	$1.08 \pm 0.30 \pm 0.26$
TPC/2 γ [51]	$\gamma\gamma \rightarrow \chi_{c2} \rightarrow J/\psi\gamma$	$3.4 \pm 1.7 \pm 0.9$
CLEO [118]	$\gamma\gamma \rightarrow \chi_{c2} \rightarrow \pi^+\pi^-\pi^+\pi^-$	$0.5 \pm 0.2 \pm 0.1$
R704 [121]	$p\bar{p} \rightarrow \chi_{c2} \rightarrow \gamma\gamma$	$2.0^{+0.9}_{-0.7} \pm 0.3$
E760 [119]	$p\bar{p} \rightarrow \chi_{c2} \rightarrow \gamma\gamma$	$0.33 \pm 0.08 \pm 0.06$
E835 [40]	$p\bar{p} \rightarrow \chi_{c2} \rightarrow \gamma\gamma$	$0.31 \pm 0.05 \pm 0.04$
Average		0.38 ± 0.10
New result	$\gamma\gamma \rightarrow \chi_{c2} \rightarrow J/\psi\gamma$	$0.97 \pm 0.31 \pm 0.21$

Table 9.5: An overview of the used values in the determination of (9.15). The last line shows the result of the analysis presented in this thesis.

CLEO [118] and E835 [40] results

$$\Gamma_{\gamma\gamma}(\chi_{c2}) = 0.38 \pm 0.10 \text{ keV.} \quad (9.15)$$

This value is strongly dominated by the measurements of the E760 [119] and E835 collaborations, where the two-photon width is measured in the reaction $p\bar{p} \rightarrow \chi_{c2} \rightarrow \gamma\gamma$. On the other hand, measurements in two-photon reactions at e^+e^- colliders point to a higher value of the two-photon width. In table 9.5 the most recent measurements have been collected. If the L3 result [49] for the decay channel $\chi_{c2} \rightarrow J/\psi\gamma \rightarrow l^+l^-\gamma$ is combined with the non-observation of events in the final states $\pi^+\pi^-\pi^+\pi^-$ and $K^+K^-\pi^+\pi^-$, a two photon width of $\Gamma_{\gamma\gamma}(\chi_{c2}) = 0.71 \pm 0.30 \pm 0.12$ keV is observed [59].

In [122] this discrepancy in $\Gamma_{\gamma\gamma}(\chi_{c2})$ between the two different kinds of experiments is discussed. All two-photon experiments at e^+e^- colliders share the same systematic effects, which does not allow one to take the average of the results. For example, in all analyses a cut on the minimum allowed photon energy is implied, where the energy spectrum of the photon is sharply decreasing. On the other hand, the results from the $p\bar{p}$ experiments depend critically on the branching ratio $\chi_{c2} \rightarrow p\bar{p}$. It might also be that in these experiments not the whole yield curve of the χ_{c2} resonance has been observed.

More recently, it has been claimed [123] that the branching ratios $\text{Br}(\chi_{c2} \rightarrow J/\psi\gamma)$ as given by the PDG [13] are overestimated. This results in an overestimation for $\Gamma_{\gamma\gamma}(\chi_{c2})$ measured in e^+e^- experiments and an underestimation for this two-photon width measured in the $p\bar{p}$ experiments. The new fit presented in [123] yields for the χ_{c2} resonance $\text{Br}(\chi_{c2} \rightarrow$

$J/\psi\gamma) = 18.7^{+2.8}_{-2.3}$ %. Changing only this branching ratio in the analysis presented in this chapter would give a two-photon width of $\Gamma_{\gamma\gamma}(\chi_{c2}) = 0.71 \pm 0.23 \pm 0.14$ keV.

It should be noted that most theoretical predictions also favour a lower $\Gamma_{\gamma\gamma}(\chi_{c2})$. In particular, in section 3.4 we have found a two-photon width $\chi_{c2} = 0.28$ keV.

9.4 Decay distributions of the χ_{c2}

Again, one can consider the distribution of the polar angle of the photon in the rest frame of the χ_{c2} resonance. If indeed the production and decay of the χ_{c2} resonance are dominated by the helicity-2 contribution, we expect a non-uniform distribution for $\cos\theta_\gamma$ of the form as given in figure 6.8.

To increase statistics, the selection requirements have been made less strict. Events are now accepted in the signal region when the invariant mass of the l^+l^- system satisfies $|M_{l^+l^-} - M_{J/\psi}| < 0.2$ GeV. Furthermore, the sidebands have been increased to $0.5 < |M_{l^+l^-} - M_{J/\psi}| < 1.0$ GeV.

We are only interested in the angular distribution of the χ_{c2} events. Therefore, only events in the window $|\Delta M - 0.46| < 0.1$ GeV have been selected. With the new set of cuts this mass window contains 66 χ_{c2} events and 70 background events. The background events are again subtracted by looking at the $\cos\theta_\gamma$ distribution of the side bands. This yields for the χ_{c2} events a spectrum as given in figure 9.11. Due to the low statistics only five bins have been used.

In this figure we have also included the predictions of the GaGaRes Monte Carlo generator where the full description of the decay, as given in section 5.4 has been included. Also the Monte Carlo predictions for a uniform decay of the χ_{c2} resonance into a photon and a J/ψ has been included. Both Monte Carlo predictions have been normalized to the number of observed χ_{c2} events.

Once more, a suppression at low values for $\cos\theta_\gamma$ is observed in both data and Monte Carlo. In analogy to the η' analysis, this is coming from the requirement of a minimum angle between the photon and the leptons in the rest frame of the χ_{c2} resonance. The effect is somewhat weaker than in the η' analysis, partly due to the choice of wider bins.

The χ^2 per degree of freedom reads for this comparison between the GaGaRes Monte Carlo predictions and data 0.092/4. This corresponds to a confidence level of 99.9 %. The χ^2 per degree of freedom reads for this comparison between the data points and the predictions for the uniform distribution of $\cos\theta_\gamma$ 1.31/4. This corresponds to a confidence level of 86 %. The errors are totally dominated by the statistical errors on the data points. The experimental data seem to slightly favour the first distribution. However, no strong conclusions can be drawn. A large increase in collected luminosity would be needed for that.

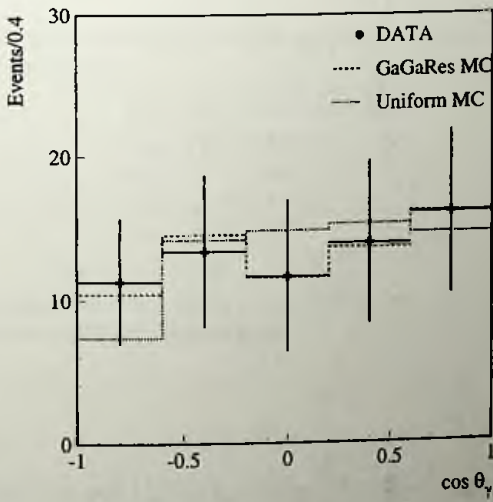


Figure 9.11: The $\cos \theta_\gamma$ distribution for data and Monte Carlo, both the results of the exact generation of the decay and a uniform distribution of $\cos \theta_\gamma$, are shown. The Monte Carlo results are scaled to the data.

Appendix A

Expressions for $\Sigma |\mathcal{M}|^2$

In the expressions for the total matrix elements squared we have used the following variables to compactify the expressions

$$\begin{aligned}
 \Sigma_{n\pm} &= s^n + s'^n \pm u^n \pm u'^n, \\
 \sigma_{2\pm} &= ss' \pm uu', \\
 s_{n\pm} &= s^n \pm s'^n, \\
 u_{n\pm} &= u^n \pm u'^n, \\
 t_{n\pm} &= t^n \pm t'^n,
 \end{aligned}
 \tag{A.1}$$

with the convention that for $n = 1$ the n is not written.

This leads us to the following expressions:

1S_0 amplitude:

$$\begin{aligned}
 \frac{1}{4} \Sigma |\mathcal{M}(^1S_0)|^2 &= \frac{e^4 c_2^2}{i^2 t'^2} \left\{ \frac{1}{2} [tt'(s_+^2 + u_+^2) - (tt' + \sigma_{2-})^2 - (tt' - \sigma_{2-})^2] \right. \\
 &\quad + m_e^2 [t_+(s_-^2 + u_-^2) + 4\sigma_{2-}\Sigma_- - 4tt'\Sigma_+ + 2s_-u_-t_-] \\
 &\quad \left. + 16m_e^4 s_+ u_+ - 64m_e^5 \Sigma_+ + 256m_e^8 \right\}.
 \end{aligned}
 \tag{A.2}$$

3P_0 amplitude:

$$\begin{aligned}
 \frac{1}{4} \Sigma |\mathcal{M}(^3P_0)|^2 &= \frac{e^4 c_2^2}{i^2 t'^2} \left\{ \frac{B^2}{2} (2\sigma_{2-}^2 + tt'(s_-^2 + u_-^2 + 2tt')) + Btt'(-s_+(\sigma_{2-} + tt') \right. \\
 &\quad + u_+(\sigma_{2-} - tt')) + 2t^2 t'^2 \sigma_{2+} + m_e^2 [B^2(t_+\Sigma_+^2 - 4\sigma_{2-}\Sigma_-) \\
 &\quad + 2tt'B(\Sigma_-^2 - 2t_+\Sigma_+ + 4tt') - 4t^2 t'^2 (\Sigma_+ - t_+)] \\
 &\quad \left. + m_e^4 [4B^2(\Sigma_-^2 - 4t_+\Sigma_+) + 32tt't_+B + 16t^2 t'^2] + 64m_e^6 B^2 t_+ \right\}.
 \end{aligned}
 \tag{A.3}$$

Here B is given by

$$B = k_1 \cdot k_2 + W^2 = \frac{3}{2}(s + s' + u + u') + t + t' - 12m_c^2 = \frac{3}{2}\Sigma_+ + t_+ - 12m_c^2. \quad (\text{A.4})$$

3P_1 amplitude:

$$\begin{aligned} \frac{1}{4} \sum |\mathcal{M}({}^3P_1)|^2 = & \frac{e^4 c_2^2}{W^2 t_+^2 t'^2} \left\{ tt' \left[tt' t_+^2 - tt' t_+ \Sigma_+ + \frac{1}{2} t_2 \Sigma_+ - 2tt' \Sigma_+ \right. \right. \\ & + (t_2 + 4tt') \sigma_2 + \sigma_2 \Sigma_2 - 4tt' s_+ u_+ + t_+ \sigma_2 \Sigma_+ \\ & + 2t(su'^2 + s^2 u' + s' u^2 + s'^2 u) + 2t'(su^2 + s^2 u + s' u'^2 + s'^2 u') \\ & + 2t^2(su' + s'u) + 2t'^2(su + s'u')] - \sigma_2^2 t_2 + \\ & + m_c^2 \left[t_3 \Sigma_+^2 - 7tt' t_+ \Sigma_+ - 26tt'(t(su' + s'u) + t'(su + s'u')) \right. \\ & + 8t_2 (ss' s_+ + uu' u_+) + 4(t_2 + tt')(ss' u_+ + uu' s_+) \\ & - 22tt' t_+ \sigma_2 - 12tt' t_3 \Sigma_+ + 32t^2 t'^2 \Sigma_+ - 2tt' \Sigma_3 + \\ & - 6tt'(ss' s_+ + uu' u_+) + 16t^2 t'^2 t_+ + 2tt'(s_+ u_2 + u_+ s_2) \\ & + 4t^2(su'^2 + s^2 u' + s' u^2 + s'^2 u) + 4t'^2(su^2 + s^2 u + s' u'^2 + s'^2 u') \\ & \left. - 10tt'(stu + st'u' + s't'u + s'tu') \right] \\ & + 16m_c^4 \left[-t_+^2 s_+ u_+ + 6tt' t_+ \Sigma_+ - t_3 \Sigma_+ - t_2 (\Sigma_2 + 4\sigma_2) \right. \\ & \left. + 4tt' t_-^2 - 2(t^2(su' + s'u) + t'^2(su + s'u')) \right] \\ & + 64m_c^6 [2(t_2 + tt') \Sigma_+ + t_3 - 5tt' t_+] \\ & \left. - 256m_c^8 t_+^2 \right\} \end{aligned} \quad (\text{A.5})$$

3P_2 amplitude:

$$\begin{aligned} \frac{1}{4} \sum |\mathcal{M}({}^3P_2)|^2 = & \frac{c_2^4 e^4}{12} \left[\frac{1}{W^4} \left\{ \frac{m_c^2}{W^4} [-8\Sigma_+^3 - 32\sigma_2 \Sigma_+ + 64s_+ u_+ \Sigma_+ \right. \right. \\ & + 192(ss' u_+ + uu' s_+)] + \frac{m_c^2}{W^2} [-4\Sigma_+^2 + 128\sigma_2 - 16s_+ u_+] \\ & + m_c^2 [-24\Sigma_+] + \frac{m_c^4}{W^4} [-192\Sigma_+^2 - 256\sigma_2 - 640s_+ u_+] \\ & \left. + \frac{m_c^4}{W^2} [-128\Sigma_+] + m_c^4 [96] + \frac{m_c^6}{W^4} [3072\Sigma_+] + \frac{m_c^6}{W^2} [512] + \frac{m_c^8}{W^4} [-8192] \right. \end{aligned}$$

$$\begin{aligned}
 & + \frac{1}{W^4} [\Sigma_+^4 - 2s_+u_+(s_+^2 + u_+^2) + 16\sigma_{2-}^2 - 8s_+u_+\sigma_{2+} \\
 & - 16(ss'u_2 + uu's_{2+}) - 4s_{2+}u_{2+} - 48ss'uu'] + \frac{1}{W^2} [4\Sigma_+^3 - 8s_+u_+\Sigma_+ \\
 & - 26\sigma_{2+}\Sigma_+ + 20(ss'u_+ + uu's_+)] + [s_+^2 + u_+^2 + 8\sigma_{2+}] \} \\
 & + \left(\frac{1}{u'^2} + \frac{1}{i^2v'} \right) \left\{ \frac{m^2}{W^4} [2\Sigma_+^4 - 128\sigma_{2-}^2 - 32\sigma_{2-}\Sigma_{2-}] \right. \\
 & + \frac{m^2}{W^2} [8\Sigma_+^3 + 8\sigma_{2-}\Sigma_-] + m_e^2 [2\Sigma_+^2] + \frac{m^4}{W^4} [-32\Sigma_+^3 - 128s_+u_+\Sigma_+ \\
 & + 256\sigma_{2-}\Sigma_-] + \frac{m^4}{W^2} [-200\Sigma_+^2 + 32s_+u_+] + m_e^4 [64\Sigma_+ \\
 & + \frac{m_e^6}{W^4} [512\Sigma_+^2 + 1024s_+u_+] + \frac{m_e^6}{W^2} [1536\Sigma_+] + m_e^6 [-256] \\
 & + \frac{m_e^8}{W^4} [-4096\Sigma_+] + \frac{m_e^8}{W^2} [-4096] + \frac{m_e^{10}}{W^4} [8192] \\
 & + \frac{1}{W^4} [8\sigma_{2-}^2 \Sigma_+] + \frac{1}{W^2} [-2\sigma_{2-}^2] \} + \frac{m^2}{u'^2} [-24(s+u)(s'+u')] \\
 & + \frac{m^2}{i^2v'} [-24(s+u')(s'+u)] + \frac{1}{i} \left\{ \frac{m^2}{W^4} [8\Sigma_+^2 + 64(s+u')(s'+u) \right. \\
 & + 128(su' + s'u) + 32t'\Sigma_+] + \frac{m^2}{W^2} [-64\Sigma_+ - 48t'] + m_e^2 [48] \\
 & + \frac{m^4}{W^4} [-640\Sigma_+ - 256t'] + \frac{m^4}{W^2} [416] + \frac{m_e^6}{W^4} [2560] + \frac{1}{W^4} [2\Sigma_+^3 \\
 & + 2t'\Sigma_+^2 - 8t'(s+u)(s'+u') - 24(ss'u_+ + uu's_+) - 8(su'(s+u') \\
 & + s'u(s'+u))] + \frac{1}{W^2} [4\Sigma_+^2 - 4(s+u)(s'+u') - 12\sigma_{2+}] \} \\
 & + \frac{1}{v'} \left\{ \frac{m^2}{W^4} [8\Sigma_+^2 + 64(s+u)(s'+u') + 128(su + s'u') + 32t\Sigma_+] \right. \\
 & + \frac{m^2}{W^2} [-64\Sigma_+ - 48t] + m_e^2 [48] \\
 & + \frac{m^4}{W^4} [-640\Sigma_+ - 256t] + \frac{m^4}{W^2} [416] + \frac{m_e^6}{W^4} [2560] + \frac{1}{W^4} [2\Sigma_+^3 \\
 & + 2t\Sigma_+^2 - 8t(s+u')(s'+u) \\
 & - 24(ss'u_+ + uu's_+) - 8(su(s+u) + s'u'(s'+u'))] \\
 & + \frac{1}{W^2} [4\Sigma_+^2 - 4(s+u')(s'+u) - 12\sigma_{2+}] \} \\
 & + \frac{1}{i^2v'^2} \left\{ \frac{m^2}{W^4} [-56\sigma_{2-}^2 \Sigma_+ - 8\sigma_{2-}\Sigma_{3-} - 8\sigma_{2-}(s_+uu' - u_+ss') \right. \\
 & + 8\sigma_{2-}(s_+u_{2+} - u_+s_{2+})] + \frac{m^2}{W^2} [-32\sigma_{2-}^2 - 8\sigma_{2-}\Sigma_{2-}] + m_e^2 [16\sigma_{2-}\Sigma_-]
 \end{aligned} \tag{A.6}$$

$$\begin{aligned}
 & + \frac{m_e^4}{W^4} [416\sigma_{2-}^2 + 160\sigma_{2-}\Sigma_{2-} + 8\Sigma_{2+}^2 - 32s_{2+}u_{2+}] + \frac{m_e^4}{W^2} [8\Sigma_+^3 + \sigma_{2-}\Sigma_- \\
 & - 32(s_+u_{2+} + u_+s_{2+}) - 64(ss'u_+ + uu's_+)] + m_e^4 [8\Sigma_+^2 + 64s_+u_+] \\
 & + \frac{m_e^6}{W^4} [-128\Sigma_+^3 - 512\sigma_{2-}\Sigma_- + 512s_+u_+\Sigma_+] + \frac{m_e^6}{W^2} [-64\Sigma_-^2] \\
 & + m_e^6 [-384\Sigma_+] + \frac{m_e^8}{W^4} [512\Sigma_-^2] + m_e^8 [1536] + \frac{1}{W^4} [2\sigma_{2-}^2\Sigma_{2+} + 4\sigma_{2-}^2\sigma_{2+} \\
 & + 4\sigma_{2-}^2s_+u_+] + \frac{1}{W^2} [2\sigma_{2-}^2\Sigma_+] + [-4\sigma_{2-}^2] \} \\
 & + \left(\frac{1}{t^2} + \frac{1}{t'^2} \right) \left\{ \frac{m_e^2}{W^4} [8\Sigma_+^3 - 32\sigma_{2-}\Sigma_-] + \frac{m_e^2}{W^2} [4\Sigma_+^2] + \frac{m_e^4}{W^4} [-160\Sigma_+^2 \right. \\
 & - 128s_+u_+] + \frac{m_e^4}{W^2} [-160\Sigma_+] + \frac{m_e^6}{W^4} [1536\Sigma_+] + \frac{m_e^6}{W^2} [640] + \frac{m_e^8}{W^4} [-4096] \\
 & \left. + \frac{1}{W^4} [8\sigma_{2-}^2] \right\} + \frac{1}{t^2} \left\{ \frac{m_e^2}{W^4} [8t'\Sigma_+^2] + \frac{m_e^2}{W^2} [24(s+u')(s'+u)] + \frac{m_e^4}{W^4} [-128t'\Sigma_+ \right. \\
 & \left. + \frac{m_e^6}{W^4} [512t'] \right\} + \frac{1}{t'^2} \left\{ \frac{m_e^2}{W^4} [8t\Sigma_+^2] + \frac{m_e^2}{W^2} [24(s+u)(s'+u')] + \frac{m_e^4}{W^4} [-128t\Sigma_+ \right. \\
 & \left. + \frac{m_e^6}{W^4} [512t] \right\} + \left\{ \frac{m_e^2}{W^4} [64\Sigma_+ + 32t_+] + \frac{m_e^2}{W^2} [-144] + \frac{m_e^4}{W^4} [-512] + \frac{1}{W^4} [2\Sigma_-^2] \right. \\
 & \left. + \frac{1}{W^2} [12\Sigma_+ + 6t_+] + [8] \right\}.
 \end{aligned}$$

1D_2 amplitude:

$$\frac{1}{4} \sum |\mathcal{M}(^1D_2)|^2 = \tilde{c}^2 \mathcal{F} \frac{1}{4} \sum |\mathcal{M}(^1S_0)|^2, \quad (\text{A.7})$$

with

$$\tilde{c} = \frac{c_5}{c_1}, \quad (\text{A.8})$$

and

$$\mathcal{F} = \frac{1}{2} \left(-t + \frac{(W^2 + t_-)^2}{4W^2} \right) \left(-t' + \frac{(W^2 - t_-)^2}{4W^2} \right) + \frac{1}{6} \left(\frac{W^2 - t_+}{2} - \frac{W^4 - (t_-)^2}{4W^2} \right)^2. \quad (\text{A.9})$$

Note that for the 1D_2 case the overall factor $\frac{e^4}{t^2 t'^2}$ is included in the 1S_0 factor.

Appendix B

Weyl-van der Waerden formalism

In this appendix we will give a very brief overview of the Weyl-van der Waerden (WvdW) formalism, to the extent that is required for our applications. We have adopted the conventions of Dittmaier [89]. For a more complete discussion of the WvdW formalism we refer to [86-89].

The basic philosophy of the WvdW formalism is to reduce all mathematical objects that belong to higher dimensional representations of the Lorentz group to the two two-dimensional irreducible representations $D(\frac{1}{2}, 0)$ and $D(0, \frac{1}{2})$. As representation we will use the covariant and contravariant WvdW spinors ψ_A and $\psi^{\dot{A}}$. The dot on top of the spinor index indicates the complex conjugation of the associated spinor.

The indices can be raised/lowered by the spinor metric ε^1

$$\varepsilon^{AB} = \varepsilon^{\dot{A}\dot{B}} = \varepsilon_{AB} = \varepsilon_{\dot{A}\dot{B}} = \begin{pmatrix} 0 & +1 \\ -1 & 0 \end{pmatrix}. \quad (\text{B.1})$$

$$\psi^A = \varepsilon^{AB} \phi_B, \quad \psi^{\dot{A}} = \varepsilon^{\dot{A}\dot{B}} \phi_{\dot{B}}, \quad \psi_A = \phi^B \varepsilon_{BA}, \quad \psi_{\dot{A}} = \psi^{\dot{B}} \varepsilon_{\dot{B}\dot{A}}. \quad (\text{B.2})$$

This spinor metric defines the (antisymmetric) spinor inner product

$$\langle \phi\psi \rangle \equiv \phi_A \psi^A = \varepsilon^{AB} \phi_A \psi_B = \phi_1 \psi_2 - \phi_2 \psi_1. \quad (\text{B.3})$$

Four-vectors:

The representation of a Minkowski four-vector $k^\mu = (k^0, \vec{k})$ in the $D(\frac{1}{2}, \frac{1}{2})$ representation is given by the following 2×2 matrix

$$K_{\dot{A}B} = k^\mu \sigma_{\mu, \dot{A}B} = \begin{pmatrix} k^0 + k^3 & k^1 + ik^2 \\ k^1 - ik^2 & k^0 - k^3 \end{pmatrix}, \quad (\text{B.4})$$

with²

$$\sigma_{\mu, \dot{A}B} = (\sigma^0, \vec{\sigma}^*), \quad (\text{B.5})$$

¹It should be noted that in [86-88] ε differs by an overall sign from (B.1).

²In [89] σ^* is called σ since σ_2 is defined with a sign opposite to the usual convention.

where σ^0 is the two-dimensional unit matrix and σ^i are the Pauli matrices. The standard Minkowski inner product is related to these WvdW bispinors by

$$2k^\mu p_\mu = K_{\dot{A}B} P^{AB}, \quad k^2 \delta_B^C = K_{\dot{A}B} K^{\dot{A}C}. \quad (\text{B.6})$$

When we introduce the WvdW spinors n_1 and n_2

$$n_{1,A} = \begin{pmatrix} e^{-i\phi} \cos \frac{\theta}{2} \\ \sin \frac{\theta}{2} \end{pmatrix}, \quad n_{2,A} = \begin{pmatrix} \sin \frac{\theta}{2} \\ -e^{i\phi} \cos \frac{\theta}{2} \end{pmatrix}, \quad (\text{B.7})$$

the WvdW bispinor corresponding to a Minkowski vector with polar angle θ and azimuthal angle ϕ can be written as

$$K_{\dot{A}B} = \sum_{i=1,2} \lambda_i n_{i,\dot{A}} n_{i,B} \equiv \sum_{i=1,2} k_{i,\dot{A}} k_{i,B}, \quad (\text{B.8})$$

where

$$\lambda_{1,2} = k^0 \pm |\vec{k}|. \quad (\text{B.9})$$

For light-like four-vectors ($k^2 = 0$) λ_2 vanishes and the WvdW bispinor reduces to a simple dyad form.

Spin- $\frac{1}{2}$ particles:

The Dirac spinors Ψ belong to the representation $D(\frac{1}{2}, 0) \oplus D(0, \frac{1}{2})$

$$\Psi = \begin{pmatrix} \phi_A \\ \psi^{\dot{A}} \end{pmatrix}. \quad (\text{B.10})$$

The results of the solution of the coupled Weyl-equations are given in table B.1. We have expressed the solutions in

$$\Psi_1^{(\pm)}(k) = \begin{pmatrix} k_{1,A} \\ \mp k_2^{\dot{A}} \end{pmatrix}, \quad \Psi_2^{(\pm)}(k) = \begin{pmatrix} \pm k_{2,A} \\ k_1^{\dot{A}} \end{pmatrix}, \quad (\text{B.11})$$

$$\bar{\Psi}_1^{(\pm)}(k) = (\mp k_2^A, k_{1,\dot{A}}), \quad \bar{\Psi}_2^{(\pm)}(k) = (k_1^A, \pm k_{2,\dot{A}}). \quad (\text{B.12})$$

For massless spin- $\frac{1}{2}$ fermions the Weyl equations decouple and the expressions simplify dramatically.

The propagator associated to a fermion going from index B to A reads

$$\begin{array}{c} \bullet \xrightarrow{k} \bullet \\ B \quad A \end{array} = \frac{i}{k^2 - m_f^2} \begin{pmatrix} m_f \delta_A^B & K_{A\dot{B}} \\ K^{A\dot{B}} & m_f \delta_B^{\dot{A}} \end{pmatrix} \quad (\text{B.13})$$

Spin-2 particles:

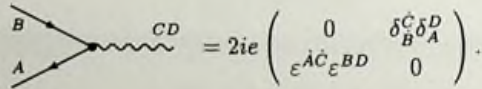
The polarization tensors for a spin-2 particle can be constructed out of the spin-1 polarization vectors using the Clebsch-Gordan (CG) coefficients.

$$\begin{aligned}
 \epsilon^{\mu\nu}(\pm 2) &= \epsilon^\mu(\pm 1)\epsilon^\nu(\pm 1) \\
 \epsilon^{\mu\nu}(\pm 1) &= \frac{\pm 1}{\sqrt{2}} (\epsilon^\mu(\pm 1)\epsilon^\nu(0) + \epsilon^\mu(0)\epsilon^\nu(\pm 1)) \\
 \epsilon^{\mu\nu}(0) &= \frac{1}{\sqrt{6}} (-\epsilon^\mu(+1)\epsilon^\nu(-1) + 2\epsilon^\mu(0)\epsilon^\nu(0) - \epsilon^\mu(-1)\epsilon^\nu(+1))
 \end{aligned}
 \tag{B.19}$$

The choice of the \pm sign in $\epsilon^{\mu\nu}(\pm 1)$ is arbitrary and for the relation between complex conjugation and reversing helicities not very convenient, since it introduces an unnecessary sign which is absent for the complex conjugation in equation (B.14).

Feynman rules:

We also need the expression for the coupling of a photon to an electron line



$$\begin{array}{c} B \\ \nearrow \\ \text{---} \\ \searrow \\ A \end{array} \begin{array}{c} \text{---} \\ \text{---} \end{array} \begin{array}{c} CD \\ \text{---} \end{array} = 2ie \begin{pmatrix} 0 & \delta_B^C \delta_A^D \\ \epsilon^{AC} \epsilon^{BD} & 0 \end{pmatrix}.
 \tag{B.20}$$

Levi-Civita tensor:

Finally one also needs a translation of the Levi-Civita tensor into the WvdW formalism. This translation is given in [88]

$$\epsilon_{\dot{A}\dot{B}\dot{X}\dot{C}\dot{Y}\dot{D}\dot{Z}} = 4i (\epsilon_{\dot{A}\dot{B}} \epsilon_{\dot{C}\dot{D}} \epsilon_{WY} \epsilon_{XZ} - \epsilon_{\dot{A}\dot{C}} \epsilon_{\dot{B}\dot{D}} \epsilon_{WX} \epsilon_{YZ}).
 \tag{B.21}$$

Appendix C

Suppression at low $W_{\gamma\gamma}$

In chapter 8 it is stated that in the $W_{\gamma\gamma}$ spectrum a suppression at bins around $W_{\gamma\gamma} = 0$ can be observed, even in the absence of cuts on the maximum allowed energy of the tags. This is illustrated in figure C.1. In this appendix it is derived that such a suppression already occurs under very mild conditions.

The following two assumptions have been made:

1. The invariant mass of the two-photon system can, in good approximation, be calculated from the photon energies by

$$W_{\gamma\gamma}^2 = 4\omega_1\omega_2 = 4Y. \quad (\text{C.1})$$

Again, we use $W_{\gamma\gamma}$ as constructed in section 8.3, i.e. $W_{\gamma\gamma} = 4Y/|Y|\sqrt{|Y|}$.

2. Both photon energies are uniformly distributed in the range $[-x_a, x_b]$, $0 < x_a < x_b$, where x_a and x_b have to be specified later on. The two distributions are independent. That this assumption holds in good approximation can be seen from figure C.2, where the experimentally found distributions are shown.

The uniform distributions of the photon energies will now be assumed to be

$$f(\omega_i) = \begin{cases} \frac{1}{Z} & -x_a < \omega_i < x_b \\ 0 & \text{otherwise} \end{cases} \quad (i = 1, 2), \quad (\text{C.2})$$

where we have defined the variable Z ,

$$Z = x_a + x_b. \quad (\text{C.3})$$

The random variable Y can be both positive and negative. Its minimum value is $-x_a x_b$, and its maximum value is x_b^2 . For a given Y not all photon energies are allowed. From Figure C.3 it follows that both photon energies have to be in the interval $I(Y)$. In the definition of $I(Y)$ one has to distinguish three regions of Y

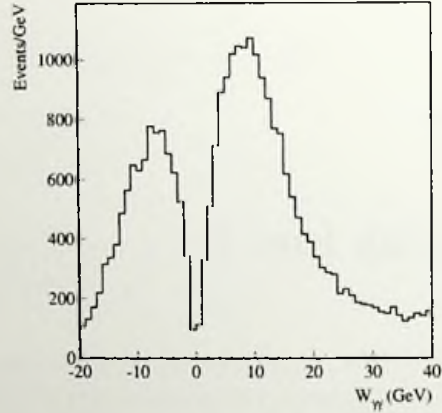


Figure C.1: $W_{\gamma\gamma}$ spectrum for LEP2. For the cuts in the PMMA, except for the cuts on the tagged energies.

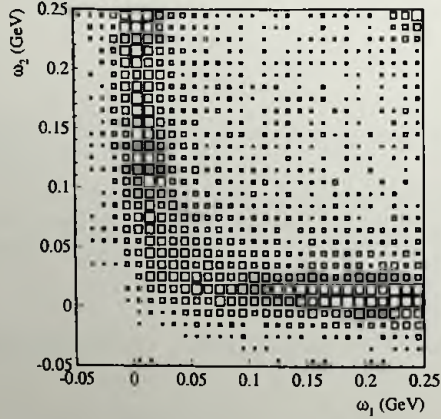


Figure C.2: Spectrum of the two photon energies normalized to the beam energy for LEP2 data, $x_i = \omega_i/E_b$. Due to the experimental resolution the x_i 's may become negative.

$$\begin{aligned}
 \text{I} : -x_a x_b < Y < 0 & : I(Y) = \{ \omega_1, \omega_2 | (\omega_1 \in [-x_a, -g_y], \omega_2 \in [f_y, x_b]) \vee \\
 & \quad (\omega_1 \in [f_y, x_b], \omega_2 \in [-x_a, -g_y]) \} \\
 \text{II} : 0 < Y < x_a^2 & : I(Y) = \{ \omega_1, \omega_2 | (\omega_1, \omega_2 \in [-x_a, -f_y]) \vee \\
 & \quad (\omega_1, \omega_2 \in [g_y, x_b]) \} \\
 \text{III} : x_a^2 < Y < x_b^2 & : I(Y) = \{ \omega_1, \omega_2 | \omega_1, \omega_2 \in [g_y, x_b] \}
 \end{aligned}$$

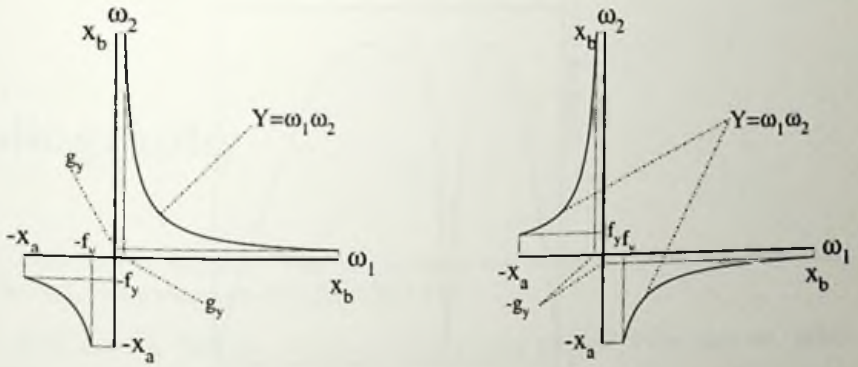


Figure C.3: The x_1 and x_2 intervals for $Y > 0$ (left plot) and $Y < 0$ (right plot). The contributions from the $(-, -)$ -quadrant only exists for $0 < Y < x_a^2$.

where we have defined

$$f_y = \frac{|Y|}{x_a}, \tag{C.4}$$

$$g_y = \frac{|Y|}{x_b}. \tag{C.5}$$

The cumulative distribution function (cdf) $G(y') = P(Y \leq y')$ is now given by

$$\begin{aligned} G(y') &= \int_{-\infty}^{y'} dy \int_{I(Y)} d^2V f(\omega_1) f(\omega_2) \delta(y - \omega_1 \omega_2) \Pi \theta \\ &= \int_{-\infty}^{y'} dy \int_{I(Y)} d^2V \frac{1}{2^2} \delta(y - \omega_1 \omega_2) \Pi \theta, \end{aligned} \tag{C.6}$$

where the volume element d^2V is given by $d^2V = d\omega_1 d\omega_2$ and $\Pi \theta$ is a shorthand notation for

$$\Pi \theta = \theta(Y + x_a x_b) \theta(x_b^2 - Y). \tag{C.7}$$

One can check that this function G is a good cdf. It is strictly increasing and

$$G(-x_a x_b) = 0, \quad G(x_b^2) = 1. \tag{C.8}$$

From this cdf we can construct the probability density function (pdf) $g(y) = G'(y)$. For the three intervals we find

$$\begin{aligned} I &: g(y) = \frac{-2}{2^2} \ln \left(\frac{|y|}{x_a x_b} \right), \\ II &: g(y) = \frac{-2}{2^2} \ln \left(\frac{y}{x_a x_b} \right), \\ III &: g(y) = \frac{1}{2^2} \ln \left(\frac{y}{x_b^2} \right). \end{aligned} \tag{C.9}$$

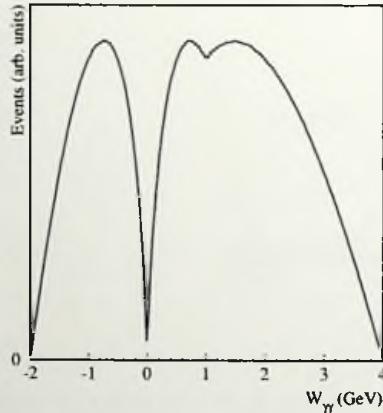


Figure C.4: $W_{\gamma\gamma}$ spectrum for two uniformly distributed random variables ω_1 and ω_2 . The vertical scale is linear. (50,000,000 events)

For $W_{\gamma\gamma} = 4 \frac{Y}{|Y|} \sqrt{|Y|}$ this results in a pdf $w(W_{\gamma\gamma})$

$$\begin{aligned}
 I & : w(W_{\gamma\gamma}) = \frac{-|W_{\gamma\gamma}|}{4Z^2} \ln \left(\frac{W_{\gamma\gamma}^2}{16x_a x_b} \right), \\
 II & : w(W_{\gamma\gamma}) = \frac{-W_{\gamma\gamma}}{4Z^2} \ln \left(\frac{W_{\gamma\gamma}^2}{16x_a x_b} \right), \\
 III & : w(W_{\gamma\gamma}) = \frac{-W_{\gamma\gamma}}{8Z^2} \ln \left(\frac{W_{\gamma\gamma}^2}{16x_b^2} \right).
 \end{aligned} \tag{C.10}$$

This pdf results in a vanishing probability to find a $W_{\gamma\gamma}$ around zero.

This has also been checked on Monte-Carlo level. In figure C.4 we have generated 50,000,000 events where both ω_1 and ω_2 were generated uniformly on the intervals $[-1,4]$, i.e. we have taken¹ $x_a = 1$ and $x_b = 4$. A clear suppression around $W_{\gamma\gamma} = 0$ can be observed. The structure with two peaks for $W_{\gamma\gamma} > 0$ can be easily understood. For $0 < W_{\gamma\gamma} < x_a = 1$ we are in region II. In this region there are two areas contributing, in contrast to region III ($1 < W_{\gamma\gamma} < 4$).

It should be noted that this vanishing probability at zero $W_{\gamma\gamma}$ follows from the two assumptions we have made. The extra term in equation (8.1), the non-uniform and dependent distributions of the photon energies and the finite width of the bins result in some events in the bins around zero, but nevertheless the suppression can clearly be observed in figure C.1.

¹This is an extreme choice for x_a and x_b . In realistic situations, one normally has $x_b \gg x_a$.

Bibliography

- [1] H. Euler and B. Kockel, "Über die Streuung von Licht an Licht nach Diracschen Theorie", *Naturwissenschaften* **23** (1935) 246.
- [2] G. Breit and J.A. Wheeler, "Collision of Two Light Quanta", *Phys. Rev.* **46** (1934) 1087.
- [3] R. Karplus and M. Neuman, "The Scattering of Light by Light", *Phys. Rev.* **83** (1951) 776.
- [4] R. Nisius, "Two Photon Physics at a Future Linear Collider", in *Photon Interactions and the Photon Structure.*, ed. T. Sjostrand, (CERN, Geneva, 1998), p. 329.
- [5] V. Telnov, "Physics Goals and Parameters of Photon Colliders", *Int. J. Mod. Phys. A* **13** (1998) 2399.
- [6] F. E. Low, "Proposal for Measuring the π^0 Lifetime by π^0 Production in Electron-Electron or Electron-Positron Collisions", *Phys. Rev.* **120** (1960) 582.
- [7] F. Calogero and C. Zemach, "Particle Creation in Electron-Electron Collisions", *Phys. Rev.* **120** (1960) 1860.
- [8] V. E. Balakin et al., "Experiment on 2 γ -Quantum Annihilation on the VEPP-2", *Phys. Lett. Cimento* **34B** (1971) 99.
- [9] C. Bacci et al., "Gamma-Gamma Interaction Processes at Adone e^+e^- Storage Ring. Measurement of the Reaction $e^+e^- \rightarrow e^+e^-e^+e^-$ ", *Lett. Nuovo Cimento* **3** (1972) 709.
- [10] P. H. W. M. Daverveldt, "Monte Carlo Simulation of Two Photon Processes", Ph.D. thesis, Rijksuniversiteit Leiden, 1985.
- [11] F. A. Berends and R. Pittau and R. Kleiss, "Excalibur: A Monte Carlo Program to Evaluate All Four Fermion Processes at LEP-200 and Beyond", *Comput. Phys. Commun.* **85** (1995) 437.
- [12] L3 Collab., M. Acciarri et al., " $K_S^0 K_S^0$ Final State in Two-Photon Collisions and Implications for Glueballs", *Phys. Lett.* **B501** (2001) 173.
- [13] D. E. Groom et al., "Review of Particle Physics", *Eur. Phys. J.* **C15** (2000) 1.

- [14] G. Jikia, "Physics at the Photon Linear Collider", in Proceedings of the 11th International Workshop on Photon-Photon Collisions, ed. A. Buijs and F. C. Ern , (World Scientific, Singapore, 1997), p. 378.
- [15] F. Mandl and G. Shaw, "Quantum Field Theory", (Wiley, Chichester, 1984).
- [16] V. M. Budnev, I. F. Ginzburg, G. V. Meledin and V. G. Serbo, "The Two photon Particle Production Mechanism. Physical Problems. Applications. Equivalent Photon Approximation", Phys. Rept. **15** (1974) 181.
- [17] E. J. Williams, "Applications of the Method of Impact Parameters in Collisions", Proc. Roy. Soc. **A139** (1933) 163.
- [18] C. F. von Weizs cker, "Ausstrahlung bei St o en sehr schneller Elektronen", Z. Physik **88** (1934) 612.
- [19] D. Ebert, R. N. Faustov and V. O. Galkin, "Relativistic Quark-Antiquark Potential and Heavy Quarkonium Mass Spectra", (2000), presented at the 5th International Workshop On Heavy Quark Physics.
- [20] D. J. Griffiths, "Introduction to Elementary Particles", (Wiley, New York, 1987).
- [21] E. E. Salpeter and H. A. Bethe, "A Relativistic Equation for Bound-State Problems", Phys. Rev. **84** (1951) 1232.
- [22] E. S. Ackleh and T. Barnes, "Two photon Widths of Singlet Positronium and Quarkonium with Arbitrary Total Angular Momentum", Phys. Rev. **D45** (1992) 232.
- [23] Z. P. Li and F. E. Close and T. Barnes, "Relativistic Effects in Gamma Gamma Decays of P Wave Positronium and q anti-q Systems", Phys. Rev. **D43** (1991) 2161.
- [24] C. R. Munz, "Two-Photon Decays of Mesons in a Relativistic Quark Model", Nucl. Phys. **A609** (1996) 364.
- [25] L. D. Landau, "Moments of 2-Photon Systems", Dok. Akad. Nauk. USSR **60** (1948) 207, (in russian) English summary in Phys. Abs. **A52** (1949), 125.
- [26] C. N. Yang, "Selection Rules for the Dematerialization of a Particle into Two Photons", Phys. Rev. **77** (1950) 242.
- [27] G. A. Schuler, F. A. Berends and R. van Gulik, "Meson Photon Transition Form Factors and Resonance Cross-Sections in e^+e^- Collisions", Nucl. Phys. **B523** (1998) 423.
- [28] TPC/Two Gamma Collab., H. Aihara et al., "Formation of Spin One Mesons by Photon-Photon Fusion", Phys. Rev. **D38** (1988) 1.
- [29] G. T. Bodwin, E. Braaten and G. P. Lepage, "Rigorous QCD Analysis of Inclusive Annihilation and Production of Heavy Quarkonium", Phys. Rev. **D51** (1995) 1125.

- [30] M. L. Mangano and A. Petrelli, "An Update on χ_c Decays: Perturbative QCD versus Data", Phys. Lett. **B352** (1995) 445.
- [31] F. L. Linde, "Charm Production in Two Photon Collisions", Ph.D. thesis, Rijksuniversiteit Leiden, 1988.
- [32] F. Halzen and A. D. Martin, "Quarks and Leptons: An Introductory Course in Modern Particle Physics", (Wiley, Chichester, 1984).
- [33] J. J. Aubert et al., "Experimental Observation of a Heavy Particle J' ", Phys. Rev. Lett. **33** (1974) 1404.
- [34] J. E. Augustin et al., "Discovery of a Narrow Resonance in e^+e^- Annihilation", Phys. Rev. Lett. **33** (1974) 1406.
- [35] S. W. Herb et al., "Observation of a Dimuon Resonance at 9.5 GeV in 400 GeV Proton-Nucleus Collisions", Phys. Rev. Lett. **39** (1977) 252.
- [36] N. Fabiano, A. Grau and G. Pancheri, "Toponium Bound States at LHC / SSC", (World Scientific, Singapore, 1994).
- [37] E. J. Eichten and C. Quigg, "Mesons with Beauty and Charm: Spectroscopy", Phys. Rev. **D49** (1994) 5845.
- [38] R. Abegg et al., "Direct measurement of the branching ratio for the decay of the η meson into two photons", Phys. Rev. **D53** (1996) 11.
- [39] R704 Collab., C. Baglin et al., "Angular Distributions in the Reactions $p\bar{p} \rightarrow \chi_{1,2} \rightarrow \gamma\psi \rightarrow \gamma e^+e^-$ ", Phys. Lett. **B195** (1987) 85.
- [40] M. Stancari, Two photon decay widths of charmonium resonances, Nucl. Phys. Proc. Suppl. **82** (2000) 306.
- [41] J. Z. Bai et al., "Study of the hadronic decays of χ_c states", Phys. Rev. **D60** (1999) 072001.
- [42] J. Gaiser et al., "Charmonium Spectroscopy from Inclusive ψ' and J/ψ Radiative Decays", Phys. Rev. **D34** (1986) 711.
- [43] R. Morrison et al., "Inclusive $\chi(2p)$ production in $\Upsilon(3s)$ decay", Phys. Rev. Lett. **67** (1991) 1696.
- [44] CLEO Collab., G. Brandenburg et al., "Measurements of the Mass, Total Width and Two-Photon Partial Width of the η_c Meson", Phys. Rev. Lett. **85** (2000) 3095.
- [45] K. W. Edwards et al., "Measurement of the mass splittings between the $b\bar{b}$ $\chi_{bJ}(1P)$ states", Phys. Rev. **D59** (1999) 032003.
- [46] R. Nernst et al., "Observation of Three P States in the Radiative Decay of $\Upsilon(2S)$ ", Phys. Rev. Lett. **54** (1985) 2195.

- [47] L3 Collab., M. Acciarri et al., "Formation of the η_c in Two-Photon Collisions at LEP", Phys. Lett. **B461** (1999) 155.
- [48] TPC/Two-Gamma Collab., H. Aihara et al., "Charmonium Production in Photon-Photon Collisions", Phys. Rev. Lett. **60** (1988) 2355.
- [49] L3 Collab., M. Acciarri et al., " χ_{c2} Formation in Two-Photon Collisions at LEP", Phys. Lett. **B453** (1999) 73.
- [50] OPAL Collab., K. Ackerstaff et al., "Production of χ_{c2} Mesons in Photon Photon Collisions at LEP", Phys. Lett. **B439** (1998) 197.
- [51] TPC/Two-Gamma Collab., D. Bauer et al., "Study of χ_{c2} Production in Photon-Photon Collisions", Phys. Lett. **B302** (1993) 345.
- [52] TPC/Two-Gamma Collab., H. Aihara et al., "Search for High-Mass narrow Resonances in Virtual Photon-Photon Interactions", Phys. Rev. Lett. **57** (1986) 3245.
- [53] TPC/Two-Gamma Collab., A. M. Eisner et al., "Resonance Formation in Photon-Photon Collisions: Recent Results from the TPC/TWO-GAMMA Collaboration", in Proceedings of the 23rd International Conf. on High Energy Physics, ed. S. C. Loken, (World Scientific, Singapore, 1987).
- [54] P. Achard on behalf of the L3 Collab., "Double-tag events study with the L3 detector at $\sqrt{s} = 189 \text{ GeV}$ ", Nucl. Phys. Proc. Suppl. **82** (2000) 61.
- [55] TPC/Two-Gamma Collab., H. Aihara et al., "Investigation of the Electromagnetic Structure of η and η' Mesons by Two Photon Interactions", Phys. Rev. Lett. **64** (1990) 172.
- [56] CELLO Collab., H. J. Behrend et al., "A Measurement of the π^0 , η and η' Electromagnetic Form-Factors", Z. Phys. **C49** (1991) 401.
- [57] L3 Collab., M. Acciarri et al., "Measurement of $\eta'(958)$ Formation in Two-Photon Collisions at LEP1", Phys. Lett. **B418** (1998) 399.
- [58] CLEO Collab., J. Gronberg et al., "Measurements of the Meson Photon Transition Form Factors of Light Pseudoscalar Mesons at Large Momentum Transfer", Phys. Rev. **D57** (1998) 33.
- [59] T. van Rhee, "Charmonium formation in two-photon collisions", Ph.D. thesis, Universiteit Utrecht, 2000.
- [60] G. Kopp, T. F. Walsh and P. Zerwas, "Hadron Production in Virtual Photon - Photon Annihilation", Nucl. Phys. **B70** (1974) 461.
- [61] G. P. Lepage and S. J. Brodsky, "Exclusive Processes in Perturbative Quantum Chromodynamics", Phys. Rev. **D22** (1980) 2157.

- [62] S. J. Brodsky, C.-R. Ji, A. Pang and D. G. Robertson, "Optimal Renormalization Scale and Scheme for Exclusive Processes", *Phys. Rev.* **D57** (1998) 245.
- [63] P. Kroll and M. Raulfs, "The $\pi \gamma$ Transition Form Factor and the Pion Wave Function", *Phys. Lett.* **B387** (1996) 848.
- [64] S. Ong, "Improved Perturbative QCD Analysis of the $\pi \gamma$ Transition Form-Factor", *Phys. Rev.* **D52** (1995) 3111.
- [65] A. V. Radyushkin and R. Ruskov, "The Asymptotics of the Transition Form Factor $\gamma \gamma^* \rightarrow \pi^0$ and QCD Sum Rules", in Proceedings of the 11th International Workshop on Photon-Photon Collisions, ed. A. Buijs and F. C. Erné, (World Scientific, Singapore, 1997).
- [66] A. Anselm, A. Johansen, E. Leader and L. Lukaszuk, "Form Factor $\pi^0 \rightarrow \gamma^* + \gamma^*$ at Different Photon Virtualities", *Z. Phys.* **A359** (1997) 457.
- [67] Th. Feldmann and P. Kroll, "Predictions for the η_c Gamma Transition Form Factor", in Proceedings of the 11th International Workshop on Photon-Photon Collisions, ed. A. Buijs and F. C. Erné, (World Scientific, Singapore, 1997).
- [68] S. J. Brodsky, "Exclusive Photon Photon Processes", in Proceedings of the 11th International Workshop on Photon-Photon Collisions, ed. A. Buijs and F. C. Erné, (World Scientific, Singapore, 1997).
- [69] G. Sterman and P. Stoler, "Hadronic Form Factors and Perturbative QCD", *Ann. Rev. of Nucl. and Part. Sc.* **47** (1997) 461.
- [70] H. Krasemann and J. A. M. Vermaseren, "The 2 gamma Reaction $e^+e^- \rightarrow e^+e^-\pi^+\pi^-$ in the Resonance Region", *Nucl. Phys.* **B184** (1981) 269.
- [71] R. N. Cahn, "Production of Spin 1 Resonances in Gamma Gamma Collisions", *Phys. Rev.* **D35** (1987) 3342.
- [72] M. Poppe, "Exclusive Hadron Production in Two Photon Reactions", *Int. J. Mod. Phys.* **A1** (1986) 545.
- [73] D. Morgan, M. R. Pennington and M. R. Whalley, "A Compilation of Data on Two Photon Reactions Leading to Hadron Final States.", *Phys. G20 Suppl.* **8A** (1994) A1.
- [74] B. Guberina, J. H. Kuhn, R. D. Peccei and R. Ruckl, "Rare Decays of the Z^0 ", *Nucl. Phys.* **B174** (1980) 317.
- [75] J. H. Kuhn, J. Kaplan and E. G. O. Safiani, "Electromagnetic Annihilation of e^+e^- into Quarkonium States with Even Charge Conjugation", *Nucl. Phys.* **B157** (1979) 125.
- [76] R. Gastmans, W. Troost and T. T. Wu, "Production of Heavy Quarkonia from Gluons", *Nucl. Phys.* **B291** (1987) 731.

- [77] R. Gastmans and T. T. Wu, "*The Ubiquitous photon: Helicity method for QED and QCD*", (Clarendon Press, Oxford, 1990).
- [78] E. J. Eichten and C. Quigg, "*Quarkonium Wave Functions at the Origin*", Phys. Rev. **D52** (1995) 1726.
- [79] W. Kwong, P. B. Mackenzie, R. Rosenfeld and J. L. Rosner, "*Quarkonium Annihilation rates*", Phys. Rev. **D37** (1988) 3210.
- [80] H. Kolanoski, "*Two Photon Physics at e^+e^- Storage Rings*", volume 105, (Springer-Verlag, 1984).
- [81] B. R. Martin and G. Shaw, "*Particle Physics*", (Wiley, Chicester, 1997).
- [82] S. Godfrey and N. Isgur, "*Mesons in a Relativized Quark Model with Chromodynamics*", Phys. Rev. **D32** (1985) 189.
- [83] S. J. Brodsky and G. R. Farrar, "*Scaling Laws for Large Momentum Transfer Processes*", Phys. Rev. **D11** (1975) 1309.
- [84] G. A. Schuler, "*Two-Photon Physics with GALUGA 2.0*", Comput. Phys. Commun. **108** (1998) 279.
- [85] J. A. M. Vermaseren, "*Symbolic Manipulation with FORM*", (CAN, Amsterdam, 1990).
- [86] F. A. Berends and W. Giele, "*The Six Gluon Process as an Example of Weyl-van-der-Waerden Spinor Calculus*", Nucl. Phys. **B294** (1987) 700.
- [87] W. T. Giele, "*Properties and Calculations of Multiparton Processes*", Ph.D. thesis, Rijksuniversiteit Leiden, 1989.
- [88] J. G. M. Kuijf, "*Multiparton Production at Hadron Colliders*", Ph.D. thesis, Rijksuniversiteit Leiden, 1991.
- [89] S. Dittmaier, "*Weyl-van-der-Waerden Formalism for Helicity Amplitudes of Massive Particles*", Phys. Rev. **D59** (1999) 016007.
- [90] H. Pilkuhn, "*The Interactions of Hadrons*", (North-Holland, Amsterdam, 1967).
- [91] P. Cho, M. B. Wise and S. P. Trivedi, "*Gluon Fragmentation into Polarized Charmonium*", Phys. Rev. **D51** (1995) 2039.
- [92] E760 Collab., T. A. Armstrong et al., "*Study of the Angular Distribution of the Reaction $\bar{p}p \rightarrow \chi_{c2} \rightarrow J/\psi\gamma \rightarrow e^+e^-\gamma$* ", Phys. Rev. **D48** (1993) 3037.
- [93] R. van Gulik, "*GaGaRes: A Monte Carlo Generator for Resonance Production in Two-Photon Physics*", Nucl. Phys. Proc. Suppl. **82** (2000) 311.
- [94] W. Metzger, "*Statistical Methods in Data Analysis*", Hoge Energie Fysica Nijmegen343, 2000.

- [95] F. James, "Monte Carlo Theory and Practice", Rept. Prog. Phys. **43** (1980) 1145.
- [96] F. A. Berends, P. H. Daverveldt and R. Kleiss, "Monte Carlo Simulation of Two Photon Processes. 1. Radiative Corrections to Multiperipheral $e^+e^- \mu^+ \mu^-$ Production", Comput. Phys. Commun. **40** (1986) 271.
- [97] F. E. Close and G. A. Schuler, "Central Production of Mesons: Exotic States versus Pomeron Structure", Phys. Lett. **B458** (1999) 127-136.
- [98] F. E. Close, "Filtering Glueball from $q\bar{q}$ Production in Proton Proton or Double Tagged $e^+e^- \rightarrow e^+e^- R$ and Implications for the Spin Structure of the Pomeron", Phys. Lett. **B419** (1998) 387.
- [99] Lep Injector Study Group, "LEP Design Report Volume I", CERN-LEP/TH/83-29 (1983).
- [100] Lep Injector Study Group, "LEP Design Report Volume II", CERN-LEP/84-01 (1984).
- [101] Lep Injector Study Group, "LEP Design Report Volume III", CERN-AC/96-01 (1996).
- [102] E. N. Koffeman, "A Luminosity Measurement at LEP using the L3 detector", Ph.D. thesis, Katholieke Universiteit Nijmegen, 1996.
- [103] L3 Collab., "The Construction of the L3 Experiment", Nucl. Instrum. Meth. **A289** (1990) 35.
- [104] L3 SMD Collab., M. Acciarri et al., "The L3 silicon microvertex detector", Nucl. Instrum. Meth. **A360** (1995) 103.
- [105] L3 F/B Muon Group, A. Adam et al., "The Forward Muon Detector of L3", Nucl. Instrum. Meth. **A383** (1996) 342.
- [106] A.-P. Colijn, "Measurement of the tau lepton lifetime", Ph.D. thesis, Universiteit van Amsterdam, 1999.
- [107] K.-T. Chao, H.-W. Huang, J.-H. Liu and J. Tang, "Pseudo-Scalar Heavy Quarkonium Decays With Both Relativistic and QCD Radiative Corrections", Phys. Rev. **D56** (1997) 368.
- [108] A. Bohrer, "Bottom Production in Two-Photon Collisions at LEP", (2001), to appear in the DIS01 conference proceedings.
- [109] R. Brun et al., "GEANT3", CERN DD-/EE/84-1 (Revised 1987).
- [110] T. Sjostrand, "High-energy Physics Event Generation with PYTHIA 5.7 and JETSET 7.4", Comput. Phys. Commun. **82** (1994) 74.

- [111] S. Jadach and W. Placzek and E. Richter-Was and B. F. L. Ward and Z. Was, "Upgrade of the Monte Carlo program BHLUMI for Bhabha scattering at low angles to version 4.04". Comput. Phys. Commun. **102** (1997) 229.
- [112] F. A. Berends and R. Kleiss, "Distributions for Electron-Positron Annihilation into Two and Three Photons", Nucl. Phys. **B186** (1981) 22.
- [113] R. Engel, "Hadronic Interactions of Photons at High Energies", Ph.D. thesis, Universität-Gesamthochschule-Siegen, 1997.
- [114] L3 Collab., M. Acciarri et al., "Higgs Candidates in e^+e^- Interactions at $\sqrt{s} = 206.6$ GeV", Phys. Lett. **B495** (2000) 18.
- [115] Aleph Collab., R. Barate et al., "Observation of an Excess in the Search for the Standard Model Higgs Boson at ALEPH", Phys. Lett. **B495** (2000) 1.
- [116] S. Jadach, B. F. L. Ward and Z. Was, "The Precision Monte Carlo Event Generator KK for Two-Fermion Final States in e^+e^- Collisions", Comput. Phys. Commun. **130** (2000) 260.
- [117] M. Wadhwa, private communications.
- [118] CLEO II Collab., B. I. Eisenstein et al., "Experimental Investigation of the Two-Photon Widths of the χ_{c0} and the χ_{c2} mesons", Phys. Rev. Lett. **87** (2001) 061801.
- [119] E760 Collab., T. A. Armstrong et al., "Measurement of the $\gamma\gamma$ Partial Width of the χ_2 Charmonium Resonance", Phys. Rev. Lett. **70** (1993) 2983.
- [120] CLEO II Collab., V. Shelkov et al., "Measurement of Two Photon Production of the χ_{c2} ", Phys. Rev. **D50** (1994) 4265.
- [121] R704 Collab., C. Baglin et al., "Direct Observation and Partial Width Measurement of $\gamma\gamma$ Decay of Charmonium States", Phys. Lett. **B187** (1987) 191.
- [122] A. Buijs, "Charmonia in Photon Photon Collisions", Acta Phys. Polon. **B31** (2000) 2371.
- [123] C. Patrignani, "On the Particle Data Group Evaluation of χ_{c1} and ψ' Branching Ratios", Phys. Rev. **D64** (2001) 034017.

List of abbreviations

<i>Abbreviation:</i>	<i>Description:</i>	<i>Section:</i>
ALR	Active Lead Rings	7.2
BGMS	Budnev, Ginzburg, Meledin and Serbo [16]	2.5
BGO	Bismuth Germanium Oxide, Bismuth Germanate ($\text{Bi}_4(\text{GeO}_4)_3$)	7.2.2
BHLumi	Monte Carlo generator for the proces $e^+e^- \rightarrow e^+e^- + n\gamma$ [111]	8.4
CERN	Conseil Européen pour la Recherche Nucléaire, European Centre for Particle Physics	7.1
CG	Clebsch Gordan	
C.L.	Confidence Level	
CM	Centre of Mass	
DCA	Distance of Closest Approach to the beam line	9.1
DPM	Dual Parton Model	8.5
DSU/DVN	Standard data format for the L3 analyses	7.3
ECAL	Electromagnetic CALorimeter	7.2.2
EMMA	Extended Missing Mass Analysis	8.5
EPA	1:Equivalent Photon Approximation	2.5
	2:Electron Positron Accumulator	7.1
FBSB	Data format to which the LUMI information is written	7.3
JETSET	Monte Carlo generator for the decay of the produced resonances	8.4
GaGaRes	(GAMMA GAMMA to RESONance) Monte Carlo generator for resonance production in two-photon physics	6.2
Galuga	Monte Carlo generator for resonance production based on the BGMS formalism [84]	
HCAL	Hadronic CALorimeter	7.2
KK2F	Monte Carlo generator for the process $e^+e^- \rightarrow f\bar{f} + n\gamma$ [116]	8.6
LEP	Large Electron Positron collider	7.1
LIL	Lep Injector Linacs	7.1
LUMI	LUMInosity monitor	7.2.3
MIP	Minimum Ionizing Particle	7.2.2
MUCH	MUon CHamber	7.2
NRQCD	Non-Relativistic QCD [29]	2.7
PDG	Particle Data Group [13]	
PHOJET	Monte Carlo generator based on the DPM for the generation of continuum hadron production in two-photon physics [113]	8.5

<i>Abbreviation:</i>	<i>Description:</i>	<i>Section:</i>
PMMA	Pure Missing Mass Analysis	8.3
PS	Proton Synchrotron	7.1
RF	Radio Frequency	7.1
RRF	Resonance Rest Frame	5.1
SMD	Silicon Microvertex Detector	7.2.1
SPS	Super Proton Synchrotron	7.1
SU(N)	Group of which the fundamental representation is given by the Special Unitary $N \times N$ matrices	
QCD	Quantum ChromoDynamics	
QED	Quantum ElectroDynamics	
TEC	Time Expansion Chamber	7.2.1
VDM	Vector-meson Dominance Model	2.8
VSAT	Very Small Angle Tagger	7.2.3
WvdW	Weyl-van der Waerden	4.2, Appendix B

Samenvatting

Wanneer men twee lichtbundels elkaar laat doorkruisen, gebeurt er ogenschijnlijk niets. Beide stralen vervolgen onverstoord hun weg. Dit verschijnsel werd al in 1690 beschreven door Christiaan Huygens in zijn verhandeling "Traité de la lumière". Dit gedrag van licht is goed te verklaren door het in termen van zich voortplantende golven te beschrijven. De bijbehorende golfvergelijkingen kunnen op zeer elegante wijze worden samengevat in de Maxwell vergelijkingen. Dit wordt de klassieke beschrijving van licht genoemd.

Zoals vaak in de natuurkunde gaan de klassieke vergelijkingen niet meer op zodra men op microscopische schaal gaat kijken. Dan blijkt er toch meer aan de hand te zijn. De lichtstralen kunnen elkaar wel degelijk verstrooien en zelfs exotischer dingen kunnen gebeuren indien het licht een voldoende korte golflengte heeft: er kunnen andere deeltjes gevormd worden. De klassieke golftheorie is niet meer toereikend om dit soort processen te beschrijven. Voor een meer adequate beschrijving heeft men de kwantummechanica nodig, in het bijzonder de kwantumveldentheorie. In deze theorie hebben de elementaire deeltjes naast golfeigenschappen ook deeltjeseigenschappen. Een lichtstraal is dan te beschouwen als een bundel lichtdeeltjes, fotonen. Deze fotonen zijn de boodschappers van de elektromagnetische kracht die tussen geladen deeltjes optreedt. Deze elektromagnetische kracht heeft een oneindig lange dracht, hetgeen impliceert dat de fotonen massaloos zijn en dat ze dientengevolge altijd met de lichtsnelheid voortbewegen.

Verstrooiing van licht kan in deze kwantummechanische context beschreven worden door het proces waarbij twee fotonen beide voor korte tijd fluctueren naar een deeltje en zijn antideeltje. Deze virtuele deeltjes kunnen vervolgens met elkaar een reactie aangaan waarna ze weer annihileren tot twee fotonen die niet per definitie dezelfde richting hoeven te hebben als de oorspronkelijke fotonen. Voor zichtbaar licht is deze kans op verstrooiing verschrikkelijk klein, maar voor fotonen met een hogere energie wordt deze kans aanzienlijk. Wanneer de fotonen voldoende energetisch zijn, met andere woorden wanneer de frequentie van de lichtbundels voldoende hoog is, is een spectaculairder effect mogelijk. Energie- en impulsbehoud staan toe dat de fotonen in de reactie verdwijnen en één of meer massieve deeltjes vormen. Dit wordt ook wel inelastische verstrooiing genoemd. Deze vorm van inelastische verstrooiing is een prachtige illustratie van de massa-energie equivalentie uit Einsteins relativiteitstheorie: uit twee energetische *massaloze* fotonen worden *massieve* deeltjes gevormd. Als de twee fotonen in de botsing één deeltje vormen, dan is dat meestal een instabiel deeltje, een resonantie, die weer in allerlei deeltjes uiteen kan vallen.

De deeltjes die bij deze inelastische verstrooiing gevormd worden zijn meestal een fermion-antifermion paar. Fermionen zijn deeltjes met een halfallige intrinsieke spin. Dit kunnen geladen leptonen of quarks zijn. De ons bekende geladen leptonen zijn het elektron, het muon, het tau-deeltje en hun antideeltjes. Van deze zes deeltjes is het elektron het meest

bekend aangezien het één van de componenten is van de atomen, de bouwstenen van alle ons omringende materie. Quarks zijn de deeltjes waaruit de twee andere bouwstenen van het atoom, de kerndeeltjes neutron en proton, opgebouwd zijn. Volgens de huidige theorie die gebruikt wordt om het gedrag van quarks te beschrijven, de kwantumchromodynamica, mogen deze quarks nooit vrij voorkomen. De theorie staat geen "vrije" quarks toe, maar alleen combinaties van een quark en een antiquark (meson) of van drie quarks (baryon) toe. Dit verschijnsel wordt quarkopsluiting genoemd. De mesonen en baryonen vormen samen de klasse der hadronen.

De hierboven beschreven processen van botsingsexperimenten met twee lichtbundels zijn momenteel nog lastig uit te voeren. Daarom wordt een andere, iets minder voor de hand liggende, methode gebruikt. In elektron-positron versnellers worden elektronen en hun antideeltjes, positronen, versneld om bij hoge energieën de annihilatiereactie tussen deze deeltjes te bestuderen. Geladen deeltjes zijn omringd door een wolk van virtuele fotonen die men op zou kunnen vatten als de boodschappers van de lading van het betreffende deeltje. Wanneer in een elektron-positron versneller het elektron en het positron elkaar nu voldoende dicht naderen kunnen twee van deze fotonen een reactie aangaan en treedt ook hier een twee-foton reactie op. Het bijzondere hier is dat het in deze reactie twee virtuele fotonen betreft die niet massaloos zijn. In dit proefschrift is verslag gedaan van zowel theoretisch als experimenteel onderzoek naar resonantie productie in twee-foton reacties in elektron-positron versnellers.

Na een algemene inleiding tot de twee-foton fysica wordt in hoofdstuk 3 een model voor het beschrijven van resonantie productie in twee-foton reacties geïntroduceerd. Dit model gaat uit van een niet-relativistische benadering. In deze benadering wordt aangenomen dat het quark en het antiquark die de resonantie vormen voldoende zwaar zijn en als gevolg daarvan niet te snel om elkaar heen draaien. Voor 'zware' quarks met de smaken charm en bottom is dit een redelijke aanname. De lichte resonanties, opgebouwd uit up, down en strange quarks, zijn echter wel degelijk relativistische systemen en correcties hierop zijn noodzakelijk. Uit dit model kan de zogenaamde twee-foton breedte van de resonanties berekend worden. Dit is een maat voor de kans dat een resonantie naar twee fotonen vervalft en is omgekeerd evenredig met de typische tijd dat de resonantie bestaat voordat hij naar twee fotonen vervalft. Wanneer de theoretische voorspellingen voor deze twee-foton breedtes vergeleken worden met de experimentele resultaten, levert dit goede overeenstemming op, ook voor de lichte resonanties. Dit laatste geeft een indicatie dat het model ook voor deze resonanties een redelijke beschrijving van de werkelijkheid geeft. Door het proces om te keren kan ook de productie van een resonantie uit twee fotonen die door het binnenkomende elektron en positron afgestraald worden bestudeerd worden. Het bijzondere van de laatste berekening is dat de virtualiteiten van de fotonen, de maat voor hoeveel de massa van de fotonen afwijkt van nul, consequent mee worden genomen. Dit resulteert in een zogenaamd matrixelement dat de twee-foton productie van een resonantie in een elektron-positron botsing beschrijft.

De kans dat een reactie optreedt bij het laten botsen van twee deeltjesbundels is naast de intensiteit van de beide bundels evenredig met de werkzame doorsnede voor de betreffende reactie. In de berekening van de werkzame doorsnede dient geïntegreerd te worden over de absolute waarde van het matrix element in het kwadraat voor de betreffende reactie. In hoofdstuk 4 worden verscheidene manieren gepresenteerd om dit kwadraat te berekenen. De

conventionele techniek leidt tot uitgebreide uitdrukkingen voor het kwadraat gesommeerd over alle spins van in- en uitgaande deeltjes. Deze uitdrukkingen zijn verzameld in appendix A. Naast deze techniek is ook het Weyl-Van der Waerden (WvdW) formalisme gebruikt om dit kwadraat te berekenen. Dit WvdW formalisme is in dit hoofdstuk tevens uitgebreid om optimaal gebruik te maken van de numerieke methodes die in de computertaal FORTRAN90 geïmplementeerd zijn. Deze WvdW methodes zijn goed bruikbaar bij het beschrijven van de productie van de resonantie.

De resonantie die in de twee-foton reactie geproduceerd is zal na korte tijd weer vervallen naar twee of meer deeltjes. Om hier een theoretisch model voor op te stellen is het kwadraat van het matrixelement gesommeerd over alle spins niet voldoende. Voor dit soort processen heeft men de zogenaamde dichtheidsmatrices voor de productie en het verval van de resonantie nodig. Deze dichtheidsmatrices bevatten de informatie over hoeveel welke spintoestand van de resonantie bijdraagt tot de productie en het verval van de resonantie. Voor het berekenen van de componenten van de dichtheidsmatrices is het eerder geïntroduceerde WvdW formalisme gebruikt. In hoofdstuk 5 zijn de dichtheidsmatrices voor de productie van de resonanties gegeven. Tevens is de dichtheidsmatrix uitgewerkt voor het verval van een spin-2 resonantie naar een massief en een massaloos spin-1 deeltje waarna het massieve spin-1 deeltje vervalt naar twee spin- $\frac{1}{2}$ deeltjes. Dit is exact het verval van de χ_{c2} resonantie: $\chi_{c2} \rightarrow J/\psi\gamma \rightarrow l^+l^-\gamma$, waar l een elektron of muon is.

De uitdrukkingen voor de matrixelementen en voor de dichtheidsmatrices zijn geïmplementeerd in het computerprogramma GaGaRes, dat beschreven is in hoofdstuk 6. Dit is een zogenaamde Monte Carlo generator. In een Monte Carlo generator wordt gebruik gemaakt van willekeurig gekozen getallen om berekeningen uit te voeren. In dit geval om de integraties uit te voeren bij het berekenen van de werkzame doorsnede. Het bijkomende voordeel is dat het programma tevens functioneert als een event generator, d.w.z. het programma kan gebeurtenissen, events, simuleren verdeeld volgens de waarschijnlijkheid die gegeven wordt door de bijbehorende werkzame doorsnede. Tevens wordt in dit hoofdstuk een aantal resultaten van GaGaRes gegeven.

Het tweede deel van het proefschrift omvat een tweetal analyses op het gebied van de twee-foton fysica. Deze analyses zijn uitgevoerd met behulp van experimentele gegevens die verzameld zijn met de L3 detector. De L3 detector is één van de vier detectoren bij de cirkelvormige LEP versneller. In LEP worden de elektronen en positronen versneld tot energieën tot ruim 200 GeV. Deze hoge energieën werden vooral nagestreefd om in annihilatie reacties de productie van paren van de zware ijkbosonen Z en W , de boodschappers van de elektrozwakke kracht, te bestuderen en om te zoeken naar het nog niet waargenomen Higgs boson, het deeltje dat via spontane symmetriebreking verantwoordelijk is voor de generatie van de massa van de elementaire deeltjes in het Standaard Model. De LEP versneller en de verschillende onderdelen van de L3 detector worden beschreven in hoofdstuk 7. Inmiddels zijn de experimenten met de LEP versneller gestaakt om plaats te maken voor de toekomstige LHC versneller.

In de eerste analyse is een ontbrekende massa techniek gebruikt. In deze techniek wordt gekeken naar de waargenomen gebeurtenissen waarbij zowel het elektron als het positron, na een foton uitgezonden te hebben, worden gedetecteerd in de detector. Uit de gemeten impuls en energie kan met behulp van energie-impuls-behoud berekend worden hoeveel energie en impuls nog ontbreken en welke massa hierbij hoort. Wanneer een resonantie met

een bepaalde massa vaak geproduceerd zou worden, zou dit een piek op moeten leveren bij die massa in het ontbrekende massa spectrum. Met deze methode is gezocht naar het η_b meson. Dit is de lichtste gebonden toestand bestaande uit twee bottom quarks. Dit deeltje is nog niet experimenteel waargenomen. Ook in de analyse in hoofdstuk 8 is geen piek waargenomen in het ontbrekende massa spectrum. Wel kon met deze analyse uit het afwezig zijn van enig signaal een bovenlimiet op de twee-foton breedte van dit deeltje berekend worden. In de analyse kon een bovenlimiet op de twee-foton breedte van deeltjes met een massa tot 150 GeV gegeven worden, dus ook voor een Higgs deeltje met een verondersteld massa van 115 GeV. In het ontbrekende massa spectrum is er bij 91 GeV wel een signaal waar te nemen. Dit is echter niet afkomstig van een resonantie die bij een twee-foton reactie gevormd is. De piek wordt veroorzaakt door events waarbij beide binnenkomende leptonen een foton afstralen alvorens te annihileren tot een Z boson. Deze afgestraalde fotonen zijn gedetecteerd en resulteren in de piek in het ontbrekende massa spectrum. Dit demonstreert de juistheid van de methode.

In de tweede analyse, die in hoofdstuk 9 gepresenteerd is, is de productie en het verval van de charmonium resonantie, χ_{c2} genaamd, bestudeerd. Deze resonantie is opgebouwd uit twee charm quarks en de totale spin van het deeltje bedraagt 2. Gekeken is naar die χ_{c2} resonanties die als volgt vervallen: $\chi_{c2} \rightarrow J/\psi\gamma \rightarrow l^+l^-\gamma$, waar het lepton l een elektron of een muon mag zijn. Dit is precies het verval waarvoor de dichtheidsmatrix is afgeleid. Uit het waargenomen aantal deeltjes is de twee-foton breedte van de χ_{c2} berekend. Ook is de hoekverdeling van het foton in het rust systeem van de χ_{c2} resonantie bepaald. Tot slot is deze hoekverdeling vergeleken met de theoretische voorspelling die met behulp van de dichtheidsmatrixberekening gedaan is.

Curriculum Vitae

Ik ben op 2 januari 1974 geboren te Vlaardingen. In deze stad haalde ik in 1992 aan het Groen van Prinsterer lyceum mijn Atheneum-B diploma.

Vervolgens ben ik in datzelfde jaar in Leiden aan de studie natuurkunde begonnen. In 1993 behaalde ik de propedeuses voor wis- en natuurkunde. In 1997 heb ik, met lof, de studie natuurkunde afgerond. Onderdelen van deze studie waren een stage aan het Nederlands Instituut voor Kernfysica en Hoge-Energie Fysica (NIKHEF) onder leiding van prof. dr. F.L. Linde en een afstudeeronderzoek op het gebied van de theoretische natuurkunde onder leiding van prof. dr. F.A. Berends en dr. W. Beenakker. Het onderwerp van mijn afstudeeronderzoek betrof harde remstralingcorrecties in de productie van W -paren in elektron-positron annihilatie reacties.

Na mijn afstuderen trad ik in 1997 als assistent in opleiding (AIO) in dienst van de Universiteit Leiden en werd gastmedewerker van het NIKHEF. Mijn promotie-onderzoek dat zowel een theoretisch als een experimenteel deel omvatte stond onder leiding van prof. dr. F.A. Berends en prof. dr. F.L. Linde. Het onderzoek betrof resonantieproductie in twee-foton reacties in elektron-positron versnellers. In het kader van het experimentele deel van mijn promotie-onderzoek verbleef ik 18 maanden op CERN nabij Genève alwaar ik deel uitmaakte van de L3 collaboratie, daartoe in staat gesteld door het NIKHEF.

In het kader van mijn promotie-onderzoek heb ik conferenties in Egmond, Lyon, Freiburg en Balatonfüred bijgewoond. Ook heb ik zomerscholen in Maria Laach, Nieuwpoort, Rolduc en Lake Geneva (VS) bezocht.

Tijdens mijn AIO-aanstelling heb ik twee maal het werkcollege bij het college kwantumveldentheorie verzorgd.

THE HISTORY OF THE

Acknowledgements

De resultaten die in dit proefschrift gepresenteerd zijn, zijn tot stand gekomen met de steun en inzet van vele mensen, zowel in Leiden als op CERN. Hierbij wil ik graag enkele mensen vermelden.

Het NIKHEF ben ik zeer erkentelijk dat het mij in de gelegenheid gesteld heeft om 18 maanden op CERN werkzaam te zijn. Het verrichten van onderzoek in een dergelijke inspirerende en competitieve omgeving is een onvergetelijke ervaring.

I specially enjoyed working with Dr. Gerhard Schuler. The discussions with him gave me more insights into the wonderful world of the interacting photons. His program Galuga was an indispensable help in performing the necessary checks of GaGaRes.

Using the data collected with a large scale experiment like the L3 detector is impossible without the enormous efforts of many people. The discussions in the two-photon group following the updates on my analysis were very useful. In particular, I would like to mention Dr. Maneesh Wadhwa. Without his help it would have been impossible to perform some parts of the missing mass analysis. I would also like to mention Dr. Simon Blyth who gave me the lists of all the fbsb files and Mr. Lachavanne from the IT department who performed the tremendous task of mounting all the raw data tapes.

Mijn voorgangster op de χ_{c2} analyse, Tasja van Rhee, ben ik zeer erkentelijk voor het mij verschaffen van de code van haar analyse programma's en de daarbij behorende uitleg.

Mijn kamergenoten op CERN, Vinod Baldew en Mark Dierckxsens, waren naast een grote bron van gezelligheid ook een onmisbare informatiebron op de momenten dat ik weer onenigheid had met één van mijn analyse programma's.

De oudere generatie L3-promovendi, Auke-Pieter Colijn, Sandra Muijs en Daniël van Dierendonck, hebben het opstarten van mijn experimentele onderzoek sterk versneld door het mij verschaffen van de daartoe benodigde tips en programma's.

Martin Blom heeft het verblijf op CERN tot een zeer aangename ervaring gemaakt. Het nauwgezet doorlezen van dit manuscript op zoek naar inconsistenties op taalkundig gebied waardeer ik zeer.

In Leiden zou ik graag nog Fabian Mettes willen vermelden. De middagpauzes met hem waren zeer aangenaam en soms zelfs leerzaam.

Ik ben mijn ouders zeer dankbaar voor het feit dat ze altijd achter de door mij gemaakte keuzes gestaan hebben. Tot slot wil ik Karensa Refos danken. Zij vormde door haar onvoorwaardelijke liefde, geduld en vertrouwen een onmisbare steun.

Resonance production in two-photon reactions

1. Het feit dat de "hard scattering approach" (HSA) hetzelfde resultaat geeft voor de symmetrische asymptotische limiet van de meson-foton-foton vormfactor $F_{P\gamma\gamma}$ voor de pseudoscalaire mesonen als het door ons beschreven model is een direct gevolg van het feit dat in beide berekeningen de vormfactor afhangt van het "harde" proces $q\bar{q} \rightarrow \gamma\gamma$ en dat in de HSA de verdelingsamplitude in deze limiet Q -onafhankelijk wordt.

Hoofdstuk 3, dit proefschrift.

G.A. Schuler, F.A. Berends and R. van Gulik, Nucl. Phys. B523, (1998) 423.

2. Het is op dimensionele gronden eenvoudig in te zien dat de laatste twee termen in formule (4) in het artikel van Close niet correct kunnen zijn. Wanneer men deze twee termen met een factor u' vermenigvuldigt, dan wordt dit deel van de uitdrukking gelijk aan het overeenkomstige deel van de in dit proefschrift gevonden uitdrukking voor het kwadraat van de absolute waarde van het matrix element behorend bij de twee-foton productie van een 1^{++} -resonantie.

Hoofdstuk 4 en Appendix A, dit proefschrift.

F.E. Close, Phys. Lett. B419, (1998) 387.

3. De energiespectra van de met de L3 detector waargenomen gebeurtenissen met aan beide zijden van het interactiepunt activiteit in de luminositeitsdetectoren en daarnaast ten hoogste twee al dan niet geladen deeltjes in de overige detectoren komen volledig overeen met de spectra uit de Monte Carlo voorspellingen voor de processen $e^+e^- \rightarrow e^+e^- + n\gamma$ en $e^+e^- \rightarrow \gamma\gamma(\gamma)$.

Hoofdstuk 8, dit proefschrift.

4. Wanneer men vergelijking (2.50) met additionele hogere orde QCD correcties [79],

$$\mathcal{R}(\chi_{c2}) = \frac{\Gamma_{gg}(\chi_{c2})}{\Gamma_{\gamma\gamma}(\chi_{c2})} = \frac{9}{8} \left(\frac{\alpha_S(m_c)}{\alpha} \right)^2 \frac{1 - \frac{2.2}{\pi} \alpha_S(m_c)}{1 - \frac{1.6}{3\pi} \alpha_S(m_c)},$$

gebruikt om uit de gemeten twee-fotonbreedte de QCD koppelingsconstante $\alpha_S(m_c)$ te bepalen, dan vindt men een waarde die aanzienlijk lager is dan men uit extrapolaties van α_S -metingen aan de Z^0 -breedte en de τ -levensduur zou verwachten. De gemeten twee-fotonbreedtes bij $p\bar{p}$ -experimenten leveren een $\alpha_S(m_c)$ die beter overeenstemt met deze verwachte waarde.

Hoofdstukken 2 en 9, dit proefschrift.

5. Indien men aanneemt dat de koppeling aan een resonantie van het J/ψ -meson met massa M of van een virtueel foton alleen in sterkte verschilt, dan vindt men voor de verhouding van de vervalsbreedtes van de χ_{c1} - en χ_{c2} -resonanties naar de eindtoestand bestaande uit een J/ψ -meson en een reëel foton

$$R_{th} = \frac{\Gamma(\chi_{c1} \rightarrow \gamma J/\psi)}{\Gamma(\chi_{c2} \rightarrow \gamma J/\psi)} = 5 \frac{M^2(M_{R_1}^2 + M^2)}{M_{R_1}^4} \left(\frac{M_{R_2}}{M_{R_1}} \right)^4 \frac{\alpha_2}{\alpha_1} \frac{1}{10 - 5\alpha_2 + \alpha_2^2} = 0.8969,$$

waarin $\alpha_i = 1 - \frac{M^2}{M_{R_i}^2}$. Deze verhouding komt zeer goed overeen met de experimenteel waargenomen verhouding $R_{exp} = 0.89 \pm 0.15$.

F. A. Berends en R. van Gulik, hep-ph/0110086.

6. In tegenstelling tot wat reeds lange tijd aangenomen werd (sinds Gorkov en Eliashberg (1965) en Denton, Mühlshlegel en Scalapino (1973)) tonen berekeningen aan dat de gemeten soortelijke warmte van een verzameling metaaldeeltjes welke beschreven kunnen worden door een Gaussisch, unitair ensemble, niet kubisch maar lineair in de temperatuur zal zijn.

F. L. Mettes, proefschrift Universiteit Leiden (september 2001).

7. Wanneer de toekomstige LHC versneller van CERN zou opereren met zware Ca-ionen die een Lorentz-factor van 3750 hebben bij een luminositeit van $4 \times 10^{30} \text{cm}^{-2}\text{s}^{-1}$, dan zouden er 36 η_b -mesonen per uur geproduceerd worden. Dit vormt een opmerkelijk verschil met de situatie bij LEP2, waar in het gunstigste geval in totaal 150 η_b -mesonen per experiment geproduceerd zijn.

K. Hencken et al., Nucl. Phys. B (Proc. Suppl.), 82 (2000), 409.

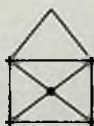
8. Wanneer men bij W -paar productie in elektron-positron botsingen in de uitdrukking voor het t -kanaal diagram de uitgaande W 's verwisselt en het verschil berekent met het oorspronkelijke t -kanaal diagram, verkrijgt men exact de uitdrukking voor het s -kanaal diagram voor hetzelfde proces. In de aanwezigheid van harde remstralingsfotonen gaat dit nog steeds op. Op deze wijze is het kwadraat van de absolute waarde van het matrix element voor het proces $e^+e^- \rightarrow W^+W^-\gamma$ op een compacte wijze in een som van een beperkt aantal relatief simpele functies uit te drukken.

R. van Gulik, "Hard Bremsstrahlung Corrections in the Process $e^+e^- \rightarrow W^+W^-$ ", doctoraalscriptie, Universiteit Leiden.

9. In een scalaire theorie waar de Lagrangiaan gegeven wordt door

$$\mathcal{L} = \frac{1}{3!}\phi^3 + \frac{1}{4!}\phi^4,$$

behoort bij het vacuümdigram, waarin de vertices met een stip aangegeven zijn,



volgens de regels uit de diagrammatica de combinatorieke factor $\frac{1}{2}$.

10. Het door minister Netelenbos geopperde plan om de maximum snelheid op de Nederlandse autosnelwegen te verlagen tot 70 km/u zou wel degelijk een effectief middel zijn in de strijd tegen het fileleed.

D. Helbing, Rev. of Mod. Phys., cond-mat/0012229.

11. Bij grootschalige natuurkunde-experimenten met een looptijd van vele jaren zou het opzetten en bijhouden van een goede en toegankelijke documentatie van de gebruikte soft- en hardware vele voordelen opleveren bij het verrichten van analyses, in het bijzonder voor mensen die niet vanaf het begin bij een dergelijk experiment betrokken zijn.
12. Vergeefs tracht men de momenten die men werkelijk gelukkig was in gedachten nogmaals te beleven. Een algemeen gevoel van weemoed is dan vaak het gevolg.

Robert van Gulik
Leiden, 22 november 2001.